

TECHNICAL REPORTS OF THE METEOROLOGICAL RESEARCH INSTITUTE NO.13

A DESCRIPTION OF THE MRI ATMOSPHERIC GENERAL  
CIRCULATION MODEL (THE MRI · GCM— I)

BY

FORECAST RESEARCH DIVISION, MRI

気象研究所技術報告

第13号

気象研究所大気大循環モデル— I (MRI · GCM— I)

予報研究部

気象研究所

METEOROLOGICAL RESEARCH INSTITUTE, JAPAN

DECEMBER 1984

## Meteorological Research Institute

Established in 1946

Director : Dr. Kiyohide Takeuchi

Forecast Research Division	Head : Mr. Taiji Yoshida
Typhoon Research Division	Head : Dr. Masahiko Aihara
Physical Meteorology Research Division	Head : Dr. Toshio Okabayashi
Applied Meteorology Research Division	Head : Mr. Tsunehiro Majima
Meteorological Satellite Research Division	Head : Dr. Keikichi Naito
Seismology and Volcanology Research Division	Head : Dr. Masaharu Ichikawa
Oceanographical Research Division	Head : Dr. Hayato Iida
Upper Atmosphere Physical Research Division	Head : Dr. Muneyasu Kano
Geochemical Research Division	Head : Mr. Tsutomu Akiyama

1-1 Nagamine, Yatabe-Machi, Tsukuba-Gun, Ibaraki-Ken, 305 Japan

### Technical Reports of the Meteorological Research Institute

*Editor-in-chief* : Tsunehiro

*Editors* : Koji Yamazaki                      Hiroki Kondoh                      Tomoyuki Ito  
                    Tomoaki Yoshikawa                      Jiro Aoyagi                      Masami Okada  
                    Masahiro Endoh                      Kunihiko Kodera                      Katsuhiko Fushimi

*Managing Editors* : Keiko Nishida, Yusai Yuhara

#### Technical Reports of the Meteorological Research Institute

has been issued at irregular intervals by the Meteorological Research Institute since 1978 as a medium for the publication of survey articles, technical reports, data reports and review articles on meteorology, oceanography, seismology and related geosciences, contributed by the members of the MRI.

## 序

大気大循環の研究プロジェクトは、昭和53年からはじめられた。気象研究所に大型計算機が導入されるまでは、比較的簡単なモデルによる研究のほかは、理論的なまたは解析的な研究に限られていた。

大気大循環の研究は、大気運動の基本を理解する多くの知見を与えてきた。これからも、地球上に現れる気候とその変動、さらには長期間の大気運動の予測に対しても欠かすことのできない研究として、その重要性はますます高まるものと思われる。

長い間期待されていた本格的な大気大循環の力学モデルは、多くの方面の理解と支持とによって、予報研究部のスタッフが中心となり開発してきたものである。このモデルによるシミュレーション実験の成果は、平均的気候の再現、気候の長期変動の記述、気候変化をもたらすさまざまな原因の究明などとなって現われている。

しかし、気候変動には多くの未解決の問題が残されており、国際的にも重要な研究課題として提示されている。これらの諸問題の解決をめざして、これからもさまざまな実験をつみ上げ、その結果を評価する仕事をつづけながら、更にモデルを拡張し改善する努力を継続する必要がある。

この報告書は、気象研究所における大気大循環の歴史的記念碑として記録にとどめるばかりではなく、これからの発達の基礎となる資料を提供することを目的として発行されたものである。

昭和59年11月

気象研究所 予報研究部長

吉 田 泰 治

## Foreword

The research project of developing an atmospheric general circulation model was commenced at the forecast research division of the Meteorological Research Institute (MRI) in 1978. In 1980 a high speed computation facility was installed for the first time at the MRI, which enhanced the activities of the project and prompted the research progress that follows.

Since the dawning of numerical investigations of weather prediction and general circulation in 1950's, the outcome from the studies have brought us a large amount of knowledge on the mechanism of the atmospheric evolutions. The important role of the dynamical simulation is still increasing in the fundamental researches of climate and climatic variations.

Although the first version of our global model was designed based on the widely recognized mathematical schemes of grid point method, various innovations developed by the staff members of the project are incorporated into the model. As described in this report, general features of the observed climate are mostly simulated by the model.

In order to understand the causes of climate variability and changes, however, unprecedented research subjects must remain to be solved. Establishment of methodology for long-range weather forecasting also confronts the worldwide meteorological community. The project activities should therefore be expanded further toward those problems through the accumulation of various experiments, analyses of the numerical results and improvement of the model.

The main purpose of the report is not only to remark a mile-stone on the course of the general circulation research at the MRI, but also to provide the basic material for further development in future.

November 1984

Taiji Yoshida, Head  
Forecast Research Division

## Contents

Preface and Introduction .....	7
Chapter 0 : Governing equations in the continuous form .....	10
0.1 The vertical coordinate .....	10
0.2 The equation of state .....	11
0.3 The hydrostatic equation .....	11
0.4 Equation of continuity .....	11
0.5 Momentum equation .....	12
0.6 Thermodynamic equation .....	13
0.7 The continuity equation of water vapor and ozone .....	13
Chapter 1 : Vertical differencing .....	14
1.1 The vertical coordinate and the vertical index .....	14
1.2 Flux form of a variable .....	15
1.3 The equation of continuity .....	16
1.4 The acceleration term .....	16
1.5 The pressure gradient force .....	16
1.6 The first law of thermodynamics .....	17
1.7 Total energy conservation and the hydrostatic equation .....	17
Chapter 2 : Upper boundary condition .....	19
2.1 Introduction .....	19
2.2 The vertical structure equation .....	20
2.3 Effect of the upper boundary condition .....	22
2.4 Sponge layer formulation .....	23
2.4.1 Basic formulation .....	23
2.4.2 Estimation of equivalent depth and frequency .....	25
2.4.3 Extention of the sponge layer model to the non-isothermal case with a constant zonal wind .....	26
A2.1 Test examples of the sponge layer model .....	27
A2.1.1 Model .....	27
A2.1.2 Propagation of a mixed Rossby-gravity wave .....	30

A2.1.3	Propagation of a Kelvin wave.....	32
A2.1.4	Propagation of a Rossby wave .....	34
A2.1.5	Propagation of a semi-diurnal wave .....	34
A2.2	Stability check of Eq. (2.1) as an upper boundary condition.....	36
Chapter 3	: Horizontal differencing.....	40
3.1	Horizontal grid and indices.....	40
3.2	The equation of continuity .....	41
3.3	The pressure gradient force .....	42
3.4	Kinetic energy generation and the first law of thermodynamics.....	42
3.5	Momentum fluxes .....	44
3.6	Coriolis force .....	46
Chapter 4	: Special treatment near the poles .....	47
4.1	Modification of the difference equation .....	47
4.2	Introduction of averaging operator to selected terms.....	49
Chapter 5	: Time integration.....	50
Chapter 6	: Transport process of moisture and ozone .....	51
6.1	Vertical differencing of the moisture equation .....	51
6.2	Vertical interpolation of moisture and "CICK".....	53
6.3	Vertical differencing of the ozone equation .....	55
6.4	Horizontal differencing.....	55
Chapter 7	: Penetrative cumulus convection.....	57
7.1	Introduction .....	57
7.2	Cloud model I: modification of the large-scale environment by cumulus clouds .....	57
7.3	Cloud model II: Cloud ensemble model .....	62
7.4	The closure assumption: quasi-equilibrium assumption .....	65
7.5	The vertical structure of the discrete model and the discretized form of the cloud model .....	69
7.5.1	The vertical structure of the discrete model .....	69
7.5.2	The mass budget .....	70

7.5.3	The moist static energy budget .....	71
7.5.4	The total water budget .....	73
7.5.5	The solution procedure for $\lambda(i)$ .....	74
7.6	The discrete form of the mass flux distribution equation .....	74
7.6.1	The discretized equation .....	74
7.6.2	The large-scale forcing .....	75
7.6.3	The mass flux kernel .....	76
7.6.4	The cloud work function .....	78
7.7	Solution of the mass flux distribution equation .....	78
7.8	The large-scale budget and cumulus cloud feedback on the large-scale fields .....	81
7.9	Ice phase parameterization .....	83
A7.1	Some results from simulation studies .....	83
A7.1.1	Precipitation .....	86
A7.1.2	Cumulus cloud base mass flux .....	88
A7.1.3	Comparison with Marshall Islands data .....	88
A7.1.4	Cloudiness .....	90
A7.2	Simple examples of the solution for the mass flux distribution equation .....	91
Chapter 8 : Planetary boundary layer .....		97
8.1	Introduction .....	97
8.2	Governing equations for the large-scale circulation .....	97
8.3	Diagnostic determination of the entrainment rate at the top of the PBL and of turbulent fluxes .....	100
8.4	Stratus layer .....	106
8.5	Vertical structure of the PBL model and the interpolation scheme .....	107
8.6	Numerical procedures .....	110
A8.1	Some examples of the PBL model performances .....	113
Chapter 9 : Convective adjustments and condensation .....		121
9.1	Some definitions of variables .....	122
9.2	Dry convective adjustment .....	123
9.3	Middle level convection .....	124

9.4	Large-scale condensation	126
Chapter 10 : Ground hydrology and thermodynamics		
10.1	Types of the earth's surface and related constants	130
10.1.1	Roughness	130
10.1.2	Thermal conductivity	130
10.1.3	Heat capacity	131
10.1.4	Bulk heat capacity	131
10.2	Land surface temperature and heat balance	131
10.3	Surface hydrology and soil water budget	132
10.3.1	Surface evapotranspiration	132
10.3.2	Snow	133
10.3.3	Interstitial moisture and interstitial ice	134
10.3.4	Runoff	134
Chapter 11 : Vertical and horizontal sub-grid-scale transports		
11.1	Cumulus transport of momentum	135
11.2	Vertical diffusion	137
11.3	Horizontal diffusion	137
Chapter 12 : Photochemical process of ozone		
12.1	Photochemical reactions	139
12.2	Governing equations for the photochemical reactions	140
12.3	Vertical distribution of absorber amounts	141
12.4	Ozone destruction at the earth's surface	142
Chapter 13 : Radiation		
13.1	Introduction	143
13.2	Terrestrial radiation	144
13.2.1	Basic equations	144
13.2.2	Simplification : Weighted mean transmission functions	145
13.2.3	Cloudless atmosphere	146
13.2.4	Cloudy atmosphere	149
13.2.5	Effective absorber amounts	150
13.2.6	Empirical transmission function equations	151

13.2.7	Long wave radiative cooling in the upper stratosphere .....	153
13.3	Solar radiation .....	154
13.3.1	Basic quantities .....	154
13.3.2	Absorptivity of water vapor .....	155
13.3.3	Absorptivity of ozone .....	156
13.3.4	Cloudless atmosphere .....	157
13.3.5	Cloudy atmosphere .....	159
13.3.6	The reflectivity and absorptivity of clouds .....	162
A13.1	Calculation of earth-sun distance and solar zenith angle .....	162
A13.1.1	Earth-sun distance .....	162
A13.1.2	Solar zenith angle .....	163
A13.2	Water vapor absorptivity function for the total solar spectrum, $A'_{H_2O}(X)$ . .....	164
A13.3	Ozone absorptivity function for the total solar spectrum, $A'_{O_3}(X)$ . .....	168
Appendix I	: Tree diagram of the MRI • GCM- I .....	170
Appendix II	: Surface boundary conditions and numerical constants used in the MRI • GCM-I .....	171
Appendix III	: Selected monthly mean fields produced by the MRI • GCM-I .....	178

## 概 要\*

気象研究所大気大循環モデル (MRI・GCM-I) は、UCLAモデル (Arakawa and Mintz, 1974; Arawawa and Lamb, 1977) を基に開発したものである。モデルで予報している変数は、風の水平成分、気温、水蒸気とオゾンの混合比、地面温度、土壌層の湿潤度、積雪の深さ、境界層の厚さおよび境界層の上端における物理量のギャップである。地表のアルベドは表面状態の簡単な関数として与えている。雲量はモデルで診断的に決め、放射の計算を通して大気加熱率に影響を与える。モデルには現実に対応する海陸分布と地形がある。海面水温と海水の分布は気候値に基づいて外部データとして与えている。モデル大気のトップに入射する太陽光は季節変化と日変化をしており、このためモデル大気には季節変化と同様に日変化が再現される。以下の節では本論に従ってモデルの概略を述べる。

### 1. 鉛直差分モデル

鉛直方向の各層への物理量は、波の分散関係等からFig. 1.1のスキームCに基づいて配置されている (Tokioaka, 1978)。層の位置はFig. 1.2のように与えている。 $p=p_i$ より上の層は $\ln p$ に関して等間隔になるように選んでいる。大気を等温大気とみなした場合、これが内部波を最もうまく表現する層の選び方になっているからである (Tokioaka, 1978)。現在、MRI・GCM-Iとして、対流圏の5層モデルと成層圏を含んだ12層モデルを採用している。

鉛直差分形の決定に際しては、全エネルギーが保存すると同時に、静力学平衡の式の精度を上げるよう配慮している。

### 2. 上部境界条件

通常、モデルの上端における境界条件として、 $p=p_t$  ( $\neq 0$ ) で $\dot{\sigma}=0$  が用いられている。これは $p=p_t$ に剛体の壁を置いて上下方向の空気の出入りを禁じたことになり、波のニセの反射をもたらす。 $p_t=0$ にした場合でもこの状況は変わらない。その場合、モデル最上層の厚さはZ座標系で見ると非常に厚くなり、この中で起こる上下方向のサブグリッドスケールの物理過程をモデルに取り入れられない限り波のニセの反射が起きてしまう。

MRI・GCM-Iでは上部境界条件として、 $p=p_t$ で $\dot{\sigma}=0$ を採用している。そして、波のニセの反射を防ぐためにモデルの最上層にスポンジ層を設定している。スポンジ層では、熱力学の第一法則の式にニュートン冷却の形の補正項を導入している。このニュートン冷却率は複素数であるの

---

\* 時岡達志・山崎孝治・谷貝勇・鬼頭昭雄：予報研究部

が特徴で、モード、特に振動数に強く依存する。ニュートン冷却率の実数部分は波を減衰させ、虚数部分は鉛直波長を変える働きをする。

### 3. 水平差分

モデルでは球面座標が用いられ、緯度方向 $\phi$ と経度方向 $\lambda$ に一定の間隔で変数が配置されている。(標準のモデルでは $\Delta\phi = 4^\circ$ 、 $\Delta\lambda = 5^\circ$ ) 各変数をどのように配置するかは波の分散と密接に関係しており、Fig. 3.1の5つの場合の中で、スキームCが現実大気を考える限り最も適切であることが知られている (Winninghoph 1968, Arakawa and Mintz 1974, Arakawa and Lamb 1977)。この結果に基づきMRI・GCM-IではスキームC (Fig. 3. 2) を採用している。

運動量の水平移流の表現は、曲率のない二次元非発散流に対してエネルギーおよびエンストロフィ (渦度の二乗の半分) を保存するスキーム (Arakawa and Mintz, 1974, Arakawa and Lamb, 1977) になっている。気圧傾度力の差分表現は、地形が存在していても気柱の循環に偽の加速を与えないものになっている。

### 4. 極付近での取り扱い

極は球面座標を用いると特異点になり、ベクトル量である風は定義できない。このため、運動方程式における移流項は極付近で特別に扱う必要がある。モデルではFig. 4. 2のように極から半グリッドずれた所に南北風 $v$ を定義している。

極付近では東西方向のグリッド間隔がせまくなる。一定の積分時間間隔 $\Delta t$ を用いても計算不安定を生じさせないためには、いくつかの項に対して東西方向の平滑化を行なえばよいことが示されている (Arakawa, 1972)。ここではこの考えに基づいて、さらに渦度に対する偽の加速を生じさせないような平滑化を行なっている。

### 5. 時間積分

Fig. 5. 1に示したように、leapfrogスキーム (図中、Lと表示) とMatsunoスキーム (M) を併用した時間積分法を用いている。非断熱項の計算はQで表わした時点で実行し、その直後にMatsunoステップを行なう。

### 6. 水蒸気とオゾンの輸送

水蒸気とオゾン、生成・消滅過程を除いて、風によって受動的に流されて変化する。ただし、水蒸気量、オゾン量は常に正であるべき量である。このため、これらの移流の計算スキームには運動量の移流スキームとは別の工夫を施している。

## 7. 積雲対流のパラメタ化

積雲対流のモデルはArakawa and Schubert (1974)の理論を基に作られていて、積雲それ自身のモデル化と積雲のマスフラックスの決定 (closure assumption) の二つの部分に分けることができる。

積雲モデルでは雲頂高度によって積雲の型を分類する。雲頂高度は、取り込み率(entrainment rate)  $\lambda$  が雲中の高度によらないとして決定される。 $\lambda$  の大きい雲は周囲の空気とよく混合し背の低い雲になり、 $\lambda$  の小さい雲は背の高い雲に対応する。積雲はそれが誘起する補償下降流によって周囲を昇温、乾燥化させる。また、雲頂で放出する飽和した気塊の蒸発、混合によって周囲の場を冷却、湿潤化する(式(7.31)参照)。積雲の根は大気境界層(PBL)にあり、PBL内の気塊を取り込む。この取り込みによってPBLの厚さは薄くなるようになっている(式(8.1)参照)。

雲頂が $-20^{\circ}\text{C}$ より低い気温の層に達した場合、 $-20^{\circ}\text{C}$ 以下の層で氷相になると仮定して氷晶過程を取り入れている。

積雲のマスフラックスの決定は次のような考えに基づいている。すなわち大規模場が湿潤不安定な状態を作ると積雲の集団が発生して、主に補償下降流の作用で不安定状態を解消する。そして大規模場が安定になると積雲の発達を抑えられる。このような相反する作用間の準平衡状態としてグリッドスケールの場合が決定されていると考えて、各型の積雲対流のマスフラックスを決定する。具体的には、積雲内の浮力による雲仕事関数(式7.48)が、大規模スケールの時間内に変化しないという準平衡の仮定を用いている。マスフラックスが決まると積雲モデルによって大規模場の気温・水蒸気量に及ぼす影響が計算される。

## 8. 大気境界層(PBL)のパラメタ化

Arakawa and Mintz (1974), Randall (1976)を基にしたモデルになっている。基本的に、PBL内の乱流は保存量の分布を上下に一様化するような乱流輸送を行なうと仮定している。地表面でのフラックスは、外部境界層まで拡張した相似則に基づくバルク法(Deardorff, 1972)で決定している。PBL上端でのフラックスを決めるにはPBL上端での自由大気を取り込み率(E)が必要となる。EはPBL内の乱流運動エネルギー収支に基づいて決定する方式を採っている。モデルを閉じさせるためには、PBLの深さ及びPBL内の平均的物理量を知る必要がある。このために、PBLの深さ及びPBL上端での物理量のギャップ量を予報変数につけ加えている。PBL内で凝結が生じた場合は層雲、それが地上まで達した場合は霧とみなしている。層雲(霧)が及ぼす放射への影響は、PBLの発達や乱流輸送量を決定する上で考慮するが、格子点の雲量には反映させていない。又、雨滴として落下することもないとしている。

## 9. 対流調節と凝結

大循環モデルの中では次の順序で調節過程を行なう。まず第1番目に乾燥対流調節を行なう。乾燥対流調節は各点で成層が絶対不安定にならないようにチェックし、不安定になった場合は乾燥静的エネルギーを保存するように中立な状態に調節する。

2番目に自由大気中の湿潤対流 (Middle level convection) の可能性を調べる。上下の2層を考えた場合、下層の湿潤静的エネルギーが上層の飽和湿潤静的エネルギーを越えると湿潤不安定な状態になる。下層がPBL内にあれば、7で述べた積雲が発生するが、自由大気中で湿潤不安定が起こると積雲対流と同様な方式で湿潤対流調節を行なう。ただし、準平衡の仮定を用いず緩和時間 $\tau$ を60分と仮定して閉じさせている。この結果、上層では対流雲から放出される湿った気塊で湿潤化され、下層では水蒸気を失い、同時に上層では対流雲の補償下降流で暖められて気層は安定化する。こうして湿潤対流に対して中立な状態に調節する。

3番目に大規模凝結の可能性を調べる。グリッドの水蒸気が過飽和になった場合、大規模凝結が起こる。この時、湿潤静的エネルギーを保存し、かつ湿潤曲線上にのるように状態を調節する。雨はすぐ下の層に落下させ、そこで一旦蒸発させる。この手順を上層から下の層に向かって繰り返していく。

最後に7で述べた積雲対流の可能性を調べる。以上4種の過程によって対流調節は完了する。

## 10. 地表面の水文過程と熱収支

モデルの中で地球の表面は、海洋、海水、陸水、湖そして陸地の5つに分類して取扱っている。海面温度及び海水分布は、気候値に基づいて与えている。海水、陸水、陸地、雪の表層温度は予報変数である。表面温度の予報は片山の方式 (Arakawa and Mintz, 1974) に基づいており、媒質中の伝導も考慮している。海水の場合は厚さが3mと仮定している。

水文過程の取扱いは、基本的にManabeの方式 (Holloway and Manabe, 1971) に基づいている。土壌中に含みうる最大含水量をデータとして与え、これを越えた水分は流出として扱おう。地面からの蒸発量は、表面がぬれているとした時の蒸発量に湿潤度 (土壌水分/最大含水量) の関数である効率因数を掛けて求める。湖の場合は湿潤度が常に1である陸地とみなして取扱っている。地面温度が氷点 ( $T_i = 273.1^{\circ}\text{K}$ ) 以下になった場合、凍結水分量も予報している。地表面気温が $T_i$ より低い場合、降水は雪であるとみなし、陸上では積雪量を予報している。

## 11. サブグリッドスケールの輸送

大気境界層中の鉛直方向のサブグリッドスケールの輸送は8で述べたように扱っている。自由大気中の積雲対流による熱及び水蒸気量輸送は7で述べた通りである。積雲対流による運動量輸送は、7で求められる各型の積雲のマスフラックスに従って保存量として、再配分されると考え

てその効果を取り入れている。その他の鉛直拡散は一切入っていない。

水平方向のサブグリッドスケールの輸送は運動量に対して、Holloway and Manabe (1971)の方式による非線型渦動拡散効果を入れている。他の物理量に対する水平拡散は一切入っていない。

## 12. オゾン光化学反応

オゾン光化学反応のパラメタリゼーションはCunnold et al. (1975)およびSchlesinger and Mintz (1979)のモデルに基づいている。100mbより上の成層圏でChapman反応および、簡単なNO-NO<sub>2</sub>サイクルを考慮してオゾン量の生成/消滅量を求めている。オゾンは地表付近の化学反応によって破壊されるが、この過程はPBLにおける鉛直方向のオゾン乱流フラックスが地表に到達して、そこで破壊されると仮定してパラメタ化している。

## 13. 放 射

Katayama (1972), Schlesinger (1976)によるモデルを採用している。モデルは地球放射によって生じる冷却率を求める部分と、太陽放射の吸収による加熱率を求める部分に分けられる。この放射モデルで用いる水蒸気とオゾン量は予報されたものを用いているが、炭酸ガスは一定の混合比を与えている。このモデルの一つの特徴は、計算が効率よく行なえるために、日変化を考慮し得る点である。

30kmより下の層での地球放射の計算ではKatayama (1972)の方式に従っている。この方式では、計算時間の効率化のため、Yamamoto (1952)に従った荷重平均の透過関数を導入している。さらに、水蒸気、炭酸ガスそしてオゾンが同時に存在する場合、全体の透過関数はそれぞれの透過関数の積で近似している。

MRI・GCM-IではFig.13. 4に模式的に示したように5種類の雲が発生する。1)大規模場の凝結による雲 2)背の高い積雲が発生した時に伴う巻雲 3)積雲 4)中層対流による凝結 5)PBLで発生する層雲

この内、最初の2つのみが現在、放射と相互作用を持つ。雲は赤外放射に対して黒体とみなすが、巻雲の場合は灰色として扱い、黒体度0.5をかけている。

上部成層圏では、平均の透過関数を用いたKatayamaの方法は精度が低下するため、モデルの30km以上ではDickinson (1973)によるパラメタリゼーションを採用している。

太陽放射の計算では、波長0.9 $\mu$ を境にしてオゾンによる吸収はあるが対流圏では主としてRayleigh散乱のみを受ける“散乱部分”(短波長側)と、より波長が長く水蒸気によって吸収を受けるがRayleigh散乱が無視できる“吸収部分”に分けて計算している。

太陽放射に関して、診断的に決定した先ほどの2種類の雲の効果を取り入れている。それらの雲のアルベドは高度と厚さの関数として与えている。これらの値は“散乱部分”と“吸収部分”

で別々の値を与えている。また、雲があった場合、雲と雲、あるいは雲と地表の間における多重反射も考慮している。エアロゾルによるMie散乱と吸収は現在のところ組み込まれていない。

5層モデルの1月、4月、7月、10月のパフォーマンスをAppendixに示す。

## Preface and Introduction\*

A description of the general circulation model of the Earth's atmosphere currently used at the Meteorological Research Institute (*i. e.* the MRI • GCM- I ) is given in this report. The main reason for us to present this description is not because we have developed an original GCM. The MRI • GCM- I is based on the previous version of the UCLA • GCM, the description of which is given by Arakawa and Mintz (1974). Mathematical part of the model is also detailed by Arakawa and Lamb (1977). Modeling principles described in both of the descriptions are closely followed by the MRI • GCM- I . Thus it might seem to be needless for us to write a description again, although revisions of the model have been made in several respects. As the description by Arakawa and Mintz (1974) has not been distributed widely, especially in Japan, physical part of the UCLA • GCM, except possibly cumulus part, has not been known widely compared to the mathematical part of it. This is the main reason for us to present this description without fearing repetitions of explanations found in Arakawa and Mintz (1974) or Arakawa and Lamb (1977). To summarize details of the MRI • GCM- I , including boundary conditions and empirical constants adopted, is another purpose of this description.

This report can be separated into two parts. One is the mathematical part, where the treatment of adiabatic fluid motions is described. Chapters 1 through 6 are devoted to this end. Chapter 1 describes vertical differencing. In Chapter 2, problems related to the upper boundary condition is discussed. Horizontal differencing is described in Chapter 3. In Chapter 4, special treatments of the horizontal differencing near the poles are given. Chapter 5 describes time differencing. In Chapter 6 is found a description of advective process of water vapor and ozone.

The other is the physical part, where diabatic processes as well as sub-grid-scale processes important for the global atmospheric circulation are described. The processes included are schematically shown in Fig. P1. They are covered in Chapters 7 through 13. Chapter 7 describes a parameterization of penetrative cumulus convection. In Chapter 8 is given a parameterization of the planetary boundary layer. Convective adjustment other than that by penetrative cumulus and condensation processes are treated in Chapter 9. In Chapter

---

\* Presented by T. Tokioka, K. Yamazaki, I. Yagai and A. Kitoh.: Forecast Research Division.

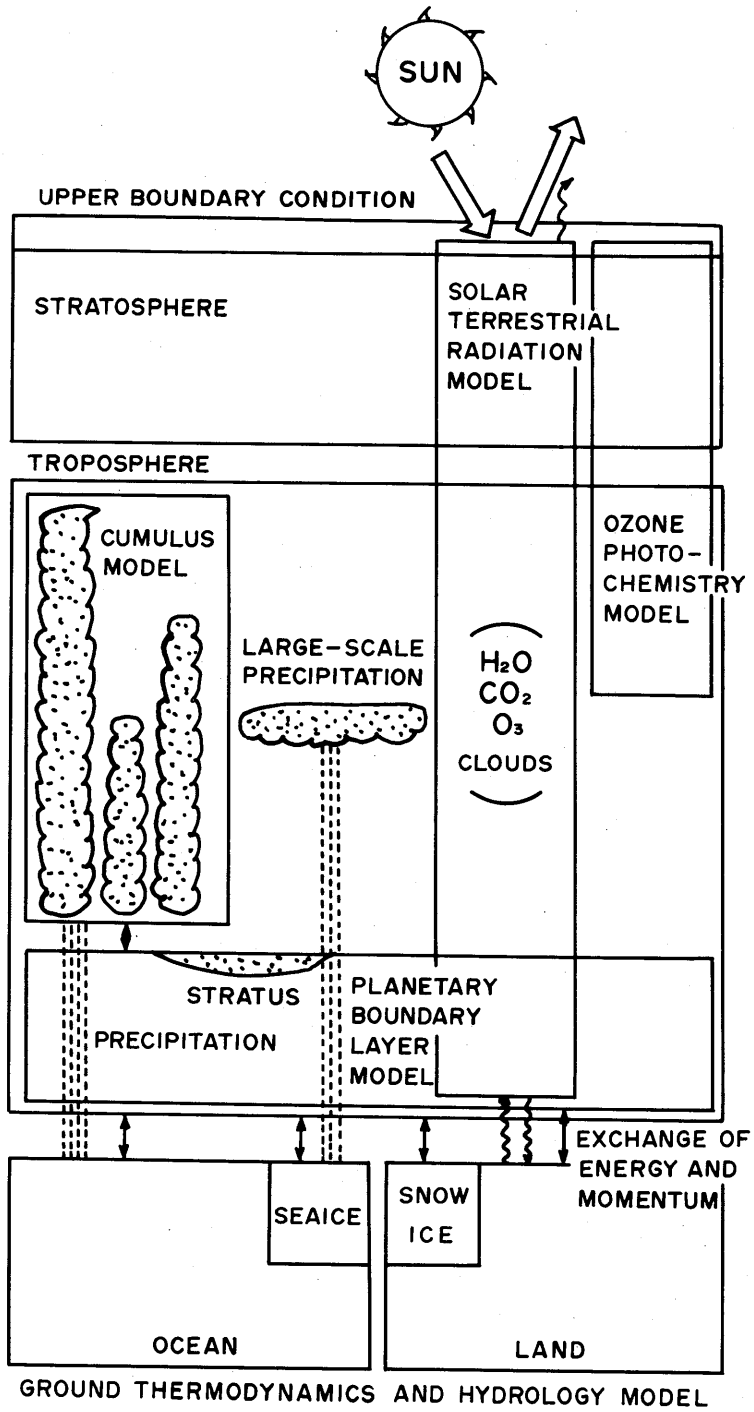


Fig. P1 Physical processes included in the GCM.

10 a description of both ground hydrology and ground thermodynamics is given. Sub-grid-scale mixing is described in Chapter 11. Source and sink of ozone is treated in Chapter 12. Finally in Chapter 13 is given a description of both solar and terrestrial radiation. In some of the chapters are included appendices to help readers understand the details and the performance of each sub-model.

At the end of this volume, another appendices are included, where selected examples of model results taken from a simulation of annual cycle with the five layer tropospheric version are shown as well as boundary conditions and list of parameters and constants currently assigned.

The authors thank Prof. Akio Arakawa of the UCLA for making the basic UCLA model available to the MRI, for giving them useful suggestions and for providing some of the members opportunities to visit the UCLA. We also thank Dr. Akira Katayama, the former head of the forecast research division of the MRI, for his encouragement and his warm support throughout this work. Thanks are due to Dr. Robert Schiffer, Office of Space & Terrestrial Applications/NASA, for offering us the Nimbus 7 ERB data. Thanks are extended to Mr. Taiji Yoshida, the head of the forecast research division, and to the former heads of the division, Mr. Hiroshi Ito and Dr. Eiji Uchida, for their continuous encouragement and patience through this work. The excellent job of drafting by Miss Hiroko Imai is also appreciated.

The numerical time integrations of the model were made on the HITAC M-200H Computer of the Meteorological Research Institute.

## 0. Governing equations in the continuous form\*

### 0.1 The vertical coordinate

The vertical coordinate adopted in the model is a combination of the  $\sigma$ -coordinate and the pressure coordinate. The  $\sigma$ -coordinate is used below the level  $p=p_l$  (see Fig.0.1), while  $p$ -coordinate above that level. The vertical coordinate is defined as

$$\sigma = \frac{p - p_l}{\pi}, \quad (0.1)$$

$$\pi = \begin{cases} p_s - p_l & \text{for } p \geq p_l \\ p_l - p_t & \text{for } p < p_l \end{cases} \quad (0.2)$$

where  $p_s$  and  $p_t$  are the pressures at the lower (surface) and the upper (top) boundaries of the model, respectively.

Therefore  $\sigma = -1, 0, 1$  at  $p = p_t, p_l, p_s$ . As  $\pi$  is constant above the level  $p = p_l$ , the  $\sigma$  coordinate defined by Eq.(0.1) is nothing but the normalized  $p$ -coordinate.

From (0.1), the individual time derivative of pressure,  $\omega$ , is given by

$$\omega \equiv \frac{dp}{dt} = \pi \dot{\sigma} + \sigma \left( \frac{\partial \pi}{\partial t} + \mathbf{v} \cdot \nabla \pi \right) \quad (0.3)$$

where  $\dot{\sigma} = d\sigma/dt$ ,  $\mathbf{v}$  is the horizontal velocity and  $\nabla$  is the horizontal gradient operator. From (0.2),  $\omega = \pi \dot{\sigma}$  for  $\sigma < 0$ .

In the  $\sigma$ -coordinate, the earth's surface is a coordinate surface as well as a material surface. The kinematical boundary condition at the earth's surface is therefore

$$\dot{\sigma} = 0 \quad \text{at } \sigma = 1 \quad (0.4)$$

At the top of the model, we assume that no air parcels cross the top boundary.

Thus,

$$\omega = \pi \dot{\sigma} = 0 \quad \text{at } \sigma = -1. \quad (0.5)$$

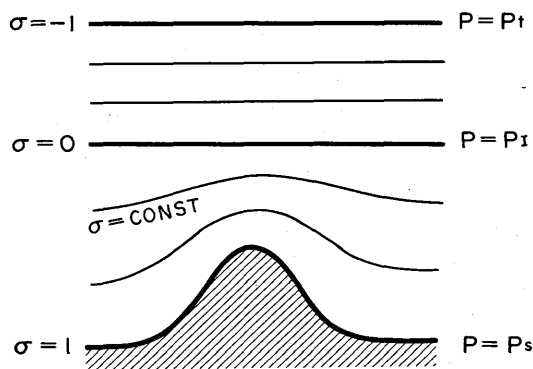


Fig. 0.1 The vertical coordinate  $\sigma$  adopted in the MRI-GCM-I.  $p$  is pressure. The lower surface is a coordinate surface. Above the level  $p=p_l$ ,  $\sigma$ -surface coincides with a pressure surface.

\* This chapter is prepared by T. Tokioka: Forecast Research Division

## 0.2 The equation of state

We consider that the model atmosphere is assumed to be a perfect gas.

Thus

$$\alpha = RT/p \quad (0.6)$$

where  $\alpha$  is the specific volume,  $T$  is the temperature, and  $R$  is the gas constant. We do not distinguish  $R$  from that of dry air except when we consider buoyancy fluxes due to sub-grid scale turbulence and cumulus convection.

## 0.3 The hydrostatic equation

The hydrostatic equation in  $p$ -coordinate,  $\frac{\partial \phi}{\partial p} = -\alpha$ , is written as

$$\delta \phi = -\pi \alpha \delta \sigma \quad (0.7)$$

with use of the identity  $\delta p = \pi \delta \sigma$ , where  $\delta$  is the differential under constant horizontal coordinate and time.  $\phi$  is the geopotential ( $=gz$ ),  $g$  is the acceleration of gravity and  $z$  is height.

The form (0.7) may be transformed into the following equivalent forms;

$$\delta \phi = -RT \delta \ln p \quad (0.8)$$

$$= -c_p \theta \delta (p/p_0)^\kappa \quad (0.9)$$

$$= c_p \frac{d \ln \theta}{d(1/\theta)} \delta (p/p_0)^\kappa \quad (0.10)$$

$$\delta(\phi \sigma) = -(\pi \sigma \alpha - \phi) \delta \sigma \quad (0.11)$$

$c_p$  is the specific heat at constant pressure,  $\kappa = R/c_p$  and  $\theta$  is the potential temperature,  $T(p/p_0)^{-\kappa}$ , where  $p_0$  is a standard pressure.

## 0.4 Equation of continuity

The equation of continuity in  $p$ -coordinate is

$$\nabla_p \cdot \mathbf{v} + \frac{\partial \omega}{\partial p} = 0 \quad (0.12)$$

where  $\nabla_p$  means  $\nabla$  operation on the constant  $p$ -surface.  $\nabla_p$  is related to  $\nabla_\sigma$  as

$$\nabla_p = \nabla_\sigma + \nabla_p \sigma \frac{\partial}{\partial \sigma} = \nabla_\sigma - \frac{\sigma}{\pi} \nabla \pi \frac{\partial}{\partial \sigma} \quad (0.13)$$

With the use of (0.13) and (0.3), (0.12) reduces to

$$(\nabla_{\sigma} \cdot \mathbf{v} - \frac{\sigma}{\pi} \nabla \pi \cdot \frac{\partial \mathbf{v}}{\partial \sigma}) + \frac{1}{\pi} \frac{\partial}{\partial \sigma} [\pi \dot{\sigma} + \sigma (\frac{\partial}{\partial t} + \mathbf{v} \cdot \nabla) \pi] = 0$$

and finally to

$$\frac{\partial \pi}{\partial t} + \nabla_{\sigma} \cdot (\pi \mathbf{v}) + \frac{\partial}{\partial \sigma} (\pi \dot{\sigma}) = 0 \quad (0.14)$$

Integrating (0.14) with respect to  $\sigma$  from  $\sigma = -1$  to  $\sigma$ , we obtain

$$\int_{-1}^{\sigma} \frac{\partial \pi}{\partial t} d\sigma + \pi \dot{\sigma} = - \int_{-1}^{\sigma} \nabla \cdot (\pi \mathbf{v}) d\sigma \quad (0.15)$$

With the use of the definition of  $\pi$ , (0.15) gives

$$\pi \dot{\sigma} = - \int_{-1}^{\sigma} \nabla \cdot (\pi \mathbf{v}) d\sigma \quad \text{for } \sigma < 0 \quad (0.16)$$

$$\sigma \frac{\partial p_s}{\partial t} + \pi \dot{\sigma} = - \int_{-1}^{\sigma} \nabla \cdot (\pi \mathbf{v}) d\sigma \quad \text{for } \sigma > 0 \quad (0.17)$$

From (0.17), we obtain

$$\frac{\partial p_s}{\partial t} = - \int_{-1}^1 \nabla \cdot (\pi \mathbf{v}) d\sigma \quad (0.18)$$

as  $\dot{\sigma} = 0$  at  $\sigma = 1$ .

### 0.5 Momentum equation

The pressure gradient force in p-coordinate,  $-\nabla_p \phi$ , is transformed into

$$-\nabla_p \phi = -\nabla_{\sigma} \phi + \frac{\sigma}{\pi} \nabla \pi \frac{\partial \phi}{\partial \sigma} = -\nabla_{\sigma} \phi - \sigma \alpha \nabla \pi \quad (0.19)$$

where use has been made of (0.13) and (0.7). Then the horizontal component of the equation of motion becomes

$$\frac{d\mathbf{v}}{dt} + f\mathbf{k} \times \mathbf{v} + \nabla_{\sigma} \phi + \sigma \alpha \nabla \pi = \mathbf{F} \quad (0.20)$$

where

$$\frac{d}{dt} = \left( \frac{\partial}{\partial t} \right)_{\sigma} + \mathbf{v} \cdot \nabla_{\sigma} + \dot{\sigma} \frac{\partial}{\partial \sigma} \quad (0.21)$$

$f$  is the vertical component of Coriolis vector ( $= 2\Omega \sin \varphi$ ,  $\Omega$  is the angular velocity of the earth,  $\varphi$  is latitude),  $\mathbf{k}$  is the vertical unit vector, and  $\mathbf{F}$  is the frictional force. Multiplying  $\pi$  and  $\mathbf{v}$  to (0.20) and (0.14) respectively and adding them, we obtain the flux form of the equation of motion

$$\begin{aligned} & \left(\frac{\partial}{\partial t}\right)_{\sigma}(\pi \mathbf{v}) + \nabla_{\sigma} \cdot (\pi \mathbf{v}) + \frac{\partial}{\partial \sigma}(\pi \dot{\sigma} \mathbf{v}) + f \mathbf{k} \times \pi \mathbf{v} + \nabla_{\sigma} \cdot (\pi \phi) + (\pi \sigma \alpha - \phi) \nabla \pi \\ & = \pi \mathbf{F} \end{aligned} \quad (0.22)$$

or with the help of (0.11)

$$\begin{aligned} & \left(\frac{\partial}{\partial t}\right)_{\sigma}(\pi \mathbf{v}) + \nabla_{\sigma} \cdot (\pi \mathbf{v}) + \frac{\partial}{\partial \sigma}(\pi \dot{\sigma} \mathbf{v}) + f \mathbf{k} \times \pi \mathbf{v} + \nabla_{\sigma}(\pi \phi) - \frac{\partial(\phi \sigma)}{\partial \sigma} \nabla \pi \\ & = \pi \mathbf{F} \end{aligned} \quad (0.23)$$

### 0.6 Thermodynamic equation

The first law of thermodynamics is written as

$$c_p \frac{dT}{dt} = \omega \alpha + Q \quad (0.24)$$

where  $Q$  is the heating rate per unit mass. Multiplying  $\pi$  and  $c_p T$  to (0.24) and (0.14) respectively and adding them, the flux form

$$\frac{\partial}{\partial t}(\pi c_p T) + \nabla_{\sigma} \cdot (\pi \mathbf{v} c_p T) + \frac{\partial}{\partial \sigma}(\pi \dot{\sigma} c_p T) = \pi(\omega \alpha + Q) \quad (0.25)$$

is derived. Substitution of (0.3) into (0.25) gives us the form,

$$\begin{aligned} & \frac{\partial}{\partial t}(\pi c_p T) + \nabla_{\sigma} \cdot (\pi \mathbf{v} c_p T) + (p/p_0)^{\kappa} \frac{\partial}{\partial \sigma}(\pi \dot{\sigma} c_p \theta) \\ & = \pi c_p T \frac{\partial \ln(p/p_0)^{\kappa}}{\partial \pi} \left( \frac{\partial}{\partial t} + \mathbf{v} \cdot \nabla \right) \pi + \pi Q \end{aligned} \quad (0.26)$$

### 0.7 The continuity equation of water vapor and ozone

Let  $q$  be the mixing ratio of either water vapor or ozone. The continuity equation of  $q$  is written by

$$\frac{dq}{dt} = S \quad (0.27)$$

where  $S$  is the source of  $q$ . The flux form of  $q$  is

$$\left(\frac{\partial}{\partial t}\right)_{\sigma}(\pi q) + \nabla_{\sigma} \cdot (\pi \mathbf{v} q) + \frac{\partial}{\partial \sigma}(\pi \dot{\sigma} q) = \pi S \quad (0.28)$$

# 1. Vertical differencing\*

## 1.1 The vertical coordinate and the vertical index

The model atmosphere is discretized by constant  $\sigma$ -levels. There are eight choices of distributing variables on the vertical levels as shown in Fig.1.1. Tokioka(1978) studied this problem from the standpoint of describing vertical dispersions of waves. Here we follow his results and adopt Scheme C'. Horizontal wind  $\mathbf{v}$  and temperature  $T$  are defined at odd levels, and geopotential  $\phi$  and  $\dot{\sigma}$  (individual time derivative of  $\sigma$ ) are defined at even levels.  $\hat{\mathbf{v}}$ ,  $\hat{T}$  and  $\hat{\phi}$  in Fig.1.1 indicate values interpolated in some ways from the non-hat values of them.

The vertical indices are given consecutively from the top to the surface as shown in Fig. 1.2. We locate vertical levels above  $p=p_1$  in equal interval in  $\ln p$ , again following Tokioka's analysis(1978), for best simulation of internal waves. Currently, we have two versions of the model. One is the 5-level tropospheric model, where  $p_1=p_1=100\text{mb}$  and  $\sigma_2=0.111111$ ,  $\sigma_4=0.333333$ ,  $\sigma_6=0.555556$ ,  $\sigma_8=0.777778$ ,  $\sigma_{10}=1.0$  (see Fig.1.2(a)). The other is the 12-level model,

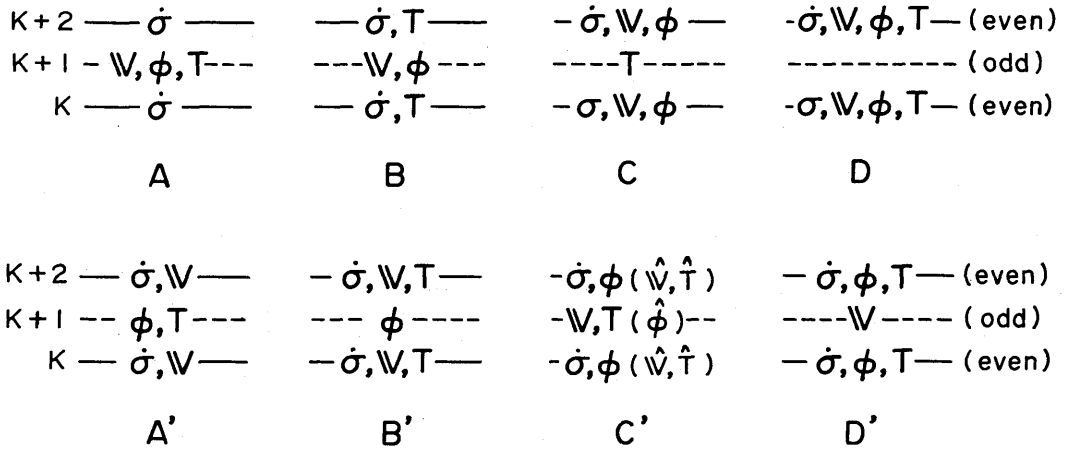


Fig. 1.1 Eight choices of distributing variables on vertical levels. Levels with solid and dashed lines are called as "even" and "odd" levels, respectively.  $\mathbf{v}$  is horizontal wind vector ;  $\dot{\sigma}$ , vertical  $\sigma$ -velocity ;  $T$ , temperature ;  $\phi$ , geopotential.  $\hat{\phantom{x}}$  is a reminder that the variable is an interpolated value from the non-hat ones. Scheme C' is adopted in the MRI · GCM-I.

\* This chapter is prepared by T. Tokioka.

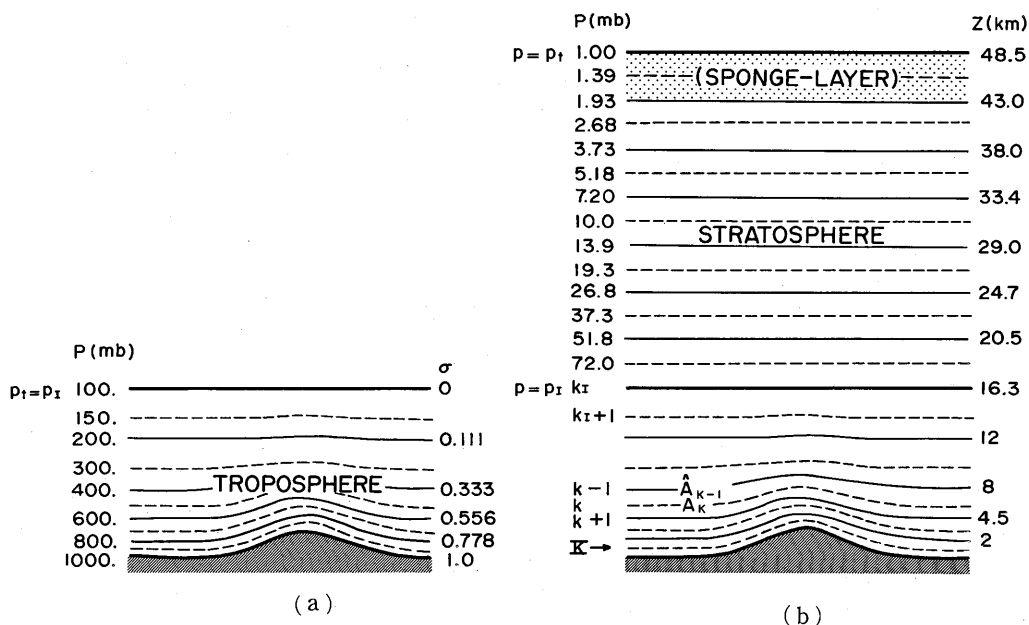


Fig. 1.2 The vertical indices and the position of vertical levels. (a) Five layer version (5L-MRI-GCM-I) and (b) twelve layer version (12L-MRI-GCM-I). As in Fig. 1.1, solid and dashed lines indicate even and odd levels, respectively. The lowest odd level is indicated as K. Approximate positions of the levels in km is shown when the surface pressure is 1000mb.

where  $p_t = 1\text{mb}$  and  $p_i = 100\text{mb}$ . The model atmosphere between  $p = p_t$  and  $p_i$  is discretized into seven levels in equal interval in  $\ln p$  (see Fig.1.2(b)). The model structure below the level  $p = p_i$  is the same as that of the 5-level model.

## 1.2 Flux form of a variable

Let  $A_k$  be a variable A defined at the odd level k and  $\hat{A}_{k+1}$ , an interpolated value of A at the even level k+1. We introduce a notation

$$\frac{D}{Dt}(\pi_k * A_k) \equiv \frac{\partial}{\partial t}(\pi_k A_k) + \nabla \cdot (\pi_k \mathbf{v}_k A_k) + \frac{1}{\Delta \sigma_k} [(\pi \dot{\sigma})_{k+1} \hat{A}_{k+1} - (\pi \dot{\sigma})_{k-1} \hat{A}_{k-1}] \quad (1.1)$$

where  $\nabla$  is the horizontal divergence operator. This is the flux form of variable A and conserves mass weighted integral of A under the vertical boundary condition  $\dot{\sigma}_0 = \dot{\sigma}_{k+1} = 0$ . We define  $\hat{A}_{k+1}$  as

$$\hat{A}_{k+1} = \frac{(G'_{k+2} A_{k+2} - G_{k-2}) - (G'_k A_k - G_k)}{G'_{k+2} - G'_k} \quad (1.2)$$

where  $G_k \equiv G(A_k)$  is an arbitrary function of variable  $A_k$  and  $G'_k \equiv dG(A_k)/dA_k$ . We can further conserve mass weighted integral of  $G$  by use of this form (Arakawa, 1972; Arakawa and Mintz, 1974; or Arakawa and Lamb, 1977)\*\*.

### 1.3 The equation of continuity

The equation of continuity, (0.14), may be expressed in a discretized form as

$$\frac{D}{Dt}(\pi_k * 1) = 0. \quad (1.3)$$

### 1.4 The acceleration term

The acceleration term in the momentum equation may be expressed as

$$\frac{D}{Dt}(\pi_k * \mathbf{v}_k) \quad (1.4)$$

In order to conserve kinetic energy in the process of vertical advections, we define

$$\hat{\mathbf{v}}_{k+1} = \frac{1}{2}(\mathbf{v}_k + \mathbf{v}_{k+2}), \quad (1.5)$$

This form is obtained from Eq.(1.2) by setting  $G(A) = A^2$ .

### 1.5 The pressure gradient force

We introduce the pressure gradient force at the odd level  $k$  as

$$\nabla(\pi_k \hat{\phi}_k) - \frac{1}{\Delta \sigma_k} (\phi_{k+1} \sigma_{k+1} - \phi_{k-1} \sigma_{k-1}) \nabla \pi_k \quad (1.6)$$

so that no spurious acceleration of a circulation may occur even in a discretized model with topography (see A, AM or AL). Keeping in mind the identity  $\nabla(\pi\phi) - \partial(\phi\sigma)/\partial\sigma \cdot \nabla\pi \equiv \pi\nabla\phi + \pi\sigma\alpha\nabla\pi$ , we define  $(\sigma\alpha)_k$  by

$$\pi_k(\sigma\alpha)_k = \hat{\phi}_k - \frac{1}{\Delta \sigma_k} (\phi_{k+1} \sigma_{k+1} - \phi_{k-1} \sigma_{k-1}) \quad (1.7)$$

where  $\alpha$  is the specific volume.

Multiplying  $-\mathbf{v}_k$  to Eq.(1.6) and rearranging the terms, we arrive at

\* \* These papers are abbreviated hereafter as A, AM and AL, respectively.

$$\begin{aligned}
 -\mathbf{v}_k \cdot [\text{Eq. (1.6)}] &= -\nabla \cdot (\pi_k \mathbf{v}_k \hat{\phi}_k) - \frac{1}{\Delta \sigma_k} \{ (\pi \dot{\sigma})_{k+1} + \sigma_{k+1} \frac{\partial \pi_k}{\partial t} \} \phi_{k+1} \\
 &- \{ (\pi \dot{\sigma})_{k-1} + \sigma_{k-1} \frac{\partial \pi_k}{\partial t} \} \phi_{k-1} - \pi_k (\omega \alpha)_k
 \end{aligned} \tag{1.8}$$

where

$$\begin{aligned}
 (\omega \alpha)_k &= (\sigma \alpha)_k \left( \frac{\partial}{\partial t} + \mathbf{v} \cdot \nabla \right) \pi_k - \frac{1}{\pi_k \Delta \sigma_k} \{ (\pi \dot{\sigma})_{k+1} (\phi_{k+1} - \hat{\phi}_k) \\
 &- (\pi \dot{\sigma})_{k-1} (\hat{\phi}_k - \phi_{k-1}) \}
 \end{aligned} \tag{1.9}$$

This is just a definition of  $(\omega \alpha)_k$  based on the identity

$$-\mathbf{v} \cdot \left( \nabla (\phi \pi) - \frac{\partial (\phi \sigma)}{\partial \sigma} \nabla \pi \right) = -\nabla \cdot (\pi \mathbf{v} \phi) - \frac{\partial}{\partial \sigma} (\pi \dot{\sigma} \phi) - \frac{\partial}{\partial \sigma} (\phi \sigma) \frac{\partial \pi}{\partial t} - \pi \alpha \omega$$

### 1.6 The first law of thermodynamics

If we define temperature at the level k by

$$\left. \begin{aligned}
 T_k &= \theta_k \cdot P_k \\
 P_k &= P(p_{k+1}, p_{k-1})
 \end{aligned} \right\} \tag{1.10}$$

the following enthalpy equation is derived as a finite difference analog of (0.26);

$$\begin{aligned}
 \frac{D}{Dt} (\pi_k * c_p T_k) &= \pi_k c_p T_k \left( \frac{\partial \ln P_k}{\partial \pi_k} \left( \frac{\partial}{\partial t} + \mathbf{v} \cdot \nabla \right) \pi_k \right. \\
 &+ \frac{1}{\Delta \sigma_k} \{ (\pi \dot{\sigma})_{k+1} c_p (\hat{T}_{k+1} - P_k \hat{\theta}_{k+1}) - (\pi \dot{\sigma})_{k-1} c_p (P_k \hat{\theta}_{k-1} - \hat{T}_{k-1}) \} + \pi_k Q_k
 \end{aligned} \tag{1.11}$$

where  $P_k$  is an analog to  $(p/p_0)^\kappa$  for the level k,  $\kappa = R/c_p$ , and  $p_0$  is a reference pressure. (1.11) is identical to the expression

$$\frac{D}{Dt} (\pi_k * \theta_k) = \frac{Q}{c_p P_k}$$

### 1.7 Total energy conservation and the hydrostatic equation

To conserve total energy in an adiabatic and non-dissipative process, the r.h.s. of (1.11) except the last term should be identical to  $\pi_k (\omega \alpha)_k$  defined by (1.9). Thus we require

$$c_p T_k \partial \ln P_k / \partial \pi_k = (\sigma \alpha)_k \tag{1.12}$$

$$\left. \begin{aligned}
 c_p (\hat{T}_{k+1} - P_k \hat{\theta}_{k+1}) &= \hat{\phi}_k - \phi_{k+1} \\
 c_p (P_k \hat{\theta}_{k-1} - \hat{T}_{k-1}) &= \phi_{k-1} - \hat{\phi}_k
 \end{aligned} \right\} \tag{1.30}$$

Eq.(1.12) is required only for  $k > k_1$ , because  $\pi_k$  is constant above the level  $k = k_1$ . Both (1.12)

and (1.13) are analogs of hydrostatic relation in discretized form.

The scheme described so far conserves momentum, kinetic energy, potential enthalpy and  $G(\theta)$  (provided that  $\hat{\theta}_{k+1}$  is determined by (1.2)) through the vertical advective process as well as mass itself. The total energy is also conserved by use of the hydrostatic relations (1.12) and (1.13), and no spurious acceleration of a circulation occurs through the pressure gradient force. In the above formulations, there remain several freedoms. They are;

- i ) the functional form of  $G(\theta)$
- ii ) the functional form of  $P(p_{k+1}, p_{k-1})$
- iii ) a hydrostatic relation that determines either  $\phi_{kl}$  or  $\hat{T}_{kl}$ .
- iv ) a hydrostatic relation that determines either  $\phi_{k+1}$  or  $\hat{T}_{k+1}$  for  $k < k_I - 3$ .

These freedoms are eliminated, after Tokioka's (1978) study, as follows;

$$i ) G(\theta) = \ln \theta \quad (1.14)$$

$$ii ) P_k = (p_k^* / p_0)^a, (p_k^*)^a = \frac{1}{1+a} \cdot \frac{p_{k+1}^{a+1} - p_{k-1}^{a+1}}{p_{k+1} - p_{k-1}}, a = 0.2 \quad (1.15)$$

$$iii ) \phi_{kl} - \hat{\phi}_{kl+1} = c_p T_{kl+1} \cdot \partial \ln P_{kl+1} / \partial p_{kl} (p_{kl+2} - p_{kl}) \quad (1.16)$$

$$iv ) \phi_{k+1} - \phi_{k-1} = -RT_k (\ln p_{k+1} - \ln p_{k-1}), k < k_I - 3 \quad (1.17)$$

The functional form (1.14) is required to describe vertical propagation of waves properly. The use of (1.14) gives us additional advantage (see AM or AL), i.e., the conservation of entropy because of (1.2) and exact thickness between the even levels for the wide range of stratification including isentropic and polytropic cases.

It may be useful, for the later convenience, to introduce the following expressions of hydrostatic relation, which are equivalent to (1.12) and (1.13),

$$\hat{\phi}_{k+2} - \hat{\phi}_k = -c_p \hat{\theta}_{k+1} (P_{k+2} - P_k) \quad (1.18)$$

$$\hat{\phi}_k = \phi_s + \sum_{k=kl+1}^K \pi_k c_p T_k \frac{\partial \ln P_k}{\partial \pi_k} - \sum_{k=kl+1}^{K-2} \sigma_{k+1} c_p \hat{\theta}_{k+1} (P_{k+2} - P_k) \quad (1.19)$$

where

$$\hat{\theta}_{k+1} = \frac{\ln(\theta_k / \theta_{k+2})}{1/\theta_{k+2} - 1/\theta_k} \quad (1.20)$$

$\Sigma'$  in (1.19) represents a summation over odd  $k$ .

## 2. Upper boundary condition\*

### 2.1 Introduction

Almost any models, so far, use  $\omega$  (the vertical p-velocity)=0 or  $w$  (the vertical velocity)=0 as the upper boundary condition, the use of which causes reflection of wave energy as demonstrated by Lindzen *et al.*(1966). If we apply the condition,  $\omega=0$ , at the level  $p=p_t$  ( $\neq 0$ ), air particles are not allowed to cross the level  $p=p_t$  from below to above it, which is not true in the real atmosphere, and thus causes wave reflections. This situation is not essentially changed at all even when  $p_t$  is replaced by 0, unless sub-grid-scale physical processes in the vertical direction are properly included parametrically in the model.

So far as the open boundary condition in the horizontal directions is concerned, several methods have been proposed (Wurtele *et al.*, 1971; Pearson, 1974; Beland and Warn, 1975; Orlanski, 1976, *etc.*). The method proposed by the above authors is essentially the implementation of Sommerfeld radiation condition. By estimating phase velocity in the normal direction to the boundary, say  $c$ , we may write Sommerfeld radiation condition as;

$$\frac{\partial \psi}{\partial t} + c \frac{\partial \psi}{\partial n} = 0 \quad (2.1)$$

for a variable  $\psi$ , where  $n$  is the coordinate normal to the boundary. The authors mentioned above discuss various ways of applying Eq. (2.1) to the unbounded hyperbolic flows. Beland and Warn (1975) have derived a transient radiation condition for both Rossby and inertia-gravity waves.

As an upper boundary condition, one may think of using Eq. (2.1), replacing  $\psi$  by  $\omega$  or  $w$ . However, this method, as is shown in the Appendix 2.2, turns out to be impractical, because the method causes instability, the growth rate of which is not small, especially in the low latitude regions.

In this paper, we describe, as an alternative method, a sponge layer model. In the sponge layer model, we include a sponge term in the thermodynamic equation, which is designed to cancel out erroneous effects caused by the inappropriate upper boundary condition,  $\omega=0$ , below the sponge layer. In another words, the sponge layer is designed so as to play an equivalent role to the radiation condition.

---

\* This chapter is prepared by T. Tokioka.

Although the sponge term is a kind of generalization of a Newtonian cooling term, it is required to be highly dependent on modes, especially on frequency, and is also required to be a complex number. The real part of the sponge term has a damping effect as a Newtonian cooling term does, while the imaginary part modifies the vertical wavenumber of a disturbance in the sponge layer.

The basic formulation of the sponge layer model has already been presented in Chapter 4 of AM (1974). In section 2.2, a discrete form of vertical structure equation is derived. The effect of upper boundary condition is demonstrated in 2.3. A "sponge layer" is formulated in 2.4, where we describe one practical way of applying the sponge layer model to the global circulation model. Some test examples of the sponge layer model are presented in the Appendix 2.1, demonstrating that the model works well to the forcings with the wide range of Lamb's parameter, when only one mode is forced from below.

## 2.2 The vertical structure equation

Using the vertical index  $k$  shown in Fig. 1.2, the equations linearized with respect to perturbations on a resting isothermal basic state, may be written in a discrete model as

$$i\sigma\hat{u}_k - 2\Omega\sin\varphi\hat{v}_k + \frac{is}{a\cos\varphi}\hat{\phi}_k = 0 \quad (2.2)$$

$$i\sigma\hat{v}_k + 2\Omega\sin\varphi\hat{u}_k + \frac{1}{a}\frac{\partial\hat{\phi}_k}{\partial\varphi} = 0 \quad (2.3)$$

$$i\sigma\hat{T}_k - \frac{T_o}{\Delta p_k}(R_k\hat{\omega}_{k-1} + S_k\hat{\omega}_{k+1}) = -M_k\hat{T}_k \quad (2.4)$$

$$\hat{\phi}_k - \hat{\phi}_{k+2} = c_p(P_k\hat{T}_k + Q_{k+2}\hat{T}_{k+2}) \quad (2.5)$$

$$is\hat{u}_k + \frac{\partial}{\partial\varphi}(\hat{v}_k\cos\varphi) + a\cos\varphi(\hat{\omega}_{k+1} - \hat{\omega}_{k-1})/\Delta p_k = 0 \quad (2.6)$$

where any variable, say  $\psi$ , has been assumed a solution of the form,

$$\psi = \text{Re}(\hat{\psi}e^{i(s\lambda + \sigma t)}) \quad (2.7)$$

$s$  is the longitudinal wavenumber and  $\sigma$  is the angular frequency.  $\text{Re}(\ )$  is an operation to take a real part of ( ). Here  $s$  is assumed to be positive. Then a positive (negative)  $\sigma$  represents a westward (eastward) moving wave. The form of the vertical differencing of the first law of thermodynamics (2.4), and the hydrostatic equation (2.5) is just a linearized version of (1.11) and (1.18). We have included a damping term in (2.4), with the coefficient  $M_k$ , for later convenience. The coefficients  $R_k$ ,  $S_k$ ,  $P_k$ , and  $Q_k$  are given the following forms;

$$R_k = \frac{1}{T_0} \left( \frac{p_k}{p_0} \right)^x (\bar{\theta}_{k-1} - \bar{\theta}_k) \quad (2.8)$$

$$S_k = \frac{1}{T_0} \left( \frac{p_k}{p_0} \right)^x (\bar{\theta}_k - \bar{\theta}_{k+1}) \quad (2.9)$$

$$P_k = \left( \frac{p_0}{p_k} \right)^x \left[ \left( \frac{p_{k+2}}{p_0} \right)^x - \left( \frac{p_k}{p_0} \right)^x \right] \frac{\partial \bar{\theta}_{k+1}}{\partial \bar{\theta}_k} \quad (2.10)$$

$$Q_{k+2} = \left( \frac{p_0}{p_{k+2}} \right)^x \left[ \left( \frac{p_{k+2}}{p_0} \right)^x - \left( \frac{p_k}{p_0} \right)^x \right] \frac{\partial \bar{\theta}_{k+1}}{\partial \bar{\theta}_{k+2}} \quad (2.11)$$

where the overbar denotes the basic state. From the definition of  $\bar{\theta}_{k+1}$ , these coefficients for the isothermal basic state become

$$P_k = S_k = \frac{(p_{k+2}/p_k)^x - 1 - \ln(p_{k+2}/p_k)^x}{(p_{k+2}/p_k)^x - 1} \quad (2.12)$$

$$Q_k = R_k = \frac{(p_{k-2}/p_k)^x - 1 - \ln(p_{k-2}/p_k)^x}{1 - (p_{k-2}/p_k)^x}$$

Eliminating  $\hat{u}$  and  $\hat{v}$  from (2.2), (2.3) and (2.6), we obtain

$$L(i\sigma\hat{\phi}_k) = 4a^2\Omega^2 \frac{\hat{\omega}_{k+1} - \hat{\omega}_{k-1}}{\Delta p_k} \quad (2.13)$$

where the differential operator  $L$  is given by

$$L = -\frac{\partial}{\partial \mu} \left( \frac{1-\mu^2}{f^2-\mu^2} \frac{\partial}{\partial \mu} \right) + \frac{1}{f^2-\mu^2} \left( \frac{s}{f} \frac{f^2+\mu^2}{f^2-\mu^2} + \frac{s^2}{1-\mu^2} \right) \quad (2.14)$$

where  $\mu = \sin \varphi$  and  $f = \sigma/2\Omega$ .

From (2.4) and (2.5), on the other hand, we obtain

$$i\sigma(\hat{\phi}_k - \hat{\phi}_{k+2}) = c_p T_0 \left\{ \frac{S_k}{\xi_k \Delta p_k} (Q_k \hat{\omega}_{k-1} + S_k \hat{\omega}_{k+1}) + \frac{Q_{k+2}}{\xi_{k+2} \Delta p_{k+2}} (Q_{k+2} \hat{\omega}_{k+1} + S_{k+2} \hat{\omega}_{k+3}) \right\} \quad (2.15)$$

Here

$$\xi_k = 1 - iM_k/\sigma.$$

Eliminating  $\hat{\phi}_k$  between (2.13) and (2.15), we obtain

$$\frac{W_{k-1} - W_{k+1}}{\Delta p_k} - \frac{W_{k+1} - W_{k+3}}{\Delta p_{k+2}} = -\frac{c_p T_0}{gh} \left\{ \frac{S_k}{\xi_k \Delta p_k} (Q_k W_{k-1} + S_k W_{k+1}) + \frac{Q_{k+2}}{\xi_{k+2} \Delta p_{k+2}} (Q_{k+2} W_{k+1} + S_{k+2} W_{k+3}) \right\} \quad (2.16)$$

where the separation of variable  $\hat{\omega}_{k+1} = F(\mu)W_{k+1}$  and the separation constant,  $h$ , defined by

$$LF = \epsilon F, \quad \epsilon = (2\Omega a)^2/gh \quad (2.17)$$

have been used.  $h$  and  $\epsilon$  are often called equivalent depth and Lamb's parameter, respectively. (2.16) is a finite difference analog of the vertical structure equation. Let's assume, to this equation, the following solution,

$$W_{k+1} = \left(\frac{p_{k+1}}{p_0}\right)^\alpha \tag{2.18}$$

Setting  $\xi_k = \xi_{k+2} = 1$  in (2.16), we obtain two solutions for  $\alpha$ , i. e.,  $\alpha_1$  and  $\alpha_2$  ( $= \alpha_1^*$  : complex conjugate of  $\alpha_1$ ). The thick solid lines in Fig. 2.1 show  $\text{Re}(\alpha_1)$  and  $-\text{Im}(\alpha_1) = n$  as a function of  $\epsilon$ .  $d = \ln(p_{k+1}/p_{k-1}) = 0.658$  (or  $e^d = 1.93$ ) and  $T_0 = 270^\circ\text{K}$  are used in the calculation. The real part is  $1/2$ , exactly as it is in the continuous case.

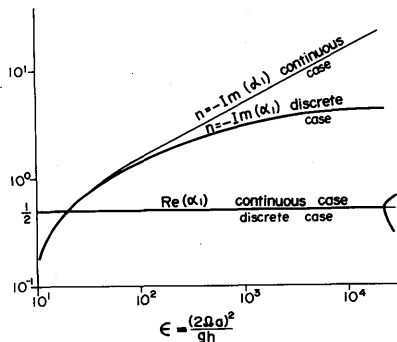


Fig. 2.1 The dependence of  $\alpha$  (see Eq. (2.18)) on Lamb's parameter  $\epsilon$  in an isothermal atmosphere ( $270^\circ\text{K}$ ) for both continuous case (thin line) and discrete case (thick line) where  $d = \ln(p_{k+1}/p_{k-1}) = 0.658$ . The vertical spacing of the MRI-GCM-I in the stratosphere (see Fig. 1. 2 (b)) is chosen to be  $d = 0.658$ .

with the increase of  $\epsilon$ . At  $\epsilon \approx 2.1 \times 10^4$ ,  $n$  is equal to  $\pi/d$ . Beyond that value,  $n$  remains equal to  $\pi/d$ , while  $\text{Re}(\alpha_1)$  is no longer equal to  $1/2$ , and damped and amplified oscillations occur. We cannot avoid these oscillations in the present discrete model, although the present vertical differencing scheme is superior to others as is discussed by Tokioka (1978).

### 2.3 Effect of the upper boundary

Here we demonstrate the effect of an upper boundary condition  $\omega = 0$ , which drastically alters the solution by thorough reflection of the wave energy and consequent resonance.

The solution of (2.16) is given by

$$W = A \left(\frac{p}{p_0}\right)^{\alpha_1} + B \left(\frac{p}{p_0}\right)^{\alpha_2}$$

If we confine our discussion to the westward moving waves ( $\sigma > 0$ ), the first term is responsible for upward propagation of wave energy and the second term is responsible for

downward propagation of wave energy. For eastward moving waves, the situation is reversed. In the following we will consider a westward moving wave as an example.

Suppose that a wave is forced from below and that its energy propagates upwards. If the upper boundary condition is such that the wave energy can radiate away through the boundary (the radiation condition), there is no downward propagation of wave energy and we have the case  $B=0$ . Let us choose  $A=1$  for convenience. This case, with  $A=1$  and  $B=0$ , is considered to be the exact solution in the following discussion.

If the upper boundary condition is  $\omega=0$ , as in most numerical models, the solution is drastically altered. The boundary conditions then become

$$W=1 \quad \text{at} \quad p=p_0,$$

$$W=0 \quad \text{at} \quad p=p_t.$$

The coefficients  $A$  and  $B$  are now complex. Fig. 2.2 shows the real and imaginary parts of  $A$  and  $B$ , as a function of  $\epsilon$  when  $p_T=1\text{mb}$ ,  $p_0=100\text{mb}$ ,  $d=\ln(p_{k+1}/p_{k-1})=0.658$  and  $T_0=270^\circ\text{K}$ . The real part of  $A$  has decreased from 1 to  $1/2$ , and the real part of  $B$  has increased from 0 to  $1/2$ . The imaginary parts of  $A$  and  $B$  become infinite when  $-n \ln(p_t/p_0)=\pi, 2\pi, 3\pi, \dots$ . For these values of  $n$ , there exist free solutions of the vertical structure equation, which satisfy  $\omega=0$  both at  $p=p_0$  and  $p=p_T$ . With non-zero values of  $\omega$  at  $p=p_0$ , a resonance occurs for discrete values of  $\epsilon$  which give those values of  $n$ . Essentially the same result has been demonstrated by Lindzen *et al.* (1966).

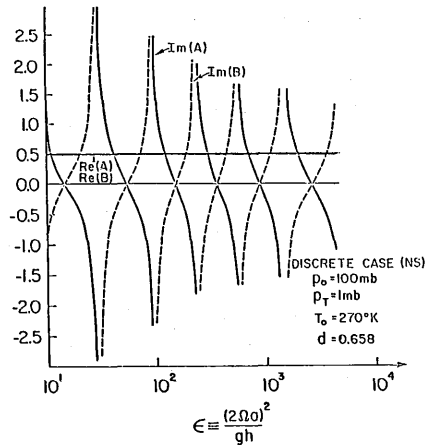


Fig. 2.2 The amplitude of the upward (A) and the downward (B) propagating modes as a function of  $\epsilon$ , where the upper boundary condition  $\sigma=0$  is applied at  $p=p_t=1\text{mb}$ , and the wave is forced at  $p=p_0=100\text{mb}$  in terms of vertical velocity. Isothermal atmosphere ( $270^\circ\text{K}$ ) is assumed with  $d=0.658$ .

## 2.4 Sponge layer formulation

### 2.4.1 Basic formulation

We now let the uppermost layer of the model be the sponge layer. Then  $\xi_k = \xi = 1 - iM/\sigma$  for  $k=1$ , and  $\xi_k=1$  for all other  $k$ . Let's again consider the isothermal case. The discrete vertical structure equation (2.16) at  $k=2$ , with the upper boundary condition  $W_0=0$ , is written

as;

$$-e^d W_2 - (W_2 - W_4) = -\frac{c_p T_0}{gh} (e^d \frac{S^2}{\xi} W_2 + Q(QW_2 + SW_4)). \quad (2.19)$$

The vertical structure equations at other levels are written as;

$$e^d (W_{k-1} - W_{k+1}) - (W_{k+1} - W_{k+3}) = -\frac{c_p T_0}{gh} [e^d S(QW_{k-1} + SW_{k+1}) + Q(QW_{k+1} + SW_{k+3})] \quad (2.20)$$

where

$$Q_k = Q = (e^{-\kappa d} - 1 + \kappa d) / (1 - e^{-\kappa d})$$

$$S_k = S = (e^{\kappa d} - 1 - \kappa d) / (e^{\kappa d} - 1).$$

By choosing  $\xi$  properly in (2.19), we can let the ratio  $W_4/W_2$  be equal to that of the exact solution in the discrete model under the radiation condition, which is determined by (2.20) for a given equivalent depth. In this way, we can simulate a solution under the radiation condition. The resultant condition is

$$\epsilon \left( \frac{1-\xi}{\xi} X + \frac{Q}{S} \right) - \frac{(2\Omega a)^2}{c_p T_0 S^2} = 0 \quad (2.21)$$

$X (= W_4/W_2)$  in the above equation is determined by

$$\left[ \epsilon + \frac{(2\Omega a)^2}{c_p T_0 S Q} \right] X^2 - \left[ \frac{(2\Omega a)^2}{c_p T_0 S Q} (e^d + 1) - \epsilon \left( e^d \frac{S}{Q} + \frac{Q}{S} \right) \right] X + e^d \left[ \epsilon + \frac{(2\Omega a)^2}{c_p T_0 S Q} \right] = 0 \quad (2.22)$$

One of the solutions of (2.22), which describes the structure of the upward energy propagating mode, should be substituted into (2.21). The upward energy propagating mode can be selected by the condition  $n/\sigma < 0$  i. e.,

$$\text{Im}(X) \cdot \sigma < 0 \quad (2.23)$$

Fig. 2.3 shows  $M/\sigma$ , thus obtained, as a function of  $\epsilon = (2\Omega a)^2/gh$  when  $T_0 = 270^\circ K$  and  $d = 0.658$ . The required coefficient of the sponge term,  $M$ , is a complex function of the equivalent depth and frequency. The real part of  $M$  thus obtained remains

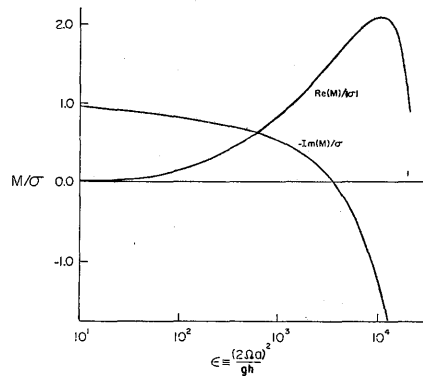


Fig. 2.3 Sponge coefficient  $M$ , normalized with frequency of a wave  $\sigma$ , as a function of Lamb's parameter  $\epsilon$ . Conditions of the discrete model are the same as those in Fig. 2. 1.

positive while the wave is treated as internal (*i. e.*,  $9.7 < \epsilon < 2.1 \times 10^4$ ), and therefore acts as damping in that range. Beyond the value  $\epsilon = 2.1 \times 10^4$ , damped and amplified oscillations occur, as shown in Fig. 2.1. Therefore, proper simulation of wave in that range itself is meaningless. When  $\epsilon$  is small ( $\epsilon \lesssim 30$ ),  $\text{Re}(M)/|\sigma|$  is quite small, while  $-\text{Im}(M)/\sigma$  is close to unity. This means that the sponge term has negligible damping effect but has exclusive effect in modifying vertical wavelength. With the increase of  $\epsilon$  (or decrease of equivalent depth), the damping effect of the sponge term increases. At  $\epsilon \simeq 3.5 \times 10^3$ ,  $\text{Im}(M)$  vanishes, *i. e.* the sponge term formally reduces to the so called Newtonian cooling term.

Because the vertical wavelength of a wave is a decreasing function of  $\epsilon$ , we may summarize the present result as follows; The sponge term is more effective in changing the vertical wavelength in the sponge layer than in damping the amplitude of the wave, for the waves with large vertical wavelengths. On the other hand, the damping effect of the sponge term becomes important to handle waves with short vertical wavelengths.

#### 2.4.2 Estimation of equivalent depth and frequency

As mentioned in 2.4.1, the sponge coefficient  $M$  is a complex function of equivalent depth and frequency, both of which are not explicitly known in a numerical model. This causes difficulties in evaluating  $M$  in initial value problems.

In the following, we describe one successful way of estimating equivalent depth and frequency in a numerical model.

From (2.4), (2.5), (2.15) and (2.17), we have;

$$i\sigma\hat{T}_3 - \frac{T_0}{\Delta p_3}(Q\hat{\omega}_2 + S\hat{\omega}_4) = 0 \quad (2.24)$$

$$\hat{\phi}_1 - \hat{\phi}_3 = c_p(S\hat{T}_1 + Q\hat{T}_3) \quad (2.25)$$

$$i\sigma\hat{\phi}_1 = gh\frac{\hat{\omega}_2}{\Delta p_1} \quad (2.26)$$

$$i\sigma\hat{\phi}_3 = gh\frac{\hat{\omega}_4 - \hat{\omega}_2}{\Delta p_3} \quad (2.27)$$

From (2.24) and (2.27), we obtain

$$gh = \frac{(2\Omega a)^2}{\epsilon} = \text{Re}\left(T_0 \cdot \frac{Q + S\hat{\omega}_4/\hat{\omega}_2}{\hat{\omega}_4/\hat{\omega}_2 - 1} \frac{\hat{\phi}_3}{\hat{T}_3}\right) \quad (2.28)$$

By knowing  $\hat{\omega}_4/\hat{\omega}_2$  and  $\hat{\phi}_3/\hat{T}_3$ ,  $\epsilon$  can be estimated by (2.28). (2.24), (2.26) and (2.27) can be used to estimate  $\sigma$ . Once we know  $\epsilon$  and  $\sigma$ ,  $X$  is determined by (2.22) and (2.23). Finally, (2.21) gives

us M.

### 2.4.3 Extension of the sponge layer model to the non-isothermal case with a constant zonal wind

We may extend the sponge layer formulation in the previous sub-section to the non-isothermal case with a constant zonal wind. We may include the effect of a constant wind by replacing  $\sigma$  with the doppler shifted frequency  $\sigma^*(=\sigma + s\bar{u}/a \cos\phi)$ . The thermodynamic equation (2.4) should be replaced by

$$i\sigma^*\hat{T}_k - \frac{\hat{T}_k}{\Delta p_k}(R_k\hat{\omega}_{k-1} + S_k\hat{\omega}_{k+1}) = -M_k\hat{T}_k - \hat{q}_k \quad (2.29)$$

where  $\hat{T}_k$  is the globally averaged temperature at the level  $k$ , and  $\hat{q}_k$  is the cooling rate due to diabatic processes other than the sponge term.  $T_o$  that appears in the definition of  $R_k$  and  $S_k$  should be replaced by  $\hat{T}_k$ .

The vertical structure equation is now written as follows;

$$\frac{W_{k-1} - W_{k+1}}{\Delta p_k} - \frac{W_{k+1} - W_{k+3}}{\Delta p_{k+2}} = -\frac{c_p T_o}{gh} \left[ \frac{\hat{T}_k}{T_o \xi_k^* \Delta p_k} (R_k W_{k-1} + S_k W_{k+1}) + \frac{\hat{T}_{k+2}}{T_o \xi_{k+2}^* \Delta p_{k+2}} (R_{k+2} W_{k+1} + S_{k+2} W_{k+3}) \right] \quad (2.30)$$

where

$$\xi_k^* = \xi_k + \hat{q}_k / i\sigma^* \hat{T}_k \quad (2.31)$$

In the following is given one practical way of evaluating sponge terms currently adopted. In order to evaluate them, we have to know both the equivalent depth and the doppler shifted frequency. For this end we estimate, at first, the vertical structure  $X (= \hat{\omega}_{k+2} / \hat{\omega}_k)$  as follows;

$$X_{r.g.} = \frac{1}{3} \left\{ \frac{\hat{\omega}_4}{\hat{\omega}_2} + \frac{\Delta p_5}{\Delta p_3} \left( \frac{\hat{\phi}_5}{\hat{\phi}_3} + \frac{\hat{T}_3}{\hat{T}_5} \cdot \frac{\xi_5^*}{\xi_3^*} \frac{\hat{T}_5}{\hat{T}_3} \right) \right\} \quad (2.32)$$

The doppler shifted frequency,  $\sigma^*$ , is estimated by use of (2.29). In doing so, a kind of time averaging is necessary to avoid a rapid fluctuation of the estimated value due to short lived waves. Currently the following form is adopted;

$$(\sigma^*)^\tau = (1 - \epsilon)(\sigma^*)^{\tau-1} + \frac{\epsilon}{2} \text{Im} \left[ \frac{1}{\Delta p_3} \cdot \frac{\hat{T}_3}{\hat{T}_3} (R_3 \hat{\omega}_2 + S_3 \hat{\omega}_4) - \frac{\hat{q}_3}{\hat{T}_3} + \frac{1}{\Delta p_5} \frac{\hat{T}_5}{\hat{T}_5} (R_5 \hat{\omega}_4 + S_5 \hat{\omega}_6) - \frac{\hat{q}_5}{\hat{T}_5} \right] \quad (2.33)$$

The averaging factor  $\epsilon$  is assigned the value 0.08. Superscript  $\tau$  indicates a time step to evaluate a sponge term. Currently this is done in every 60 min. The equivalent depth is

estimated, now, with the use of a similar equation to (2.33), as follows;

$$(gh)^\tau = (1 - \epsilon)(gh)^{\tau-1} + \frac{\epsilon}{2} \text{Re} \left[ \left( \frac{\hat{T}_3 \hat{\phi}_3}{\hat{\xi}_3^* \hat{T}_3} + \frac{\hat{T}_5 \hat{\phi}_5}{\hat{\xi}_5^* \hat{T}_5} \right) \cdot \frac{\bar{S} X_{f.g.} + \bar{R}}{X_{f.g.} - 1} \right] \quad (2.34)$$

where  $\bar{S}$  and  $\bar{R}$  are representative values of  $S_k$  and  $R_k$  in the highest three levels.  $\epsilon$  is again set to 0.08.

We are now able to recalculate the vertical structure  $X$  by use of the vertical structure equation (2.30) applied at the level  $k=4$ . This gives us two solutions for  $X$ , *i. e.*,  $X_1$  and  $X_2$ . We choose  $X_1$  when  $X_1$  satisfies either

$$|X_1| > |X_2|$$

or

$$|X_1| = |X_2| \quad \text{and} \quad \text{Im}(X_1)\sigma^* < \text{Im}(X_2)\sigma^* \quad (2.35)$$

The sponge coefficient  $M$  is determined by use of the vertical structure  $X_1$  thus determined and the vertical structure equation applied at the level  $k=2$ . Currently, sponge terms are calculated for each latitude circle for the zonal wavenumber up to 4.

## A2.1 Test examples of the sponge layer model

### A2.1.1. Model

We apply the sponge layer model designed in 2.4 to the linearized equatorial  $\beta$ -plane model. We assume rest, isothermal atmosphere as a basic state and consider the following form of a perturbation motion,

$$\begin{pmatrix} u \\ v \\ \omega \\ T \\ \phi \end{pmatrix} = \text{Re} \begin{pmatrix} \tilde{u} \\ \tilde{v} \\ \tilde{\omega} \\ \tilde{T} \\ \tilde{\phi} \end{pmatrix} \cdot e^{imx}$$

where  $m$  is a wavenumber in the zonal direction. Then we obtain a following set of linearized equations;

$$\delta_t \tilde{u}_j - \frac{1}{2} f_j (\tilde{v}_{j+1} + \tilde{v}_{j-1}) = -im \tilde{\phi}_j \quad (A2.1.1)$$

$$\delta_t \tilde{v}_j + \frac{1}{2} (f_{j+1} \tilde{u}_{j+1} + f_{j-1} \tilde{u}_{j-1}) = -\frac{1}{\Delta y} (\tilde{\phi}_{j+1} - \tilde{\phi}_j) \quad (A2.1.2)$$

$$\delta_t \tilde{T}_k - \frac{T_0}{\Delta p_k} (Q \tilde{\omega}_{k-1} + S \tilde{\omega}_{k+1}) = -M_k \tilde{T}_k \quad (A2.1.3)$$

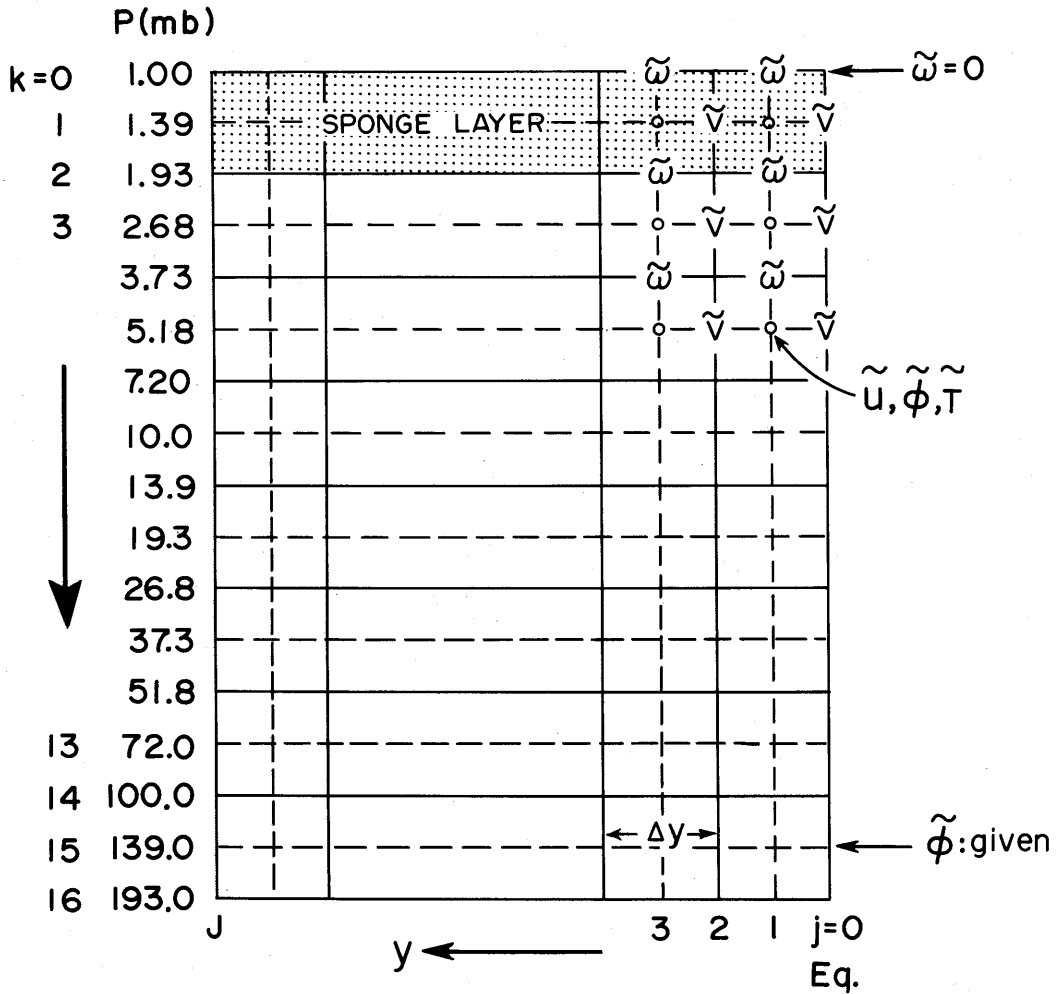


Fig. A2.1.1 The vertical and the horizontal structure of the discrete model used for the test calculations. Vertical structure is the same as that in Fig. 1.2(b).

$$\tilde{\phi}_k - \tilde{\phi}_{k+2} = c_p (S\hat{T}_k + Q\hat{T}_{k+2}) \quad (\text{A2.1.4})$$

$$im\tilde{u}_j^k + \frac{1}{\Delta y} (\tilde{v}_{j+1}^k - \tilde{v}_{j-1}^k) + \frac{1}{\Delta p_k} (\tilde{\omega}_j^{k+1} - \tilde{\omega}_j^{k-1}) = 0 \quad (\text{A2.1.5})$$

where

$$f_j = \frac{j}{2} \Delta y \frac{2\Omega}{a}$$

$M_k$  is set to zero except the one at  $k=1$ , which is estimated by the procedure described in section 2.4. Location of variables is shown in Fig. A2.1.1. Horizontal location of variables corresponds to the scheme adopted by the MRI • GCM-I. Q and S in (A2.1.3) and (A2.1.4) are

Table A2.1.1

Numerical parameters and lateral boundary conditions used in initial value problems.  $\Delta y$  is a grid size in the meridional direction,  $J$  the number of grids in  $y$ -direction,  $\Delta t$  a time increment, and  $m$  a wavenumber in the longitudinal direction.

Case	$\Delta y(\text{km}), J$	$\Delta t(\text{sec})$	$m(M^{-1})$	Lateral Boundary Condition	Assigned Frequency ( $\text{sec}^{-1}$ )	$\epsilon = \frac{(2\Omega a)^2}{gh}$
Mixed Rossby-Gravity Wave	444.78 ( $J=22$ )	450.	$6.2784 \times 10^{-7}$	$\tilde{u}_1 = \tilde{u}_{-1}$ $\tilde{v}_j = 0$	$6.2784 \times 10^{-6}$	$2.030 \times 10^3$
Kelvin Wave	444.78 ( $J=22$ )	450.	$1.5696 \times 10^{-7}$	$\tilde{v}_0 = 0$ $\tilde{v}_j = 0$	$-6.0602 \times 10^{-5}$	$5.760 \times 10^3$
Rossby Wave	600. ( $J=22$ )	600.	$3.1392 \times 10^{-7}$	$\tilde{v}_0 = 0$ $\tilde{v}_j = 0$	$8.0 \times 10^{-6}$	$1.230 \times 10^2$
Semi-Diurnal Wave	600. ( $J=21$ )	600.	$3.1392 \times 10^{-7}$	$\tilde{v}_0 = 0$ $\tilde{\phi}_j = 0$	$1.4526 \times 10^{-4}$	$1.219 \times 10^1$

the ones defined in (2.12). Vertical index  $k$  and latitudinal index  $j$  are dropped in the momentum equations, and in the thermodynamic and hydrostatic equations, respectively. As for the time differencing,  $\delta_t$ , we use the centered scheme with a periodical insertion of the Euler backward step.

By use of the separation relation;

$$\frac{1}{\Delta p_k} (\tilde{\omega}_{k+1} - \tilde{\omega}_{k-1}) = \frac{i\sigma}{gh} \tilde{\phi}_k \quad (\text{A2.1.6})$$

and (A2.1.1), (A2.1.2) and (A2.1.5), a difference analog of the horizontal structure equation is obtained. The equivalent depth, or Lamb's parameter, and the eigenfunction for geopotential,  $\mathbf{F}$ , are obtained by solving it under the lateral boundary conditions listed in Table A2.1.1. The eigenfunction thus obtained is used as the forcing to the model. Geopotential at the lowest level ( $k=15$ ) is prescribed as

$$\tilde{\phi}_j^{15} = \Phi \mathbf{F} e^{i\sigma \Delta t \tau} \quad (\text{A2.1.7})$$

where  $\tau$  is a time step, and  $\Phi$  is a constant chosen to be  $|\phi_{j=1}^{15}| = 10.0 \text{m}^2 \text{sec}^{-2}$ . Prescribed frequency  $\sigma$  is not used in any other places than in (A2.1.7), in the model. Integrations are started from a rest condition in the interior.

Four examples of the initial value problem are demonstrated in the following. They are the propagation of a mixed Rossby-gravity wave, a Kelvin wave, a Rossby wave and a semi-diurnal wave (see Table A2.1.1). Lamb's parameter  $\epsilon$  are chosen in such a way as to be close

to the resonance points except a semi-diurnal wave case. Arrows in Fig. A2.1.2 show the location of Lamb's parameters listed in Table A2.1.1. The differences between Fig. 2.2 and A2.1.2 are due to the differences in the forcing level and the way in which waves are forced. In Fig. A2.1.2, waves are forced by  $\phi$  at the level  $k=15$ , while they are forced by  $\omega$  at the level  $k=14$  in Fig. 2.2.

### A2.1.2. Propagation of a mixed Rossby-gravity wave

As the first test, we simulate a propagation of a mixed Rossby-gravity wave. This is observed in the equatorial lower stratosphere. The parameter in Table A2.1.1 roughly simulates the observed waves.

The equivalent depth is  $gh=424m^2 \text{ sec}^{-2}$  or  $\epsilon=2.03 \times 10^3$ . Therefore the vertical wavelength in the present discrete model is estimated approximately as 12.5km with the aid of Fig. 2.1. While the continuous model gives about 5km for the same value of  $\epsilon$ . The horizontal profile of  $F$ , used as the boundary forcing, is proportional to the one shown in Fig. A2.1.3 (c) by E.

The time change of the amplitude of  $\phi_{j=1}^3$  is shown in Fig. A2.1.3 (a), where the solid line with (S) is the case with the sponge layer, and the dashed line with (NS) is the case without the sponge layer. The thin solid line with (E) shows the steady state amplitude of the exact solution with the sponge layer, which is identical to the exact solution under the radiation condition below the sponge layer. We do not observe any significant differences between Cases (S) and (NS) until about 240 hours. However, the amplitude of (NS) still continues to increase and tends to have a large value after that. On the other hand, the amplitude of (S) fluctuates around the exact value.

The vertical structure at  $j=1$  (Fig. A2.1.3 (b)) and the horizontal structure at  $k=3$  (Fig. A2.1.3 (c)) of geopotential field show that the sponge layer well suppresses artificial reflections,

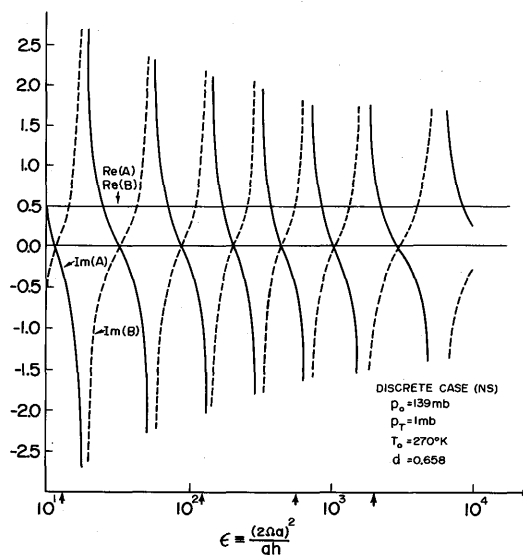
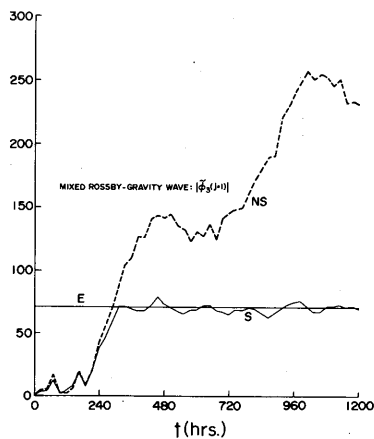
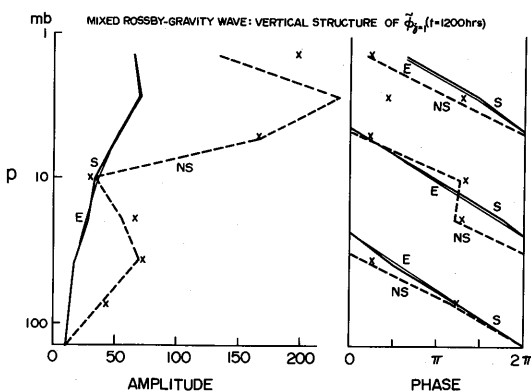


Fig. A2.1.2 Same as in Fig. 2.2 except that waves are forced at the level  $p=139\text{mb}$  in terms of geopotential. Arrows indicate positions of Lamb's parameter used as the forcing in the present test (see Table A2.1.1).

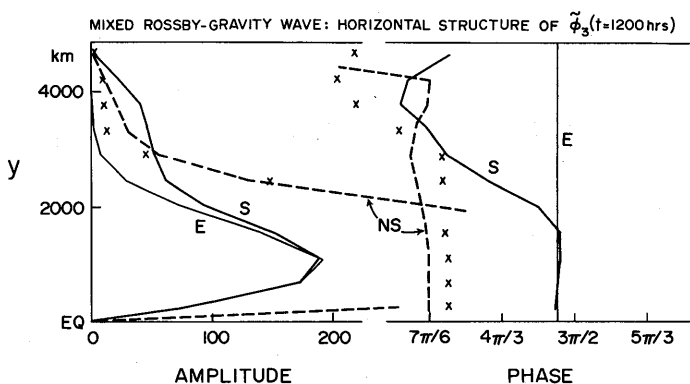
Fig. A2.1.3 (a) The time change of geopotential amplitude at the grid point  $j=1, k=3$  for the mixed Rossby-gravity wave case (unit :  $m^2 \cdot s^{-2}$ ). "S" and "NS" indicate the case with and without the sponge layer, respectively. "E" is the exact steady solution with the sponge. The exact solution is identical to the solution under the radiation condition, below the sponge layer.



(a)



(b)



(c)

(b) The vertical structure of geopotential at  $j=1$  after 1200 hours of integration for the mixed Rossby-gravity case. Amplitude is shown in unit of  $m^2 \cdot s^{-2}$ . The phase is measured relative to that at the bottom layer ( $k=15$ ). Crosses indicate the results where Rayleigh friction terms with the damping rate  $10^{-5} s^{-1}$  are included in the momentum equations at the level  $k=1$  as well as a Newtonian cooling term with a constant cooling rate  $10^{-5} s^{-1}$  in the thermodynamic equation at  $k=1$ .

(c) The horizontal structure of geopotential at  $k=3$  after 1200 hours of integration for the mixed Rossby-gravity case. Amplitude unit is  $m^2 \cdot s^{-2}$ .

caused by the upper boundary condition  $\omega = 0$ , below the sponge layer. The solution below that layer is almost identical to the exact one, in this example. Vertical profile of  $|\phi|$  in (NS) clearly shows the existence of a nodal point caused by reflections at the top.

When there is a Rayleigh friction term in the momentum equation, simple analysis of the effect of the term is prohibited because of the change in the horizontal structure between the layers with and without the Rayleigh friction term. Because the Rayleigh friction term is sometimes included in the model for the purpose of dissipating reflected waves caused by the upper boundary, the method is tested numerically.

In the numerical test, a Newtonian cooling term is also retained in the model with a constant cooling rate. Both the momentum damping rate and the cooling rate are set to  $10^{-5} \text{ sec}^{-1}$  and those damping terms are included only in the highest layer. Crosses in Fig. A2.1.3 (b) and (c) show the geopotential field after 1200 hrs. of integration. Gross features are very close to those without sponge (NS). The case with the damping rate of  $10^{-6} \text{ sec}^{-1}$  has also been tested. However, the change in the damping rate does not cause much differences in the results except in the highest three levels.

### A2.1.3. Propagation of a Kelvin wave

Kelvin waves are also dominantly observed in the tropical lower stratosphere. The parameters in Table A2.1.1 roughly simulates observed Kelvin waves.

Because  $\tilde{v}_j \equiv 0$  in the Kelvin wave, the dispersion relation reduces simply to

$$\sigma = -\sqrt{gh}m \quad (\text{A2.1.8})$$

This gives us  $1.49 \times 10^3 \text{ m}^2\text{sec}^{-2}$  as  $gh$  (or  $\epsilon = 576$ ). The vertical group velocity  $W_g$  of the Kelvin wave, in the present discrete model, can be evaluated with the aid of the following relation;

$$W_g = -H_o \frac{\partial \sigma}{\partial n} = \frac{H_o \sigma}{2} \cdot \frac{\partial \ln \epsilon}{\partial n} \quad (\text{A2.1.9})$$

where  $H_o$  is the equivalent depth ( $= C_p T_o / g$ ) and use has been made of (A2.1.8).  $\partial \ln \epsilon / \partial n$  in the present model can be evaluated from Fig. 2.1. Thus we obtain  $2 \text{ km} \cdot \text{d}^{-1}$  as an approximate value of  $W_g$  for the present choice of parameters.

Fig. A2.1.4 (a) shows the time change of  $|\tilde{\phi}_{j=1}^3|$ . We notice a great difference between Cases (S) and (NS) after about 380 hrs. The value 380 hrs is compared well with the value 400 hrs, which is an approximate time required for the bottom disturbance to arrive at the level  $k=3$ .

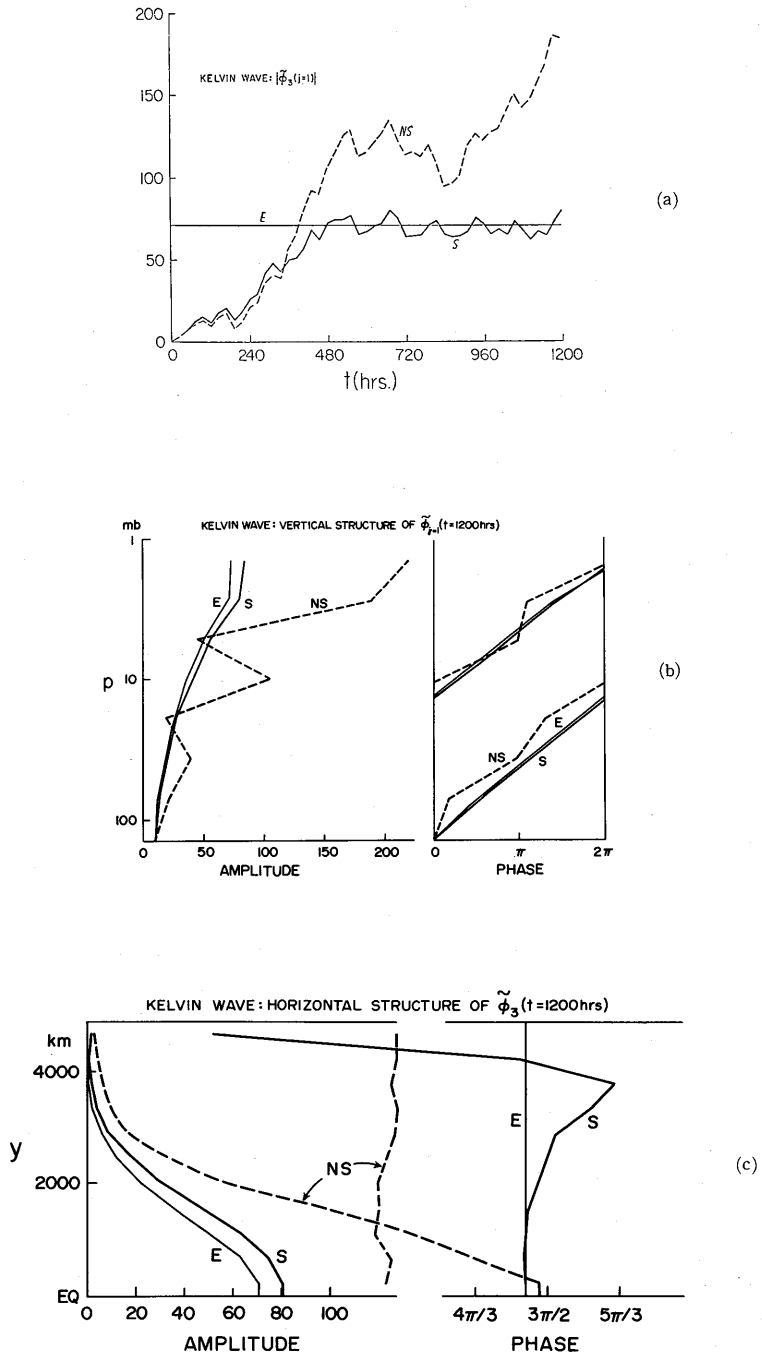


Fig. A2.1.4 Same as in Fig. A2.1.3 (a), (b) (c) except for the case with a Kelvin wave forcing (see Table A2.1.1).

After 400 hrs, the amplitude of the case with sponge (S) fluctuates around the exact value (E). While the amplitude of (NS) seems to settle at a large value. This is a plausible result because the Lamb's parameter ( $\epsilon = 576$ ) is close to a resonance point (see Fig. A2.1.2).

Vertical and horizontal structures of geopotential at 1200 hrs are shown in Fig. A2.1.4 (b) and (c). From those figures, again, we see that (S) is close to (E) except near the north boundary region where the amplitude of geopotential itself is small. We may conclude that the sponge layer is effective in this case.

#### A2.1.4. Propagation of a Rossby wave

The third example is a Rossby wave's case. The parameters in Table A2.1.1 are chosen so as to locate Lamb's parameter around  $10^2$ . The value is about 123, and this value is also close to a resonance point (see Fig. A2.1.2).

The time change of geopotential amplitude at  $j=1$  and  $k=3$  is shown in Fig. A2.1.5 (a). The amplitude of (S) follows the exact value (E) more closely than that of (NS) after about 300hrs of integration. However, there still remains larger fluctuation in (S) around the exact value than those observed in the previous two cases.

Although we do not see much preference of (S) over (NS) from Fig. A2.1.5 (a) alone, the vertical structure in Fig. A2.1.5 (b) clearly reveals differences between (S) and (NS). Both amplitude and phase of geopotential in (S) are close to the exact values. On the other hand, we notice two sharp nodes in (NS). One of the nodes is located at the level  $k=3$ .

Judging from both Figs. A2.1.5 (b) and (c), we may say that not bad horizontal structure of geopotential in (NS) at a particular level  $k=3$  (Fig. A2.1.5 (c)) has happened by chance.

#### A2.1.5. Propagation of a semi-diurnal wave

As the last example, we test a propagation of  $\Theta (2,2)$  mode of the semi-diurnal tidal motion (see Chapman and Lindzen (1970) for further details). By use of the parameters in Table A2.1.1, the simulated  $\Theta (2,2)$  mode in the present discrete model gives  $gh = 7.04 \times 10^4 \text{ m}^2\text{sec}^{-2}$  or  $\epsilon = 12.2$ , which gives about 190km as the vertical wavelength.

Fig. A2.1.6 (a) shows the time change of geopotential amplitude at  $j=1$ , and  $k=3$ . Corresponding to the very large vertical wavelength, the vertical group velocity is also quite large. Within 12 hrs, wave energy arrives at the sponge layer. However, the amplitude of (S) does not converge to the exact one. There still remains a large fluctuation even after 1200 hrs, and no preference of (S) over (NS) is found both in the horizontal and vertical structures of

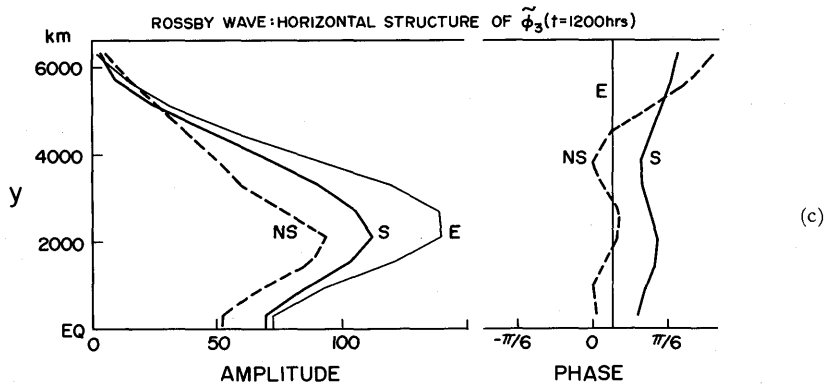
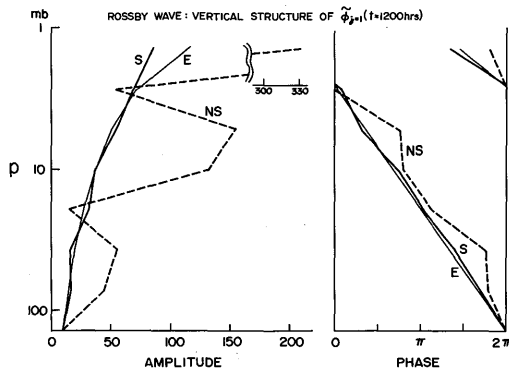
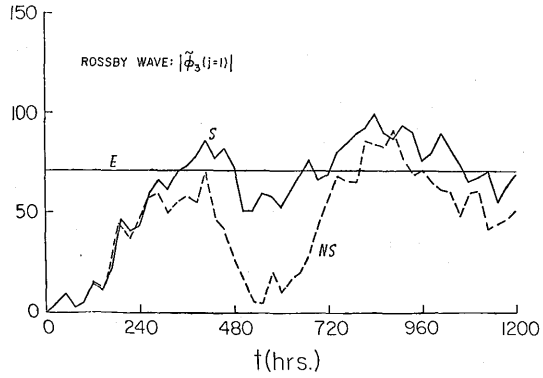


Fig. A2.1.5 Same as in Fig. A2.1.3 (a), (b) (c) except for the case with a Rossby wave forcing (see Table A2.1.1).

geopotential shown in Fig. A2.1.6 (b) and (c).

In the previous three cases, especially in the first two, the sponge layer was quite effective in suppressing reflection of waves below the sponge layer. While, in the present case, it is not. One reason for the ineffective sponge in the present case may be explained as follows; Because we have assumed a steady state in designing the sponge layer model, there is no surprise even when the sponge did not work at the arrival of wave fronts. If the vertical group velocity is small, in vague sense, not much noise may be created at the arrival of the main wave front. On the other hand, if it is large, as is the case for the mode  $\Theta(2,2)$ , much noise might be created, which might cause the sponge model ineffective.

Another reason may be due to the small value of  $\text{Re}(M)/|\sigma|$  for the mode  $\Theta(2,2)$  (see Fig. 2.3). Because there are no dissipative mechanisms other than the sponge term in the present linearized numerical model, secondary noise may not be suppressed well by the sponge term alone.

One may point out, as one of the reasons for the ineffective sponge in the present case, the way in estimating the sponge term. It is estimated by use of the informations in the highest three levels, the depth of which is too thin compared to the vertical wavelength of  $\Theta(2,2)$ . We admit that the estimated value of  $M$  had not a small fluctuation around the expected value of it. However, we do not consider this as the major cause for the unsatisfactory results in the present case because the run where  $M$  was fixed to the exact value, expected in the steady state, did not show much improvement over (S).

### A2.2 Stability check of Eq. (2.1) as an upper boundary condition

When we apply Eq. (2.1) as an upper boundary condition, we may rewrite it as follows,

$$\frac{\partial}{\partial t} \left( \frac{\omega}{\sqrt{p}} \right) + c \frac{\partial}{\partial p} \left( \frac{\omega}{\sqrt{p}} \right) = 0 \quad (\text{A2.2.1})$$

We discuss in this appendix the stability characteristics of free modes when the use has been made of (A2.2.1) as an upper boundary condition.

Because  $c$ , in (A2.2.1), is to be chosen in such a way as to radiate vertically propagating wave energy outward,  $c$  must be a positive value.

Let's consider a rest, isothermal model in which there are no variations of variables in the north-south direction, and the Coriolis parameter  $f$  is constant. We assume the following form of a solution to the linearized system equations:

$$q_k = \text{Re}(\hat{q}_k e^{i(\sigma t + m x)}) \quad (\text{A2.2.2})$$

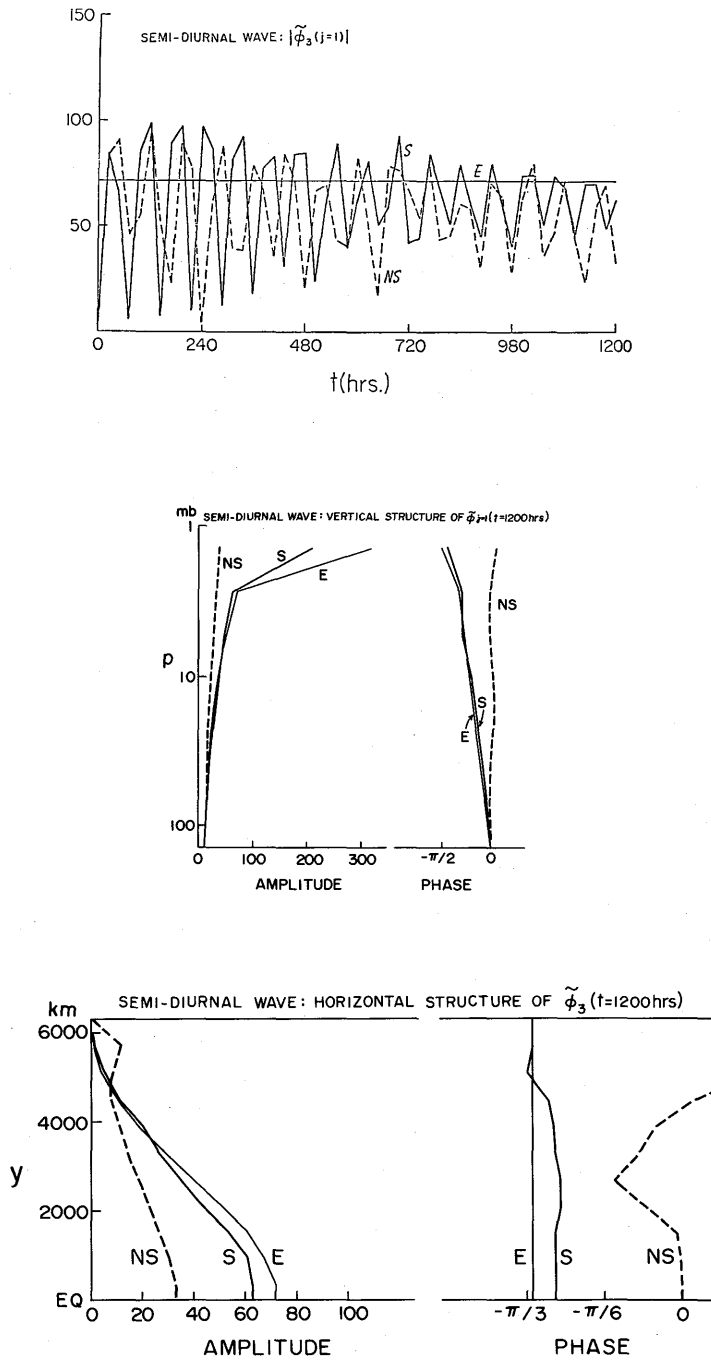


Fig. A2.1.6 Same as in Fig. A2.1.3 (a), (b) (c) except for the case with a semi-diurnal wave forcing (see Table A2.1.1).

We use the same notations as have been used in the text. Then, the linearized system of equations are written as follows:

$$i\sigma\hat{u}_k - f\hat{v}_k = -im\hat{\phi}_k, \tag{A2.2.3}$$

$$i\sigma\hat{v}_k + f\hat{u}_k = 0, \tag{A2.2.4}$$

$$i\sigma\hat{T}_k - \frac{T_0}{\Delta p_k}(S\hat{\omega}_{k+1} + Q\hat{\omega}_{k-1}) = 0, \tag{A2.2.5}$$

$$\hat{\phi}_k - \hat{\phi}_{k+2} = c_p(S\hat{T}_k + Q\hat{T}_{k+2}), \tag{A2.2.6}$$

$$im\hat{u}_k + \frac{1}{\Delta p_k}(\hat{\omega}_{k+1} - \hat{\omega}_{k-1}) = 0, (k=1, 3, \dots, 2K-1). \tag{A2.2.7}$$

From these five equations, we obtain the following equation:

$$e^d A \hat{\omega}_{k-1} - B \hat{\omega}_{k+1} + A \hat{\omega}_{k+3} = 0, \tag{A2.2.8}$$

where

$$A = X^2 - c_p T_0 m^2 Q S - f^2,$$

$$B = (1 + e^d) X^2 + c_p T_0 m^2 (e^d S^2 + Q^2) + (1 + e^d) f^2,$$

$$X = i\sigma,$$

$$e^d = \Delta p_k / \Delta p_{k-2}$$

We apply the bottom boundary condition as

$$\hat{\omega}_{2K} = 0. \tag{A2.2.9}$$

As for the top boundary condition, we express (A2.2.1) in the following form,

$$X(\hat{\omega}_0 + e^{-\frac{d}{2}} \hat{\omega}_2) - \gamma(\hat{\omega}_0 - e^{-\frac{d}{2}} \hat{\omega}_2) = 0,$$

$$\text{where } \gamma = 2c / \Delta p_1. \tag{A2.2.10}$$

Equations (A2.2.8), (A2.2.9) and (A2.2.10) determine eigen-value X. When we apply  $\hat{\omega}_0 = 0$  instead of (A2.2.10) as the top boundary condition, all eigen solutions are neutral, of course, and there are no computational modes in the solutions.

If we use (A2.2.10) as the top boundary condition, instead, all inertio-gravity modes suffer slight damping (stabilization) for positive value of  $\gamma$ . In the present system,

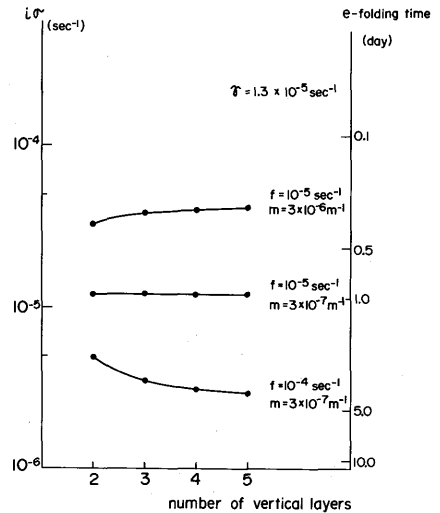


Fig. A2.2.1 The growth rate of the unstable mode as a function of the number of vertical layers, K, when Eq. (A2.2.1) is the upper boundary condition.  $f$  and  $m$  are the Coriolis parameter and the zonal wavenumber. The same vertical gridding as is shown in Fig. A2.1.1 is used.  $T_0$  is set to  $270^\circ\text{K}$ .

however, we have one additional computational mode due to the use of (A2.2.10). This mode is unstable. The growth rate of the solution is shown in Fig. A2.2.1 for a particular value of  $\gamma$ . Numerical values used for the calculation are as follows:

$$d=0.658, T_o=270K, c_p=1004m^2s^{-2}K^{-1}, S=9.1 \times 10^{-2},$$

$$Q=9.7 \times 10^{-2}, \Delta p_1=1.93mb \text{ and } \gamma=1.3 \times 10^{-5}s^{-1}.$$

The growth rate of the unstable mode does not change much with the increase of the number of the vertical layers  $K$ . We see that this mode becomes more unstable with the decrease of the Coriolis parameter  $f$  and with the increase of the zonal wavenumber  $m$ . To make the situation worse, the growth rate is quite large. The rapid growth of errors (about 1/4 day in e-folding time) was observed in the initial value problem test when Eq. (A2.2.1) was used as the upper boundary condition with the same Rossby wave forcing as listed in Table A2.1.1, in which  $\gamma$  is approximately equal to  $1.3 \times 10^{-5} s^{-1}$ .

### 3. Horizontal differencing\*

#### 3.1 Horizontal grid and indices

Spherical coordinate is adopted in the model. Grids on the sphere are distributed in equal intervals in both longitudinal and latitudinal directions. Winninghoff (1968) has shown that the geostrophic adjustment process depends on how the variables are distributed over the grid points. Among five ways of distributing the dependent variables (see Fig. 3.1), Scheme C gives the best dispersion relation for inertio-gravity waves, where  $u$  and  $v$  are velocity components in both "i" and "j" directions, respectively and  $\phi$  is geopotential.

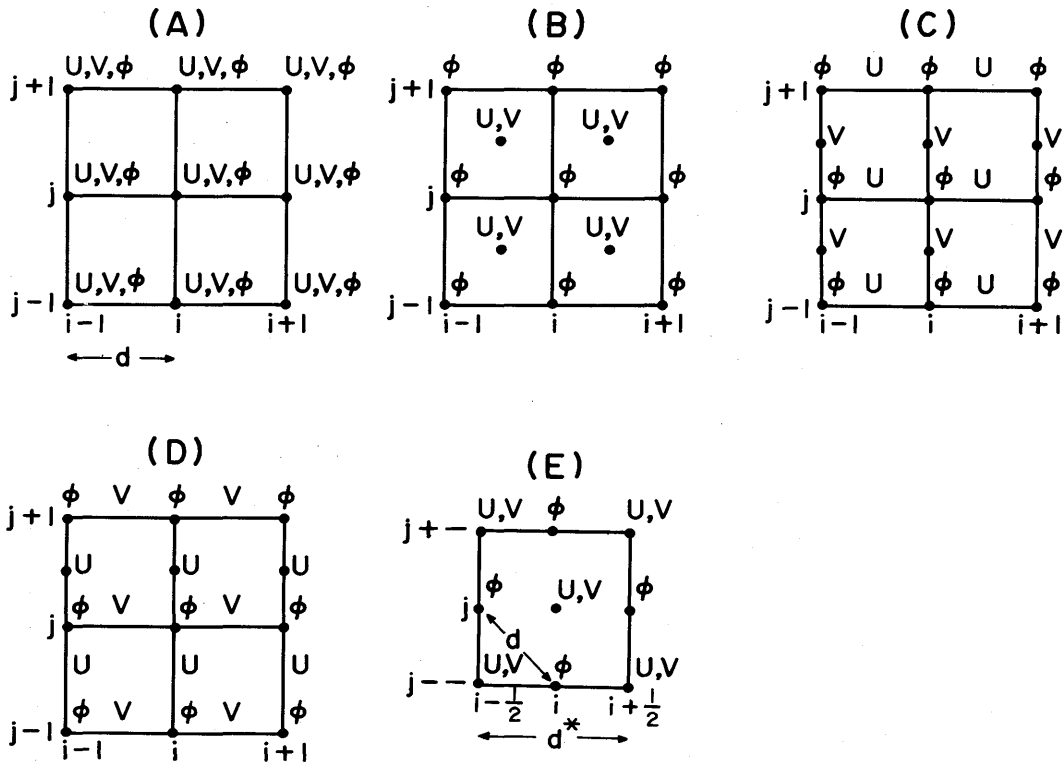


Fig. 3.1 Five ways of distributing variables on the horizontal grids. (Taken from AL)  $u$  and  $v$  are horizontal components of wind in "i" and "j" directions, respectively.  $\phi$  indicates geopotential.

\* This chapter is prepared by T. Tokioka.

Based on the above results, Scheme C is adopted in distributing variables over the sphere. Indices "i" and "j" are used to indicate grid position in longitudinal and latitudinal directions respectively (see Fig. 3.2). Surface pressure  $p_s$ , geopotential  $\phi$ , temperature  $T$ , mixing ratios of water vapor  $q$  and ozone  $O_3$ , and vertical velocity  $\dot{\sigma}$  are defined at the  $\pi$ -point in Fig.3.2.

The details of the horizontal differencing described below are the same as that described by AM or AL except for some special treatments near the poles.

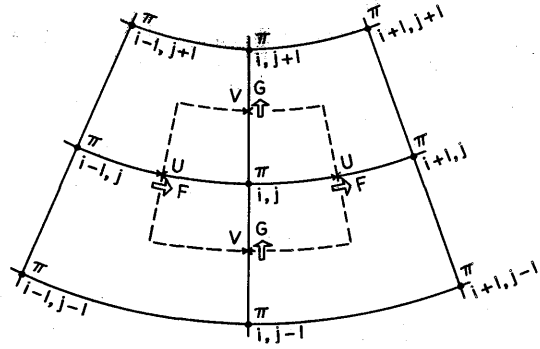


Fig. 3.2 Horizontal indices and location of variables. At  $\pi$ -points, all thermodynamic variables, including water vapor and ozone, are carried. As for the definitions of F and G, see text. (Taken from AL)

### 3.2 The equation of continuity

The equation of continuity (0.14) is expressed as follows;

$$\frac{\partial \Pi_{ij}}{\partial t} + F_{i+\frac{1}{2},j}^k - F_{i-\frac{1}{2},j}^k + G_{i,j+\frac{1}{2}}^k - G_{i,j-\frac{1}{2}}^k + \frac{1}{\Delta \sigma_k} (\dot{S}_{ij}^{k+1} - \dot{S}_{ij}^{k-1}) = 0 \quad (3.1)$$

where

$$\Pi \equiv \pi \frac{\Delta \xi \Delta \eta}{mn}, \quad F \equiv \pi u \frac{\Delta \eta}{n}, \quad G \equiv \pi v \frac{\Delta \xi}{m}, \quad \dot{S} \equiv \Pi \dot{\sigma} \quad (3.2)$$

and

$$\xi = \lambda, \quad \eta = \varphi, \quad \frac{1}{m} = a \cos \varphi \quad \text{and} \quad \frac{1}{n} = a \quad (3.3)$$

The mass flux F and G are defined as follows;

$$\left. \begin{aligned} F_{i+\frac{1}{2},j}^k &= \frac{1}{2} \overline{\left( u \frac{\Delta \eta}{n} \right)}_{i+\frac{1}{2},j}^k (\pi_{i+1,j} + \pi_{i,j}) \\ G_{i,j+\frac{1}{2}}^k &= \frac{1}{2} \overline{\left( v \frac{\Delta \xi}{m} \right)}_{i,j+\frac{1}{2}}^k (\pi_{i,j+1} + \pi_{i,j}) \end{aligned} \right\} \quad (3.4)$$

For the time being, ignore the superior bar operators in (3.4), which are linear smoothing operators in  $\xi$ .

### 3.3 The pressure gradient force

The pressure gradient force in the  $\xi$  -direction is

$$-\frac{\pi}{n} \left[ \frac{\partial \phi}{\partial \xi} + \sigma \alpha \frac{\partial \pi}{\partial \xi} \right]$$

For the first term, we choose the form

$$-\left( \frac{\pi \partial \phi}{n \partial \xi} \right)_{i+\frac{1}{2},j}^k = -\frac{1}{\Delta \xi \Delta \eta} \left( \frac{\Delta \eta}{n} \right)_j \frac{1}{2} \overline{(\pi_{i+1,j} + \pi_{i,j}) (\hat{\phi}_{i+1}^k - \hat{\phi}_{ij}^k)} \quad (3.5)$$

As for the second term, we choose the form

$$-\left( \frac{\pi \sigma \alpha \partial \pi}{n \partial \xi} \right)_{i+\frac{1}{2},j}^k = -\frac{1}{\Delta \xi \Delta \eta} \left( \frac{\Delta \eta}{n} \right)_j \cdot \frac{1}{2} \overline{\{ (\pi \sigma \alpha)_{i+1,j}^k + (\pi \sigma \alpha)_{ij}^k \} (\pi_{i+1,j} - \pi_{i,j})} \quad (3.6)$$

Rearranging the right hand side of (3.5), we confirm that both (3.5) and (3.6), with the help of (1.7), guarantee the relation (1.6) at each grid point.

Similarly, the pressure gradient force in the  $\eta$ -direction is

$$-\left( \frac{\Delta \xi}{m} \right)_{j+1/2} \cdot \frac{1}{2} \left[ \overline{(\pi_{i,j+1} + \pi_{i,j}) (\hat{\phi}_{i,j+1}^k - \hat{\phi}_{ij}^k)} + \overline{\{ (\pi \sigma \alpha)_{ij+1}^k + (\pi \sigma \alpha)_{ij}^k \} (\pi_{i,j+1} - \pi_{i,j})} \right] \quad (3.7)$$

### 3.4 Kinetic energy generation and the first law of thermodynamics

The contribution of the pressure gradient force to the kinetic energy generation

$$\frac{\partial}{\partial t} (\Pi \cdot \frac{1}{2} u^2)_{i+\frac{1}{2},j}^k$$

is obtained by multiplying (3.5) and (3.6) by  $u_{i+\frac{1}{2},j}^k$ . Then the kinetic energy generation is

$$-\frac{1}{2} \left( u \frac{\Delta \eta}{n} \right)_{i+\frac{1}{2},j}^k \left[ \overline{(\pi_{i+1,j} + \pi_{i,j}) (\hat{\phi}_{i+1,j}^k - \hat{\phi}_{ij}^k)} + \overline{\{ (\pi \sigma \alpha)_{i+1,j}^k + (\pi \sigma \alpha)_{ij}^k \} (\pi_{i+1,j} - \pi_{i,j})} \right] \quad (3.8)$$

As the superior bar indicates a linear smoothing operator in  $\xi$ , the summation of (3.8) over  $i$  is identical to that of the following,

$$-\frac{1}{2} \left( u \frac{\Delta \eta}{n} \right)_{i+\frac{1}{2},j}^k \left[ (\pi_{i+1,j} + \pi_{ij}) (\hat{\phi}_{i+1,j}^k - \hat{\phi}_{ij}^k) + \{ (\pi \sigma \alpha)_{i+1,j}^k + (\pi \sigma \alpha)_{ij}^k \} (\pi_{i+1,j} - \pi_{ij}) \right] \quad (3.9)$$

This can be written as;

$$(3.9) = -F_{i+\frac{1}{2},j}^k (\hat{\phi}_{i+1,j}^k - \hat{\phi}_{i,j}^k) - \frac{1}{2} \overline{(u \frac{\Delta \eta}{n})}_{i+\frac{1}{2},j}^k \{ (\pi \sigma \alpha)_{i+1,j}^k + (\pi \sigma \alpha)_{i,j}^k \} (\pi_{i+1,j} - \pi_{i,j}) \quad (3.9)'$$

Therefore we can show that

$$\begin{aligned} \sum_i (3.9) &= \sum_i (F_{i+\frac{1}{2},j}^k - F_{i-\frac{1}{2},j}^k) \hat{\phi}_{i,j}^k - \frac{1}{4} \overline{(u \frac{\Delta \eta}{n})}_{i+\frac{1}{2},j}^k \{ (\pi \sigma \alpha)_{i+1,j}^k + (\pi \sigma \alpha)_{i,j}^k \} (\pi_{i+1,j} - \pi_{i,j}) \\ &\quad - \frac{1}{4} \overline{(u \frac{\Delta \eta}{n})}_{i-\frac{1}{2},j}^k \{ (\pi \sigma \alpha)_{i,j}^k + (\pi \sigma \alpha)_{i-1,j}^k \} (\pi_{i,j} - \pi_{i-1,j}) \end{aligned} \quad (3.10)$$

Similarly, the contribution of the pressure gradient force to

$$\frac{\partial}{\partial t} (\Pi \frac{1}{2} v^2)$$

is given by

$$\begin{aligned} \sum_{i,j} (G_{i,j+\frac{1}{2}}^k - G_{i,j-\frac{1}{2}}^k) \hat{\phi}_{i,j}^k - \frac{1}{4} \overline{(v \frac{\Delta \xi}{m})}_{i,j+\frac{1}{2}}^k \{ (\pi \sigma \alpha)_{i,j+1}^k + (\pi \sigma \alpha)_{i,j}^k \} (\pi_{i,j+1} - \pi_{i,j}) \\ - \frac{1}{4} \overline{(v \frac{\Delta \xi}{m})}_{i,j-\frac{1}{2}}^k \{ (\pi \sigma \alpha)_{i,j}^k + (\pi \sigma \alpha)_{i,j-1}^k \} (\pi_{i,j} - \pi_{i,j-1}) \end{aligned} \quad (3.11)$$

The sum of both (3.10) and (3.11), with the use of continuity equation (3.1), is transformed into the following form;

$$\begin{aligned} \text{kinetic energy generation} &= -\sum_{i,j} \frac{1}{\Delta \sigma_k} \left[ (\dot{S}_{i,j}^{k+1} + \sigma_{k+1} \frac{\partial \Pi^k}{\partial t}) \phi_{i,j}^{k+1} - (\dot{S}_{i,j}^{k-1} + \sigma_{k-1} \frac{\partial \Pi^k}{\partial t}) \phi_{i,j}^{k-1} \right] \\ &\quad - \sum \Pi_{i,j}^k (\omega \alpha)_{i,j}^k \end{aligned}$$

provided that  $(\omega \alpha)_{i,j}^k$  is defined by

$$\begin{aligned} \Pi_{i,j}^k (\omega \alpha)_{i,j}^k &= (\pi \sigma \alpha)_{i,j}^k \frac{\partial \Pi^k}{\partial t} + \frac{1}{4} \{ (\pi \sigma \alpha)_{i+1,j} + (\pi \sigma \alpha)_{i,j} \} \overline{(u \frac{\Delta \eta}{n})}_{i+\frac{1}{2},j}^k (\pi_{i+1,j} - \pi_{i,j}) \\ &\quad + \frac{1}{4} \{ (\pi \sigma \alpha)_{i,j} + (\pi \sigma \alpha)_{i-1,j} \} \overline{(u \frac{\Delta \eta}{n})}_{i-\frac{1}{2},j}^k (\pi_{i,j} - \pi_{i-1,j}) \\ &\quad + \frac{1}{4} \{ (\pi \sigma \alpha)_{i,j+1} + (\pi \sigma \alpha)_{i,j} \} \overline{(v \frac{\Delta \xi}{m})}_{i,j+\frac{1}{2}}^k (\pi_{i,j+1} - \pi_{i,j}) \\ &\quad + \frac{1}{4} \{ (\pi \sigma \alpha)_{i,j} + (\pi \sigma \alpha)_{i,j-1} \} \overline{(v \frac{\Delta \xi}{m})}_{i,j-\frac{1}{2}}^k (\pi_{i,j} - \pi_{i,j-1}) \\ &\quad - \frac{1}{\Delta \sigma_k} \{ \dot{S}_{i,j}^{k+1} (\phi_{i,j}^{k+1} - \hat{\phi}_{i,j}^k) + \dot{S}_{i,j}^{k-1} (\hat{\phi}_{i,j}^k - \phi_{i,j}^{k-1}) \} \end{aligned} \quad (3.13)$$

This expression may be compared with the definition given by (1.9).

Thus the thermodynamic energy equation (1.11) may be written as

$$\begin{aligned}
 \frac{\partial}{\partial t} (\Pi_{i,j} T_{i,j}^k) + F_{i+\frac{1}{2},j}^k \frac{T_{i+1,j}^k + T_{i,j}^k}{2} - F_{i-\frac{1}{2},j}^k \frac{T_{i,j}^k + T_{i-1,j}^k}{2} + G_{i,j+\frac{1}{2}}^k \frac{T_{i,j+1}^k + T_{i,j}^k}{2} - G_{i,j-\frac{1}{2}}^k \frac{T_{i,j}^k + T_{i,j-1}^k}{2} \\
 + \frac{1}{\Delta \sigma_k} [ \dot{S}_{i,j}^{k+1} P_{i,j}^k \hat{\theta}_{i,j}^{k+1} - \dot{S}_{i,j}^{k-1} P_{i,j}^k \hat{\theta}_{i,j}^{k-1} ] = \frac{1}{c_p} [ (\pi \sigma \alpha)_{i,j}^k \frac{\partial \Pi_{i,j}}{\partial t} \\
 + \frac{1}{4} \overline{(u \frac{\Delta \eta}{n})}_{i+\frac{1}{2},j} \{ (\pi \sigma \alpha)_{i+\frac{1}{2},j}^k + (\pi \sigma \alpha)_{i,j}^k \} (\pi_{i+\frac{1}{2},j} - \pi_{i,j}) \\
 + \frac{1}{4} \overline{(u \frac{\Delta \eta}{n})}_{i-\frac{1}{2},j} \{ (\pi \sigma \alpha)_{i,j}^k + (\pi \sigma \alpha)_{i-\frac{1}{2},j}^k \} (\pi_{i,j} - \pi_{i-\frac{1}{2},j}) \\
 + \frac{1}{4} \overline{(v \frac{\Delta \xi}{m})}_{i,j+\frac{1}{2}} \{ (\pi \sigma \alpha)_{i,j+\frac{1}{2}}^k + (\pi \sigma \alpha)_{i,j}^k \} (\pi_{i,j+\frac{1}{2}} - \pi_{i,j}) \\
 + \frac{1}{4} \overline{(v \frac{\Delta \xi}{m})}_{i,j-\frac{1}{2}} \{ (\pi \sigma \alpha)_{i,j}^k + (\pi \sigma \alpha)_{i,j-\frac{1}{2}}^k \} (\pi_{i,j} - \pi_{i,j-\frac{1}{2}}) \\
 + \Pi_{i,j} Q_{i,j}^k ] \quad (3.14)
 \end{aligned}$$

### 3.5 Momentum fluxes

The expression of momentum fluxes in the finite difference form strictly follows the one developed by Arakawa (see AM or AL). We choose for

$$\frac{\partial}{\partial t} (\pi \frac{\Delta \xi \Delta \eta}{mn} u) + \Delta \xi \frac{\partial}{\partial \xi} (\pi u \frac{\Delta \eta}{n}) + \Delta \eta \frac{\partial}{\partial \eta} (\pi v \frac{\Delta \xi}{m}) + \frac{\partial}{\partial \sigma} (\pi \sigma \frac{\Delta \xi \Delta \eta}{mn} u)$$

the form;

$$\begin{aligned}
 \frac{\partial}{\partial t} (\Pi_{i,j}^{(u)} u_{i,j}^k) + \frac{1}{2} (F_{i+\frac{1}{2},j}^{(u)} (u_{i+1,j} + u_{i,j}) - F_{i-\frac{1}{2},j}^{(u)} (u_{i,j} + u_{i-1,j})) \\
 + G_{i,j+\frac{1}{2}}^{(u)} (u_{i,j+1} + u_{i,j}) - G_{i,j-\frac{1}{2}}^{(u)} (u_{i,j} + u_{i,j-1}) \\
 + \tilde{F}_{i+\frac{1}{2},j+\frac{1}{2}}^{(u)} (u_{i+1,j+1} + u_{i,j}) - \tilde{F}_{i-\frac{1}{2},j-\frac{1}{2}}^{(u)} (u_{i,j} + u_{i-1,j-1}) \\
 + \tilde{G}_{i-\frac{1}{2},j+\frac{1}{2}}^{(u)} (u_{i-1,j+1} + u_{i,j}) - \tilde{G}_{i+\frac{1}{2},j-\frac{1}{2}}^{(u)} (u_{i,j} + u_{i+1,j-1}) \\
 + \frac{1}{\Delta \sigma_k} \cdot \frac{1}{2} [ \dot{S}_{i,j}^{(u)k+1} (u_{i,j}^{k+2} + u_{i,j}^k) - \dot{S}_{i,j}^{(u)k-1} (u_{i,j}^k + u_{i,j}^{k-2}) ] \quad (3.15)
 \end{aligned}$$

where  $\Pi^{(u)}$ ,  $S^{(u)}$ ,  $F^{(u)}$ ,  $G^{(u)}$ ,  $\widetilde{F}^{(u)}$  and  $\widetilde{G}^{(u)}$  are not defined yet. When  $u$  is constant both in space and time, (3.15) should be zero. Then we get a continuity equation;

$$\frac{\partial \Pi_{ij}^{(u)}}{\partial t} + (F_{i+\frac{1}{2},j}^{(u)} - F_{i-\frac{1}{2},j}^{(u)} + G_{ij+\frac{1}{2}}^{(u)} - G_{ij-\frac{1}{2}}^{(u)})^k + (\widetilde{F}_{i+\frac{1}{2},j+\frac{1}{2}}^{(u)} - \widetilde{F}_{i-\frac{1}{2},j-\frac{1}{2}}^{(u)} + \widetilde{G}_{i-\frac{1}{2},j+\frac{1}{2}}^{(u)} - \widetilde{G}_{i+\frac{1}{2},j-\frac{1}{2}}^{(u)})^k + \frac{1}{\Delta \sigma_k} (\dot{S}_{ij}^{(u)k+1} - \dot{S}_{ij}^{(u)k-1}) = 0 \quad (3.16)$$

Following AM or AL, we let

$$\left. \begin{aligned} F_{i+\frac{1}{2},j}^{(u)} &= \frac{1}{6} (F_{i+\frac{1}{2},j+1}^* + 2F_{i+\frac{1}{2},j}^* + F_{i+\frac{1}{2},j-1}^*) \\ G_{ij+\frac{1}{2}}^{(u)} &= \frac{1}{6} (G_{i+\frac{1}{2},j}^* + G_{i+\frac{1}{2},j+1}^* + G_{i-\frac{1}{2},j}^* + G_{i-\frac{1}{2},j+1}^*) \\ \widetilde{F}_{i+\frac{1}{2},j+\frac{1}{2}}^{(u)} &= \frac{1}{12} (G_{i+\frac{1}{2},j}^* + G_{i+\frac{1}{2},j+1}^* + F_{i+\frac{1}{2},j}^* + F_{i+\frac{1}{2},j+1}^*) \\ \widetilde{G}_{i-\frac{1}{2},j-\frac{1}{2}}^{(u)} &= \frac{1}{12} (G_{i-\frac{1}{2},j}^* + G_{i-\frac{1}{2},j+1}^* - F_{i-\frac{1}{2},j}^* - F_{i-\frac{1}{2},j+1}^*) \end{aligned} \right\} \quad (3.17)$$

where  $F^*$  and  $G^*$  are defined by

$$\begin{aligned} F_{i,j}^* &= \frac{1}{2} (F_{i+1/2,j} + F_{i-1/2,j}) \\ G_{i,j}^* &= \frac{1}{2} (G_{i,j+1/2} + G_{i,j-1/2}) \end{aligned} \quad (3.18)$$

With the use of (3.17) and (3.18), it is shown that (3.16) is identical to (3.1) provided that

$$\Pi_{i+\frac{1}{2},j}^{(u)} = \frac{1}{8} (\Pi_{i+1,j+1} + \Pi_{i,j+1} + \Pi_{i,j-1} + \Pi_{i+1,j-1} + 2(\Pi_{i+1,j} + \Pi_{i,j})) \quad (3.19)$$

and

$$\dot{S}_{i+\frac{1}{2},j}^{(u)} = \frac{1}{8} (\dot{S}_{i+1,j+1} + \dot{S}_{i,j+1} + \dot{S}_{i,j-1} + \dot{S}_{i+1,j-1} + 2(\dot{S}_{i+1,j} + \dot{S}_{i,j})) \quad (3.20)$$

For  $v$ -component, we use a form identical to (3.15), with  $u$  replaced by  $v$ . Corresponding to (3.17), (3.19) and (3.20), we let

$$\begin{aligned} F_{i+\frac{1}{2},j}^{(v)} &= \frac{1}{6} (F_{i+1,j+\frac{1}{2}}^* + F_{i+1,j-\frac{1}{2}}^* + F_{ij+\frac{1}{2}}^* + F_{ij-\frac{1}{2}}^*) \\ G_{ij+\frac{1}{2}}^{(v)} &= \frac{1}{6} (G_{i+1,j+\frac{1}{2}}^* + 2G_{ij+\frac{1}{2}}^* + G_{ij-\frac{1}{2}}^*) \end{aligned}$$

$$\widetilde{F}_{i+\frac{1}{2},j+\frac{1}{2}}^{(v)} = \frac{1}{12} (G_{i+1,j+\frac{1}{2}}^* + G_{i,j+\frac{1}{2}}^* + F_{i+1,j+\frac{1}{2}}^* + F_{i,j+\frac{1}{2}}^*) \quad (3.21)$$

$$\widetilde{G}_{i-\frac{1}{2},j+\frac{1}{2}}^{(v)} = \frac{1}{12} (G_{i,j+\frac{1}{2}}^* + G_{i-1,j+\frac{1}{2}}^* - F_{i,j+\frac{1}{2}}^* - F_{i-1,j+\frac{1}{2}}^*)$$

$$\Pi_{i,j+\frac{1}{2}}^{(v)} = \frac{1}{8} (\Pi_{i+1,j+1} + \Pi_{i+1,j} + \Pi_{i-1,j+1} + \Pi_{i-1,j} + 2(\Pi_{i,j+1} + \Pi_{i,j})) \quad (3.22)$$

$$\dot{S}_{i,j+\frac{1}{2}}^{(v)} = \frac{1}{8} (\dot{S}_{i+1,j+1} + \dot{S}_{i+1,j} + \dot{S}_{i-1,j+1} + \dot{S}_{i-1,j} + 2(\dot{S}_{i,j+1} + \dot{S}_{i,j})) \quad (3.23)$$

In the limit of two-dimensional non-divergent flow, the flux form described above guarantees the conservation of enstrophy as well as kinetic energy as shown by A, AM or AL.

### 3.6 Coriolis force

Coriolis force plus the metric term which contributes to  $\frac{\partial}{\partial t}(\Pi u)$  is

$$\left[ f \frac{\Delta \xi \Delta \eta}{mn} - u \Delta \xi \Delta \eta \frac{\partial}{\partial \eta} \left( \frac{1}{m} \right) \right] \pi v \quad (3.24)$$

and the Coriolis force which contributes to  $\frac{\partial}{\partial t}(\Pi v)$  is

$$- \left[ f \frac{\Delta \xi \Delta \eta}{mn} - u \Delta \xi \Delta \eta \frac{\partial}{\partial \eta} \left( \frac{1}{m} \right) \right] \pi u \quad (3.25)$$

Defining  $C_{ij}^k$  at  $\pi$ -point as follows,

$$C_{ij}^k = f_j \left( \frac{\Delta \xi \Delta \eta}{mn} \right)_j - \frac{1}{2} (u_{i+\frac{1}{2},j} + u_{i-\frac{1}{2},j})^k \left\{ \left( \frac{\Delta \xi}{m} \right)_{j+1/2} - \left( \frac{\Delta \xi}{m} \right)_{j-1/2} \right\} \quad (3.26)$$

we express (3.24), at  $u$ -point  $(i+\frac{1}{2},j)$ , in the following way,

$$\frac{1}{4} \left[ \pi_{i+1,j} C_{i+1,j}^k (v_{i+1,j+1/2} + v_{i+1,j-1/2})^k + \pi_{i,j} C_{i,j}^k (v_{i,j+1/2} + v_{i,j-1/2})^k \right] \quad (3.27)$$

(3.25), at  $v$ -point  $(i,j+\frac{1}{2})$ , is expressed as

$$- \frac{1}{4} \left[ \pi_{i,j+1} C_{i,j+1}^k (u_{i+1/2,j+1} + u_{i-1/2,j+1})^k + \pi_{i,j} C_{i,j}^k (u_{i+1/2,j} + u_{i-1/2,j})^k \right] \quad (3.28)$$

Note that exact cancellation of kinetic energy generation through Coriolis force is guaranteed by the forms (3.27) and (3.28).

## 4. Special treatment near the poles\*

### 4.1 Modifications of the difference equation

As the poles are singular points in the spherical coordinate, velocity components cannot be defined there. Therefore, we let the poles be  $\pi$ -points. The mass at the poles changes through the meridional mass flux,  $G$ , at all the  $v$ -points surrounding the poles, as shown in Fig.4.1. We let the north pole be  $j=p$ , and treat it as if it were a group of points, just for simplifying the computation. Each point has index  $i$  and represents the area shaded in Fig.4.1.

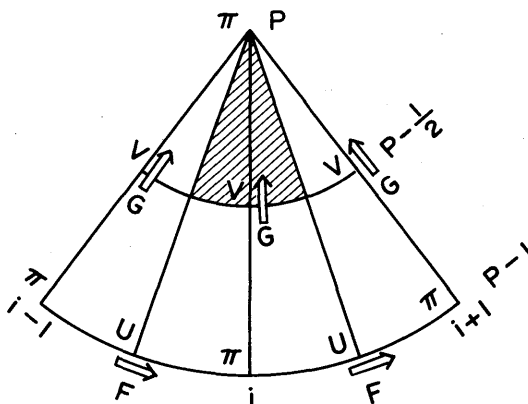


Fig. 4.1 Horizontal indices and location of variables in vicinity of the north pole.

Defining  $\Pi_{i,p}$  and  $S_{i,p}$  based on that area, we

apply the equation of continuity (4.1) to  $j=p$ , omitting all horizontal mass flux terms except  $G_{i,p-1/2}$ . After computing  $\partial \Pi / \partial t$  and  $S$  for all  $i$ , we take the average.

$$\frac{\partial}{\partial t} \sum_i \Pi_{i,p}^k - \sum_i G_{i,p-1/2} + \frac{1}{\Delta \sigma_k} (\dot{S}_{i,p}^{k+1} - \dot{S}_{i,p}^{k-1}) = 0 \quad (4.1)$$

The advective terms in the  $v$ -momentum equation at the point  $(i,p-1/2)$  are given the following form;

$$\begin{aligned} & \frac{\partial}{\partial t} (\Pi^{(v)} \mathbf{v})_{i,p-1/2}^k + \frac{1}{2} (F_{i+1/2,p-1/2}^{*(v)} (\mathbf{v}_{i,p-1/2} + \mathbf{v}_{i+1,p-1/2}) \\ & \quad - F_{i-1/2,p-1/2}^{*(v)} (\mathbf{v}_{i,p-1/2} + \mathbf{v}_{i-1,p-1/2})) \\ & \quad - G_{i,p-1}^{(v)} (\mathbf{v}_{i,p-1/2} + \mathbf{v}_{i,p-3/2}) \\ & \quad - \tilde{F}_{i-1/2,p-1}^{(v)} (\mathbf{v}_{i,p-1/2} + \mathbf{v}_{i-1,p-3/2}) \\ & \quad - \tilde{G}_{i+1/2,p-1}^{(v)} (\mathbf{v}_{i,p-1/2} + \mathbf{v}_{i+1,p-3/2}) \end{aligned}^k$$

---

\* This chapters is prepared by T. Tokioka.

$$+ \frac{1}{\Delta \sigma_k} \cdot \frac{1}{2} (\dot{S}^{(v)k+1} (v^{k+2} + v^k) - \dot{S}^{(v)k-1} (v^k + v^{k-2}))_{i,p-1/2} \quad (4.2)$$

The form of  $\Pi_{i,p-1/2}^{(v)}$  should be,

$$\begin{aligned} \Pi_{i,p-1/2}^{(v)} = & \frac{1}{8} \{ \Pi_{i+1,p} + \Pi_{i+1,p-1} + 2(\Pi_{i,p} + \Pi_{i,p-1}) + \Pi_{i-1,p} + \Pi_{i-1,p-1} \} \\ & + \frac{1}{8} (\Pi_{i+1,p} + 2\Pi_{i,p} + \Pi_{i-1,p}) \end{aligned} \quad (4.3)$$

so that the global sum of  $\Pi^{(v)}$  is equal to the global sum of  $\Pi^{(u)}$ .  $\dot{S}_{i,p-1/2}^{(v)}$  is defined, also, by (4.3) by replacing  $\Pi$  with  $\dot{S}$ . If we replace  $v$  in (4.2) by a constant value, it reduces to an analog of the continuity equation. In order that the equation is compatible with the continuity equation (3.1) and (4.1),

$$F_{i+1/2,p-1/2}^{*(v)} = \frac{1}{6} (F_{i,p-1}^{*} + F_{i+1,p-1}^{*}) \quad (4.4)$$

In a similar way, advective terms in the u-momentum equation at the grid point  $(i+1/2, p-1, k)$ ,  $\Pi_{i+1/2,p-1}^{(u)}$  and  $F_{i,p-1}^{*(u)}$  are

$$\begin{aligned} & \frac{\partial}{\partial t} (\Pi^{(u)} u)_{i+1/2,p-1}^k + \frac{1}{2} (F_{i+1,p-1}^{*(u)} (u_{i+3/2,p-1} + u_{i+1/2,p-1}) \\ & - F_{i,p-1}^{*(u)} (u_{i+1/2,p-1} + u_{i-1/2,p-1}) \\ & - G_{i+1/2,p-1/2}^{(u)} (u_{i+1/2,p-1} + u_{i+1/2,p-2}) - \tilde{F}_{i,p-3/2}^{(u)} (u_{i+1/2,p-1} + u_{i-1/2,p-2}) \\ & - \tilde{G}_{i+1,p-3/2}^{(u)} (u_{i+3/2,p-2} + u_{i+1/2,p-1}))^k \\ & + \frac{1}{\Delta \sigma_k} \cdot \frac{1}{2} (\dot{S}^{(u)k+1} (u^{k+2} + u^k) - \dot{S}^{(u)k-1} (u^k + u^{k-2}))_{i+1/2,p-1} \end{aligned} \quad (4.5)$$

$$\begin{aligned} \Pi_{i+1/2,p-1}^{(u)} = & \frac{1}{8} \{ \Pi_{i,p} + \Pi_{i+1,p} + 2(\Pi_{i,p-1} + \Pi_{i+1,p-1}) + \Pi_{i,p-2} + \Pi_{i+1,p-2} \} \\ & + \frac{1}{8} \{ 3(\Pi_{i,p} + \Pi_{i+1,p}) + \Pi_{i,p-1} + \Pi_{i+1,p-1} \} \end{aligned} \quad (4.6)$$

$$F_{i,p-1}^{*(u)} = \frac{1}{6} (4F_{i,p-1}^{*} + F_{i,p-2}^{*}) \quad (4.7)$$

$\dot{S}_{i+1/2,p-1}^{(u)}$  is readily defined by replacing  $\Pi$  in (4.6) by  $\dot{S}$ .

#### 4.2 Introduction of averaging operator to selected terms

The grid interval in the east-west direction decreases with the increase of latitude. In order to avoid the use of a small time interval with that decrease, we have introduced an averaging operator in the east-west direction to selected terms, following Arakawa's analysis (AM or AL). The averaging operator is required to the pressure gradient force in the east-west direction and  $\partial(\pi u/n)/\partial\xi$  in the continuity equation. In order to maintain conservation of kinetic energy in the advective process still after the modification of the continuity equation, several terms in the momentum equations should also be replaced by the smoothed value of them. The superior bars in Chapter 3 are the reminders that those terms should be smoothed somehow in the east-west direction.

The momentum equations can be transformed into the vorticity equation. In order that the vorticity equation thus derived does not have terms with no correspondence in the continuous form of it, the terms with the double superior bars should also be replaced by the smoothed values of them. The averaging operators denoted by both the single and the double superior bars are identical. The different notations are used just to remind that the operator is required from the different reasons.

Let  $d\xi$  and  $d\eta$  be the longitudinal and latitudinal grid sizes. Arakawa's analysis show that the amplitude of Fourier component of the term in the longitudinal direction with the wavenumber  $k$  should be multiplied by the factor  $S(j,k)$ ;

$$S(j,k) = \min(1, \frac{d\xi_j}{d\eta} / \sin(\frac{k}{2}d\xi_j)) \quad (4.8)$$

where  $\min(,)$  is the operation to take the less value between the two in the parenthesis. As the operation is linear, we can define the corresponding operator in the real grid space, which is nothing but the superior bar operator. Actually, approximate forms of the operator is adopted currently for the economy of computation.

## 5. Time integration\*

The time integration of the model is carried out in the leapfrog scheme with the periodical use of the Euler backward (Matsuno) scheme. To explain the procedure, we write the equation symbolically in the following form ;

$$dA/dt=f(A) \quad (5.1)$$

The leapfrog scheme (L) is

$$(A^{\tau+1}-A^{\tau-1})/2\Delta t=f(A^{\tau}) \quad (5.2)$$

The Matsuno scheme (M) is a combination of the following two steps ;

$$\begin{aligned} (A^{*\tau+1}-A^{\tau})/\Delta t=f(A^{\tau}) & : \text{Euler (foreward)} \\ (A^{\tau+1}-A^{\tau})/\Delta t=f(A^{*\tau+1}) & : \text{Backward} \end{aligned} \quad (5.3)$$

The time integration scheme is schematically shown in Fig. 5.1.

At present, diabatic terms, dissipative terms and the vertical flux convergence terms of both the mixing ratio of water vapor and ozone are calculated in every eight time steps at the Euler (Foreward) stage, as shown by the arrows.

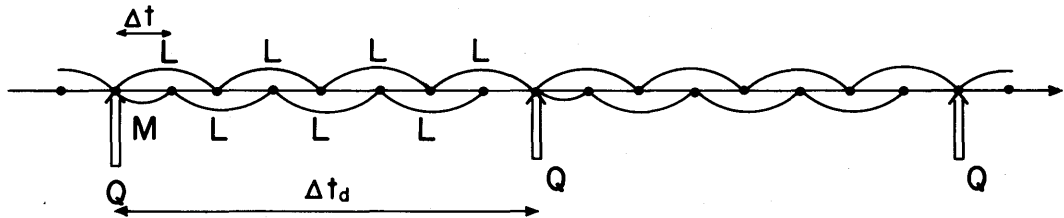


Fig. 5.1 Schematic figure of time integration. M indicates Matsuno step and L, leap-frog step. Time integration of adiabatic part of the model is performed with the time interval  $\Delta t$ , while diabatic effects Q, including diffusions, are calculated with the time interval  $\Delta t_d$ .

\* This chapter is prepared by T. Tokioka.

## 6 Transport process of moisture and ozone\*

In this chapter the transport process of passive quantities, namely, moisture and ozone, is described. Moisture and ozone are passive quantities in the sense that they are conveyed by the advection process besides sources and sinks and do not affect the dynamical fields directly. Therefore their finite differencing schemes seem to be relatively straightforward. There is, however, the difficulty which comes from their large spacial variations and existence of the lower limit (i.e. zero). As for moisture, another difficulty named as CICK ("conditional instability of computational kind") must be avoided. These problems are partially solved by choosing interpolation values for the half-integer levels appropriately as described in this chapter. See Arakawa and Mintz (1974, hereafter referred to as AM) for details.

### 6.1 Vertical differencing of the moisture equation

The continuity equation for water vapor (0.28) is repeated here with  $S$  replaced by  $-C$ ,

$$\frac{\partial}{\partial t}(\pi q) = -\nabla \cdot (\pi \mathbf{v} q) - \frac{\delta(\pi \dot{\sigma} q)}{\delta \sigma} - \pi C \quad (6.1)$$

where  $C$  is the sink of water vapor per unit mass of dry air. Using the continuity equation (1.3), (6.1) may be rewritten as

$$\begin{aligned} \left( \frac{\partial}{\partial t} + \mathbf{v} \cdot \nabla \right) q_k = & -\frac{1}{(\pi \delta \sigma)_k} [ (\pi \dot{\sigma})_{k+1/2} (\hat{q}_{k+1/2} - q_k) + (\pi \dot{\sigma})_{k-1/2} (q_k - \hat{q}_{k-1/2}) ] \\ & - C_k \end{aligned} \quad (6.2)$$

This form of vertical differencing is also used for ozone transport. Consider, first, a moist adiabatic process. Let the saturation mixing ratio be  $q^*_k = q^*(T_k, p_k)$ . When the layer  $k$  is saturated and remains saturated, (6.1) may be written as

$$\begin{aligned} \left( \frac{\partial}{\partial t} + \mathbf{v} \cdot \nabla \right) q^*_k = & -\frac{1}{(\pi \delta \sigma)_k} [ (\pi \dot{\sigma})_{k+1/2} (\hat{q}_{k+1/2} - q^*_k) + (\pi \dot{\sigma})_{k-1/2} (q^*_k - \hat{q}_{k-1/2}) ] \\ & - C_k \end{aligned} \quad (6.3)$$

and then as

---

\* This chapter is prepared by K. Yamazaki : Forecast Research Division

$$\begin{aligned} \left(\frac{\partial q^*}{\partial T}\right)_{pk} \left(\frac{\partial}{\partial t} + \mathbf{v}_k \cdot \nabla\right) T_k &= - \left(\frac{\partial q^*}{\partial p}\right)_{Tk} \sigma_k \left(\frac{\partial}{\partial t} + \mathbf{v}_k \cdot \nabla\right) \pi_k \\ &- \frac{1}{(\pi \delta \sigma)_k} \{ (\pi \dot{\sigma})_{k+1/2} (\hat{q}_{k+1/2} - q^*_k) + (\pi \dot{\sigma})_{k-1/2} (q^*_k - \hat{q}_{k-1/2}) \} - C_k \end{aligned} \quad (6.4)$$

where

$$\left(\frac{\partial q^*}{\partial T}\right)_{pk} = \left(\frac{\partial q_k^*}{\partial T_k}\right)_{pk}, \quad \left(\frac{\partial q^*}{\partial p}\right)_{Tk} = \left(\frac{\partial q_k^*}{\partial p_k}\right)_{Tk} \quad (6.5)$$

The thermodynamic energy equation is, from (1.11),

$$\begin{aligned} \left(\frac{\partial}{\partial t} + \mathbf{v}_k \cdot \nabla\right) T_k &= - \frac{1}{c_p} \alpha_k \sigma_k \left(\frac{\partial}{\partial t} + \mathbf{v}_k \cdot \nabla\right) \pi_k \\ &- \frac{1}{(\pi \delta \sigma)_k} \{ (\pi \dot{\sigma})_{k+1/2} (p_k \hat{\theta}_{k+1/2} - T_k) + (\pi \dot{\sigma})_{k-1/2} (T_k - p_k \hat{\theta}_{k-1/2}) \} \\ &+ C_k \end{aligned} \quad (6.6)$$

where  $\alpha \equiv c_p \theta (\partial p / \partial \pi) / \sigma$  and  $\sigma \equiv (p - p_1) / \pi$ . Eqs. (6.4) and (6.6) give

$$\begin{aligned} C_k &= \frac{1}{1 + \frac{L}{c_p} \left(\frac{\partial q^*}{\partial T}\right)_{pk}} \left\{ \left[ \left(\frac{\partial q^*}{\partial p}\right)_{Tk} + \frac{\alpha_k}{c_p} \left(\frac{\partial q^*}{\partial T}\right)_{pk} \right] \sigma_k \left(\frac{\partial}{\partial t} + \mathbf{v}_k \cdot \nabla\right) \pi_k \right. \\ &- \left. \left(\frac{\partial q^*}{\partial T}\right)_{pk} \frac{p_k}{(\pi \delta \sigma)_k} \{ (\pi \dot{\sigma})_{k+1/2} (\hat{\theta}_{k+1/2} - \theta_k) + (\pi \dot{\sigma})_{k-1/2} (\theta_k - \hat{\theta}_{k-1/2}) \} \right. \\ &+ \left. \frac{1}{(\pi \delta \sigma)_k} \{ (\pi \dot{\sigma})_{k+1/2} (\hat{q}_{k+1/2} - q^*_k) + (\pi \dot{\sigma})_{k-1/2} (q^*_k - \hat{q}_{k-1/2}) \} \right\} \end{aligned} \quad (6.7)$$

Substituting (6.7) into (6.6), we obtain

$$\begin{aligned} \left(\frac{\partial}{\partial t} + \mathbf{v}_k \cdot \nabla\right) T_k &= \left(\frac{\partial T}{\partial p}\right)_{mk} \left(\frac{\partial}{\partial t} + \mathbf{v}_k \cdot \nabla\right) \pi_k - \frac{1}{1 + \frac{L}{c_p} \left(\frac{\partial q^*}{\partial T}\right)_{pk}} \frac{1}{(\pi \delta \sigma)_k} \times \\ &\quad \{ (\pi \dot{\sigma})_{k+1/2} [p_k (\hat{\theta}_{k+1/2} - \theta_k) + \frac{L}{c_p} (\hat{q}_{k+1/2} - q^*_k)] \\ &\quad + (\pi \dot{\sigma})_{k-1/2} [p_k (\theta_k - \hat{\theta}_{k-1/2}) + \frac{L}{c_p} (q^*_k - \hat{q}_{k-1/2})] \} \end{aligned} \quad (6.8)$$

where

$$\left(\frac{\partial T}{\partial p}\right)_{mk} \equiv \frac{\frac{\alpha_k}{c_p} - \frac{L}{c_p} \left(\frac{\partial q^*}{\partial p}\right)_{Tk}}{1 + \frac{L}{c_p} \left(\frac{\partial q^*}{\partial T}\right)_{pk}} \quad (6.9)$$

The coefficient of  $(\pi \dot{\sigma})_{k+1/2}$  in (6.8) is

$$\begin{aligned}
 & p_k (\hat{\theta}_{k+1/2} - \theta_k) + \frac{L}{c_p} (\hat{q}_{k+1/2} - q^*_k) \\
 &= \frac{1}{c_p} [(c_p \hat{T}_{k+1/2} + \phi_{k+1/2} + L \hat{q}_{k+1/2}) - (c_p T_k + \phi_k + L q^*_k)] \\
 &= \frac{1}{c_p} (\hat{h}_{k+1/2} - h^*_k) \tag{6.10}
 \end{aligned}$$

where (1.13) and (1.14) and the definition of  $h$  have been used. Similarly, the coefficient of  $(\pi\dot{\sigma})_{k-1/2}$  in (6.8) is

$$\frac{1}{c_p} [(h^*_k - \hat{h}_{k-1/2})] \tag{6.11}$$

Thus (6.8) can be written as

$$\begin{aligned}
 & \left(\frac{\partial}{\partial t} + \mathbf{v}_k \cdot \nabla\right) T_k = \left(\frac{\partial T}{\partial p}\right)_{mk} \left(\frac{\partial}{\partial t} + \mathbf{v}_k \cdot \nabla\right) \pi_k \\
 & - \frac{1}{c_p + L \left(\frac{\partial q^*}{\partial T}\right)_{pk}} \frac{1}{(\pi\dot{\sigma})_k} [(\pi\dot{\sigma})_{k+1/2} (h_{k+1/2} - h_p^*) + (\pi\dot{\sigma})_{k-1/2} (\hat{h}_{k-1/2})] \tag{6.12}
 \end{aligned}$$

The choice of  $q$  (or equivalently,  $h$ ) at the levels remains to be specified.

## 6.2 Vertical interpolation of moisture and "CICK"

From (6.12) it is clear that a negative  $(\pi\dot{\sigma})_{k+1/2}$  has a warming effect for  $\hat{h}_{k+1/2} > h^*_k$ . This may occur even when  $h^*_{k+1} < h^*_k$ , that is, when no conditional instability exists between the integer levels  $k+1$  and  $k$ . The same effect can similarly occur for a negative  $(\pi\dot{\sigma})_{k-1/2}$  when  $h^*_k > \hat{h}_{k-1/2}$ , even when  $h^*_k < h^*_{k-1}$ . Any moist convective instability produced by such a warming effect is the result merely of a poor choice of  $\hat{q}_{k+1/2}$ . This type of computational instability is termed as the "conditional instability of computational kind" (CICK). See AM for details.

The CICK can be avoided if the choice of  $\hat{q}_{k+1/2}$  and thus  $\hat{h}_{k+1/2}$  satisfies the following requirements when  $h^*_{k+1} < h^*_k$ :

$$\hat{h}_{k+1/2} < h^*_k \quad \text{when } r_k = 1 \tag{6.13}$$

and

$$h^*_{k+1} < \hat{h}_{k+1/2} \quad \text{when } r_{k+1} = 1 \tag{6.14}$$

where  $r_k$  is the relative humidity of the level  $k$ , given by

$$r_k = q_k / q^*_k \tag{6.15}$$

Let us write  $\hat{h}_{k+1/2}$  as

$$\begin{aligned}\hat{h}_{k+1/2} &\equiv \hat{s}_{k+1/2} + L\hat{q}_{k+1/2} \\ &= \hat{s}_{k+1/2} + L\hat{r}_{k+1/2}\hat{q}_{k+1/2}^* \\ &= \hat{s}_{k+1/2} + \hat{r}_{k+1/2}(\hat{h}_{k+1/2}^* - \hat{s}_{k+1/2}) \\ &= (1 - \hat{r}_{k+1/2})\hat{s}_{k+1/2} + \hat{r}_{k+1/2}\hat{h}_{k+1/2}^*\end{aligned}\quad (6.16)$$

where  $\hat{r}_{k+1/2}$  is a properly defined relative humidity at level  $k+1/2$ , and

$$\hat{s}_{k+1/2} \equiv c_p \hat{T}_{k+1/2} + \phi_{k+1/2} \quad (6.17)$$

Substitutions of (6.16) into (6.13) and (6.14) give

$$(1 - \hat{r}_{k+1/2})\hat{s}_{k+1/2} + \hat{r}_{k+1/2}\hat{h}_{k+1/2}^* < h_k^* \quad \text{when } r_k = 1$$

and

$$h_{k+1}^* < (1 - \hat{r}_{k+1/2})\hat{s}_{k+1/2} + \hat{r}_{k+1/2}\hat{h}_{k+1/2}^* \quad \text{when } r_{k+1} = 1 \quad (6.18)$$

Suppose that  $\hat{h}_{k+1/2}^*$  is an interpolation of  $h^*$  from the level  $k$  and  $k+1$  to the level  $k+1/2$  that guarantees  $h_{k+1}^* < \hat{h}_{k+1/2}^* < h_k^*$  if  $h_{k+1}^* < h_k^*$ . If we choose  $\hat{r}_{k+1/2} = 1$  when either  $r_k = 1$  or  $r_{k+1} = 1$ , the inequalities (6.18) are satisfied, regardless of the actual form of the interpolation for  $h_{k+1/2}^*$  under the condition  $h_{k+1}^* < h_k^*$ . The form given below satisfies the above requirement.

$$\hat{r}_{k+1/2} = \frac{r_k + r_{k+1} - 2r_k r_{k+1}}{2 - r_k - r_{k+1}} \quad (6.19)$$

(When both  $r_k$  and  $r_{k+1}$  are 1,  $\hat{r}_{k+1/2}$  is set to 1).

The form of the interpolation used to obtain  $h^*$  is important, however, in relation to the interpolation chosen for  $\hat{s}_{k+1/2}$ . Since

$$h_k^* = Lq_k^* + s_k \quad (6.20)$$

an interpolation for  $\hat{h}_{k+1/2}^*$  independent of for  $\hat{s}_{k+1/2}$  could in theory allow the implicit generation of a negative  $\hat{q}_{k+1/2}^*$ . To avoid this, the interpolation for  $\hat{h}_{k+1/2}^*$  is chosen proportional to that for  $s_{k+1}$ :

$$\begin{aligned}\hat{h}_{k+1/2}^* - h_k^* &= A(\hat{s}_{k+1/2} - s_k) \\ h_{k+1}^* - \hat{h}_{k+1/2}^* &= A(s_{k+1} - \hat{s}_{k+1/2})\end{aligned}\quad (6.12)$$

and

$$A \equiv \frac{h_{k+1}^* - h_k^*}{s_{k+1} - s_k} \quad (6.22)$$

Recall that (1.12) and (1.13) give

$$\begin{aligned}\hat{s}_{k+1/2} - s_k &= P_k c_p (\hat{\theta}_{k+1/2} - \theta_k) \\ s_{k+1} - \hat{s}_{k+1/2} &= P_{k+1} c_p (\theta_{k+1} - \hat{\theta}_{k+1/2})\end{aligned}\quad (6.23)$$

Then we obtain

$$s_{k+1} - s_k = P_k C_p (\hat{\theta}_{k+1/2} - \theta_k) + P_{k+1} C_p (\theta_{k+1} - \hat{\theta}_{k+1/2}) \quad (6.24)$$

which determines the denominator of (6.22). Eq. (6.16) gives

$$q_{\text{CICK}} \equiv \hat{q}_{k+1/2} = \frac{1}{L} \hat{r}_{k+1/2} (\hat{h}_{k+1/2}^* - \hat{s}_{k+1/2}) \quad (6.25)$$

There is no reason to choose this  $q$ , however, if condensation processes are not involved. For the relatively dry case, it is more important to guarantee that  $q$  remains positive or zero. The simple arithmetic average,  $\hat{q}_{k+1/2} = \frac{1}{2}(q_k + q_{k+1})$  is not a good choice. Because, if  $q_k = 0$ ,  $q_{k+1} > 0$  and  $(\pi\sigma)_{k+1/2} > 0$ , then downward current removes a positive amount from zero. Presumably, the application of (1.20) to water vapor mixing ratio is a better choice for the relatively dry case. It is given by

$$q_{\text{in}} \equiv \hat{q}_{k+1/2} = \frac{\ln q_k - \ln q_{k+1}}{1/q_{k+1} - 1/q_k} \quad (6.26)$$

In fact, with that choice,  $\hat{q}_{k+1/2}$  is zero when either  $q_{k+1}$  or  $q_k$  is zero.

In the present model, the following formula is used as a compromise.

$$\hat{q}_{k+1/2} = \hat{r}_{k+1/2} q_{\text{CICK}} + (1 - \hat{r}_{k+1/2}) q_{\text{in}} \quad (6.27)$$

### 6.3 Vertical differencing of the ozone equation

The ozone equation does not have the difficulty such as CICK mentioned in the previous section. We simply adopt the vertical interpolation (1.20) for ozone mixing ratio.

$$\hat{O}_{s_{k+1/2}} = \frac{\ln O_{s_k} - \ln O_{s_{k+1}}}{1/O_{s_{k+1}} - 1/O_{s_k}} \quad (6.28)$$

where  $O_3$  is the mixing ratio of ozone. The vertical differencing scheme for ozone is the same as (6.2) except that  $-C_k$  term is replaced by the source term of ozone due to photochemical processes described in Chapter 12.

### 6.4 Horizontal differencing

The finite horizontal differencing schemes for both moisture and ozone are the same in the MRI-GCM-I. In the following only the scheme for moisture is shown.

Using eqs. (3.1) through (3.4), the horizontal flux term of the moisture equation (6.1) can be written as

$$\begin{aligned} \frac{\partial}{\partial t} (\pi_{i,j} q_{i,j}) = & -F_{i+1/2,j} \hat{q}_{i+1/2,j} + F_{i-1/2,j} \hat{q}_{i-1/2,j} \\ & -G_{i,j+1/2} \hat{q}_{i,j+1/2} + G_{i,j-1/2} \hat{q}_{i,j-1/2} \end{aligned} \quad (6.29)$$

+ other terms

The  $\hat{q}$  is defined by the arithmetic average, for example,

$$\hat{q}_{i+1/2,j} = \frac{1}{2}(q_{i,j} + q_{i+1,j}) \quad (6.30)$$

The difficulty, which comes from the existence of the lower limit of  $q$  (that is,  $q=0$ ), also exists in the horizontal differencing. Therefore,  $\hat{q}$  is defined as

$$\hat{q}_{i+1/2,j} = \frac{2q_{i,j}q_{i+1,j}}{q_{i,j} + q_{i+1,j}} \quad (6.31)$$

when  $F_{i+1/2,j} > 0$  and  $q_{i,j} < q_{i+1,j}$  or  $F_{i+1/2,j} < 0$  and  $q_{i,j} > q_{i+1,j}$ . Note that this form is formally derived from (1.2) if we choose  $G(x) = 1/x$ . Otherwise, eq. (6.30) is used in the present model.

$\hat{q}_{i-1/2,j}$ ,  $\hat{q}_{i,j+1/2}$  and  $\hat{q}_{i,j-1/2}$  are defined in a similar way.

## 7. Penetrative cumulus convection\*

### 7.1 Introduction

The horizontal scale of a cumulus cloud ranges from about 1 to 10 km and this scale is much smaller than the horizontal resolution of the GCM which is about 100~500 km. Therefore, it is impossible to resolve each cumulus cloud in the GCM. On the other hand, the cumulus clouds sometimes extend to about 10 km or more in the vertical direction and play an important role in the vertical transfer of heat, moisture and momentum.

Deep cumuli are a major heating source in the ITCZ and a driving force of Hadley circulation. Thus a cumulus cloud parameterization is essential in simulating global climate by the GCM.

For the parameterization be possible, we have to assume that effects of cumulus cloud ensemble can be determined by the large-scale environment. In other words, the parameterization problem is how to determine grid-scale heat, moisture and momentum changes due to cumulus cloud ensemble in terms of grid-scale fields.

The cumulus parameterization scheme of the MRI-GCM is based on Arakawa-Schubert cumulus parameterization (hereafter abbreviated as the A-S cumulus parameterization. For details, see Arakawa and Schubert, 1974, Lord and Arakawa, 1980, Lord, 1982, Lord, Chao and Arakawa, 1982, etc.). The A-S cumulus parameterization consists of two major parts. One is the cloud model which is described in sections 7.2 and 7.3, and the other is the closure assumption which is described in section 7.4. The discretized form of the parameterization is described in sections 7.5 through 7.8. Section 7.9 describes the parameterization of ice phase cumuli. Appendix 7.1 gives the selected results from the MRI-GCM-I integrations and discussions. Appendix 7.2 gives simple examples of the solution for the mass flux distribution equation.

### 7.2 Cloud Model I : Modification of the large-scale environment by cumulus clouds

The dry static energy  $s$  and the moist static energy  $h$  are used in the A-S parameterization.  $s$  is an approximately conserved variable during the dry adiabatic process. On the other hand,  $h$  is an approximately conserved variable during the moist adiabatic

---

\* This chapter is prepared by K. Yamazaki.

process. They are defined by

$$s = c_p T + gz \quad (7.1)$$

$$h = s + Lq = c_p T + gz + Lq \quad (7.2)$$

respectively, where  $c_p$  is the specific heat of air under constant pressure,  $T$  the temperature,  $g$  gravity,  $z$  height,  $L$  the latent heat per unit mass of water vapor and  $q$  the mixing ratio of water vapor.

All the cumulus clouds are assumed to have their roots in the planetary boundary layer (PBL). Other types of clouds are considered separately and described in Chapter 9.

Consider an area which is large enough to contain an ensemble of cumulus clouds but small enough to have a quasi-uniform large-scale environment. There might be various types and stages of cumulus clouds, for example, deep or shallow clouds in developing, mature or decaying stages in the area at a specific moment. Of course, it is impossible to describe each individual cloud by using the GCM. Only the overall statistical effects of the cumulus ensemble can be considered.

We assume that a cloud ensemble can be divided into a cloud subensemble of which thermal stratification in clouds and large-scale effects due to clouds are uniquely defined by a single parameter. We choose the cloud top pressure level  $P_a$  as this characteristic parameter instead of the entrainment rate  $\lambda$  as A-S did.  $\lambda$  is the fractional rate of entrainment from environment to the cloud air and assumed to be constant with height. Larger entrainment rate makes the cloud lose its buoyancy sooner, and decrease its cloud height. The highest cloud is realized when the entrainment rate  $\lambda$  is equal to zero. There is a one-to-one correspondence between  $\lambda$  and  $P_a$ .

We assume that the height of cloud top is equal to the height of the vanishing buoyancy level. An overshooting effect is neglected. The overshooting, that is, cloud air keeps going upward due to its inertia even after losing its buoyancy, occurs in the real atmosphere. Although overshooting is noticeable for deep cumulonimbus, overshooting depth is small when compared with model's vertical resolution. The detrainment of the cloud air occurs at the level  $P_a$ . So,  $P_a$  is also called as the detrainment pressure level. Note that  $P_a$  is not the height of the individual cloud at the moment. The cloud top does not reach the  $P_a$  level until the cloud reaches the mature stage, and the cloud detrains cloud air after it reaches the mature stage. We will discuss the cloud ensemble model in more detail in the next section.

The static energy and moisture budgets for the total area are

$$\rho \frac{\partial \bar{s}}{\partial t} = -\overline{\nabla \cdot (\rho \mathbf{v} s)} - \frac{\partial}{\partial z} (\overline{\rho w s}) + L (\sum_i C_i - \epsilon) \quad (7.3)$$

$$\rho \frac{\partial \bar{q}}{\partial t} = -\overline{\nabla \cdot (\rho \mathbf{v} q)} - \frac{\partial}{\partial z} (\overline{\rho w q}) - (\sum_i C_i - \epsilon) \quad (7.4)$$

where  $\rho$  is the density which depends only on  $z$ ,  $\mathbf{v}$  is the horizontal velocity,  $w$  the vertical velocity,  $\nabla$  the horizontal del operator,  $C_i$  the condensation rate of water vapor per unit height in the type- $i$  cloud subensemble,  $\epsilon$  the evaporation of the liquid water detrained from the clouds per unit height. The overbar ( $\bar{\quad}$ ) indicates the area average. Storage term in the clouds and radiation effects are neglected.

The total transport of  $s$  and  $q$  can be expressed by the sum of cloud parts and environmental parts.

$$\begin{aligned} \overline{\rho w s} &= \rho (\sum_i \sigma_i w_i s_i + (1 - \sigma_c) \tilde{w} \tilde{s}) \\ &= \sum_i M_i s_i + \tilde{M} \tilde{s} \end{aligned} \quad (7.5)$$

$$\overline{\rho w q} = \sum_i M_i q_i + \tilde{M} \tilde{q} \quad (7.6)$$

The tilde ( $\tilde{\quad}$ ) indicates the environmental mean value, subscript  $c$  indicates total cloud mean value and subscript  $i$  indicates the mean value over type- $i$  cloud subensemble.  $\sigma_i$  is the fractional area covered by the type- $i$  cloud subensemble.

$$\sigma_c = \sum_i \sigma_i \quad (7.7)$$

$$\tilde{M} = \rho (1 - \sigma_c) \tilde{w} \quad (7.8)$$

$$M_c = \rho \sum_i \sigma_i w_i \quad (7.9)$$

$$\rho \tilde{w} = M_c + \tilde{M} \quad (7.10)$$

$\sigma_c$  is the total fractional area covered by all clouds.  $M_c$  is the total vertical mass flux by all clouds,  $\tilde{M}$  is the vertical mass flux of environment.

The mass continuity equation is

$$\overline{\nabla \cdot (\rho \mathbf{v})} + \frac{\partial}{\partial z} (\overline{\rho w}) = 0 \quad (7.11)$$

Neglecting the net lateral horizontal transport across the boundary of the large-scale area by cumulus clouds, the following equations can be obtained

$$\overline{\nabla \cdot (\rho \mathbf{v})} \cong \nabla \cdot (\rho \bar{\mathbf{v}}) \quad (7.12)$$

$$\overline{\nabla \cdot (\rho \mathbf{v} s)} \cong \nabla \cdot (\rho \bar{\mathbf{v}} \bar{s}) \quad (7.13)$$

$$\overline{\nabla \cdot (\rho \mathbf{v} q)} \cong \nabla \cdot (\rho \bar{\mathbf{v}} \bar{q}) \quad (7.14)$$

Then, the continuity equation (7.11) becomes

$$\nabla \cdot (\rho \bar{\mathbf{v}}) + \frac{\partial}{\partial z} (\rho \bar{w}) = 0 \quad (7.15)$$

Using eqs. (7.13) and (7.15), eq. (7.3) can be written as

$$\begin{aligned} \rho \frac{\partial \bar{s}}{\partial t} = & \bar{s} \frac{\partial}{\partial z} (\rho \bar{w}) - \rho \bar{\mathbf{v}} \cdot \nabla \bar{s} - \frac{\partial}{\partial z} \sum_i s_i M_i \\ & - \bar{s} \frac{\partial \tilde{M}}{\partial z} - \tilde{M} \frac{\partial \bar{s}}{\partial z} + L (\sum_i C_i - \epsilon) \end{aligned} \quad (7.16)$$

Using eqs. (7.14) and (7.15), eq. (7.4) can be written as

$$\begin{aligned} \rho \frac{\partial \bar{q}}{\partial t} = & \bar{q} \frac{\partial}{\partial z} (\rho \bar{w}) - \rho \bar{\mathbf{v}} \cdot \nabla \bar{q} - \frac{\partial}{\partial z} \sum_i q_i M_i \\ & - \bar{q} \frac{\partial \tilde{M}}{\partial z} - \tilde{M} \frac{\partial \bar{q}}{\partial z} - (\sum_i C_i - \epsilon) \end{aligned} \quad (7.17)$$

Assuming no accumulative storage of mass,  $s$  and  $q$  within the cloud ensemble, we obtain

$$E - D - \frac{\partial M_c}{\partial z} = 0 \quad (7.18)$$

$$E \bar{s} - D s_d - \frac{\partial}{\partial z} (\sum_i M_i s_i) - L \sum_i C_i = 0 \quad (7.19)$$

$$E \bar{q} - D q_d - \frac{\partial}{\partial z} (\sum_i M_i q_i) - \sum_i C_i = 0 \quad (7.20)$$

where subscript  $d$  denotes the values in cloud ensemble which detrain at the level under consideration,  $D$  is the detrainment and  $E$  is the entrainment. We assume that the evaporation of the detrained liquid water takes place at the same level where the water is detrained from the clouds, that is, at the cloud top. Then,

$$\epsilon = D \ell_d \quad (7.21)$$

where  $\ell_d$  is the mixing ratio of liquid water in the air detrained from the cloud subensemble.

Using eqs. (7.10), (7.18), (7.19), (7.20) and (7.21), eqs. (7.16) and (7.17) can be rewritten as

$$\rho \frac{\partial \bar{s}}{\partial t} = D \{ (s_d - L \ell_d) - \bar{s} \} + (\bar{s} - \tilde{s}) \frac{\partial \tilde{M}}{\partial z}$$

$$-\tilde{M} \frac{\partial \tilde{s}}{\partial z} - \rho \bar{v} \cdot \nabla \tilde{s} \quad (7.22)$$

$$\begin{aligned} \rho \frac{\partial \bar{q}}{\partial t} = & D \{ (q + l)_a - \bar{q} \} + (\bar{q} - \tilde{q}) \frac{\partial \tilde{M}}{\partial z} \\ & - \tilde{M} \frac{\partial \tilde{q}}{\partial z} - \rho \bar{v} \cdot \nabla \bar{q} \end{aligned} \quad (7.23)$$

Note that the cloud condensation term does not appear in eqs. (7.22) and (7.23).

By definition and using (7.7), we obtain

$$\bar{s} = (1 - \sigma_c) \tilde{s} + \sum_i \sigma_i s_i = \tilde{s} + \sum_i (s_i - \tilde{s}) \sigma_i \quad (7.24)$$

$$\bar{q} = (1 - \sigma_c) \tilde{q} + \sum_i \sigma_i q_i = \tilde{q} + \sum_i (q_i - \tilde{q}) \sigma_i \quad (7.25)$$

We assume

$$\sigma_c \ll 1 \quad (7.26)$$

This means that the fractional horizontal area covered by the clouds is much less than unity.

We then get

$$\bar{s} \approx \tilde{s} \quad (7.27)$$

$$\bar{q} \approx \tilde{q} \quad (7.28)$$

In order that eq. (7.28) be a good approximation, the environment must not be extremely dry.

Substituting (7.27) and (7.28) into (7.22) and (7.23) respectively and using (7.10), we finally obtain

$$\begin{aligned} \rho \frac{\partial \bar{s}}{\partial t} = & D \{ (s - L l)_a - \bar{s} \} + M_c \frac{\partial \bar{s}}{\partial z} \\ & - \rho \bar{v} \cdot \nabla \bar{s} - \rho \bar{w} \frac{\partial \bar{s}}{\partial z} + Q_r \end{aligned} \quad (7.29)$$

$$\begin{aligned} \rho \frac{\partial \bar{q}}{\partial t} = & D \{ (q + l)_a - \bar{q} \} + M_c \frac{\partial \bar{q}}{\partial z} \\ & - \rho \bar{v} \cdot \nabla \bar{q} - \rho \bar{w} \frac{\partial \bar{q}}{\partial z} \end{aligned} \quad (7.30)$$

We have restored a radiation term  $Q_r$  in eq. (7.29). Except  $Q_r$ , the second lines of (7.29) and (7.30) are the large-scale advection terms which can be calculated by large-scale process of the GCM and the first lines of the r. h. s. of (7.29) and (7.30) are the cloud terms which should be

given by cumulus parameterization scheme. Adding (7.29) to (7.30), we obtain the time change equation of  $h$ ,

$$\begin{aligned} \rho \frac{\partial \bar{h}}{\partial t} = & D(h_d - \bar{h}) + M_c \frac{\partial \bar{h}}{\partial z} \\ & - \rho \bar{v} \cdot \nabla \bar{h} - \rho \bar{w} \frac{\partial \bar{h}}{\partial z} + Q_r \end{aligned} \quad (7.31)$$

According to eqs. (7.29) and (7.30), large-scale fields are modified by clouds through two effects. One is the cloud detrainment effect (D-term) which is the first term of the r. h. s. of (7.29) and (7.30), and the other is the term due to compensating downward motion of environmental air ( $M_c$ -term) which is the second term of the r. h. s. of eqs. (7.29) and (7.30). Under usual circumstances, D-term acts to cool and moisten the large-scale fields and  $M_c$ -term acts in the opposite way.

### 7.3 Cloud Model II : Cloud ensemble model

$M_c(z)$ , the cloud mass flux at level  $z$  can be divided into contributions from cloud subensemble as

$$M_c(z) = \int_0^{P_b} m(z, P_d) dP_d \quad (7.32)$$

where  $P_b$  is the pressure at the top of the PBL,  $m(z, P_d)$  is the cloud mass flux of which the top is  $P_d$  (hereafter we call this cloud subensemble as  $P_d$ -cloud), at  $z$  level. As mentioned in section 7.2, we have adopted  $P_d$  as a characteristic parameter instead of an entrainment rate  $\lambda$ . And also  $\lambda$  is assumed to be constant with height for  $P_d$ -cloud. Then

$$\frac{\partial}{\partial z} m(z, P_d) = \lambda m(z, P_d) \quad \text{for } z_b \leq z < z_d \quad (7.33)$$

where  $z_b$  is the PBL top height,  $z_d$  the detrainment level (corresponding to  $P_d$ ). Integrating eq. (7.33), we obtain the subcloud mass flux profile as

$$m(z, P_d) = \begin{cases} m_b(P_d) e^{\lambda(z-z_b)} & \text{for } z_b \leq z \leq z_d \\ 0 & \text{for } z_d < z \end{cases} \quad (7.34)$$

where  $m_b(P_d)$  is the mass flux of  $P_d$ -cloud at the PBL top. We define normalized cloud mass flux  $\eta$  for convenience.

$$\eta(z) = \begin{cases} e^{\lambda(z-z_b)} & \text{for } z_b \leq z \leq z_d \\ 0 & \text{for } z_d < z \end{cases} \quad (7.35)$$

We can write down the budget equation of  $h$  and total water content for  $P_d$ -cloud in a similar fashion

$$\frac{\partial}{\partial z} \{m(z, P_d) h_c(z, P_d)\} = \lambda \bar{h}(z) \quad (7.36)$$

$$\begin{aligned} \frac{\partial}{\partial z} \{m(z, P_d) [q_c(z, P_d) + \ell(z, P_d)]\} \\ = \lambda m(z, P_d) \bar{q}(z) - m(z, P_d) r(z, P_d) \end{aligned} \quad (7.37)$$

where  $h_c(z, P_d)$ ,  $q_c(z, P_d)$  and  $\ell(z, P_d)$  are  $h$ ,  $q$  and liquid water in the  $P_d$ -cloud respectively and  $r(z, P_d)$  is the precipitation rate which depends on parameterization of the precipitation process. In the current MRI-GCM, precipitation takes place proportional to the excess water.

Let us consider  $s$ ,  $q$  and  $h$  in the clouds. In the clouds, the air is saturated. Neglecting pressure difference between the in-the-cloud and in the environment, we can write

$$\begin{aligned} q_c(z, P_d) &= q_c^*(T_c, P_d) \\ &\cong \bar{q}^*(z) + \frac{1}{c_p} \left( \frac{\partial \bar{q}^*}{\partial T} \right)_p (s_c(z, P_d) - \bar{s}(z)) \end{aligned} \quad (7.38)$$

where asterisk (\*) denotes the saturation value. Using definition of  $h$  and eq. (7.38), we obtain

$$s_c(z, P_d) - \bar{s}(z) \cong \frac{1}{1 + \gamma} \{h_c(z, P_d) - \bar{h}^*(z)\} \quad (7.39)$$

$$q_c(z, P_d) - \bar{q}^*(z) \cong \frac{\gamma}{1 + \gamma L} \{h_c(z, P_d) - \bar{h}^*(z)\} \quad (7.40)$$

where

$$\gamma \equiv \frac{L}{c_p} \left( \frac{\partial \bar{q}^*}{\partial T} \right)_p \quad (7.41)$$

If  $m_b(P_d)$  and  $\lambda$  are given, and if  $h_c$  and  $q_c$  at PBL top, i. e.,  $h_c(z_b, P_d)$  and  $q_c(z_b, P_d)$ , are given and further if precipitation parameterization is specified, we can compute  $h_c(z, P_d)$ ,  $q_c(z, P_d)$  and  $\ell(z, P_d)$ . Since we assume cumulus clouds have their roots within the PBL, it is plausible to assume

$$h_c(z_b, P_d) = h_m \quad (7.42)$$

$$q_c(z_b, P_d) = q_m \quad (7.43)$$

where  $h_m$  and  $q_m$  are  $h$  and  $q$  averaged over the PBL depth.

There then remain two unknowns, i. e.,  $\lambda$  and  $m_b(P_d)$ . To determine  $\lambda$ , non-buoyancy assumption at the cloud top is utilized. The buoyancy is measured by the virtual static energy  $s_v$ .  $s_v$  is approximately expressed by

$$s_v = s + c_p \bar{T} (\delta q - \ell) \quad (7.44)$$

where  $\delta = 0.608$ . The non-buoyancy condition is given by  $s_v(z_d) = s_{vc}(z_d, P_d)$ , i. e.,

$$\begin{aligned} \bar{s}(z_d) + c_p \bar{T}(z_d) \delta q(z_d) = s_c(z_d, P_d) \\ + c_p \bar{T}(z_d) (\delta q_c(z_d, P_d) - \ell(z_d, P_d)) \end{aligned} \quad (7.45)$$

Using (7.39) and (7.40), eq. (7.45) can be rewritten as

$$h_c(z_d, P_d) - \hat{h}^*(z_d) = 0 \quad (7.46)$$

where

$$\hat{h}^*(z_d) \equiv \bar{h}^*(z_d) - \frac{(1+\gamma)L\varepsilon}{1+\gamma\varepsilon\delta} \{ \delta [\bar{q}^*(z_d) - \bar{q}(z_d)] - \ell(z_d, P_d) \} \quad (7.47)$$

where  $\varepsilon = c_p \bar{T}/L$ .

Eq. (7.46) is the equation which determines  $\lambda$  from given  $P_d$ . Since the equations are too intricate to be solved analytically, an iterative method is adopted in the MRI • GCM-I.

The second term in the r. h. s. of (7.47) is usually small compared with  $\bar{h}^*$ . Fig. 7.1 shows a typical thermal structure of both clouds and environment in the tropics. As you can see in Fig. 7.1, the highest possible cloud ensemble should have zero entrainment. In that case,  $h_c$  is equal to  $h_m$ . Then if an inequality  $h_m < \bar{h}^*(z)$  holds, there are no clouds that can reach the level  $z$  or above that level. In the MRI • GCM-I, the model checks this criterion and if the condition is met, such cloud ensemble is excluded from the possible existing cloud ensemble.

Suppose if we have a situation like the one shown in Fig. 7.2. In the range  $\lambda_1 < \lambda < \lambda_2$ , there are three possible cloud top heights that satisfy the non-buoyancy condition. Branch II

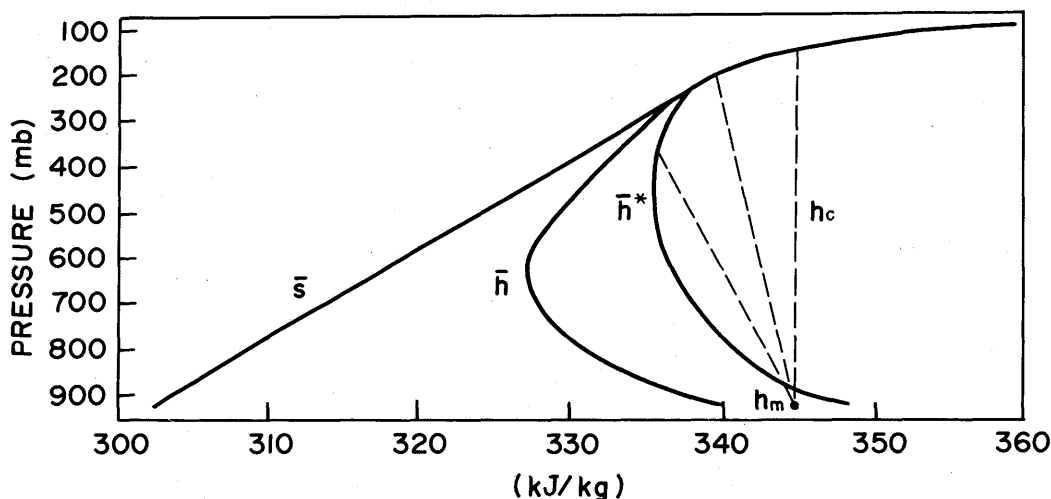


Fig. 7.1 Typical profiles of dry static energy  $s$ , moist static energy  $\bar{h}$  and saturation moist static energy  $\bar{h}^*$ . The profiles are taken from Jordan's (1958) mean West Indies sounding. Dashed lines show schematic profiles of moist static energy  $h$  in the clouds.

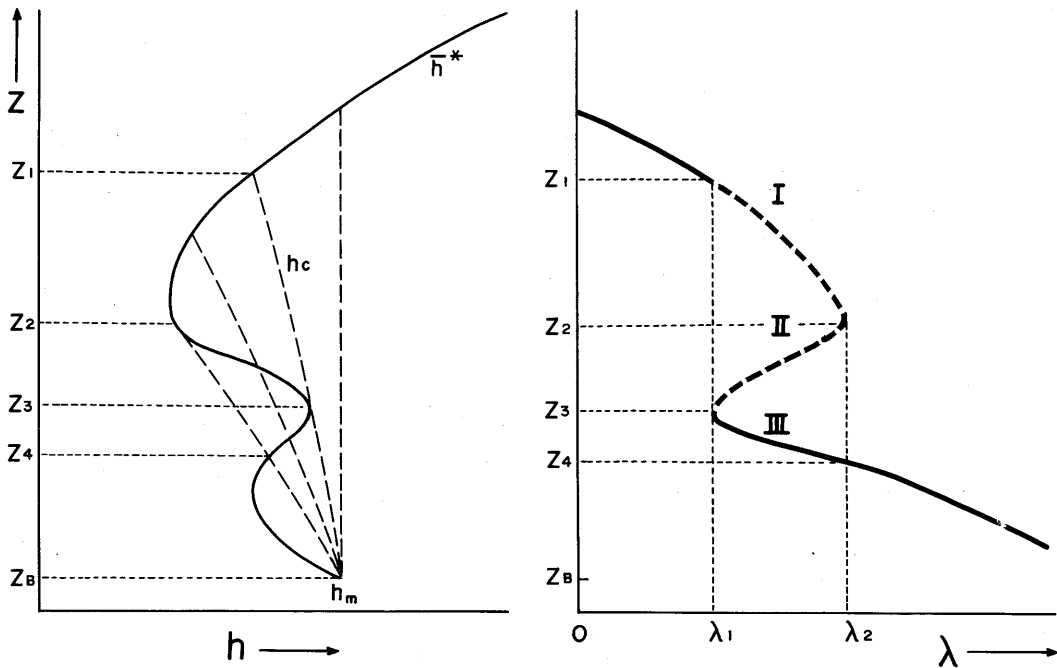


Fig. 7.2 Schematic diagrams of non-buoyancy levels for a special case. In the left panel, the solid line shows saturation moist static energy  $\bar{h}^*$  for the environmental air. The dashed lines show the moist energy  $h$  in the clouds. The right hand panel shows the variation of the entrainment rate  $\lambda$  with the cloud top height.

in Fig. 7.2 is obviously not realized, because non-buoyancy level is bounded by a positive buoyancy layer above and a negative buoyancy layer below hence the level is unstable. In the real atmosphere, branch I might be possible due to overshooting. However, since we have assumed no-overshooting at the cloud top, branch I should be discarded. Branch III is then the desired choice. The artificial cloud types are excluded currently by checking the  $\lambda$  variation with height.

#### 7.4 The closure assumption : Quasi-equilibrium assumption

As mentioned in the introduction, some kind of statistical balance must exist between the cumulus cloud ensemble and the large-scale (grid-scale) fields for a cumulus parametrization. When the large-scale processes tend to generate the moist convective instability, the cumulus cloud ensemble tends to destruct the instability mainly by compensating subsidence in the environment. In the A-S parameterization, this balance is stated by the quasi-equilibrium of "cloud work function". The cloud work function  $A$  ( $P_d$ ) is defined as a work done by the

buoyancy force per unit cloud-base mass flux, i. e.,

$$A(P_d) = \int_{z_b}^{z_d} \frac{g}{T(z)} \eta(z, P_d) [T_{vc}(z, P_d) - \bar{T}_v(z)] dz \quad (7.48)$$

where  $T_{vc}(z, P_d)$  and  $\bar{T}_v(z)$  are the subensemble and environmental virtual temperature respectively. Note that the cloud work function depends upon the thermal stratification only. Using moist static energy, eq. (7.48) can be written as

$$A(P_d) = \int_{z_b}^{z_d} \frac{g}{c_p \bar{T}(z)} \frac{[1 + \gamma(z) \epsilon(z) \delta]}{[1 + \gamma(z)]} \eta(z, P_d) [h_c(z, P_d) - \hat{h}^*(z)] dz \quad (7.49)$$

The work  $A(P_d)$  generates the kinetic energy of cloud subensemble, while the cloud-scale dissipation acts to prevent the increase of the cloud kinetic energy. Thus, the kinetic energy budget for the cloud subensemble is described as

$$\frac{d}{dt} K(P_d) dP_d = [A(P_d) - D(P_d)] m_b(P_d) dP_d \quad (7.50)$$

where  $K(P_d) dP_d$  is the cloud-scale kinetic energy for the subensemble  $P_d$  with cloud top between  $P_d$  and  $P_d + dP_d$ ,  $D(P_d)$  is the cloud-scale kinetic energy dissipation per unit cloud-base mass flux. For the first approximation,  $D(P_d)$  depends upon only cloud depth. When we consider the time scale much longer than the decay time of clouds, the l. h. s. of (7.50) can be neglected. Eq. (7.50) then becomes

$$A(P_d) \approx D(P_d) \quad \text{for } m_b(P_d) > 0 \quad (7.51)$$

In case that  $A(P_d)$  is less than  $D(P_d)$ , the cloud can not be sustained. Therefore,

$$m_b(P_d) = 0 \quad \text{for } A(P_d) < D(P_d) \quad (7.52)$$

These equations (7.51) and (7.52) express the "kinetic energy quasi-equilibrium" for each cumulus subensemble. Equation (7.51) poses very strict constraint for the stratification, because  $A(P_d)$  is the function of the stratification and cloud depth, while  $D(P_d)$  is the function of cloud depth only. When cloud subensemble exists ( $m_b(P_d) > 0$ ), the temperature and/or humidity must change with time, but  $A(P_d)$  must remain constant. This implies temperature field and moisture field can not vary independently. When clouds exist the stratification remains "neutral" in a sense.

Let it be clear by taking the derivative of eq. (7.51) with respect to time

$$\frac{d}{dt} A(P_d) \approx \frac{d}{dt} D(P_d) \approx 0 \quad (7.53)$$

The time derivative of  $A(P_d)$  can be divided into two parts, one representing the effects of cumulus feedback on the large-scale fields and the other representing the effects of the large

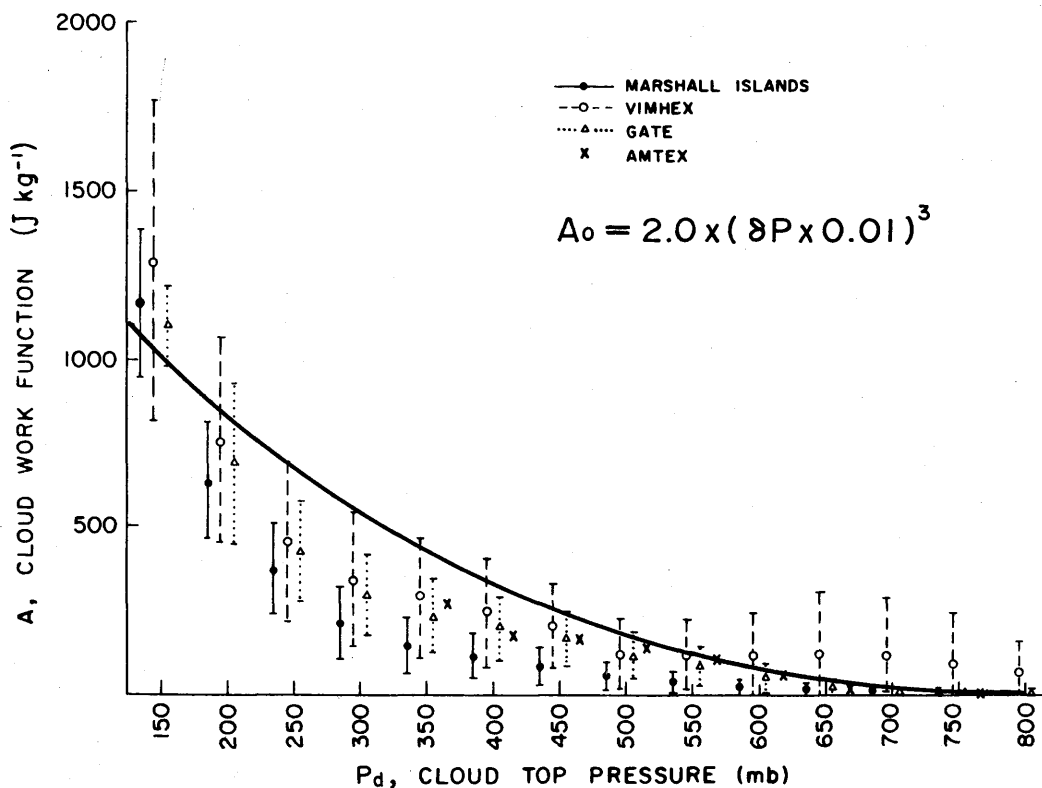


Fig. 7.3 Mean values and standard deviations of the cloud work function versus cloud top pressure  $P_d$  calculated from the Marshall Islands, VIMHEX, GATE and AMTEX datasets. Error bars represent one standard deviation from the mean. Adopted from Fig. 9 of Lord and Arakawa (1980). Thick solid line is added to show the base line cloud work function  $A_0(P_d)$  used in the MRI • GCM-I.

-scale process. Eq. (7.53) then becomes

$$\left[ \frac{d}{dt} A(P_d) \right]_{cu} + \left[ \frac{d}{dt} A(P_d) \right]_{ls} = \frac{d}{dt} A(P_d) \cong 0 \quad (7.54)$$

where the subscript CU refers to cumulus effects and LS refers to the large-scale effects.

CLOSURE ASSUMPTION

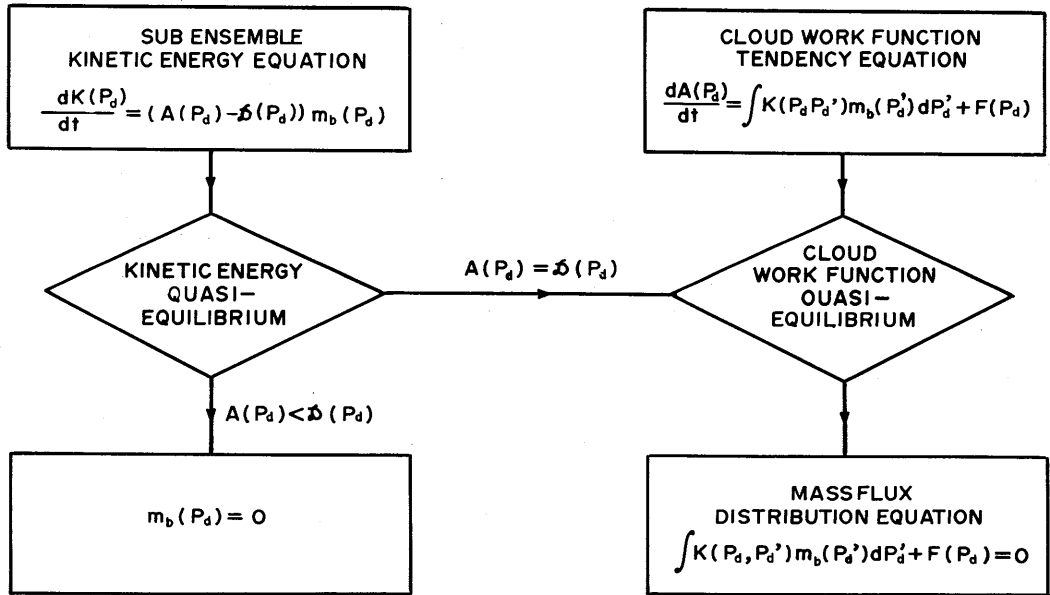


Fig. 7.4 A summary of the derivation of the mass flux distribution equation using the kinetic energy quasi-equilibrium and the cloud work function quasi-equilibrium. Adopted from Fig. 2 of Lord and Arakawa (1980) with minor changes.

The large-scale term is called the large-scale forcing and denoted as  $F(P_d)$ . Positive  $F(P_d)$  means destabilization for the cloud subensemble. The cumulus term represents the cloud-cloud interaction and can be written as

$$\left[ \frac{d}{dt} A(P_d) \right]_{cc} = \int_0^{P_b} K(P_d, p') m_b(p') dp' \quad (7.55)$$

where the kernel  $K(P_d, p')$  represents the effect of  $p'$  cloud on  $P_d$  cloud. Since cumulus clouds tend to stabilize the stratification, typically the kernel  $K(p, p')$  takes negative value. From eqs. (7.54) and (7.55), we obtain

$$\int_0^{P_b} K(P_d, p') m_b(p') dp' + F(P_d) = 0 \quad \text{for } m_b(P_d) > 0 \quad (7.56a)$$

This is a statement of "cloud-work function quasi-equilibrium" for cumulus ensemble. In case of zero  $m_b(P_d)$ , cloud work function may be reducing with time.

$$\int_0^{P_b} K(P_d, p') m_b(p') dp' + F(P_d) \leq 0 \quad \text{for } m_b(P_d) = 0 \quad (7.56b)$$

$D(P_d)$  is an intrinsic cloud subensemble variable and does not depend on the large-scale

fields. From eq. (7.51),  $D(P_a)$  can be estimated by computing the observed cloud work function. Lord and Arakawa (1980) computed the cloud work function for various geographical areas and situations (Fig. 7.3). The thick solid line in Fig. 7.3 is the characteristic cloud work function  $A_o(P_a)$  currently used in the MRI-GCM-I (see section 7.6.2 for details).

The closure assumption of the A-S cumulus parameterization is summarized in Fig. 7.4.

## 7.5 The vertical structure of the discrete model and the discretized form of the cloud model.

This section describes the discretized form of the parametrization whose continuous form is described in sections 7.2 and 7.3. In the MRI-GCM-I preadjustments of the large-scale thermodynamic structure are made before the cumulus parameterization is applied. The preadjustments include dry convective adjustment, middle level convection and large-scale precipitation, and are performed in this order. Details of the preadjustments are found in Chapter 9.

### 7.5.1 The vertical structure of the discrete model

The vertical structure of the MRI-GCM-I is shown in Fig. 7.5. The left hand side of the figure shows the vertical structure of the large-scale model. The dashed lines indicate levels with integer index  $k$  where the large-scale temperature  $T(k)$  and water vapor mixing ratio  $q(k)$  are predicted. In other chapters the levels are identified as "odd levels". The solid lines indicate half-integer levels where the large-scale vertical  $p$ -velocity is defined ("even levels"). The region bounded by levels  $k-1/2$  and  $k+1/2$  is referred to as "layer  $k$ ". The PBL top in the MRI-GCM-I is not the sigma surface. Although the top of the PBL is assumed within the lowest layer LM in this figure, it can be in upper layers, of course. Thermal structures within the PBL are determined in a way described in Chapter 8.

The right hand side of Fig. 7.5 shows the vertical indices for the cumulus parameterization. The part of layer LM above the PBL is referred to as layer KB (In other chapters, this layer is identified as E layer. See Fig. 8.4 for example.). When the PBL top lies within the lowest layer, LM is equal to KB.

The cloud top is placed at the integer levels as shown in Fig. 7.6. In the following it is convenient to identify each cloud ensemble with the vertical index of each cloud top. The left-hand ensemble in Fig. 7.6 is the type- $i$  cloud, for example. Height-dependent variables of a cloud subensemble are represented by double arguments. The subensemble vertical mass flux for type- $i$  cloud, defined at the half-integer level, is denoted by  $m(i, k-1/2)$  and can be

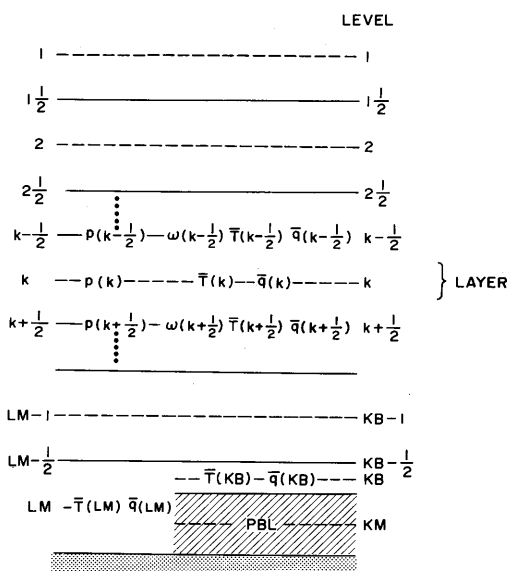


Fig. 7.5 The vertical structure and indices of the model. Indices on the r. h. s. are used in the cumulus parameterization model. Ones on the l. h. s. are for the large-scale model. KM is the index of the PBL and KB denotes the part of the layer immediately above the PBL.

expressed as

$$m(i, k-1/2) = \eta(i, k-1/2) m_b(i) \quad (7.57)$$

where  $m_b(i)$  is the cloud-base mass flux for type- $i$  cloud and  $\eta(i, k-1/2)$  is the normalized subensemble vertical mass flux at level  $k-1/2$ . In general, the first argument corresponds to the cloud type and the second one corresponds to the layer concerned. The entrainment of environment of environment air, denoted by  $E(i, k)$ , occurs at all integer levels penetrated by the cloud including the cloud top layer. The detrainment of cloud air, denoted by  $D(i)$ , occurs only at the cloud top level (see Fig. 7.6).

### 7.5.2 The mass budget

A discretized form of the subensemble mass budget equation (7.33) of section 7.3 for layer  $k$ ,  $k \neq i$ , can be written as

$$\frac{\eta(i, k-1/2) - \eta(i, k+1/2)}{\Delta z(k)} = \lambda(i) \eta(i, k+1/2) \quad (7.58)$$

from which

$$\eta(i, k-1/2) = \eta(i, k+1/2) [1 + \lambda(i) \Delta z(k)] \quad (7.59)$$

is obtained. Here  $\Delta z(k) = z(k-1/2) - z(k+1/2)$ . The mass budget for the cloud top layer

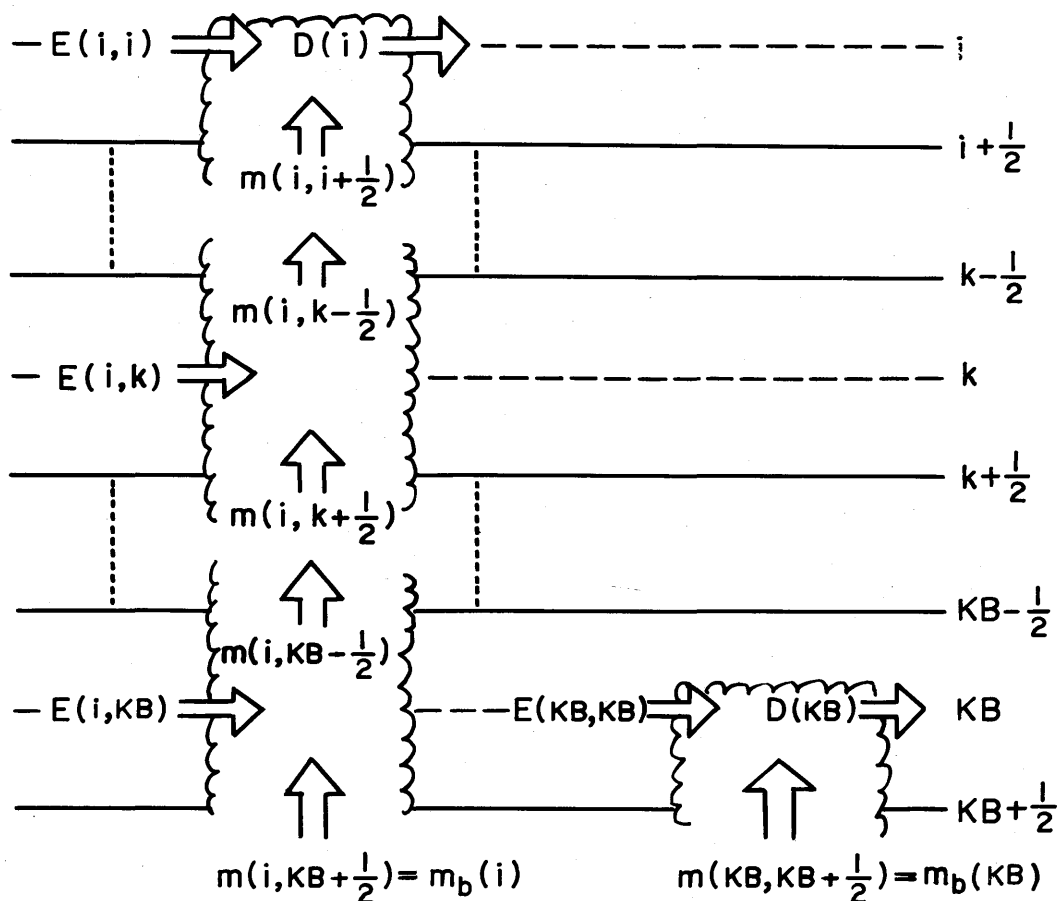


Fig. 7.6 Vertical structures of type-i cloud (on the left) and type-KB cloud (on the right). Entrainment  $E$  takes place at all integer levels penetrated by the cloud including the cloud top level, while detrainment  $D$  takes place at the cloud top level only. The subensemble cloud mass flux is calculated at the half-integer levels.

$k=i$  is given by

$$d(i) = \eta(i, i+1/2) [1 + \lambda(i) \Delta z(i)] \quad (7.60)$$

where  $d(i)$  is the cloud top mass detrainment integrated over layer  $i$  and normalized by the cloud-base mass flux  $m_b(i)$ , and  $\Delta z(i) = z(i) - z(i, 1/2)$ .

### 7.5.3 The moist static energy budget

For layer  $k$  and type- $i$  cloud, let  $h(i, k+1/2)$  be the subensemble moist static energy before entrainment and let  $h(i, k-1/2)$  be the subensemble moist static energy after

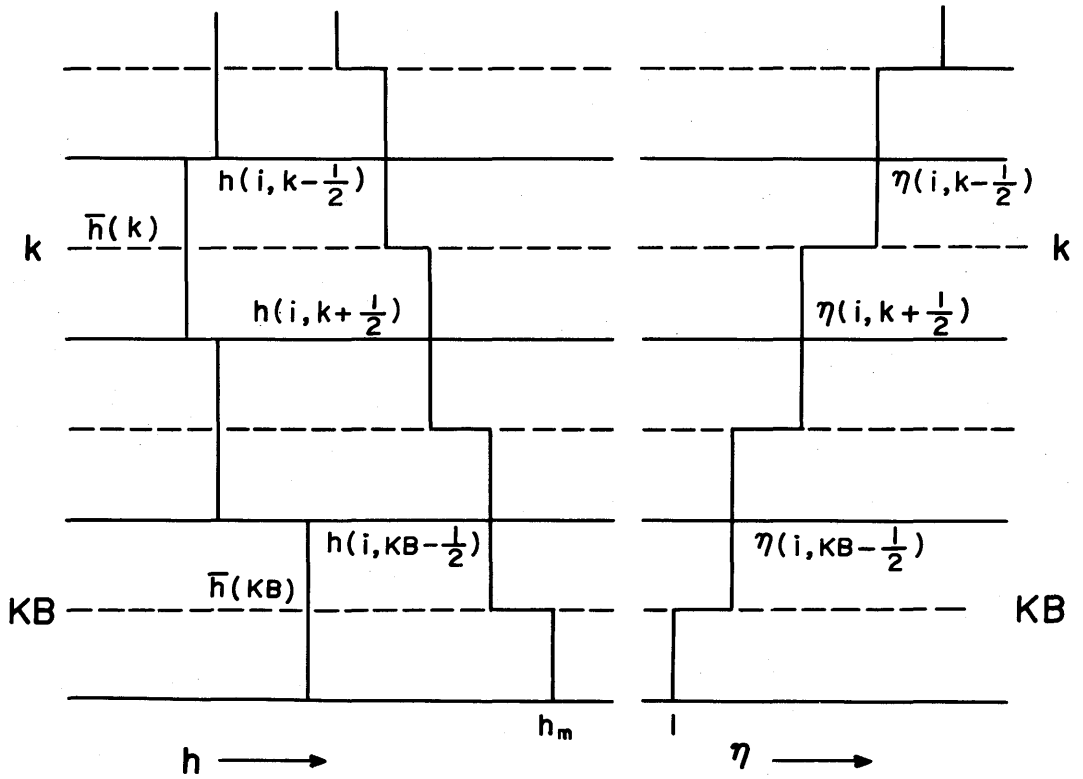


Fig. 7.7 Typical vertical profiles of normalized cloud mass flux  $\eta$  and moist static energy  $h$  for the type- $i$  cloud. The l. h. s. profile shows  $h$  for the environment.

entrainment (Fig. 7.7). Then the discretized subensemble moist static energy budget integrated over layer  $k$  can be written as

$$\eta(i, k-1/2) h(i, k-1/2) = \eta(i, k+1/2) h(i, k+1/2) + \lambda(i) \Delta z(k) \eta(i, k+1/2) \bar{h}(k) \quad (7.61)$$

From eq. (7.61), we obtain

$$h(i, k-1/2) = \frac{h(i, k+1/2) + \lambda(i) \Delta z(k) \bar{h}(k)}{1 + \lambda(i) \Delta z(k)} \quad (7.62)$$

When  $k = KB$  in eqs. (7.62),  $h(i, KB+1/2) = h_m$ , the mean  $h$  in the PBL (see (8.36)). In the cloud-top detrainment layer (7.62) becomes

$$\hat{h}(i) = \frac{h(i, i+1/2) + \lambda(i) \Delta z(i) \bar{h}(i+1/4)}{1 + \lambda(i) \Delta z(i)} \quad (7.63)$$

where  $\hat{h}(i)$  is the moist static energy at the cloud-top and  $\bar{h}(i+1/4) = 0.5 \cdot (\bar{h}(i) + \bar{h}(i+1/2))$ . Sequential substitutions of (7.62) into (7.63) with  $i+1 \leq k \leq KB$  result in a complicated

expression for  $\hat{h}(i)$  which depends on the known  $h_m$ ,  $h(k)$  for  $i \leq k \leq KB$  and the unknown  $\lambda(i)$ . By requiring non-buoyancy at the cloud-top, i. e.,  $\hat{h}(i) = \hat{h}^*(i)$  (see eq. (7.46) and (7.47)),  $\lambda(i)$  may be determined iteratively as shown in the section 7.5.5.

#### 7.5.4 The total water budget

The budget for total cloud water is calculated in two steps as described below. Let  $q^t(i, k+1/2)$  be the value of the total cloud water (vapor and suspended liquid water) mixing ratio entering layer  $k$  from below for type- $i$  cloud. And let  $q(i, k)$  be the value after entrainment but before the precipitation process. And let  $q^t(i, k-1/2)$  be the value after the precipitation process, which also is the value leaving layer  $k$ . Also, let  $q_l(i, k)$  be the cloud suspended liquid water mixing ratio before precipitation, and  $q_l^t(i, k-1/2)$  the value after the precipitation process.

The first step in the total cloud water budget is calculated in the similar manner as eq. (7.62)

$$q(i, k) = \frac{q^t(i, k+1/2) + \lambda(i) \Delta z(k) \bar{q}(k)}{1 + \lambda(i) \Delta z(k)} \quad (7.64)$$

where  $\bar{q}(k)$  is the large-scale total water mixing ratio. Since the large-scale precipitation process is implemented before the cumulus parameterization is applied,  $\bar{q}(k)$  is identical to water vapor mixing ratio  $\bar{q}_v(k)$ . When  $k=KM$  in eq. (7.64),  $q(i, KB+1/2) = q_m$ .

The second step in the total water budget calculation determines the amount of precipitation produced in layer  $k$  from type- $i$  cloud. When the cloud is saturated at level  $k$  the cloud water vapor mixing ratio  $q_v(i, k)$  is calculated from a discretized form of eq. (7.40) of section 7.3,

$$q_v(i, k) = \bar{q}_v^*(k) + \frac{\gamma(k)}{(1 + \gamma(k)) L} [h(i, k-1/2) - \bar{h}^*(k)] \quad (7.65)$$

where  $\gamma(k) = L/c_p [\partial \bar{q}_v^*(k) / \partial T]_p$ .

The resulting suspended liquid water mixing ratio before precipitation is

$$q_l(i, k) = q(i, k) - q_v(i, k) \quad (7.66)$$

Part of  $q_l(i, k)$  is converted into precipitation by assuming a constant conversion rate per unit height. Therefore

$$q_l^t(i, k-1/2) = q_l(i, k) - C_0 \Delta z(k) q_l^t(i, k-1/2) \quad (7.67)$$

from which

$$q_{\ell}^{\dagger}(i, k-1/2) = \frac{q_{\ell}(i, k)}{1 + C_0 \Delta Z(k)} \quad (7.68)$$

A conversion coefficient  $C_0$  in eqs. (7.67) and (7.68) is set to  $0.004 \text{ m}^{-1}$  for the cloud-top layer and  $0.002 \text{ m}^{-1}$  for the rest of layers. Lord (1978) has shown that this values of  $C_0$  produce good agreement with observed liquid water content in hurricanes summarized by Ackerman (1963). Similar calculation by Schubert (1973) for Marshall Islands data also have shown good agreement with observations.

### 7.5.5 The solution procedure for $\lambda(i)$

Let a functional  $F[\lambda(i)]$  be defined by

$$F[\lambda(i)] = (\hat{h}(i) - \hat{h}^*(i)) \eta(i, i) \quad (7.69)$$

where  $F$  depends on  $\lambda(i)$  through  $\hat{h}(i)$ ,  $\eta(i, i)$  and  $\hat{h}^*(i)$  (see eq. (7.47)). If the virtual temperature effects are neglected,  $\hat{h}^*(i)$  does not depend on  $\lambda(i)$ . Since virtual temperature effects are small, dependence of  $\hat{h}^*(i)$  on  $\lambda(i)$  is weak. The non-bouyancy condition at cloud top is

$$F[\lambda(i)] = 0 \quad (7.70)$$

which is an implicit equation for  $\lambda(i)$  and may be solved iteratively by the Newton-Raphson method. Let  $\nu$  be the number of iterations and let  $\lambda_{\nu}(i)$  be  $\lambda(i)$  at the  $\nu$ -th iteration. For the first guess,  $\lambda_1(i) = 0$  is used. For succeeding iterations,  $\lambda_{\nu+1}(i)$  can be obtained as

$$\lambda_{\nu+1}(i) = \lambda_{\nu}(i) - \frac{F[\lambda_{\nu}(i)]}{F'[\lambda_{\nu}(i)]} \quad (7.71)$$

where  $F'[\lambda_{\nu}(i)]$  is the value of the first derivative of  $F[\lambda(i)]$  with respect to  $\lambda(i)$  at  $\lambda(i) = \lambda_{\nu}(i)$ . When  $F'[\lambda_{\nu}(i)]$  is computed,  $\hat{h}^*(i)$  is assumed to be constant with respect to  $\lambda$ . The iteration is repeated until  $|\hat{h}(i) - \hat{h}^*(i)| \leq 1.0 \text{ J kg}^{-1}$  which is equivalent to a cloud-top/environment temperature difference of about  $10^{-3} \text{ K}$ .

In case that the iteration does not converge after 15 iterations for type- $i$  cloud, such cloud is discarded. Also if cloud air is not saturated at the cloud top, such cloud type is discarded. After we get all possible cloud types, the order of computed values of  $\lambda$  is checked according to the consideration mentioned in section 7.3.

## 7.6 The discrete form of the mass flux distribution equation

### 7.6.1 The discretized equation

The mass flux distribution equation for the continuous case is given by (7.46) in section 7.4. This equation is discretized and integrated over a time step  $\Delta t_d$  (see Fig. 5.1) and is

written as

$$m_b(i)\Delta t_d > 0 \quad \text{and} \\ \sum_{j=1}^{i_{\max}} [K(i, j) m_b(j)\Delta t_d] + F(i)\Delta t_d = 0 \quad (7.72a)$$

or

$$m_b(i)\Delta t_d = 0 \quad \text{and} \\ \sum_{j=1}^{i_{\max}} [K(i, j) m_b(j)\Delta t_d] + F(i)\Delta t_d \leq 0 \quad (7.72b)$$

for  $1 \leq i \leq i_{\max}$ . Here  $i_{\max}$  is the number of possible existing subensembles ;  $K(i, j)$ , for  $1 \leq i, j \leq i_{\max}$ , is a discrete form of the mass flux kernel which gives the stabilization of the type- $i$  cloud subensemble through modification of the large-scale environment by the type- $j$  cloud subensemble ; and  $F(i)$  is the large-scale forcing for the type- $i$  cloud subensemble. Note that there is an equal sign in the second equation of (7.72b). This equal sign is placed in order to assure the existence of solution (there is no equal sign in Arakawa and Schubert's eq. (74) *etc.*). Let us consider the simplest case in which  $i_{\max} = 1$ . Then equation becomes

$$\begin{cases} m_b\Delta t_d > 0 & \text{and} \\ K m_b\Delta t_d + F\Delta t_d = 0 \end{cases} \quad (7.72a')$$

or

$$\begin{cases} m_b\Delta t_d = 0 & \text{and} \\ K m_b\Delta t_d + F\Delta t_d \leq 0 \end{cases} \quad (7.72b')$$

where we omitted suffices for simplicity. If an equal sign in the second equation of (7.72b)' is dropped, (7.72b)' becomes

$$\begin{cases} m_b\Delta t_d = 0 & \text{and} \\ K m_b\Delta t_d + F\Delta t_d < 0 \end{cases} \quad (7.72c')$$

If  $F$  is exactly zero and  $K \neq 0$ ,  $m_b = 0$  is the solution of the equations of (7.72a)' and (7.72b)'. However there are no solutions for equations (7.72a)' and (7.72c)'. This modification is also justified from the physical consideration. Under completely neutral and steady condition, the cloud work function also must be steady and  $m_b$  should be zero.

## 7.6.2 The large-scale forcing

The large-scale forcing for the type- $i$  cloud subensemble is defined in section 7.4 as the change in cloud work function due to large-scale processes. Let the large-scale thermodynamical variables (temperature, water vapor mixing ratio, *etc.*) be denoted

collectively by  $\bar{\psi}_0$  where the subscript denotes a particular time  $t_0$ . The effects of the large-scale processes (*e.g.*, large-scale vertical and horizontal advections of temperature and moisture, radiative heating and boundary layer processes) are added over  $\Delta t_d$  to give the change

$$\bar{\psi}' = \bar{\psi}_0 + \left[ \frac{\partial \bar{\psi}}{\partial t} \right]_{LS} \Delta t_d \quad (7.73)$$

where  $\left[ \frac{\partial \bar{\psi}}{\partial t} \right]_{LS}$  represents the time change of  $\bar{\psi}$  due to the large-scale processes. Let the cloud work function for the type-*i* cloud subensemble calculated from  $\bar{\psi}'$  be denoted by  $A'(i)$ . The large-scale forcing is then written as

$$F(i) = \frac{A'(i) - A_0(i)}{\Delta t_d} \quad (7.74)$$

Although  $A_0(i)$  is the cloud work function at  $t_0$  by definition,  $A_0(i)$  can be replaced by a characteristic value for the type-*i* cloud subensemble. The replacement of  $A_0(i)$  by a characteristic value is justified by the kinetic energy quasi-equilibrium (*e.g.*, see (7.51) and the following discussion). Lord and Arakawa (1880) showed that when both large-scale and cloud processes are operating, cloud work function values fall into a well-defined narrow range for each subensemble, and the variation in the cloud work function becomes negligible over the time scale of the large-scale motions. It follows that the values based on observed time-mean cloud work function may be used as  $A_0(i)$  in the GCM. Modification of  $\bar{\psi}'$  by the cumulus mass flux obtained from (7.74) should restore  $A'(i)$  to the characteristic value  $A_0(i)$ . Currently,

$$A_0(i) = 2 \times 10^{-6} \{P_b - p(i)\}^3 \quad (7.75)$$

is used for simplicity, where  $P_b$  and  $p(i)$  are values in mb (see Fig. 7.3).

### 7.6.3 The mass flux kernel

The kernel element  $K(i, j)$  is defined as the time rate of change of the cloud work function for the type-*i* cloud subensemble due to modification of the large-scale environment by a unit mass flux of the type-*j* cloud subensemble. The changes in the large-scale environment by the cumulus terms are given by the first lines of the r. h. s. of (7.29) and (7.30). These terms are written in the discrete form as eqs. (7.82) and (7.83) in section 7.8. After the above definition of  $K(i, j)$ , it is evaluated in the following way. The large-scale environment, represented by  $\bar{\psi}'$  from eq. (7.73) is modified by an arbitrarily chosen amount of mass per unit area from the type-*j* cloud subensemble  $m_b''(j)\Delta t''$  to give

$$\bar{\psi}''(k) = \bar{\psi}'(k) + \delta_j [\bar{\psi}(k)] m_b''(j) \Delta t'' \quad (7.76)$$

Here the index  $k$  has been added to indicate the level in the large-scale model,  $\delta_j [\bar{\psi}(k)]$  refers to the time rate of change in  $\bar{\psi}(k)$  per unit mass flux of the type- $j$  cloud subensemble, and the double prime denotes a value used in the mass flux kernel element calculation. A new fractional entrainment rate  $\lambda''(i)$  and the cloud work function  $A''(i)$  are then calculated for the type- $i$  cloud subensemble using  $\lambda''$ . Finally, the kernel element is calculated as

$$K(i, j) = \frac{A''(i) - A'(i)}{m_b''(j) \Delta t''} \quad (7.77)$$

The test mass flux  $m_b''(j) \Delta t''$  is arbitrarily chosen to be  $100 \text{ kg m}^{-2}$ . The choice of a particular value for  $m_b''(j) \Delta t''$  is not important because non-linearity of  $A''(i) - A'(i)$  on the test mass flux is weak.

Since a given cloud type tends to stabilize the large-scale fields for all cloud types, the kernel elements  $K(i, j)$  should be typically negative. In particular, a given subensemble must reduce its own cloud work function, *i. e.*, for all  $i$ ,

$$K(i, i) < 0 \quad (7.78)$$

Otherwise, such cloud subensemble is unstable and develops by itself. However, under very unusual circumstances, the calculated value of  $K(i, i)$  may not satisfy (7.78) primarily due to too coarse a vertical resolution. Therefore,  $K(i, i) = -\xi$ , where  $\xi$  is arbitrarily chosen to be

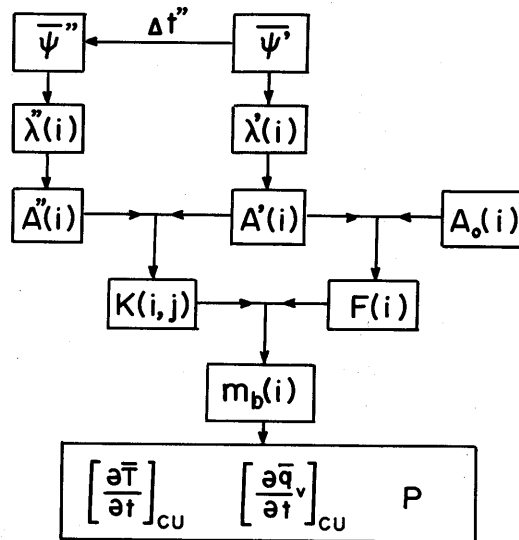


Fig. 7.8 A schematic diagram of the procedure applying the discretized cumulus model to a large-scale prognostic model. Adopted from Fig. 5 of Lord *et al.* (1982).

$5 \times 10^{-3} \text{ J m}^{-2} \text{ kg}$ , is enforced. Note that when  $i=i_{\max}=1$ , eq. (7.78) is a necessary and sufficient condition for the existence of a unique solution of  $m_b \Delta t_d$  for (7.72a)' and (7.72b)'. Incidentally, the mass flux distribution equations (7.72a) and (7.72b) do not necessarily have their unique solution. This mathematical aspect of equations is discussed in Appendix 7.2.

The procedure for obtaining the cloud base mass flux distribution in the GCM is summarized in Fig. 7.8. The thermodynamical variables after modification by the large-scale processes ( $\bar{\psi}'$ ) are the inputs to this cumulus parameterization scheme. From these variables  $\lambda'(i)$  and  $A'(i)$  are calculated for each subensemble. Using an empirically defined characteristic cloud work function  $A_0(i)$ , the large-scale forcing is calculated from eq. (7.74). The large-scale environment is then modified by the test mass flux  $m_b''(j) \Delta t''$  to produce thermodynamical variables  $\bar{\psi}''$  which are then utilized to calculate a new value of the cloud work function  $A''(i)$ . The kernel elements are calculated from (7.77) and the  $m_b(i)$  are determined from the mass flux distribution equations (7.72a) and (7.72b). The method to solve the equations (7.72a) and (7.72b) is described in the next section.

#### 7.6.4 The cloud work function

To compute the large-scale forcing and the kernel elements, the cloud work function must be computed. The discrete form of the cloud work function is written straightforwardly from eq. (7.49) as

$$A(i) = \sum_{k'=i+1}^{KB+1} \frac{g}{c_p T(k'-1/2)} \eta(i, k'-1/2) \times \left[ \frac{h(i, k'-1/2) - \hat{h}^*(i, k'-1/2)}{1 + \gamma(k'-1/2)} \right] [z(k'-1) - z(k')] \quad (7.79)$$

where  $z(KB+1) = z_b$ .

#### 7.7 Solution of the mass flux distribution equation

The mass flux distribution equation (7.72) must be solved subject to the constraints of non-negative  $m_b(i)$  and the inequality conditions (7.72b). For convenience, eq.(7.72) is rewritten here, replacing  $m_b(i) \Delta t_d$  with  $x(i)$  and  $F(i) \Delta t_d$  with  $c(i)$ .

$$\left\{ \begin{array}{l} x(i) > 0 \quad \text{and} \\ \sum_{j=1}^{i_{\max}} K(i, j) x(j) + c(i) = 0 \end{array} \right. \quad (7.80a)$$

or

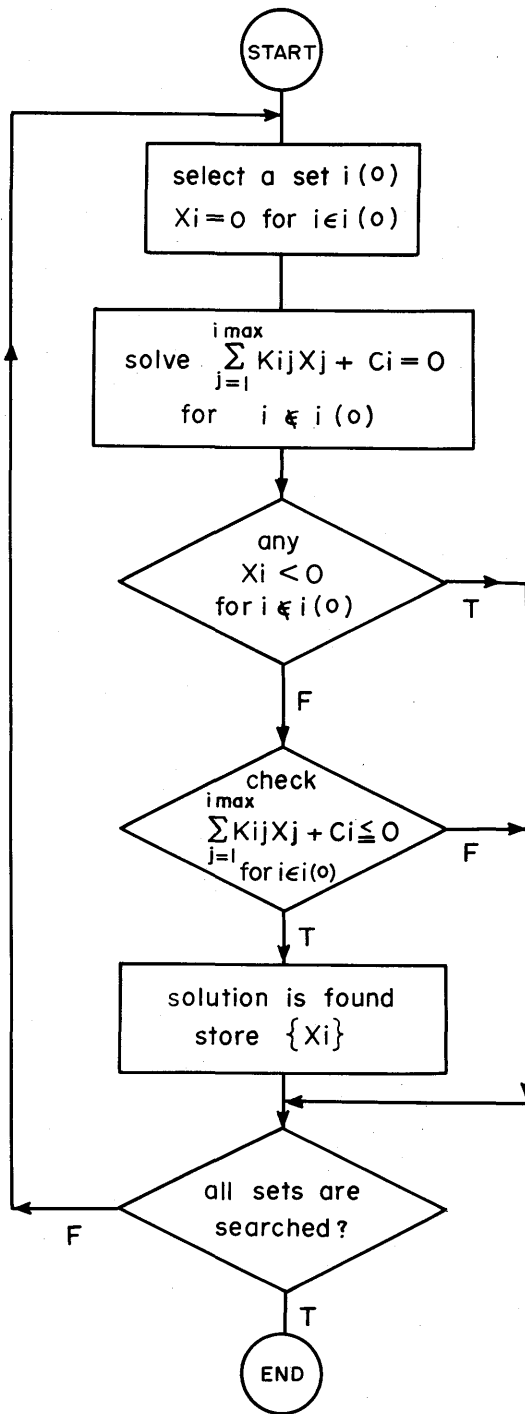


Fig. 7.9 Flow diagram for the exact direct method used in the MRI • GCM-I for solving the mass flux distribution equation.

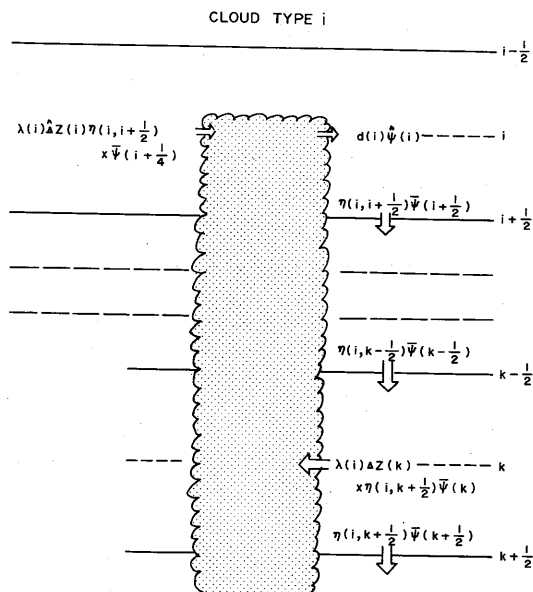


Fig. 7.10 A schematic diagram of the large-scale budget of  $\psi$  for type- $i$  cloud.

$$\left\{ \begin{array}{l} x(i)=0 \quad \text{and} \\ \sum_{j=1}^{i \max} K(i,j) x(j) + c(i) \leq 0 \end{array} \right. \quad (7.80b)$$

Schubert (1973) proposed an initial-value iterative method of solving the equation and Lord *et al.* (1982) discussed both a direct solution method and a linear programming method. It is mentioned that neither of these methods guarantee exact solutions. In the following we introduce, as an alternative, an "exact direct method" adopted in the MRI-GCM-I.

$x(i)$  can be either positive or zero. Since there are two possibilities for each  $x(i)$ , there are  $2^{i \max}$  possibilities in all. Suppose if  $i(0)$  be the set whose elements are non-existing cloud types. In other words,  $i(0)$  is the set which satisfies the condition below

$$x(i)=0 \quad \text{for} \quad i \in i(0) \quad (7.81)$$

The first step is to solve the equation (7.80a) for  $i \notin i(0)$  by Gaussian elimination. The second step is to examine the solution,  $x(i)$  for  $i \notin i(0)$ . If  $x(i) < 0$  for any  $i$ , this set  $i(0)$  is not the right one, thus select another set and repeat the procedure from the beginning. Otherwise, we proceed the third step. The third step is to examine inequality conditions (7.80b) for  $i \in i(0)$ . If equations (7.80b) are satisfied, the solution is the right one and stored. This procedures are repeated  $2^{i \max}$  times. The exact direct method is illustrated in Fig. 7.9.

Although one set of solutions is uniquely obtained under usual circumstances, there are unusual cases where two sets or more are obtained. In the A-S cumulus parameterization

theory, no selection rule among sets of solutions is derived. Therefore, as the true set, we tentatively select the one which has the maximum number of existing cloud type. In case we have many sets of solutions of which numbers of existing cloud types are the same, we arbitrarily choose the first found set.

In the current MRI-GCM, the number of tropospheric layers is 5. Then  $i_{\max}$  is 5 at most and the number of possibilities that the exact direct method must examine is  $2^5=32$  at most. Therefore, the exact direct method is not so time-consuming even if compared with other methods. And, of course, the exact direct method guarantees the exact solution except roundoff errors. In the 12-layer version, the search for possible penetrated cumuli with their top above  $p=p_1=100$  mb is suppressed from the beginning currently.

### 7.8 The large-scale budget and cumulus cloud feedback on the large-scale fields.

Lower part of Fig. 7.10 shows the large-scale budget of  $\psi$  (h or q) for layer k and type -i cloud. The downward fluxes of  $\bar{\psi}$  per unit cloud base mass flux at the top and the bottom of the layer are given by  $\eta(i, k-1/2) \bar{\psi}(k-1/2)$  and  $\eta(i, k+1/2) \bar{\psi}(k+1/2)$ , respectively. The entrainment of  $\bar{\psi}$  is  $\lambda(i) \Delta z(k) \eta(i, k+1/2) \bar{\psi}(k)$ . Let  $\delta_i[\bar{\psi}(k)]$  represent a change in  $\bar{\psi}(k)$  per unit  $m_b(i)$  and let the mass per unit area at layer k be  $\Delta p(k)/g$ , where  $\Delta p(k) = p(k+1/2) - p(k-1/2)$ . Then the change in the large-scale budget of  $\bar{\psi}$  is written as

$$\begin{aligned} \frac{\Delta p(k)}{g} \delta_i[\bar{\psi}(k)] &= \eta(i, k-1/2) \bar{\psi}(k-1/2) - \eta(i, k+1/2) \bar{\psi}(k+1/2) - \lambda(i) \Delta z(k) \eta(i, k+1/2) \bar{\psi}(k) \\ &= \eta(i, k-1/2) [\bar{\psi}(k-1/2) - \bar{\psi}(k)] + \eta(i, k+1/2) [\bar{\psi}(k) - \bar{\psi}(k+1/2)] \quad (7.82) \end{aligned}$$

Upper part of Fig. 7.10 shows the large-scale budget of  $\psi$  in the cloud top layer for the i-th cloud type. At the cloud top the detrainment of  $\psi$  per unit  $m_b(i)$  is  $d(i) \hat{\psi}(i)$ . The downward flux of  $\bar{\psi}$  at the layer is  $\eta(i, i+1/2) \bar{\psi}(i+1/2)$  and the entrainment of  $\bar{\psi}$  is assumed to be  $\lambda(i) \Delta z(i) \eta(i, i+1/2) \bar{\psi}(i+1/4)$ . Therefore, the counterpart to (7.82) for the cloud top layer is

$$\begin{aligned} \frac{\Delta p(i)}{g} \delta_i[\bar{\psi}(i)] &= d(i) \hat{\psi}(i) - \eta(i, i+1/2) \bar{\psi}(i+1/2) \\ &\quad - \lambda(i) \Delta z(i) \eta(i, i+1/2) \bar{\psi}(i+1/4) \\ &= \eta(i, i+1/2) \{ [1 + \lambda(i) \Delta z(i)] \times \\ &\quad [\hat{\psi}(i) - \bar{\psi}(i+1/4)] + \bar{\psi}(i+1/4) - \bar{\psi}(i+1/2) \} \quad (7.83) \end{aligned}$$

In this model all detrained liquid water is assumed to evaporate instantaneously at the detrainment level. Consequently, the changes in  $\bar{T}(k)$  and  $\bar{q}_v(k)$  are calculated from  $\delta_i [\bar{h}(k)]$  and  $\delta_i [\bar{q}(k)]$  as

$$\delta_i [\bar{q}_v(k)] = \delta_i [\bar{q}(k)] \quad (7.84a)$$

and

$$\delta_i [\bar{T}(k)] = \frac{1}{C_p} \{ \delta_i [\bar{h}(k)] - L \delta_i [\bar{q}(k)] \} \quad (7.84b)$$

The large-scale budget described above and the cumulus induced subsidence at the PBL top are used to compute the kernel elements. After solving mass distribution equation, results of the large-scale budget calculation are used for obtaining the cumulus feedback on the large-scale fields, too.

The total temperature and moisture changes at each level over the time  $\Delta t_d$  due to cumulus convection are given by

$$\left[ \frac{\partial T(k)}{\partial t} \right]_{cc} \Delta t_d = \sum_{j=1}^{i \max} \delta_j [\bar{T}(k)] m_b(j) \Delta t_d \quad (7.85a)$$

and

$$\left[ \frac{\partial q_v(k)}{\partial t} \right]_{cc} \Delta t_d = \sum_{j=1}^{i \max} \delta_j [\bar{q}_v(k)] m_b(j) \Delta t_d \quad (7.85b)$$

where the form of  $\delta_j$  is given by (7.82) and (7.83). The cumulus mass flux at the PBL top,  $M_B$  is given by

$$M_B \Delta t_d = \sum_{j=1}^{i \max} m_b(j) \Delta t_d \quad (7.86)$$

The amount of precipitation  $P \Delta t_d$  is given by

$$P \Delta t_d = \sum_{i=1}^{i \max} \left\{ \sum_{k=i+1}^{KB} C_0 \Delta z(k) q_\ell^t(i, k-1/2) m(i, k-1/2) + \hat{C}_0 \Delta \hat{z}(i) q_\ell^t(i, i-1/2) m(i, i-1/2) \right\} \Delta t_d \quad (7.87)$$

where  $C_0 = 2 \times 10^{-3} \text{ m}^{-1}$  and  $\hat{C}_0 = 4 \times 10^{-3} \text{ m}^{-1}$  (see section 7.5.4 for details).

Momentum changes due to cumulus convection are also computed in a similar way by assuming that momentum is conserved within cloud ensemble. Details are described in Chapter 11.

The cloudiness of cumulus clouds in the model is neglected, unless cloud top is above 400 mb level or 233°K level. If the cloud top is above such level, we regard that anvil clouds spread out as cirrus from the cloud top. The cloudiness of such cloud is set to unity at the cloud-top

layer though its blackness is regarded as 0.5 in the radiation calculation. For details, see Chapter 13.

## 7.9 Ice phase parameterization

So far, we have not mentioned ice phase parameterization to avoid complexity. In the current MRI-GCM-I, the effects of ice phase are incorporated in a simple manner described below.

When the environmental temperature  $T(z)$  is less than the critical temperature  $T_{cr}$  (currently  $-20^\circ\text{C}$  is assumed), we introduce  $y$  defined below instead of  $h$ .

$$y = h + L_1 q_v = c_p T + gz + L_r q_v \quad (7.88)$$

where  $L_r = L + L_1$  and  $L$  is the latent heat of vaporization per unit mass of water vapor,  $L_1$  is the latent heat of fusion, and  $L_r$  is the latent heat of sublimation.

In the ice phase layer where  $T(z) \leq -20^\circ\text{C}$ ,  $y$  is approximately conserved, while in the liquid phase layer where  $T(z) > -20^\circ\text{C}$ ,  $h$  is approximately conserved. We assume that phase change occurs abruptly at the level of  $T_{cr}$ . Because of the difference between saturation water vapor pressure on ice and water, excess water vapor sublimates in the layer above. At the same time, cloud liquid water freezes and releases the latent heat. The temperature change due to those process at  $T_{cr}$  is

$$\Delta T = (L_r \Delta q + L_1 \ell) / c_p \quad (7.89)$$

where  $\ell$  is liquid water content,  $\Delta q$  is difference between the saturated mixing ratio on ice and on water. In the discrete model, temperature at the integer level  $\bar{T}(k)$  is compared with  $T_{cr}$ . If  $\bar{T}(k)$  is less than  $T_{cr}$ , the layer  $k$  is assumed to be the ice phase layer and the phase change is assumed to happen at the bottom of the layer  $k$  (*i. e.*,  $k+1/2$  level).

These additional heating in the cloud due to phase change generates buoyancy and makes cloud work function larger. This means that cloud top is raised when the ice phase is included in the cumulus parameterization. We assume that precipitation from ice phase layer is in ice phase (*i. e.*, snowfall), and snowfall melts at  $0^\circ\text{C}$  level to cool the environment.

Although inclusion of ice phase makes the cumulus parameterization program complicated, its effect seems to be minor and not so significant.

### A7.1 Some results from simulation studies

In this Appendix, we describe the selected results related to cumulus parameterization. Materials are taken from the forthcoming paper by Tokioka, Kitoh, Yagai and Yamazaki

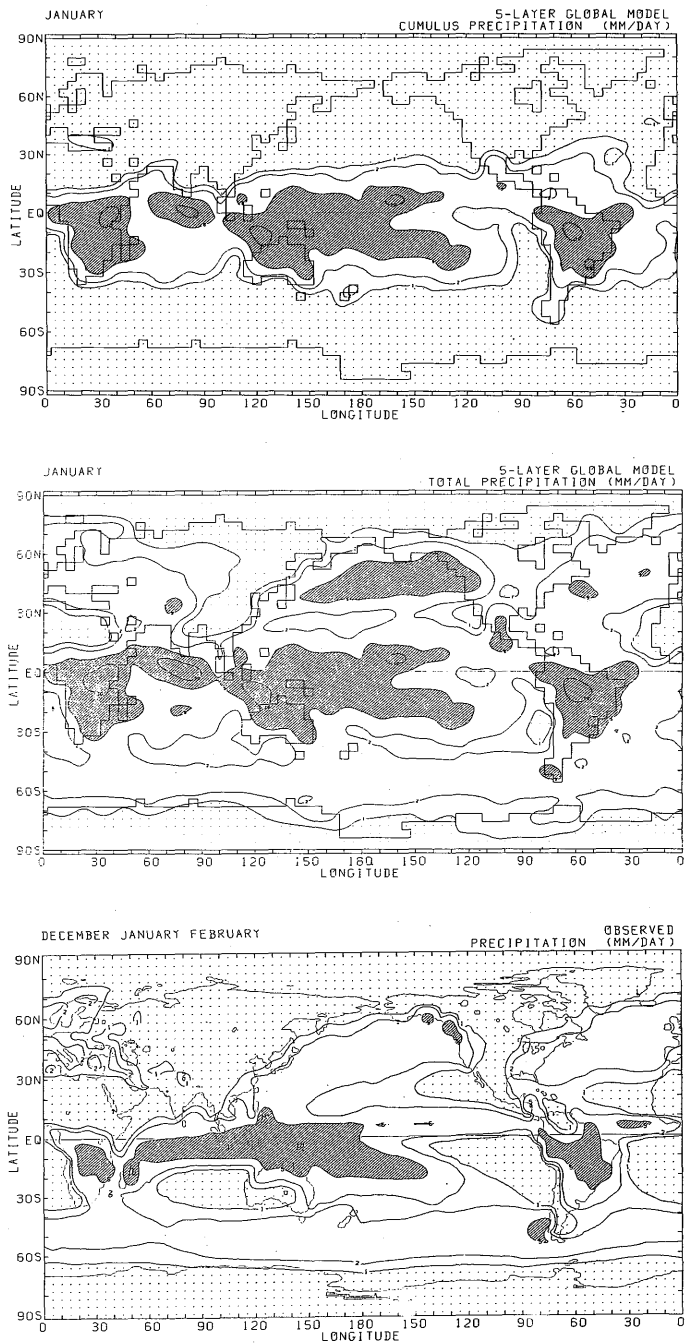


Fig. A7.1.1 January mean cumulus precipitation rate (top) and total precipitation rate (middle) simulated by the MRI • GCM-I. The observed precipitation rate for December, January and February is shown at the bottom. Contours are 1, 2, 5 and 10 mm day<sup>-1</sup>. Regions greater than 5 mm day<sup>-1</sup> are shaded and less than 1 mm day<sup>-1</sup>, dotted. The observed data are from Schutz and Gates (1972).

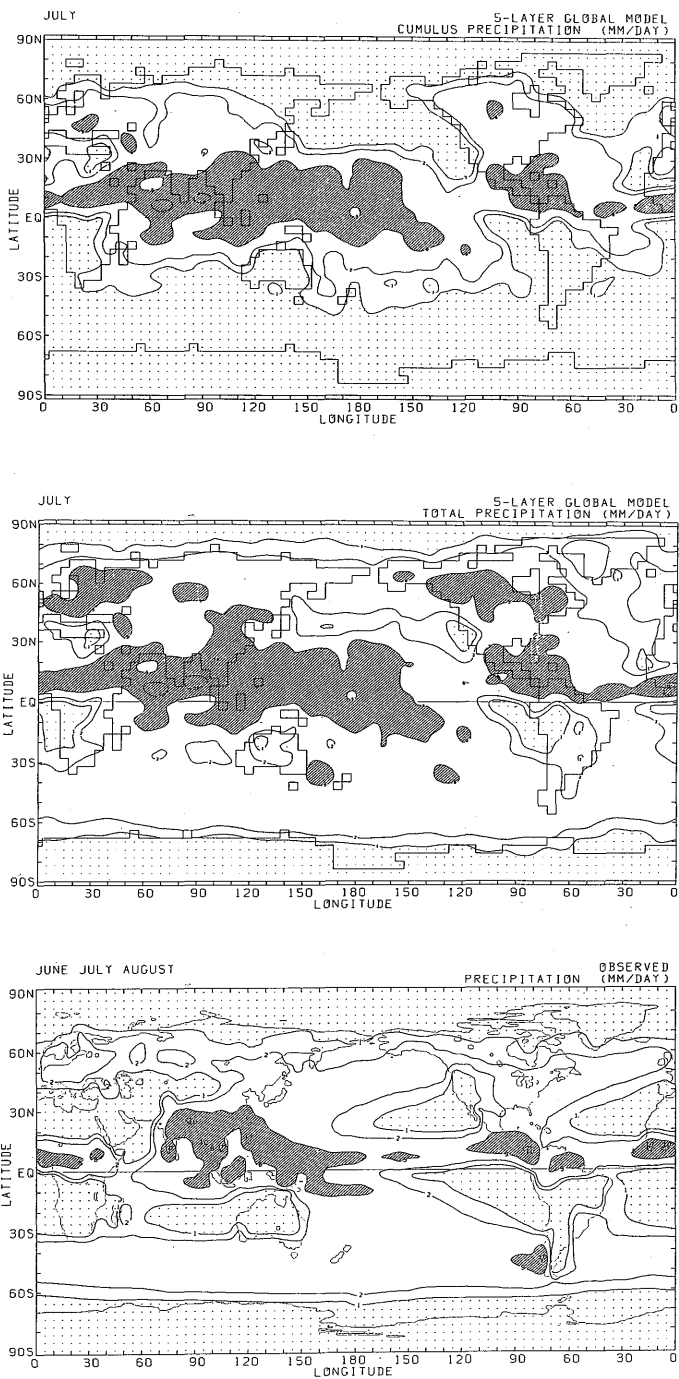


Fig. A7.1.2 Same as Fig. A7.1.1 except for July (top and middle) and June, July, August (bottom).

(1985) and Kitoh and Tokioka (1985). The simulation is made with the 5-layer tropospheric version of the MRI-GCM-I with a seasonal cycle.

#### A7.1.1 Precipitation

Precipitation in the model is produced through three processes, namely, large-scale precipitation, mid-level convection, and cumulus precipitation. Among them, precipitation caused by mid-level convection is small compared with other two. Figs. A7.1.1a and b show the cumulus and the total precipitation rates in the model for January. Cumulus precipitation is mainly produced in the tropical region (20°N-30°S). The cumulus precipitation accounts for most of the total precipitation there. It is also noted that the model favorably simulates the observed heavy precipitation area (see Fig. A7.1.1c), namely, north equatorial Pacific ITCZ, band-like area extending from the equatorial Pacific Ocean to the southeastern Pacific, the area over Indonesia extending to northern Australia, the ITCZ over equatorial Indian Ocean, the area from central Africa to Madagascar Island, and the area over Brazil. Although the central Atlantic ITCZ in the model is not active, precipitation is maximum there. The simulated amount of precipitation shows relatively good agreement with the observed amount, although the simulated one is slightly larger than the observed.

The distribution of precipitation rate for July is shown in Fig. A7.1.2. Over the tropical region, precipitation mainly consists of cumulus precipitation. Noticeable observed features are well simulated by the model. The heavy precipitation area along 10°N latitude over the African continent, the north Atlantic ITCZ, the area extending from the northern part of Brazil to the central America, the ITCZ over north equatorial Pacific starting from southeast Asia, high precipitation band along 5-10°S over south central Pacific, and the monsoon area over India and Indian Ocean are among them. Though, there are a few deficiencies in the precipitation of the model. The ITCZ over north central Pacific is broad and extends to too far north in the model, which corresponds to insufficient southward expansion of subtropical high pressure over north Pacific. There also are fictitious heavy precipitation area over the western Arabian Sea and southern Arabian Peninsula.

Cumulus clouds produce heavy precipitation not only over tropical region, but also over mid-latitude continent in the summer hemisphere. The precipitation over summer mid-latitude continent in the model is too high compared with the observation. This may allude some shortcomings of the model's ground hydrology and/or cumulus parameterization. Suarez and Arakawa (1981) showed that the ground wetness and cumulus convection have

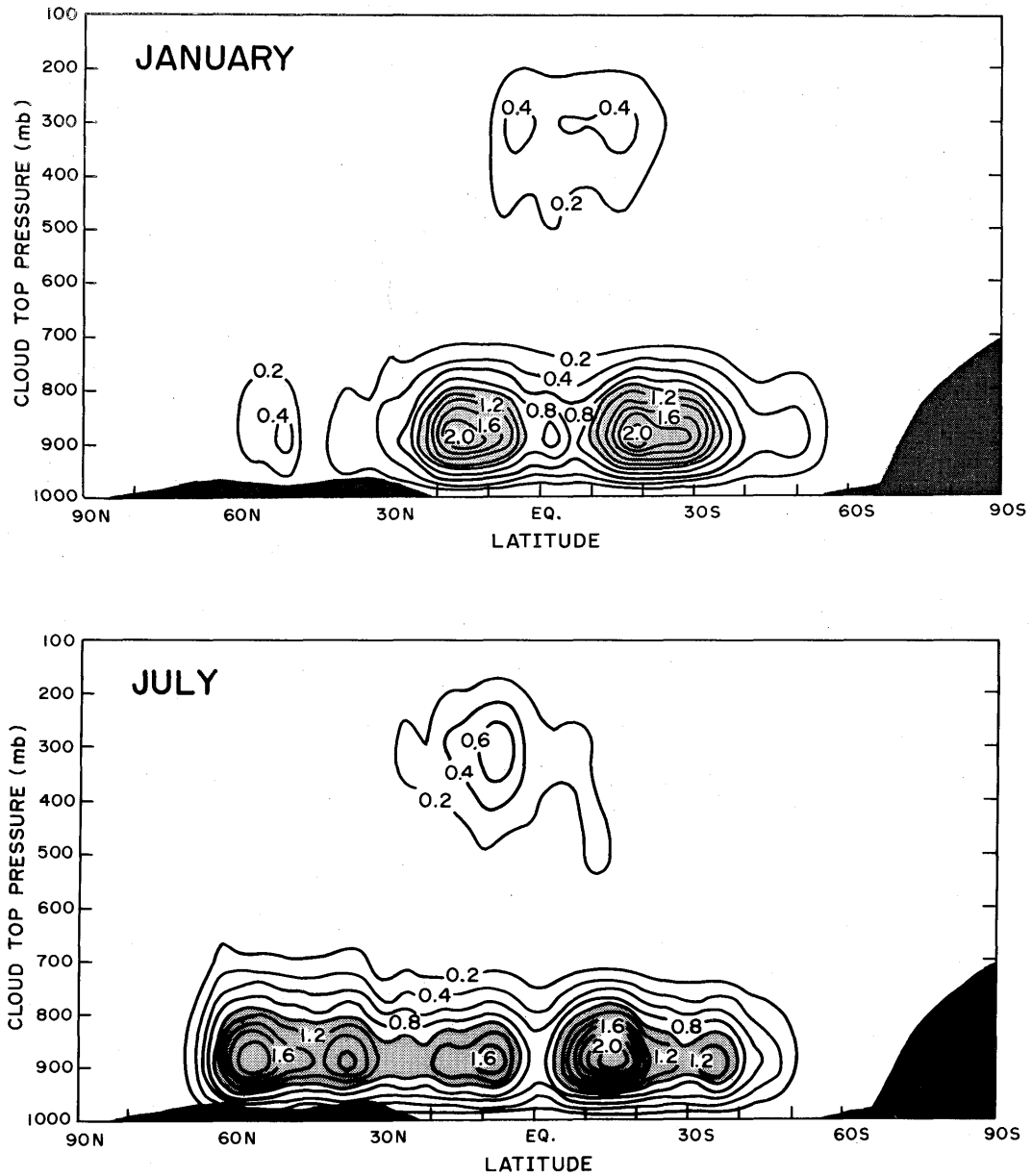


Fig. A7.1.3 Simulated zonal mean cloud base mass flux  $m_b(P_a)$  for January (top) and July (bottom). Note that the ordinate indicates the cloud top pressure. Contour interval is 0.2 mb/hour. Values larger than 1 mb/hour are shaded.

positive feedback due to enhanced transfer of moisture through diurnal change of the PBL depth. Therefore, precipitation over summer continent is very sensitive to the ground wetness. Most of the cumulus precipitation over mid-latitude continent are caused by shallow clouds. Hence, the present cumulus parameterization may overestimate precipitation from shallow clouds.

#### **A7.1.2 Cumulus cloud base mass flux.**

Fig. A7.1.3 shows the zonal mean cloud base mass flux for January and July. Over tropics, bi-modal mass flux distribution is noticeable, namely the deep clouds, whose top lie at 300mb, and shallow clouds ( $\sim 900$ mb) are predominant. In January the peaks of deep cloud mass fluxes are located at  $5^{\circ}\text{N}$  and  $15^{\circ}\text{S}$ , whereas in July, one peak appears at  $10^{\circ}\text{N}$ . The shallow cloud dominates over the subtropical region. In July, shallow cloud extends to mid-latitude ( $\sim 60^{\circ}\text{N}$ ). As seen in subsection A7.1.1, this mid-latitude shallow cloud is predominant over the continent and produces excessive amount of precipitation there.

#### **A7.1.3 Comparison with Marshall Islands data.**

Yanai, Chu, Stark and Nitta (1976) analyzed the upper air and surface observation in the Marshall Islands region from 15 April through 22 July, 1956. They computed the mean apparent heat source and moisture sink by the budget analysis and estimated the cloud base mass flux  $m_b$  as a function of detrainment level by using the spectral cloud ensemble model similar to the model described in this chapter. Fig. A7.1.4 shows Yanai *et al.*'s estimate and results of the five-layer MRI-GCM-I over the corresponding region (average of values at 6 grid points within the square enclosed by  $6^{\circ}\text{N}$ ,  $10^{\circ}\text{N}$ ,  $160^{\circ}\text{E}$ , and  $170^{\circ}\text{E}$ ) for the same season. The observation clearly shows the dominance of mass fluxes associated with very shallow and very deep clouds. The model's calculation shows the similar pattern, but the mass fluxes are much smaller than the observed ones (note the difference of the vertical resolutions between observation and simulation). The dominant deep cloud in the model has its top at 300 mb level, whereas the observed one has at 125 mb level. In the observation shallow clouds have much mass flux than deep clouds, whereas the simulation shows opposite feature. The observed precipitation rate is 10.1 mm/day and simulated one is 7.2 mm/day which is 30% less than the observed.

There might be ambiguity in the observation and large interannual variability of cumulus activity over the equatorial Pacific region. However, comparison of simulated results and

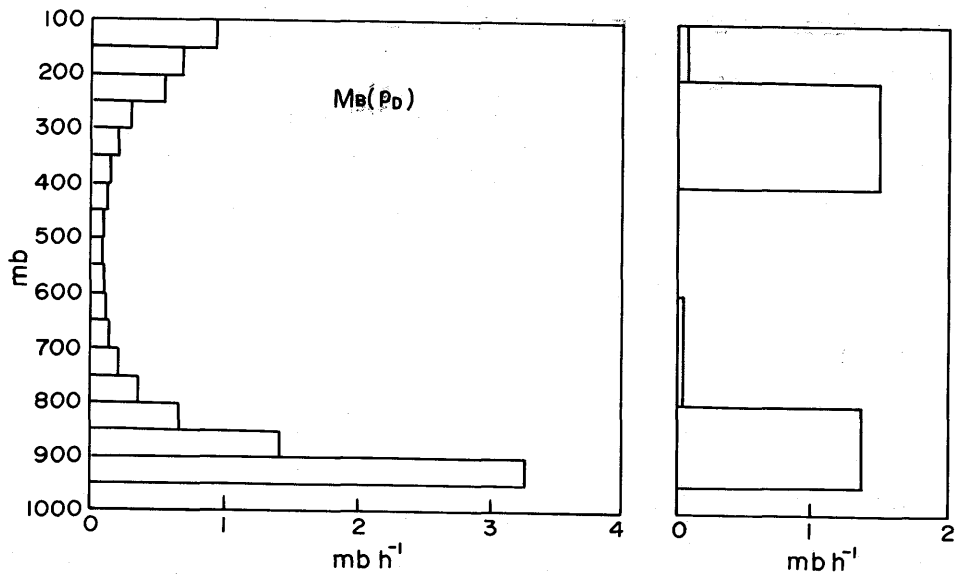


Fig. A7.1.4 The observed (left) and the simulated (right) mean cloud base mass flux  $m_b(P_d)$  over the Marshall Islands region during the period 15 April through 22 July. The observed data are taken from Fig. 5 of Yanai *et al.* (1976). See text for details.

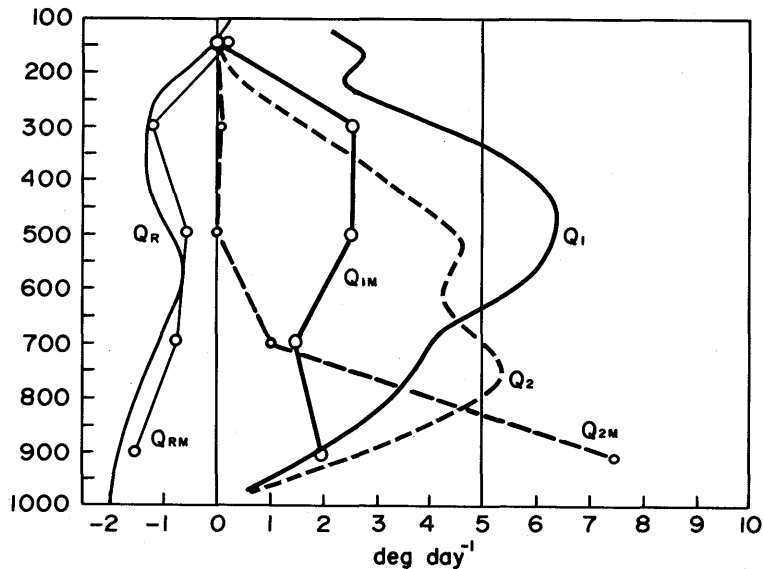


Fig. A7.1.5 The mean apparent heat source  $Q_1$  (solid), moisture sink  $Q_2$  (dashed) and radiational heating rate  $Q_R$  (thin solid) given by Dopplack (1970) over the Marshall Islands region. Adopted from Yanai *et al.* (1976). Simulated results by the MRI • GCM-I are also shown by corresponding lines with small open circles. The suffix M indicates the simulated values by the model.

observation seems to allude the drawback in the cumulus model. The drawback can be seen more clearly in the apparent heat source  $Q_1$  and moisture sink  $Q_2$  (Fig. A7.1.5).  $Q_1$  in the model is the rate of temperature change due to cumulus clouds,  $Q_2$  is the rate of change of  $-L q_v$  due to cumulus clouds.  $Q_1$  and  $Q_2$  in the model are less than the observed values except in the lowest layer. For the lowest layer, cumulus clouds in the model make the environment too dry.

#### A7.1.4 Cloudiness

The simulated zonally averaged total cloudiness in July is shown in Fig. A7.1.6, together with the observed one (Dopplick, 1979). As mentioned in section 7.8, the cloudiness of cumulus cloud is zero except anvil of cirrus cloud. Fig. A7.1.6 shows that the model underestimates the cloudiness over tropics. The shallow cloud is responsible for this discrepancy between the simulation and observation. As far as radiation is concerned, shallow clouds act to cool the middle and upper troposphere. The Hadley circulation in the model is somewhat weaker than

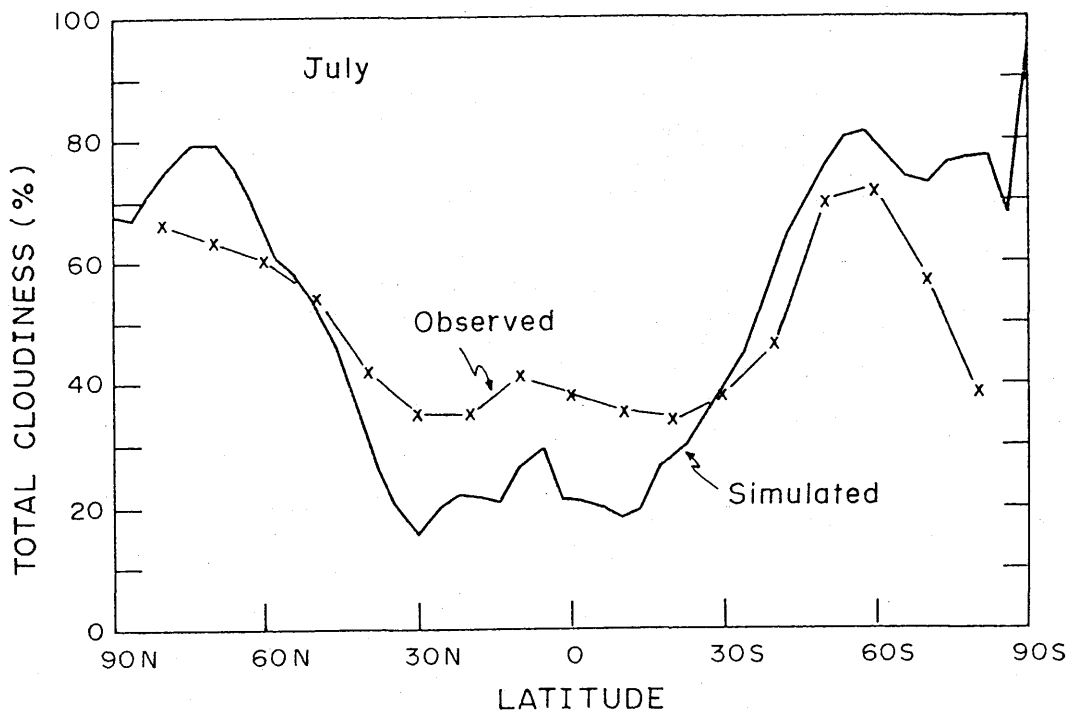


Fig. A7.1.6 The solid line shows the latitudinal distribution of the zonally averaged total cloudiness (%) for July. The observed distribution is shown by thin solid line with crosses and taken from Dopplick (1979).

observation (Tokioka *et al.*, 1985, Kitoh and Tokioka, 1985). Therefore, magnitude of the Hadley cell may become stronger by taking into account of shallow cloudiness into the radiation calculation.

The model simulates the precipitation pattern relatively well. But, there are some drawbacks in the simulated results such as too much precipitation over summer extratropic continent, too much dryness of the low layer in the tropics. The origin of these drawbacks probably does not lie solely in the cumulus parametrization. Nevertheless, it is necessary to seek for the improvement and sophistication of cumulus parameterization for better simulation by the GCM.

**A7.2 Simple examples of the solution for the mass flux distribution equation**

The simple 2nd order equation will be considered to elucidate the character of the mass flux distribution equation. Cloud type 1 is regarded as deep cloud ensemble and cloud type 2 as shallow cloud ensemble. Without loss of generality, we can assume the diagonal elements of K matrix are  $-1$ .

Example 1.

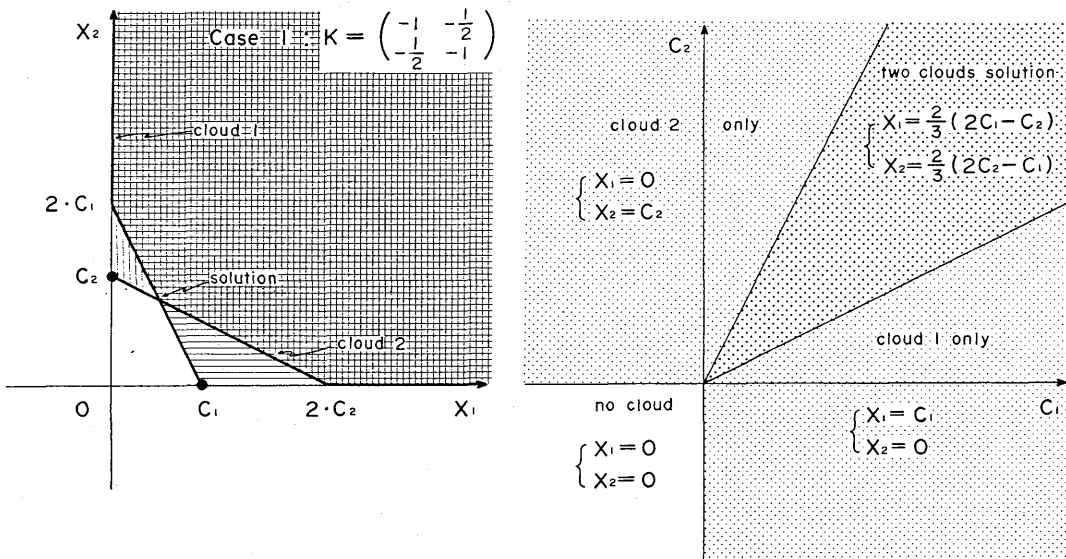


Fig. A7.2.1 Graphical representations of the equation (left) and solutions (right) for example 1. See text for details.

$$K = \begin{bmatrix} -1 & -1/2 \\ -1/2 & -1 \end{bmatrix}$$

The graphical representation of the equation for cloud 1 and 2 is shown in Fig. A7.2.1. A unique solution is found at the intersection point of two lines. The solution is shown on the two dimensional forcing  $C_1 - C_2$  plane in the right hand side of Fig. A7.2.1. When the forcings for both clouds are comparable, both clouds can exist. When the forcing for the certain cloud is negative, such cloud can not exist. In any case, the solution is unique. Fig. A7.2.2 shows the variation of mass flux  $x_1$  with forcing  $C_1$  when  $C_2$  is fixed. It is seen that the cloud-cloud interaction has reduced the mass flux when the forcing  $C_1$  is less than  $2 C_2$ .

Example 2.

$$K = \begin{bmatrix} -1 & 1/2 \\ -1/2 & -1 \end{bmatrix}$$

In this case  $K(1, 2)$  is positive which means that the cloud 2 affects to enhance the cloud 1. The possibility that this type of situation occurs in the real atmosphere can not be excluded. In the special circumstances, the shallow cloud (cloud 2) might have an positive effect on the deep cloud (cloud 1) through the moistening process of the lower atmosphere at the top of the shallow cloud. Graphical representation of the equation and the solution are shown in Fig. A7.2.3 in the same manner as in Fig. A7.2.1. In this case even if the forcing for cloud 1 is negative mass flux of cloud 1 can have non-zero values. The solution for this example is also unique.

Example 3.

$$K = \begin{bmatrix} -1 & -2 \\ -2 & -1 \end{bmatrix}$$

In this case the interactions between two types of clouds are stronger than the self-interactions. Occurrence of such a situation is unlikely but possible in the GCM due to its coarse vertical resolution and/or any computational errors. There exist three solutions when

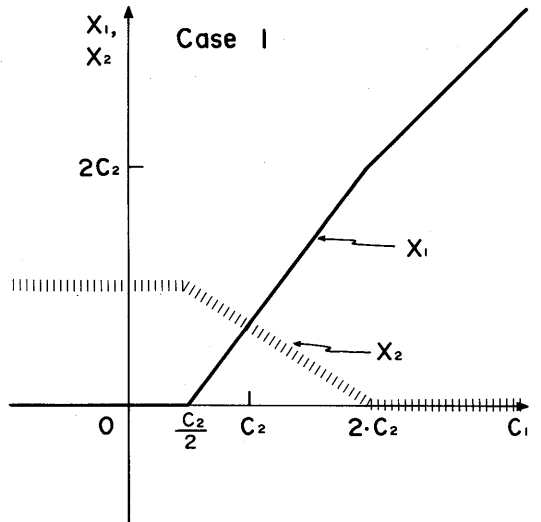


Fig. A7.2.2 Variations of the solutions with the cloud 1 forcing  $C_1$  for example 1, provided the cloud 2 forcing  $C_2$  is held constant. See text for details.

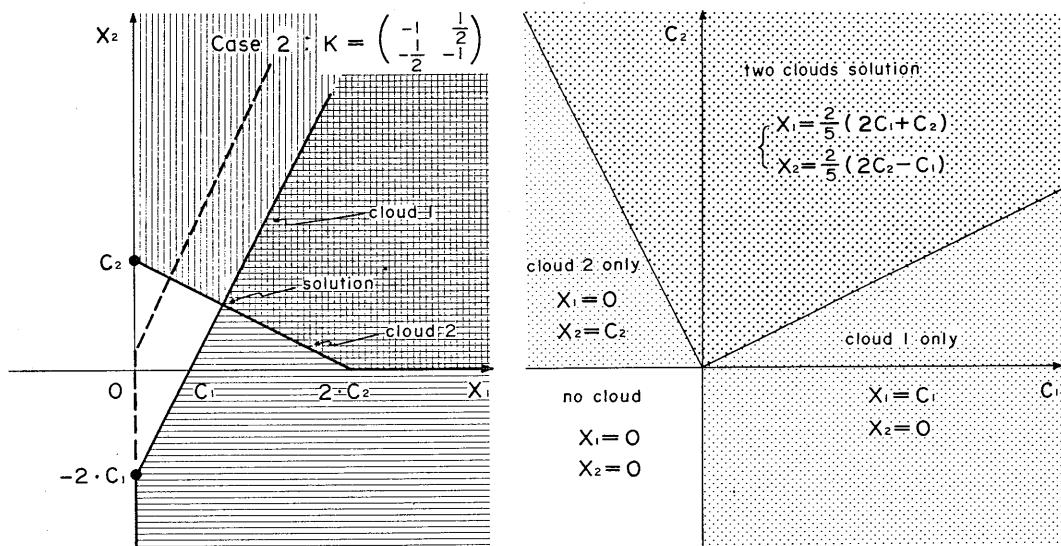


Fig. A7.2.3 Same as Fig. A7.2.1 except for example 2.

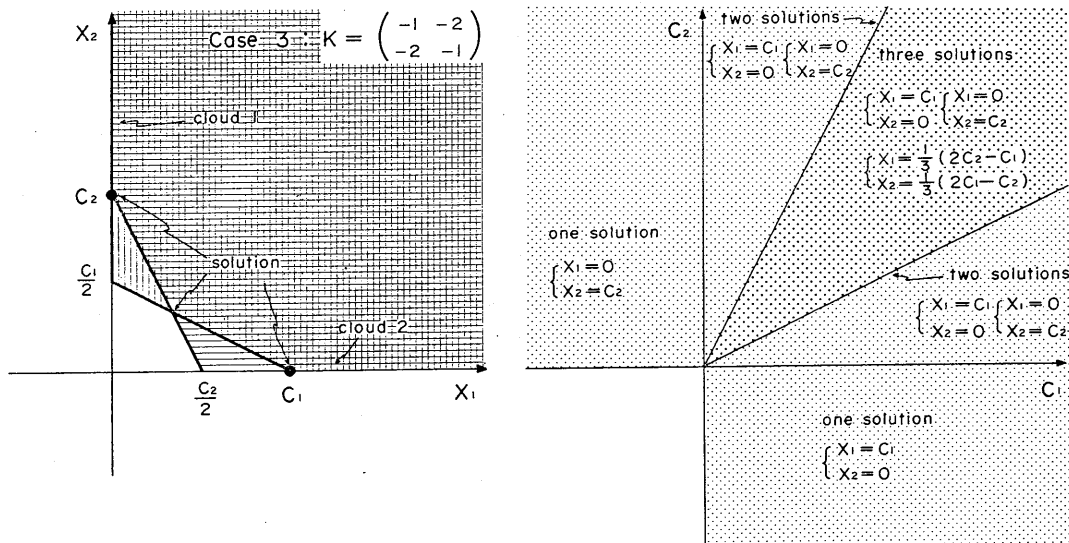


Fig. A7.2.4 Same as Fig. A7.2.1 except for example 3.

$C_2/2 < C_1 < 2C_2$ . (see Fig. A7.2.4). There is no selection rule among three solutions. Fig. A5 shows the variation of  $x_1$  with  $C_1$  when  $C_2$  is fixed. Discontinuity of the solution takes place at  $C_2/2$  and  $2C_2$ . Until  $C_1$  increases from zero to  $C_2/2$ ,  $x_1$  remains zero. When  $C_1$  is larger than  $2C_2$ ,  $x_1$  is  $C_1$ . Between  $C_2/2$  and  $2C_2$ ,  $x_1$  can have three values. In this example, there is no unique solution.

It is of interest to check whether the right solution will be obtained by the overadjustment simplex method proposed by Lord *et al.* (1982). In the overadjustment simplex method, the solution which minimizes linear objective function  $Z$  is searched, over the shaded region in Fig. A7.2.1, where  $Z$  is defined as

$$Z = \sum_{i=1}^{i \max} | \sum_{j=1}^{j \max} K(i, j) x_j + c_j | \quad (A7.2.1)$$

See Lord *et al.* (1982) for details. It is known that solution should occur at the extreme points on the boundary of the region. When  $x_1$  and  $x_2$  are positive, the solution given by the overadjust simplex method agrees with the

right solution for examples 1 and 2. For example 3, however, the overadjustment simplex method can choose only one solution. Let us consider the simple case that  $C_1 = C_2 = 3$ . In this case there are three solutions, namely,  $(x_1, x_2)$  equals to 1) (1,1), 2) (3,0), 3) (0,3). The simplex method chooses the first solution. Next let us consider the case that  $C_1 = 3, C_2 = 1$ . The right solution is (3,0). In this case, however, the overadjustment simplex method chooses (0,3/2) which is not the solution (see Fig. A7.2.5).

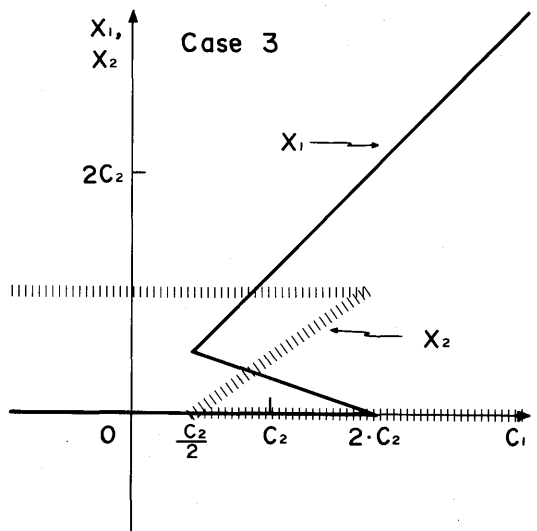


Fig. A7.2.5 Same as Fig. A7.2.2 except for example 3.

Theorem :

$$\begin{aligned} x_1 + ax_2 = C_1 \text{ and } x_1 > 0 \text{ or } x_1 = 0 \text{ and } ax_2 \geq C_1 \\ bx_1 + x_2 = C_2 \text{ and } x_2 > 0 \text{ or } x_2 = 0 \text{ and } bx_1 \geq C_2 \end{aligned} \quad (A7.2.2)$$

The necessary and sufficient condition for the above equation to have an unique solution is

$$1 - ab \equiv D > 0, \text{ i. e., } \det | -K | > 0 \quad (A7.2.3)$$

There are four cases for the solution.

1)  $x_1 = x_2 = 0$  then,

$$0 \geq C_1 \tag{A7.2.4}$$

$$0 \geq C_2 \tag{A7.2.5}$$

2)  $x_1 = 0, x_2 > 0$  then,

$$ax_2 \geq C_1 \tag{A7.2.6}$$

$$x_2 = C_2 > 0 \tag{A7.2.7}$$

3)  $x_1 > 0, x_2 = 0$  then,

$$x_1 = C_1 > 0 \tag{A7.2.8}$$

$$bx_1 \geq C_2 \tag{A7.2.9}$$

4)  $x_1 > 0, x_2 > 0$  then,

$$x_1 = (C_1 - aC_2)/D > 0 \tag{A7.2.10}$$

$$x_2 = (C_2 - bC_1)/D > 0 \tag{A7.2.11}$$

We will show that these four cases are mutually exclusive provided  $\det | -K | > 0$ .

Proof :

Suppose case 1) holds ;

Then it is clear that case 2) and 3) contradict the case 1).

Suppose 4) holds too.

Then, from (A7.2.3) and (A7.2.10)

$$C_1 - aC_2 > 0 \text{ then } C_1 > aC_2.$$

From (A7.2.4),  $0 > aC_2$ .

Then  $a > 0$  from (A7.2.5)

From (A7.2.11)  $C_2 - bC_1 > 0$

Multiply  $a > 0$  to the above equation and after slight manipulation, we get

$$C_1 - aC_2 < C_1 (1 - ab) < 0$$

This contradicts the condition (A7.2.10).

Suppose case 2) holds.

Suppose case 3) also holds, then  $C_1 > 0, C_2 > 0, a > 0, b > 0$ .

From (A7.2.6), (A7.2.7), (A7.2.8), and (A7.2.9)

$$aC_2 \geq C_1$$

$$bC_1 \geq C_2$$

Then  $abC_2 \geq bC_1 \geq C_2$

$$-(1 - ab) C_2 \geq 0 \text{ This lead to a contradiction to (A7.2.3).}$$

Suppose case 4) also holds, then  $aC_2 \geq C_1$ . We can derive the relation

$0 \geq C_1 - aC_2$  which contradicts (A7.2.10).

We can easily lead the contradiction for case 3) as same as case 2).

Let us check the determinants for the previous examples.

Example 1 :  $\det | -K | = 3/4$

Example 2 :  $\det | -K | = 5/4$

Example 3 :  $\det | -K | = -3$

Therefore, the examples 1 and 2 have their unique solutions while the example 3 does not.

For the equation of general order, the necessary and sufficient condition to have a unique solution is that all the small determinants  $\det | -K' |$  are positive. But this theorem has not been proved yet.

## 8. Planetary boundary layer\*

### 8.1 Introduction

The layer adjacent to the earth's surface is called the planetary boundary layer (PBL), where turbulent motions are dominant in redistributing sensible heat, moisture and momentum in the vertical direction. The atmosphere above the PBL is called the free atmosphere. We idealize in modeling the PBL that turbulent fluxes are completely absent in the free atmosphere except in the cumulus ensembles. This simplification introduces the existence of gaps in physical variables at the top of the PBL.

Variety of informations of the earth's surface is conveyed to the free atmosphere through the PBL. Therefore the depth and the structure of the PBL, and thus the turbulent fluxes of energy and momentum in it are greatly controlled by the surface conditions as well as by synoptic conditions in the free atmosphere.

The PBL model of the MRI-GCM-I is based on the model by Randall and Arakawa described in AM and by Randall (1976) with minor changes in several respects. The model predicts the depth and the mean structure of the PBL by taking account of the interactions with large-scale circulations as well as with the surface conditions. It also interacts with a sophisticated parameterization of cumulus convection described in Chapter 7, which is based on the theory of Arakawa and Schubert (1974). The possible existence of stratus or stratocumulus clouds within the PBL is also taken account of in the diagnostic determination of the turbulent fluxes.

Governing equations for the large-scale circulation are described in 8.2. The diagnostic determination of turbulent fluxes and the entrainment rate at the top of the PBL is given in 8.3. The treatment of the stratus layer is given in 8.4 and the vertical interpolation scheme and numerical procedures are given in 8.5 and 8.6, respectively. Some examples of the model performance are shown in the Appendix 8.1.

### 8.2 Governing equations for the large-scale circulation

The conservation of mass in the  $\sigma$ -coordinate system is given by (0.14). Let  $\sigma_B$  and  $\delta\sigma_m$  ( $=1-\sigma_B$ ) be the top and the depth of the PBL in  $\sigma$ -space respectively. Vertical integration of

---

\* This chapter is prepared by T. Tokioka.

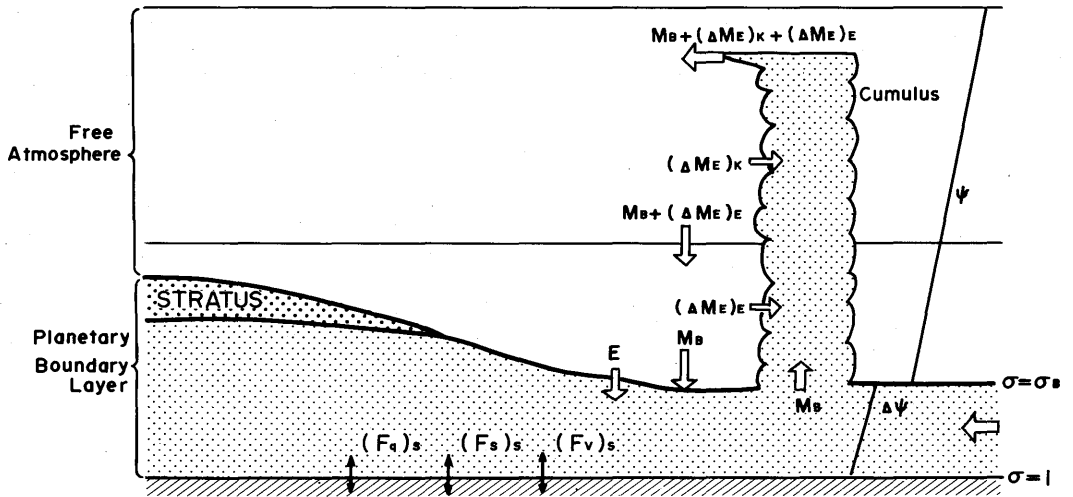


Fig. 8.1 Schematic figure of the PBL model in the GCM. The PBL interacts with the free atmosphere, with the ensemble of cumulus and with the lower surface of the atmosphere. White arrows show mass flows related to the mass budget of the PBL.

(0.14) from  $\sigma = \sigma_B$  to 1 results in the following equation:

$$\frac{\partial}{\partial t}(\pi \delta \sigma_m) + \nabla \cdot (\pi \delta \sigma_m \mathbf{v}_m) - g(E - M_B) = 0 \quad (8.1)$$

where

$$E - M_B = -\frac{\pi}{g} \left( \frac{\partial \sigma_B}{\partial t} + \mathbf{v}_B \cdot \nabla \sigma_B - \dot{\sigma}_B \right) \quad (8.2)$$

and

$$\mathbf{v}_m = \frac{1}{\delta \sigma_m} \int_{\sigma_B}^1 \mathbf{v} d\sigma$$

The right hand side of (8.2) indicates the net downward mass flux across the PBL top, and the term is decomposed into two parts, *i. e.*  $E$  and  $M_B$ , for the later convenience.  $E$  is the rate at which mass is entrained into the PBL from the free atmosphere, and  $M_B$  is the rate at which mass is lost from the PBL into the cumulus cloud ensembles (see Fig. 8.1). If we integrate (0.14) from the level just above the PBL  $\sigma = \sigma_{B+}$  to  $\sigma = \sigma_B$ , then we get

$$\pi \Delta(\mathbf{v} \cdot \nabla \sigma_B - \dot{\sigma}) = 0 \quad (8.3)$$

where  $\Delta\psi$  indicates a gap in the quantity  $\psi$  at the PBL top.

The diabatic term  $\pi Q$  in the thermodynamic equation (0.26) is expressed as

$$\pi Q = g \frac{\partial}{\partial \sigma} (F_s + R) + \pi (LC + Q_s) \quad (8.4)$$

where  $F_s$  is the upward turbulent flux of sensible heat;  $R$ , the net upward flux of radiation; and  $C$  is the net condensation rate due to processes other than cumulus convection. The heating due to a possible ensemble of cumulus clouds is expressed as  $Q_s$ . If we integrate (0.28) from  $\sigma = \sigma_{B+}$  to  $\sigma = \sigma_B$ , we get

$$(F_s)_B - \Delta R + \frac{\pi}{g} \int_{\sigma_{B+}}^{\sigma_B} LC \, d\sigma + E c_p \Delta T = 0 \quad (8.5)$$

where use has been made of (8.2) and (8.3), and the following assumption

$$\pi \int_{\sigma_{B+}}^{\sigma_B} Q_s \, d\sigma = -g \int_{\sigma_{B+}}^{\sigma_B} M \frac{\partial s}{\partial \sigma} \, d\sigma = g M_B c_p \Delta T$$

$M_B$  is the cumulus ensemble mass flux at  $\sigma = \sigma_B$ , and  $s$  indicates dry static energy,  $c_p T + \phi$ . The second and the third terms of (8.5) are zero except when the upper portion of the PBL is filled with stratus (cloud-topped PBL).

In a non-precipitable moist process, both moist static energy  $h (=s + Lq)$  and total water substance  $q_w (=q + l)$ , where  $l$  is the mixing ratio of liquid water, are conserved. By analogy with (8.5), we have

$$(F_h)_B - \Delta R + E \Delta h = 0 \quad (8.6)$$

and

$$(F_{q_w})_B + E \Delta q_w = 0 \quad (8.7)$$

where  $(F_h)_B$  and  $(F_{q_w})_B$  are the vertical turbulent fluxes of  $h$  and  $q_w$  at the PBL top. From (8.5), (8.6) and (8.7), we get

$$-\frac{\pi}{g} \int_{\sigma_{B+}}^{\sigma_B} LC \, d\sigma = L [(F_l)_B - E l_B] \quad (8.8)$$

where  $(F_l)_B$  is the vertical turbulent flux of  $l$  at  $\sigma = \sigma_B$ .

In a similar way, we obtain

$$\frac{\pi}{g} \int_{\sigma_{c+}}^{\sigma_{c-}} LC \, d\sigma = L F_{lc+} \quad (8.9)$$

where  $\sigma_{c\pm}$  indicate the positions immediately above and below the stratus cloud base.

From the momentum equations, we obtain

$$(F_v)_B + E \Delta v = 0 \quad (8.10)$$

where  $(F_v)_B$  indicates vertical flux vector of horizontal momentum at  $\sigma = \sigma_B$ .

Here we introduce a new coordinate  $\sigma' = \sigma - \sigma_B$ . The PBL top is just  $\sigma' = 0$  in this

coordinate. With use of the relation

$$\left(\frac{\partial}{\partial \xi}\right)_{\sigma} = \left(\frac{\partial}{\partial \xi}\right)_{\sigma} - \frac{\partial \sigma_B}{\partial \xi} \frac{\partial}{\partial \sigma} \quad (8.11)$$

where  $\xi$  is either time or horizontal coordinate, we can rewrite thermodynamic equation (0.26), conservation equation of total water substance (0.28) and momentum equation (0.23). From those equations, we can derive following jump equations:

$$c_p \pi \frac{\partial \Delta T}{\partial t} = -c_p \left[ \Delta(\pi \mathbf{v} \cdot \nabla_{\sigma} T) + g(E - M_B) \Delta \left( \frac{\partial s}{\partial \sigma} \right) \right] + \pi \Delta \left[ \left( \frac{\partial p_B}{\partial t} + \mathbf{v} \cdot \nabla p_B \right) \alpha \right] + g \left[ \Delta \left( \frac{\partial R}{\partial \sigma} \right) - \left( \frac{\partial F_s}{\partial \sigma} \right)_B \right] + \pi \Delta (LC + Q_s) \quad (8.12)$$

$$\pi \frac{\partial \Delta q_w}{\partial t} = -\Delta(\pi \mathbf{v} \cdot \nabla_{\sigma} q_w) - g(E - M_B) \Delta \left( \frac{\partial q_w}{\partial \sigma} \right) - \left[ \Delta \left( \frac{\partial r}{\partial \sigma} \right) + g \left( \frac{\partial F_{q_w}}{\partial \sigma} \right)_B \right] \quad (8.13)$$

$$\pi \frac{\partial \Delta \mathbf{v}}{\partial t} = -\nabla[\pi \mathbf{v} \cdot \nabla_{\sigma} \mathbf{v}] - g(E - M_B) \Delta \left( \frac{\partial \mathbf{v}}{\partial \sigma} \right) - \pi \Delta \alpha \nabla p_B - \pi \left[ \mathbf{f} \mathbf{k} \times \Delta \mathbf{v} + \frac{\tan \varphi}{a} \mathbf{k} \times \Delta(u\mathbf{v}) \right] - g \left( \frac{\partial \mathbf{F}_v}{\partial \sigma} \right)_B \quad (8.14)$$

where  $r$  is the downward flux of water substance due to precipitation.

In deriving (8.12), use has been made of

$$\omega_B = \frac{\partial p_B}{\partial t} + \mathbf{v}_B \cdot \nabla p_B + g(E - M_B) = \omega_{Bt} - \Delta \mathbf{v} \cdot \nabla p_B$$

It is pointed out that the balance between the term  $\pi \Delta \alpha \nabla p_B$  and  $\pi \mathbf{f} \mathbf{k} \times \Delta \mathbf{v}$  in (8.14) may be understood as an extension of Margules' relation to the wind and density discontinuities at the PBL top.

### 8.3 Diagnostic determination of the entrainment rate at the top of the PBL and of turbulent fluxes

Turbulent kinetic energy equation in the planetary boundary layer may be written as

$$\frac{dq^2}{dt} + \frac{\partial}{\partial z} \overline{w' \left( \frac{p'}{\rho} + q^2 \right)} = \frac{\tau}{\rho} \cdot \frac{\partial \mathbf{v}}{\partial z} + \frac{g}{s_v} \overline{w' s_v'} - \delta \quad (8.15)$$

where  $q^2$  is turbulent kinetic energy density,  $w$  is vertical velocity,  $\tau$  is stress ( $=\rho \overline{v'w'}$ ),  $\rho$  is density,  $\delta$  is the dissipation rate of turbulent kinetic energy, and  $s_v$  is the virtual dry static energy ( $=s + \epsilon L (0.61q - l)$ ,  $\epsilon = c_p T/L$ ). Dash is an indicator of turbulent quantity and a superior bar is an average operation. In deriving (8.15), turbulence is assumed to be homogeneous in the horizontal direction.

We integrate (8.15) from the surface ( $z=0$ ) to the top of the PBL ( $z=z_B$ ). Then the left hand side of (8.15) may be approximated as

$$\rho z_B \frac{Dq_m^2}{Dt} + \rho E q_m^2 \quad (8.16)$$

where

$$\frac{D}{Dt} = \frac{\partial}{\partial t} + \mathbf{v}_m \cdot \nabla$$

The subscript "m" indicates that the value is a representative value in the PBL.

The first term on the r.h.s. of (8.15) is the generation of turbulent kinetic energy by the vertical wind shear, which is considered to be large both near the surface and the PBL top where the vertical wind shear is usually large. Therefore we introduce the following approximation,

$$\int_0^{z_B} \rho \cdot \frac{\tau}{\rho} \cdot \frac{\partial \mathbf{v}}{\partial z} dz = a_1 \rho u_*^3 + a_2 \rho |\Delta \mathbf{v}|^3 \quad (8.17)$$

where  $u_*$  is the friction velocity.  $a_1$  and  $a_2$  are constants yet undetermined.

The second term on the r.h.s. of (8.15) is the generation of the turbulent kinetic energy due to buoyancy flux. The buoyancy flux, based on its definition, is related to the turbulent flux of  $h$  and  $q_w$  as follows:

$$\overline{w' s_v'} = \begin{cases} (1 + 0.61\bar{q})\overline{w'h'} - (1 - 0.61\bar{\epsilon} + 0.61\bar{q})L\overline{w'q_w'} & : \text{outside clouds} \\ \left( \alpha + \frac{0.61\bar{q} - \bar{l}}{1 + \gamma} \right) \overline{w'h'} - \bar{\epsilon}L\overline{w'q_w'} & : \text{inside clouds} \end{cases}$$

where

$$h = s + Lq$$

$$q_w = q + l$$

$$s_v = s + \epsilon L(0.61q - l) \quad (8.18)$$

$$\alpha = (1 + 1.61\gamma\epsilon)/(1 + \gamma)$$

$$\gamma = \frac{L}{c_p} \left( \frac{\partial q^*}{\partial T} \right)_p$$

$$\epsilon = c_p T_o/L$$

$q^*$  : saturation mixing ratio of water vapour

Here, we introduce the following assumption:

Turbulent fluxes within the PBL tend to mix moist static energy  $h$  and the mixing ratio of total water substance  $q_w$ , *i.e.* the turbulent flux profile of both  $h$  and  $q_w$  is linear with height in the PBL.

Then we have a similar result to the one obtained by Deardorff (1976),

$$\int_0^{z_h} \rho \frac{g}{S_v} \overline{w' s_v'} dz = \frac{g Z_B}{(\overline{S_v})_m} (A - \rho E B) \quad (8.19)$$

where

$$A = \mu_1 (F_h)_s + \mu_2 \Delta R - \mu_3 L (F_q)_s$$

$$B = \mu_2 \Delta h - \mu_4 L \Delta q_w$$

$$\mu_1 = \frac{1}{2} (1 + 0.61 \bar{q}) + \frac{1}{2} \left( \alpha + \frac{0.61 \bar{q} - \bar{l}}{1 + \gamma} - 1 - 0.61 \bar{q} \right) (1 - \xi)^2$$

$$\mu_2 = \frac{1}{2} (1 + 0.61 \bar{q}) + \frac{1}{2} \left( \alpha + \frac{0.61 \bar{q} - \bar{l}}{1 + \gamma} - 1 - 0.61 \bar{q} \right) (1 - \xi^2)$$

$$\mu_3 = \frac{1}{2} (1 + 0.61 \bar{q} - 0.61 \bar{e}) + \frac{1}{2} (\bar{e} - 1 - 0.61 \bar{q} + 0.61 \bar{e}) (1 - \xi)^2$$

$$\mu_4 = \frac{1}{2} (1 + 0.61 \bar{q} - 0.61 \bar{e}) + \frac{1}{2} (\bar{e} - 1 - 0.61 \bar{q} + 0.61 \bar{e}) (1 - \xi^2)$$

$$\xi = z_c / Z_B$$

$z_c$  : height of the stratus cloud base

$(F_h)_s$  and  $(F_{q_w})_s$  mean  $F_h$  and  $F_{q_w}$  at the surface. From (8.16), (8.17), (8.18) and (8.19), we obtain the following budget equation of turbulent kinetic energy in the PBL,

$$\rho E q_m^2 = a_1 \rho u_*^3 + a_2 \rho |\Delta \mathbf{v}|^3 + \frac{g Z_B}{S_v} (A - \rho B E) - \rho \left( \delta + \frac{D q_m^2}{D t} \right) Z_B \quad (8.20)$$

Fig. 8.2 schematically summarizes the above relation. The last term in (8.20) may be proportional to the energy generation terms. Thus we assume

$$\rho \left( \delta + \frac{D q_m^2}{D t} \right) Z_B = a_3 \rho u_*^3 + a_4 \rho |\Delta \mathbf{v}|^3 + a_5 \frac{g Z_B}{S_v} \text{Max}(A, 0) + \rho \delta_o Z_B \quad (8.21)$$

with adding possible background dissipation rate  $\delta_o$  as suggested by Kim (1976). The term  $A$  may be negative, especially at night. As negative  $A$  means the destruction of turbulent kinetic energy, we set the term zero in that case. We introduce the representative turbulent kinetic energy  $q_m^2$  within the PBL in deriving (8.20). We assume, following Randall (1976), that  $q_m^2$  is a linear combination of  $u_*^2$ , the representative value of the purely dynamical boundary layer, and  $w_*^2$ , the representative value of the thermodynamical boundary layer defined by

$$w_*^2 = \max \left( 0, \frac{g}{S_v} \int_0^{z_h} \overline{w' s_v'} dz \right), \quad (8.22)$$

*i.e.*,

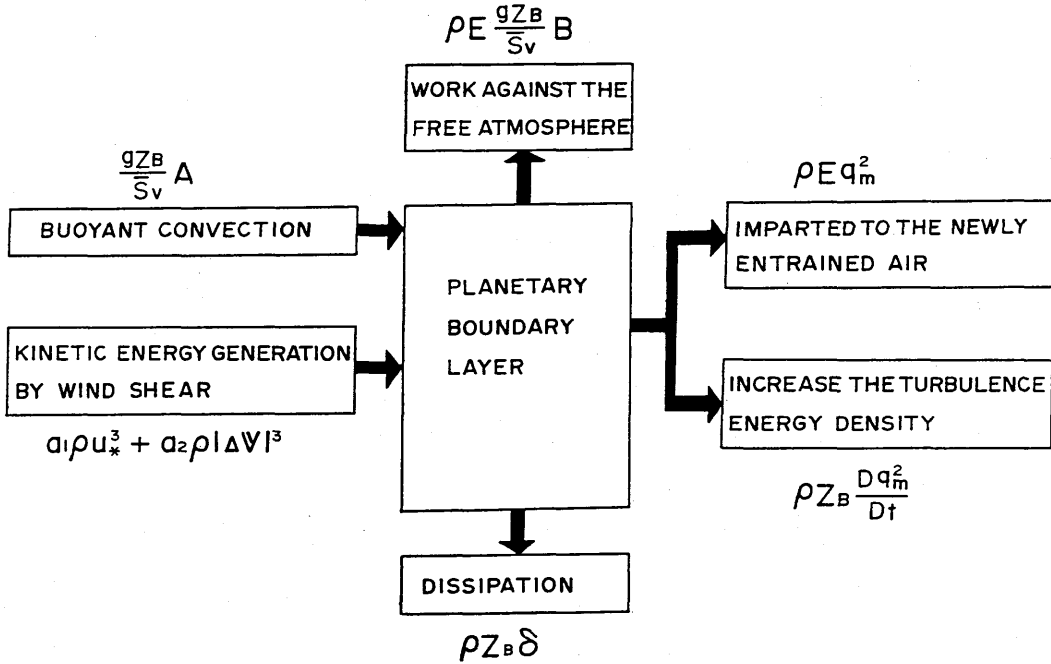


Fig. 8.2 Schematic figure of turbulent kinetic energy budget of the PBL. See text for details.

Table 8.1 Entrainment velocity experimentary determined under different situations.

Case	Entrainment Velocity	Investigator
Very Unstable PBL With Strong Inversion	$E = 0.2F_{sv}(0)/\rho\Delta s_v$	Betts (1973) and others
Very Unstable PBL With Weak Inversion	$E = 0.27w_*$	Deardorff (1974)
Stable PBL With Strong Inversion	$E = 2.5u_*^3 / \frac{gZ_B}{S_v} \Delta s_v$	Kato and Phillips (1969)
Stable PBL With Weak Inversion	$E = 0.28u_*^3$	Lundgren and Wang (1973)
Stable PBL With Strong Wind Gap and Strong Inversion	$E = 0.001  \Delta V ^3 / \frac{gZ_B}{S_v} \Delta s_v$	Stull (1976)

$$q_m^2 = b_1 w_*^2 + b_2 u_*^2. \quad (8.23)$$

where  $b_1$  and  $b_2$  are yet undetermined constants. In the daytime,  $w_*^2$  is usually larger than  $u_*^2$ , i.e.  $q_m^2 = b_1 w_*^2$ . While in the night time,  $q_m^2 = b_2 u_*^2$  because usually  $w_*^2 = 0$ . If we substitute the assumptions (8.21) and (8.23) into (8.20), the resultant equation has five constants yet undetermined,  $a_1 - a_3$ ,  $a_2 - a_4$ ,  $a_5$ ,  $b_1$  and  $b_2$ . These constants can be determined based on observations and laboratory and numerical experiments. Table 8.1 summarizes studies adopted for determining those constants. The resulting equation is expressed as

$$E = \frac{2 \frac{gZ_B}{\rho S_v} A - 2w_*^3 + 2.5u_*^3 + 0.001 |\Delta v|^3 - 2\delta_0 z_B}{2 \frac{gZ_B}{S_v} B + 1.85w_*^2 + 8.92u_*^2} \quad (8.24)$$

Currently the terms proportional to  $|\Delta v|^3$  and the background dissipation are dropped, because both terms still include some numerical uncertainties.

Turbulent fluxes at the surface are given by the bulk method based on similarity theory of turbulence in the surface layer. Many workers (Businger *et al.*, 1971; Yamada, 1976, *etc.*) have now shown that the bulk method is extended to include outer boundary layer. In the latter bulk method, the surface fluxes may be written,

$$\begin{aligned} (F_s)_s &= \bar{\rho} |\mathbf{v}_m| C_H C_D (s_g - s_m) \\ (F_q)_s &= \beta \bar{\rho} |\mathbf{v}_m| C_H C_D (q_g^* - q_{wm}) \\ |\tau_s| &= \bar{\rho} C_D^2 |\mathbf{v}_m|^2 = \bar{\rho} u_*^2 \end{aligned} \quad (8.25)$$

$s_g$  is the dry static energy of the earth's surface,  $\beta$  is an efficiency factor of evaporation and is a function of ground wetness (see Chapter 10),  $C_H$  and  $C_D$  are transfer coefficients of heat and momentum.  $s_m$  and  $q_{wm}$  are the representative values of  $s$  and  $q_w$  within the PBL, and not the values at the surface. As for  $C_H$  and  $C_D$ , Deardorff's value (1972) shown in Fig. 8.3 is adopted. They depend both on the bulk Richardson's number  $Ri_B$  and the depth of the PBL normalized by the surface roughness length  $z_0$  (see (10.1)).  $Ri_B$  is given by

$$Ri_B = - \frac{gZ_B (s_{vg} - s_{vm})_e}{c_p T_s |\mathbf{v}_m|^2} \quad (8.26)$$

$(s_{vg} - s_{vm})_e$  indicates effective difference of virtual static energy to estimate buoyancy flux

$$F_{S_v} = \begin{cases} F_s + \epsilon L (0.61 F_q - F_l) & : \text{outside clouds} \\ (1 + \gamma) \alpha F_s - \epsilon L F_{q_w} & : \text{within clouds} \end{cases} \quad (8.27)$$

and is given by

$$(s_{vg} - s_{vm})_e = \begin{cases} (s_g - s_m) + 0.61 \epsilon \beta L (q_g^* - q_{wm}) & : \text{outside clouds} \\ (1 + \gamma) (s_g - s_m) - \epsilon \beta L (q_g^* - q_{wm}) & : \text{inside clouds} \end{cases} \quad (8.28)$$

When the depth of the PBL increases, there may be more than one GCM layers in the

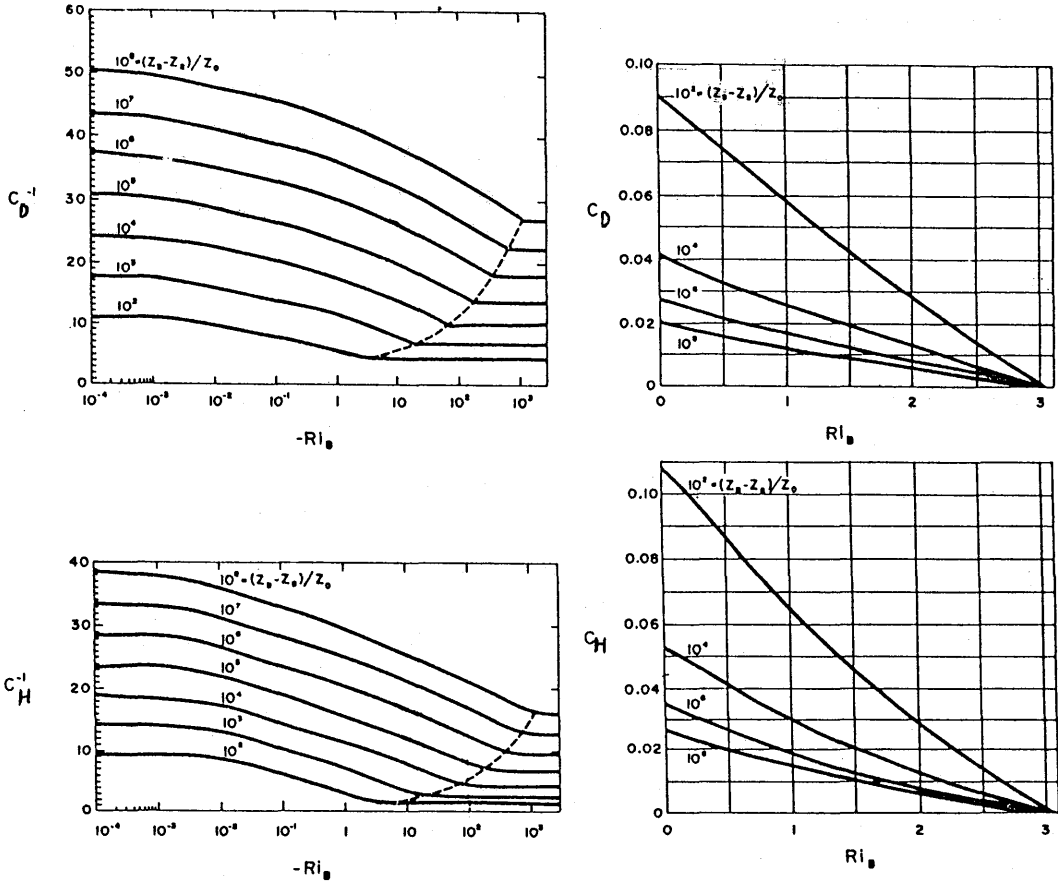


Fig. 8.3 Transfer coefficients  $C_D$  and  $C_H$  currently adopted. (Deardorff, 1972) Abscissa is the bulk Richardson number given by (8.26). Parameters are the depth of the PBL normalized with roughness length  $z_0$ .

PBL. In order to assure the fluxes of  $h$ ,  $q_w$  and  $v$  to be in the down-gradient direction, additional fluxes are added besides the linear vertical profile terms, *i. e.*,

$$\begin{aligned}
 F_h &= (F_h)_B + ((F_h)_s - (F_h)_B) \cdot \frac{\sigma - \sigma_B}{\delta \sigma_m} + K \frac{(\sigma - \sigma_B)(1 - \sigma)}{\delta \sigma_m^2} \frac{\partial h}{\partial p} \\
 F_{q_w} &= (F_{q_w})_B + ((F_{q_w})_s - (F_{q_w})_B) \cdot \frac{\sigma - \sigma_B}{\delta \sigma_m} + K \frac{(\sigma - \sigma_B)(1 - \sigma)}{\delta \sigma_m^2} \frac{\partial q_w}{\partial p} \\
 F_v &= (F_v)_B + ((F_v)_s - (F_v)_B) \cdot \frac{\sigma - \sigma_B}{\delta \sigma_m} + K_m \frac{(\sigma - \sigma_B)(1 - \sigma)}{\delta \sigma_m^2} \frac{\partial v}{\partial p}
 \end{aligned}
 \tag{8.29}$$

$K = K_m = 18 \text{ kg}^2 \text{ m}^{-3} \text{ s}^{-3}$  is currently adopted.

### 8.4 Stratus layer

We describe here a diagnostic determination of the stratus layer and its stability. Vertical profiles of the mixing ratio of total water substance  $q_w$  is determined in a similar manner as is described in 8.5. At first, saturation condition is checked at  $\sigma = \sigma_B$ . If  $q_w(\sigma_B) > q^*(\sigma_B, T_B)$ , then stratus is assumed within the PBL. The mixing ratio of liquid water at  $\sigma = \sigma_B$ ,  $l_B$ , is then determined. Secondly, the cloud base is determined based on the known distribution of  $T(\sigma)$  and  $q_w(\sigma)$ .

When the PBL is capped with stratus, the stability of the stratus layer against the entrainment should be checked, because very dry air parcel entrained from above into the stratus may suffer negative buoyancy due to cooling and moistening through evaporation from the stratus.

When the PBL is cloud-free, the buoyancy gap at the top of the PBL,  $\Delta s_v$ , and the buoyancy flux there are

$$\Delta s_v = \Delta h - (1 - 0.61\epsilon)L\Delta q_w \quad (8.30)$$

$$(F_{s_v})_B = -E\Delta s_v \quad (8.31)$$

If  $\Delta s_v$  is negative,  $(F_{s_v})_B$  is positive and the rapid growth of the PBL depth may result. If  $\Delta s_v < 0$  happens in the model, the PBL is renewed, currently, to the shallowest possible condition with no gaps in physical variables at its top. 5mb is assigned as the shallowest possible depth of the PBL.

For a cloud-topped PBL, the stability condition becomes complicated because the evaporation of cloud must be considered in the stability analysis.  $\Delta s_v$  and  $(F_{s_v})_B$  in a cloud-topped case are

$$\Delta s_v = \Delta h - (1 - 1.61\epsilon)L\Delta q - \epsilon L\Delta q_w \quad (8.32)$$

$$(F_{s_v})_B = \alpha(F_h)_B - \epsilon L(F_{q_w})_B = -E(\alpha\Delta h - \epsilon L\Delta q_w) + \alpha\Delta R \quad (8.33)$$

where use has been made of (8.6) and (8.7). (8.33) is transformed into

$$\left. \begin{aligned} (F_{s_v})_B &= -E(\Delta s_v - (\Delta s_v)_{crit}) + \alpha\Delta R \\ (\Delta s_v)_{crit} &= \frac{1 - 1.61\epsilon}{1 + \gamma} L \cdot (q_{B^*}^* - q_{B^*}) \end{aligned} \right\} \quad (8.33)^*$$

where use has been made of the relation

$$L\Delta q = L\Delta q^* - L(q_{B^*}^* - q_{B^*}) = \frac{1}{1 + \gamma} [\gamma\Delta h - L(q_{B^*}^* - q_{B^*})]$$

(8.33)\* shows that  $(\Delta s_v)_{crit}$  is positive and is a measure of the relative humidity of the air

above the stratus layer. When  $\Delta s_v < (\Delta s_v)_{crit}$ , entrainment tends to make  $(F_{s_v})_B$  positive. This helps to supply turbulent energy to the entrained air, causing large entrainment, rapid vertical mixing and evaporation of the layer cloud. This type of stability was pointed out first by Arakawa (1975) as the cause of transition from the stratus regime into the cumulus regime, and the criterion explained above was derived by Randall (1980) and Deardorff (1980). Currently, when  $\Delta s_v < (\Delta s_v)_{crit}$  occurs in the model, the PBL is renewed to the shallowest possible condition with no gaps in physical variables at its top.

$\Delta R$  is a gap in the net upward radiative flux at the PBL top. When cloud is free,  $\Delta R = 0$ . While stratus clouds occupy the upper portion of the PBL,

$$\Delta R = 55 \cdot \text{Min} (1., \delta p_{stratus}/12.5) \text{ (W/m}^2\text{)}$$

is assumed.  $\delta p_{stratus}$  is the depth of the stratus layer in mb.

### 8.5 Vertical structure of the PBL model and the interpolation scheme

Fig. 8.4 illustrates the vertical structure of the discrete model. Let KB be the vertical index of the GCM layer which contains the PBL top at each grid point, at each time step. The layer KB is divided into two sublayers; layer P lies between  $\sigma = \sigma_B$  and  $\sigma = \sigma_{KB+1}$ , while layer E lies between  $\sigma = \sigma_{KB-1}$  and  $\sigma = \sigma_B$ . The depths of these layers are  $\delta\sigma_p$  and  $\delta\sigma_E$ , respectively.

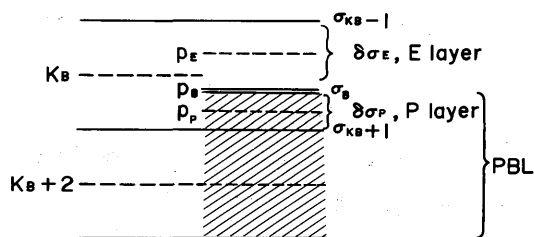


Fig. 8.4 Vertical indices related to the PBL.

Let  $\psi$  be  $u, v, T$  or  $q_w$ . We define  $\psi_k$  ( $k$ : odd),  $\psi_p$  and  $\psi_E$  as;

$$\psi_k = \frac{1}{\delta\sigma_k} \int_{\sigma_{k-1}}^{\sigma_{k+1}} \psi d\sigma, \quad \psi_p = \frac{1}{\delta\sigma_p} \int_{\sigma_B}^{\sigma_{KB+1}} \psi d\sigma, \quad \psi_E = \frac{1}{\delta\sigma_E} \int_{\sigma_{KB-1}}^{\sigma_B} \psi d\sigma \quad (8.34)$$

Then it follows that

$$\delta\sigma_{KB} \psi_{KB} = \delta\sigma_E \psi_E + \delta\sigma_p \psi_p \quad (8.35)$$

and

$$\delta\sigma_m \psi_m = \delta\sigma_p \psi_p + \sum_{k=KB+2}^K \delta\sigma_k \psi_k \quad (8.36)$$

$\psi_E, \psi_p$  and  $\psi_{KB}$  may be significantly different from each other as  $\Delta\psi$  is not equal to zero in general. There may be three candidates for a prognostic variable of the PBL, *i.e.*,  $\psi_p$  (or  $\psi_E$ ),  $\psi_m$  and  $\Delta\psi$ . However,  $\psi_p$  is not suitable as a direct prognostic variable because the PBL top

may move from one GCM layer to the other from one time to the next. The prediction of  $\psi_m$  might cause numerical troubles in determining  $\psi_p$  when  $\delta\sigma_p \rightarrow 0$  (see (8.36)). Thus we have chosen  $\Delta\psi$  as a prognostic variable.

In the following, we derive a method of determining  $\psi_p$  and  $\psi_E$  from  $\Delta\psi$  and  $\psi_k$ . First we let  $\psi_p$  be

$$\psi_p = I_\Delta \Delta\psi + \sum I_k \psi_k \quad (8.37)$$

(8.37) is transformed, with use of (8.35), into

$$\psi_{B^*} - \psi_B = L_P \psi_p + L_E \psi_E + \sum_{k \neq KB} L_k \psi_k$$

where

$$L_P = -\frac{1}{I_\Delta} [I_{KB}(1 - \xi) - 1] \quad (8.38)$$

$$L_E = -\frac{1}{I_\Delta} I_{KB} \xi$$

$$L_k = -\frac{I_k}{I_\Delta} \quad (k \neq KB)$$

$$\xi = \delta\sigma_E / \delta\sigma_{KB}$$

In order to determine L, we have to specify extrapolation form for  $\psi_{B^*}$  and  $\psi_B$ . We introduce here a new variable

$$\Psi = \psi p^{-\beta} \quad (8.39)$$

so that the variation of  $\Psi$  with respect to pressure is much less than that of  $\psi$ .  $\Psi_{B^*}$  may be extrapolated as

$$\Psi_{B^*} = \Psi_E + (\Psi_E - \Psi_{KB-2}) \delta\sigma_E / (\delta\sigma_E + \delta\sigma_{KB-2}) \quad (8.40)$$

and  $\psi_{B^*}$  is given by

$$\psi_{B^*} = \{1 + \delta\sigma_E / (\delta\sigma_E + \delta\sigma_{KB-2})\} \left(\frac{P_B}{P_E}\right)^{\beta_{B^*}} \psi_E - \delta\sigma_E / (\delta\sigma_E + \delta\sigma_{KB-2}) \cdot \left(\frac{P_B}{P_E}\right)^{\beta_{B^*}} \psi_{KB-2} \quad (8.41)$$

$\beta_{B^*}$  is determined by

$$\beta_{B^*} = |\tilde{\beta}_{B^*} \cdot \beta_s|^{1/2} \cdot \text{sign}(\tilde{\beta}_{B^*}) \quad (8.42)$$

where

$$\tilde{\beta}_{B^*} = \ln(\psi_{KB-2} / \psi_{KB}) / \ln(P_{KB-2} / P_{KB}) \quad (8.43)$$

and  $\beta_s$  is a standard value currently specified as

$$\beta_s = \begin{cases} 0.16 & \text{for } \psi = T \\ 3.20 & \text{for } \psi = q_w \\ 0.0 & \text{for } \psi = u \text{ or } v \end{cases} \quad (8.44)$$

sign ( $\beta_{B^*}$ ) is an operation to take the same sign as  $\beta_{B^*}$ .

$\Psi_B$  may be extrapolated as

$$\Psi_B = \Psi_p - \begin{cases} (\Psi_{KB+2} - \Psi_p) \delta\sigma_p / (\delta\sigma_{KB+2} + \delta\sigma_p) & KB < K \\ 0 & KB = K \end{cases} \quad (8.45)$$

thus

$$\psi_B = \begin{cases} [1 + \delta\sigma_p / (\delta\sigma_{KB+2} + \delta\sigma_p)] \left(\frac{P_B}{P_p}\right)^{\beta_n} \psi_p - \delta\sigma_p / (\delta\sigma_{KB+2} + \delta\sigma_p) \cdot \left(\frac{P_B}{P_p}\right)^{\beta_n} \psi_{KB+2} & KB < K \\ \left(\frac{P_B}{P_p}\right)^{\beta_n} \psi_p & KB = K \end{cases} \quad (8.46)$$

When  $KB < K$ ,  $\beta_B$  in (8.46) is determined by (8.42) but with  $\beta_{B^*}$  replaced by

$$\beta_B = \ln(\psi_{KB} / \psi_{KB+2}) / \ln(P_{KB} / P_{KB+2}) \quad (8.47)$$

When  $KB = K$ , and the PBL is thermally stable ( $(F_n)_s < 0$ ), we assume  $\beta_B = \beta_s$ . When  $KB = K$  and  $(F_n)_s > 0$ ,

$$\beta_B = \begin{cases} R/c_p & \text{for } \psi = T, \text{ unsaturated} \\ R/c_p / (1 + \gamma) & \text{for } \psi = T, \text{ saturated} \\ 0 & \text{for } \psi = q, u, v \end{cases} \quad (8.48)$$

The comparison of (8.38) with (8.41) and (8.46) gives us:

$$\left. \begin{aligned} L_E &= \{1 + \delta\sigma_E / (\delta\sigma_E + \delta\sigma_{KB-2})\} \left(\frac{P_B}{P_E}\right)^{\beta_{B^*}} \\ L_{KB-2} &= 1 - L_E \\ L_p &= - \left(\frac{P_B}{P_p}\right)^{\beta_n} - \begin{cases} 0 & KB = K \\ \left(\frac{P_B}{P_p}\right)^{\beta_n} \delta\sigma_p / (\delta\sigma_{KB+2} + \delta\sigma_p) & KB < K \end{cases} \\ L_{KB+2} &= -1 - L_p \end{aligned} \right\} \quad (8.49)$$

As  $I_\Delta$ ,  $I_{KB}$  and  $I_k$  ( $k \neq KB$ ) are

$$\left. \begin{aligned} I_\Delta &= -\xi / (L_E(1 - \xi) - L_p \xi) \\ I_{KB} &= L_E / (L_E(1 - \xi) - L_p \xi) \\ I_k &= \xi L_k / (L_E(1 - \xi) - L_p \xi) \end{aligned} \right\} \quad (8.50)$$

$\psi_p$  is determined with the help of (8.37) and (8.49).  $\psi_E$  is now obtained from (8.41), or

$$\begin{aligned}
 \psi_E &= \varepsilon_\Delta \Delta \psi + \sum \varepsilon_k \psi_k \\
 \text{where} & \\
 \varepsilon_\Delta &= (1 - \xi) / (L_E(1 - \xi) - L_p \xi) \\
 \varepsilon_{kB} &= -L_p / (L_E(1 - \xi) - L_p \xi) \\
 \varepsilon_k &= -L_k(1 - \xi) / (L_E(1 - \xi) - L_p \xi)
 \end{aligned}
 \tag{8.51}$$

## 8.6 Numerical procedures

Numerical procedures of the PBL processes are summarized in this section. The depth of the PBL is predicted with (8.1), where  $E$  is given by (8.24) and  $M_B$  is given by the cumulus model described in Chapter 7. The discretized form of the horizontal mass flux convergence within the PBL is identical to the one described in Chapter 6 (see Eq.(6.29)) with  $q$  replaced by  $\delta\sigma_m$  and with the interpolation (6.30) and (6.31) for  $\hat{q}_{i+1/2,j}$  replaced by

$$(\delta\hat{\sigma}_m)_{i+1/2,j} = \frac{1}{2} [(\delta\sigma_m)_{i+1,j} + (\delta\sigma_m)_{i,j}]
 \tag{8.52}$$

Gaps at the PBL top of temperature, total water substance and momentum are predicted by (8.12), (8.13) and (8.14), respectively. Currently underlined terms in those equations are neglected for simplicity. The time change of the momentum gap is calculated at the  $\pi$ -point where thermodynamic variables are defined (see Fig. 4.1). As  $u$  and  $v$  are defined on the staggered grids, the time change of the momentum gap at the  $u$  and  $v$  points are interpolated simply as

$$\left(\frac{\partial \Delta u}{\partial t}\right)_{i+1/2,j} = \frac{1}{2} \left[ \left(\frac{\partial \Delta u}{\partial t}\right)_{i,j} + \left(\frac{\partial \Delta u}{\partial t}\right)_{i+1,j} \right]$$

$$\left(\frac{\partial \Delta v}{\partial t}\right)_{i,j+1/2} = \frac{1}{2} \left[ \left(\frac{\partial \Delta v}{\partial t}\right)_{i,j} + \left(\frac{\partial \Delta v}{\partial t}\right)_{i,j+1} \right]$$

In evaluating a gap in the vertical gradient of  $\psi$ , *i. e.*,  $\Delta \left(\frac{\partial \psi}{\partial \sigma}\right)$ , the extrapolation scheme introduced in 8.5 is followed, *i. e.*,

$$\Delta \left(\frac{\partial \psi}{\partial \sigma}\right) = \pi \left[ \Delta \left(\frac{\partial \Psi}{\partial p} p^\beta\right) + \frac{1}{p} \Delta(\beta \psi) \right]
 \tag{8.53}$$

where  $\partial \Psi / \partial p$  is given by (8.40) and (8.45).

The vertical gradient of the vertical flux of  $\psi$  at the PBL top, *i. e.*  $(\partial F_\psi / \partial \sigma)_B$  is evaluated by (8.29) where  $\partial \psi / \partial p$  is estimated in the way stated in section 8.5 and the fluxes

both at the surface and the PBL top are determined as described in the last part of this section.

In determining the entrainment rate  $E$ , turbulent flux profiles are required. While, the profiles of the turbulent fluxes depend on  $E$ . Therefore both  $E$  and turbulent flux profiles are determined by iteration. The process is schematically shown in Fig. 8.5. After determining transfer coefficients  $C_D$  and  $C_H$  in terms of  $Ri_b$  and the normalized depth of the PBL, the turbulent fluxes at the surface are given by (8.25). By giving the first guess of turbulent fluxes at the PBL top, the entrainment velocity is determined by (8.24). After this, turbulent fluxes at the PBL top are evaluated with the use of (8.6), (8.7) and (8.10).  $w^*$  defined by (8.22) is calculated with the new profiles of turbulent fluxes given by (8.29). Convergence of the iteration is checked with the value of  $w^*$ . Currently the number of iteration is allowed up to 10.

In the following, numerical procedure of determining turbulent fluxes are given based on backward implicit differencing (Randall, 1976). The need for this is to avoid linear computational instability in the course of rapid growth of gaps. Thermal energy fluxes are given by (8.6), (8.7) and (8.25). The first relation of (8.25) may be rewritten in terms of turbulent energy flux of moist static energy as follows;

$$\begin{aligned} (F_h)_s &= \mu_5 (F_s)_s + \mu_6 L (Fq_w)_s \\ &= \mu_5 V (s_g - s_m) + \mu_6 L \beta V (q_g - q_{wm}) \end{aligned} \tag{8.54}$$

where

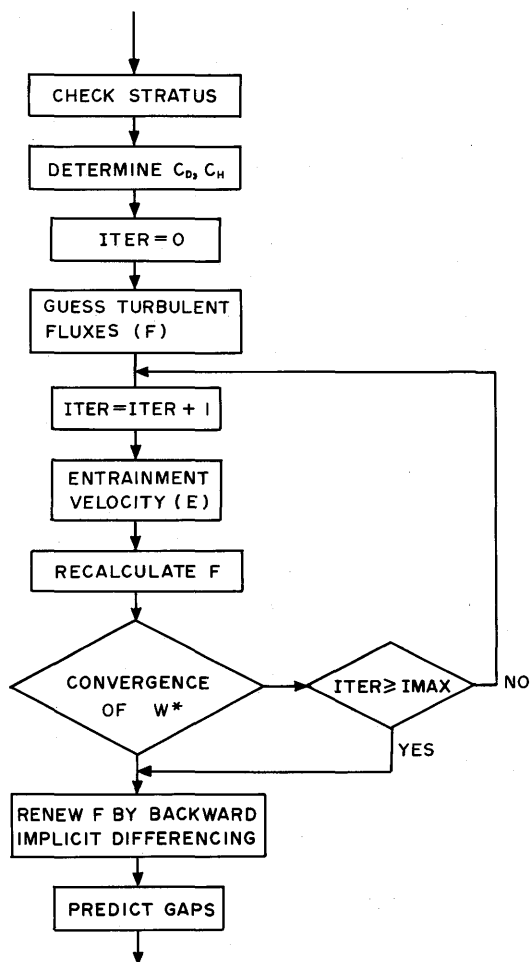


Fig. 8.5 Flow diagram of predicting gaps at the PBL top.

$$\mu_5 = \begin{cases} 1 + \gamma_s & : \text{saturated (fog)} \\ 1 & : \text{otherwise} \end{cases}$$

$$\mu_6 = \begin{cases} 0 & : \text{saturated (fog)} \\ 1 & : \text{otherwise} \end{cases}$$

and  $V = \bar{\rho} |v_m| C_D C_H$ .  $\gamma_s$  is  $\gamma = \frac{L}{c_p} \left( \frac{\partial q^*}{\partial T} \right)_p$  at the surface. Let  $\tau$  be the time step with the time interval  $\Delta t_d$  (see Fig. 5.1). Then (8.54), (8.25), (8.6) and (8.7) may be expressed as follows:

$$(F_h)_s^{\tau+1} = (F_h)_s^\tau + V \{ \mu_5 [c_p (T_g^{\tau+1} - T_g^\tau) - (s_m^{\tau+1} - s_m^\tau)] + \mu_6 \beta L [(q_g^{*\tau+1} - q_g^{*\tau}) - (q_{wm}^{\tau+1} - q_{wm}^\tau)] \} \quad (8.55)$$

$$(F_{qw})_s^{\tau+1} = (F_{qw})_s^\tau + \beta V [(q_g^{*\tau+1} - q_g^{*\tau}) - (q_{wm}^{\tau+1} - q_{wm}^\tau)] \quad (8.56)$$

$$(F_h)_B^{\tau+1} = -E \Delta h^{\tau+1} + \Delta R = (F_h)_B^\tau - E(\Delta h^{\tau+1} - \Delta h^\tau) + (\Delta R^{\tau+1} - \Delta R^\tau) \quad (8.57)$$

$$(F_{qw})_B^{\tau+1} = (F_{qw})_B^\tau - E(\Delta q_w^{\tau+1} - \Delta q_w^\tau) \quad (8.58)$$

(8.55) ~ (8.58) are closed by introducing

$$\begin{aligned} s_m^{\tau+1} - s_m^\tau &= \frac{g \Delta t_d}{\pi (\delta \sigma_m)^{\tau+1}} [(F_s)_s^{\tau+1} - (F_s)_B^{\tau+1}] \\ &= \frac{g \Delta t_d}{\pi (\delta \sigma_m)^{\tau+1}} \left[ \frac{1}{\mu_5} \{ (F_h)_s^{\tau+1} - \mu_6 (F_{qw})_s^{\tau+1} \} - \mu_7 (F_h)_B^{\tau+1} + \mu_8 L (F_{qw})_B^{\tau+1} \right] \end{aligned} \quad (8.59)$$

$$c_p (T_g^{\tau+1} - T_g^\tau) = \frac{c_p \Delta t_d}{C} [- (F_h)_s^{\tau+1} - R_6 - 4\sigma (T_g^\tau)^3 (T_g^{\tau+1} - T_g^\tau) + S_6^\tau + H_1^\tau] \quad (8.60)$$

$$\Delta h^{\tau+1} - \Delta h^\tau = - (h_m^{\tau+1} - h_m^\tau) = - \frac{g \Delta t_d}{\pi (\delta \sigma_m)^{\tau+1}} [(F_h)_s^{\tau+1} - (F_h)_B^{\tau+1}] \quad (8.61)$$

$$\Delta q_w^{\tau+1} - \Delta q_w^\tau = - (q_{wm}^{\tau+1} - q_{wm}^\tau) = - \frac{g \Delta t_d}{\pi (\delta \sigma_m)^{\tau+1}} [(F_{qw})_s^{\tau+1} - (F_{qw})_B^{\tau+1}] \quad (8.62)$$

where

$$\mu_7 = \begin{cases} \frac{1}{1 + \gamma_B} & : \text{saturated (stratus)} \\ 1 & : \text{otherwise} \end{cases}$$

$$\mu_8 = \begin{cases} 0 & : \text{saturated (stratus)} \\ 1 & : \text{otherwise} \end{cases}$$

$\pi\delta\sigma_m$  is the depth of the PBL. (8.60) is derived from (10.10) and (10.11).  $C$  is the bulk heat capacity of the ground surface,  $R_6$  is the net upward flux of terrestrial radiation,  $S_6$  is the solar radiation absorbed at the ground surface, and  $H_1$  is the upward heat conduction within the ground. With the help of (8.59)~(8.62), (8.55)~(8.58) are solved for  $(F_h)_s^{\tau+1}$ ,  $(F_h)_B^{\tau+1}$ ,  $(F_{q_w})_s^{\tau+1}$  and  $(F_{q_w})_B^{\tau+1}$ . These fluxes are used for the prediction of gaps.

Momentum fluxes are renewed in a similar way. From the third equation of (8.25) and (8.10), we get

$$(\mathbf{F}_v)_s^{\tau+1} = (\mathbf{F}_v)_s^{\tau} - \frac{g\Delta t_d}{\pi(\delta\sigma_m)^{\tau+1}} \hat{V} [(\mathbf{F}_v)_s^{\tau+1} - (\mathbf{F}_v)_B^{\tau+1}] \quad (8.63)$$

and

$$(\mathbf{F}_v)_B^{\tau+1} = (\mathbf{F}_v)_B^{\tau} + \frac{g\Delta t_d}{\pi(\delta\sigma_m)^{\tau+1}} E [(\mathbf{F}_v)_s^{\tau+1} - (\mathbf{F}_v)_B^{\tau+1}] \quad (8.64)$$

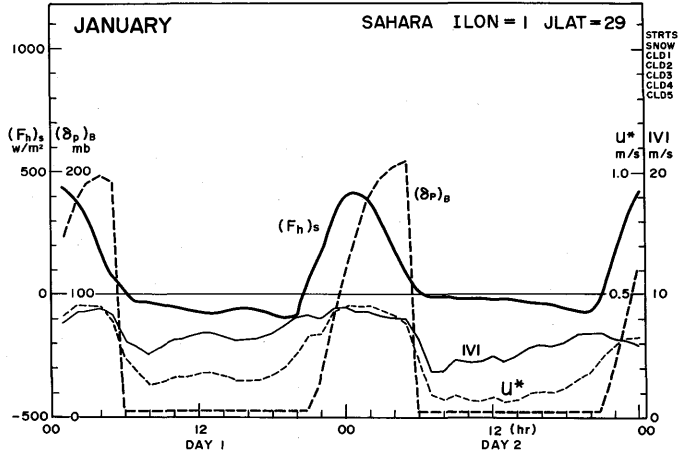
where  $\hat{V} = \bar{\rho} |v_m| C_D^2$ .  $(\mathbf{F}_v)_s^{\tau+1}$  and  $(\mathbf{F}_v)_B^{\tau+1}$  are obtained from (8.63) and (8.64).

### A 8.1 Some examples of the PBL model performance

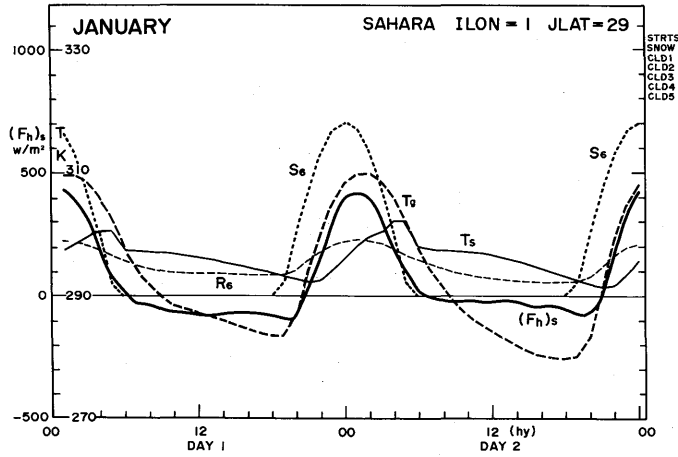
Some examples of time evolutions of the planetary boundary layer are shown in this appendix. All the examples are taken from the January simulation with the 5 layer tropospheric model. Data are sampled at four locations for two days. The locations are:

- (0°, 22°N)···(This point is identified as "Sahara"),
- (45°E, 80°S)···(This point is identified as "Mizuho"),
- (180°, 6°N)···(This point is identified as "Equatorial Pacific"),
- (95°E, 34°N)···(This point is identified as "Himalaya").

Fig. A8.1.1 (a) and (b) show time evolutions of the PBL at Sahara.  $(\delta p)_B$  indicates the depth of the PBL in mb,  $u_*$ ; the friction velocity in m/s,  $|v|$ ; the mean wind speed within the PBL in m/s,  $(F_h)_s$ ; the turbulent moist static energy flux at the surface in W/m<sup>2</sup>,  $T_s$ ; surface air temperature in K,  $T_g$ ; ground surface temperature in K,  $S_6$ ; the net downward flux of the solar radiation at the surface in W/m<sup>2</sup>,  $R_6$ ; the net upward flux of the terrestrial



( a )

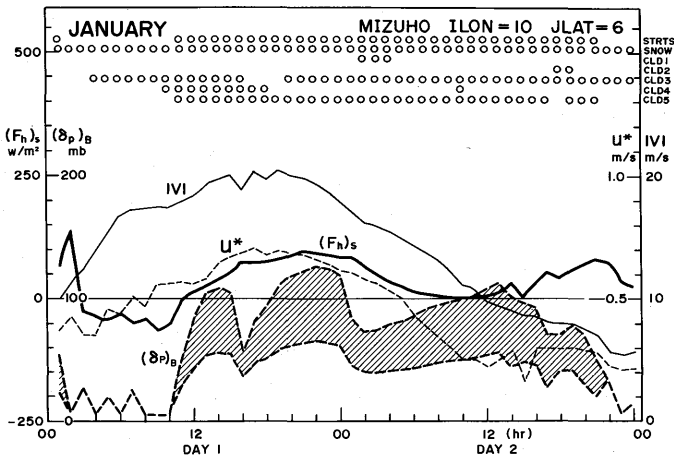


( b )

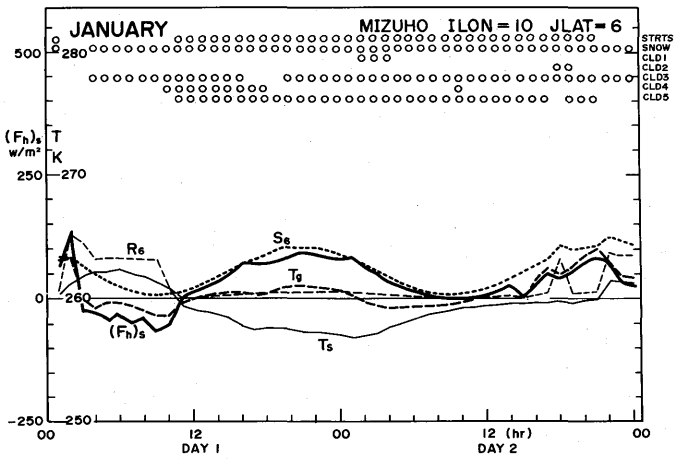
Fig. A8.1.1 Time change of variables related to the PBL at the grid point ( $0^\circ$ ,  $22^\circ\text{N}$ ) identified as "Sahara". Data are taken from a January simulation with 5L-GCM.

(a)  $(\delta p)_s$  is the depth of the PBL in mb ;  $(F_h)_s$ , upward turbulent flux of moist static energy at the surface ;  $u_*$ , friction velocity ;  $|v|$ , mean wind velocity in the PBL.

(b)  $S_s$  is the solar flux absorbed at the surface ;  $R_s$ , the net upward flux of terrestrial radiation at the surface ;  $T_s$ , the surface air temperature ;  $T_g$ , the ground surface temperature.



( a )



( b )

Fig. A8.1.2 Same as in Fig. A8.1.1 but for the grid point (45°E, 80°S) identified as "Mizuho". White circles in the upper part of the figure show the incidence of stratus, snow and large-scale clouds at each level. CLD5, for example, indicates clouds in the lowest (5th) level. Hatched area show the stratus layer.

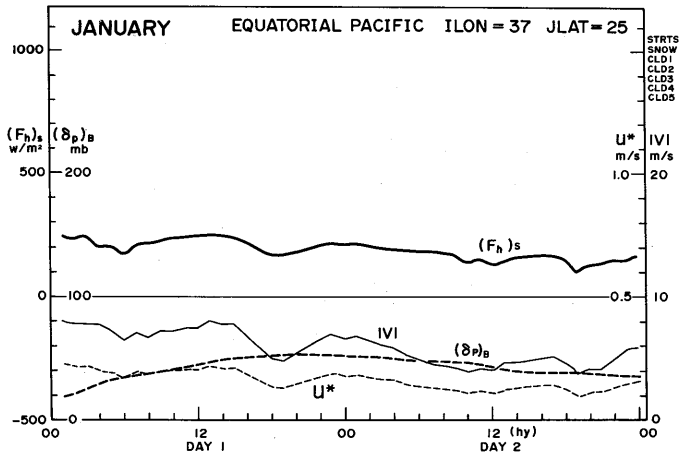
radiation at the surface in  $W/m^2$ . A simple diurnal variation is seen in every field in Fig. A8.1.1. About 2 hours after sunrise,  $(F_h)_s$  changes its sign from negative to positive. The rapid deepening of the PBL immediately follows the change. There is a sudden decrease of the PBL depth at the sunset. This is caused by the change of the sign of  $A$  in (8.19). It is interesting to note that the maximum  $T_s$  occurs immediately before the sunset at this point.

Mizuho point is located in the Antarctica. The elevation is 1840m and the surface is covered with snow. Fig. A8.1.2 (a) and (b) show the time evolutions. Notations are the same as those used in Fig. A8.1.1. At the third (middle) and the fifth (lowest) levels exist clouds due to large scale condensation (see Chapter 9 and 13) most of the time. We can confirm that the increase in the net upward flux of the terrestrial radiation at the surface closely follows the disappearance of the lowest cloud. Around  $t=10hr$  of the first day, the surface air temperature starts to decrease probably due to large scale advection. The depth of the PBL starts to increase with the decrease of  $T_s$ , and the stratus is diagnosed within the PBL. Towards the end of the second day, the PBL depth decreases with the increase of  $T_s$ .

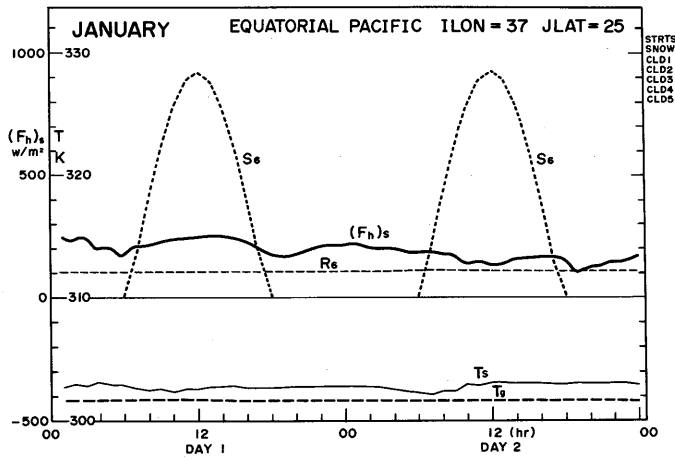
Fig. A8.1.3 (a) and (b) show the evolution at Equatorial Pacific. As the sea surface temperature ( $T_g$ ) is almost constant and as no clouds appear during this period,  $R_e$  is almost constant. It is commented that the variations of  $R_e$  and  $S_e$  do not directly influence the PBL over the ocean, because the sea surface temperature is given as external data in the present model. Roughly constant  $(F_h)_s$  maintains the quasi-steady PBL. The positive  $(F_h)_s$  is exclusively due to the upward water vapor flux as  $T_g$  is less than  $T_s$ .

Fig. A8.1.4 (a) and (b) show the PBL evolution at Himalaya. This point is characterized with the high elevation (4329m). The surface is covered with snow. Therefore the maximum  $S_e$  is only as much as  $100 W/m^2$ .  $R_e$  exceeds  $S_e$  even during the daytime on the first day. The energy loss of the ground surface through radiation is compensated by negative  $(F_h)_s$ . Although friction velocity is relatively large, probably reflecting the high elevation, it is not enough to maintain thick PBL. During the last 9 hours of this period, the lowest level is covered with cloud. Corresponding to this change,  $R_e$  decreases and changes its sign. There is also a net downward flux of solar radiation. Thus a rapid increase of the ground surface temperature occurs, causing the sign change of  $(F_h)_s$ .

Fig. A8.1.5 and A8.1.6 show global distributions of the PBL depth and the stratus incidence averaged over July. Shaded area in Fig. A8.1.5 shows the area where the depth is over 150 mb. Deep PBL exists over oceans, especially in the southern hemisphere around  $30^\circ S-60^\circ S$  zone. It is difficult to verify present results against observations. Global features are

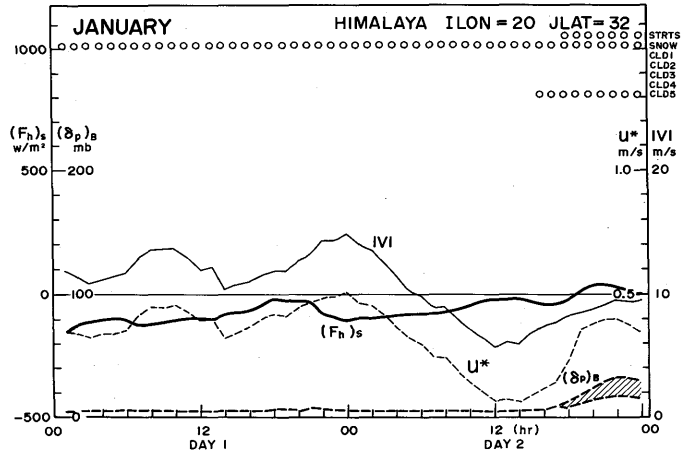


( a )

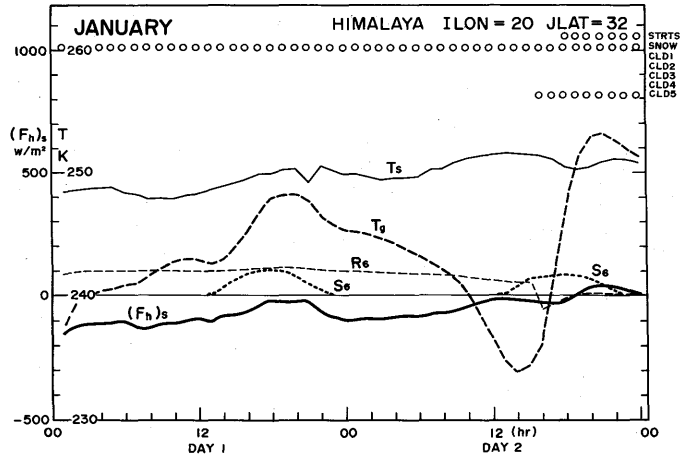


( b )

Fig. A8.1.3 Same as in Fig. A8.1.1 but for the grid point (180°, 6°N) identified as "Equatorial Pacific".



(a)



(b)

Fig. A8.1.4 Same as in Fig. A8.1.1 and Fig. A8.1.2 but for the grid point (95°E, 34° N) identified as "Himalaya".

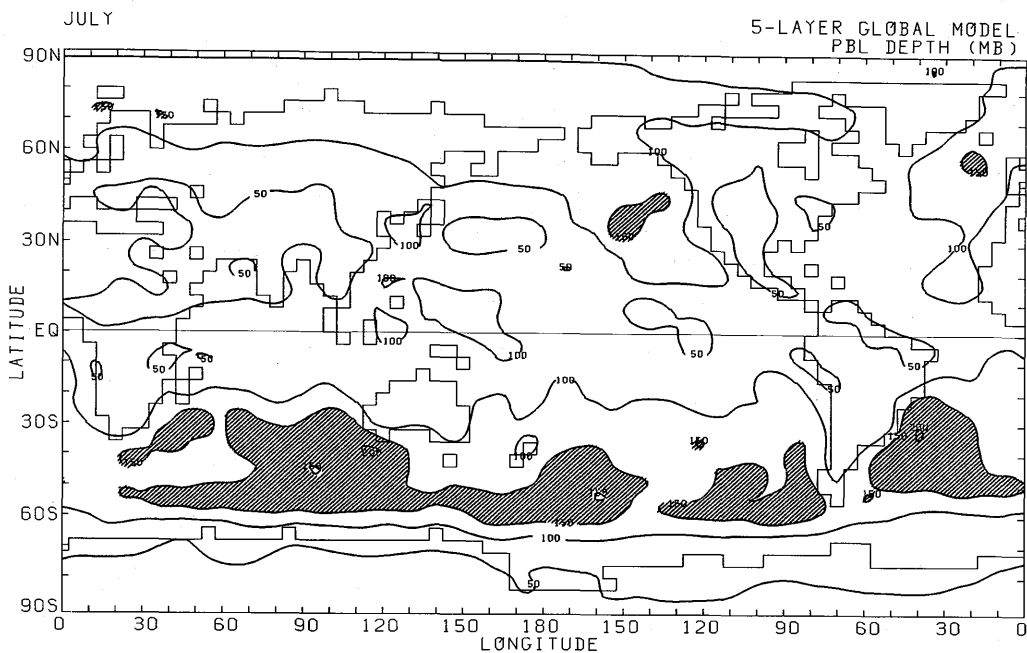


Fig. A8.1.5 : Global distribution of monthly mean depth of the PBL for July (unit: mb). The area where the depth is over 150mb is shaded.

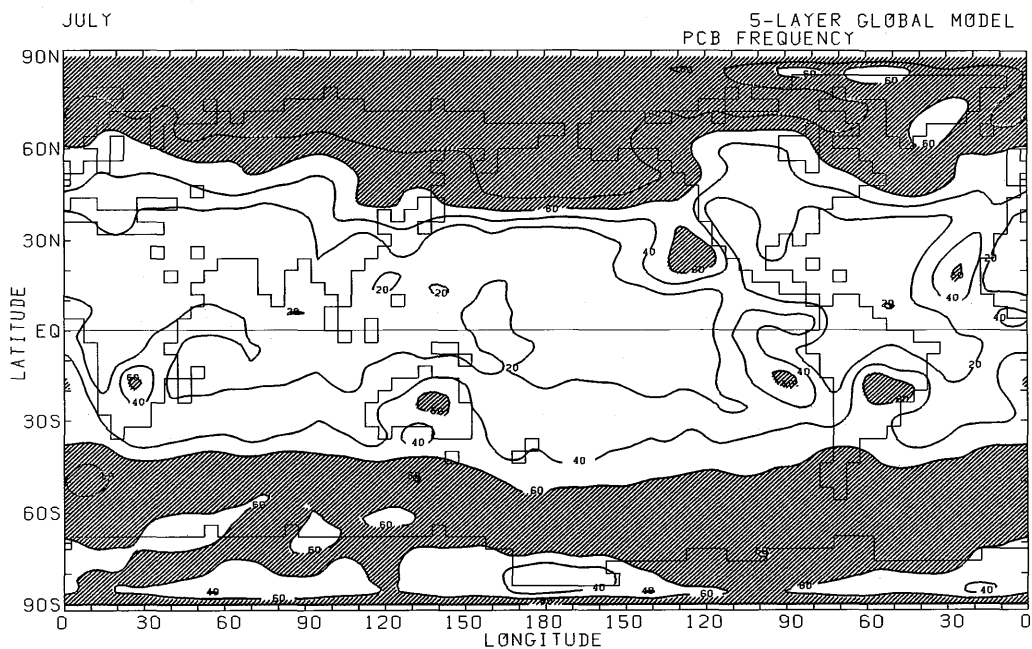


Fig. A8.1.6 : Global distribution of monthly mean stratus incidence for July in %. The area over 60% is shaded.

similar to the simulated results by Suarez, Arakawa and Randall (1983), although the PBL depth of the present model is almost twice as thick as that reported by Suarez *et al.*(1983).

Frequency of stratus incidence shown in Fig. A8.1.6 is high off the west coast of North America, South America, South Africa and North Africa. Shades indicate the area where stratus occurs with the chance of 60% or more. Stratus incidence is also high over the Arctic Ocean as well as over the Antarctic Ocean. These areas correspond to the observed maxima of stratocumulus clouds, although further qualitative comparison has not been made. High stratus incidence over southern Africa has no counterpart in the observation. It is mentioned that this high incidence has a close connection to the wet ground surface condition there.

## 9. Convective adjustment and condensation\*

Latent heat is released within the model atmosphere in three different ways. They are (1) precipitation due to large-scale condensation, (2) cumulus precipitation and (3) middle level convective precipitation. Description about the second process is given in Chapter 7. The remaining two are described in this chapter.

In the model, adjustment processes are taken into consideration in the following order. First, dry convective adjustment; second, moist convective adjustment (except for penetrative cumulus convection); third, large-scale condensation; and finally, penetrative cumulus convection. The flow diagram is shown in Fig. 9.1. In their definitions, "penetrative cumulus convection" means a convection which has its origin in the planetary boundary layer (PBL); "middle level convection", a convection which has its origin in the free atmosphere. "Large-scale condensation" means the condensation associated with a supersaturation at the grid point. "Dry convective adjustment" occurs when the air becomes unstable dry statically. This

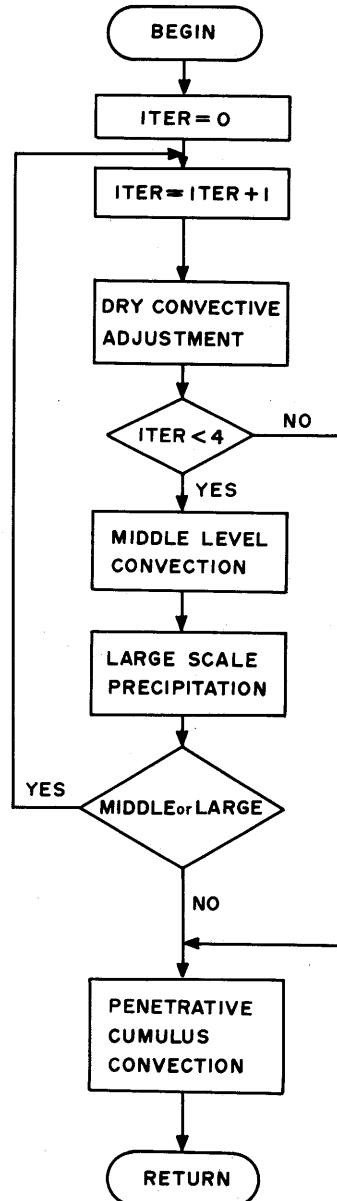


Fig. 9.1 Flow diagram of convective adjustment.

\* This chapter is prepared by A. Kitoh: Forecast Research Division

process does not accompany any condensation.

### 9.1 Some definitions of variables

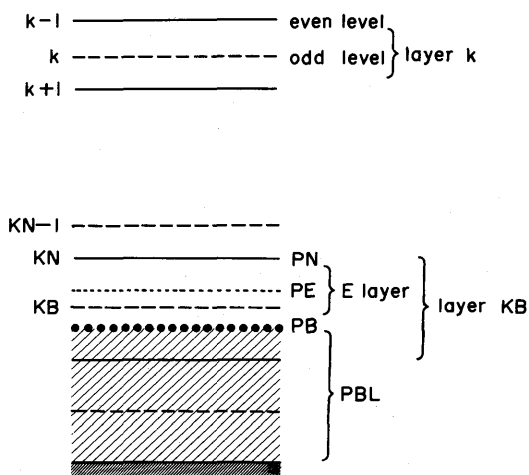


Fig. 9.2 Vertical indices.

The definition of vertical layers in this chapter is found in Fig. 9.2.  $T$ ,  $q$  and  $z$  are temperature, the water vapor mixing ratio, and the geopotential height. We define the following environmental variables at level  $k$ :

Dry static energy

$$s_k = c_p T_k + gz_k; \quad (9.1)$$

Moist static energy

$$h_k = s_k + Lq_k; \quad (9.2)$$

Saturation moist static energy

$$h_k^* = s_k + Lq_k^*; \quad (9.3)$$

Cloud dry static energy at the

vanishing buoyancy level

$$\hat{s}_k = s_k - \frac{L \epsilon_k \delta}{1 + \gamma_k \epsilon_k \delta} (q_k^* - q_k); \quad (9.4)$$

Cloud moist static energy at the vanishing buoyancy level

$$\hat{h}_k = h_k - \frac{(1 + \gamma_k) L \epsilon_k \delta}{1 + \gamma_k \epsilon_k \delta} (q_k^* - q_k), \quad (9.5)$$

$c_p$  is the specific heat at constant pressure,  $g$  is the acceleration of gravity,  $L$  is the latent heat of condensation,  $*$  is the saturated value,  $\hat{\phantom{x}}$  is the even level value,  $\gamma = \frac{L}{c_p} \left( \frac{\partial q^*}{\partial T} \right)$ ,  $\epsilon = \frac{c_p T}{L}$  and  $\delta = 0.609$ .

The saturation mixing ratio is given by

$$q^*(T) = \frac{M_w}{M_d} \cdot \frac{e_s(T)}{p - e_s(T)}, \quad (9.6)$$

where  $M_w$  and  $M_d$  are the mean molecular weight of water vapor and dry air, respectively ( $M_w/M_d = 0.622$ ), and  $p$  is the pressure. The saturation vapor pressure  $e_s$  is given by Tetens equation

$$e_s(T) = e_0 10^{\frac{at}{b+t}}, \quad (9.7)$$

where  $t = T - 273.1$  is the temperature in Celsius,  $a = 7.5$ ,  $b = 237.3$ , and  $e_0 (= 6.11 \text{ mb})$  is the vapor pressure at  $T = 273.1 \text{ K}$ . The saturation mixing ratio gradient is given by

$$\left(\frac{\partial q^*}{\partial T}\right)_{T=T_v} = B_e \frac{q^*(T_v)}{T_v^2}, \tag{9.8}$$

using the another approximate relation

$$e_s(T) = e_1 \exp(A_e - B_e/T), \tag{9.9}$$

where  $e_1 = 1 \text{ mb}$ ,  $A_e = 21.656$ , and  $B_e = 5417.98 \text{ K}$ .

We define E-layer as the layer located between the top of the PBL and the upper boundary of the layer KB. We define  $s$  and  $h$  in the E-layer as  $s_E$  and  $h_E$  in the same manner.

### 9.2 Dry convective adjustment

If the model atmosphere is found to be dry-adiabatically unstable after the advective process, *i.e.*,

$$\theta_k < \theta_{k+2} \text{ for any odd } k, \tag{9.10}$$

subgrid scale dry convection is assumed to occur, bringing the layer back to a dry adiabatic lapse rate. This adjustment is done between adjacent two layers in the order of increasing  $k$ . If the condition (9.10) is satisfied in more than two layers in contact, we adjust those layers collectively. See Fig. 9.3.

In adjusting layers from  $k = \text{KBEGIN}$  to  $k = \text{KEND}$ , the new temperatures  $T'_k$  are determined in the following way:

$$\sum_{k=\text{KBEGIN}}^{\text{KEND}} T'_k \Pi_k \Delta \sigma_k = \sum_{k=\text{KBEGIN}}^{\text{KEND}} T_k \Pi_k \Delta \sigma_k, \tag{9.11}$$

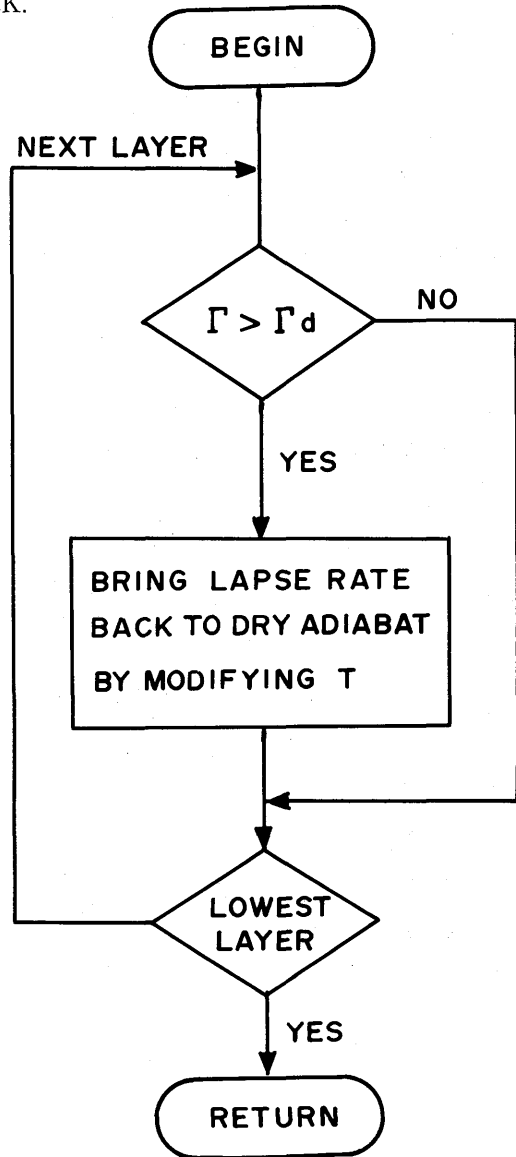


Fig. 9.3 Flow diagram of dry convective adjustment.

$$\theta'_{KBEGIN} = \theta'_{KBEGIN+2} = \dots = \theta'_{KEND}, \tag{9.12}$$

where  $\Sigma'$  is the summation over odd k's only. Primed variables indicate those after adjustment. Using the definition of  $\theta_k$ ,

$$\theta_k = T_k (p_k)^{-\kappa} \tag{9.13}$$

, (9.11) and (9.12), adjusted potential temperature  $\theta_{new}$  is given by

$$\theta_{new} = \frac{\sum_{k=KBEGIN}^{KEND} T_k \Pi_k \Delta \sigma_k}{\sum_{k=KBEGIN}^{KEND} (p_k)^{\kappa} \Pi_k \Delta \sigma_k} \tag{9.14}$$

Then,

$$T'_k = \theta_{new} (p_k)^{\kappa} \text{ for } KBEGIN \leq k \leq KEND. \tag{9.15}$$

### 9.3 Middle level convection

In this section moist convective adjustment which has a root in the free atmosphere is treated. The flow chart is shown in Fig. 9.4. The moist convective adjustment occurs whenever either

$$h_{k+2} > \hat{h}_k^*, \tag{9.16}$$

for any odd k ( $\leq K-2$ ) or

$$h_E > \hat{h}_{KN-1}^*. \tag{9.17}$$

The moist static energy of a saturated non-buoyant air parcel is given by

$$\hat{h}_k^* = h_k^* - \frac{(1 + \gamma_k) L \epsilon_k \delta}{1 + \gamma_k \epsilon_k \delta} (q_k^* - q_k). \tag{9.18}$$

If  $h_{k+2} > \hat{h}_k^*$ , an air parcel rising from the lower level will have positive buoyancy at the upper level k. At present we

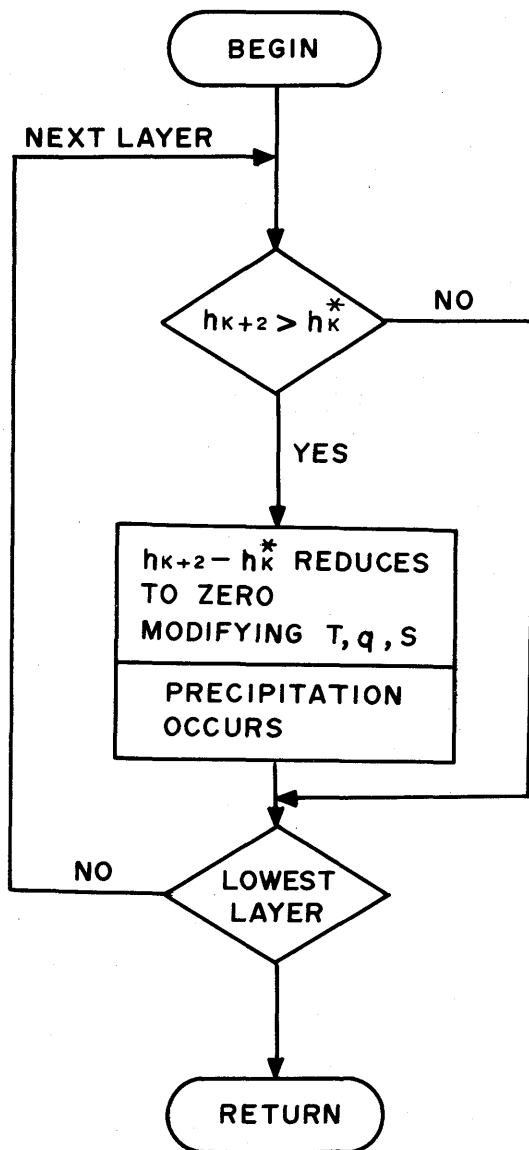


Fig. 9.4 Flow diagram of middle level convection.

approximate  $\hat{h}_k^*$  by  $h_k^*$ , so when  $h_k^* < h_{k+2}$  for any odd  $k$  ( $\leq K-2$ ), we assume that moist convection occurs in such a way as to reduce  $h_{k+2} - h_k^*$  to zero.

The mixing ratio of cloud air which detrains at the upper level is given by

$$(q_c)_k = q_k^* + \frac{\gamma_k}{1 + \gamma_k} \cdot \frac{1}{L} (h_{k+2} - h_k^*) \quad (9.19)$$

If  $(q_c)_k > q_{k+2}$ , we adjust  $(q_c)_k$  to  $q_{k+2}$ .

The moisture budget for the two layers are

$$\frac{\Delta p_k}{g} \frac{\partial q_k}{\partial t} = \eta [(q_c)_k - q_{k+1}], \quad (9.20)$$

$$\frac{\Delta p_{k+2}}{g} \frac{\partial q_{k+2}}{\partial t} = \eta (q_{k+1} - q_{k+2}), \quad (9.21)$$

where  $\eta$  is the mass flux at level  $k+1$ .

The dry static energy budget for the two layers are

$$\frac{\Delta p_k}{g} \frac{\partial s_k}{\partial t} = \eta \left[ \frac{1}{1 + \gamma_k} (h_{k+2} - h_k^*) + s_k - s_{k+1} \right], \quad (9.22)$$

$$\frac{\Delta p_{k+2}}{g} \frac{\partial s_{k+2}}{\partial t} = \eta (s_{k+1} - s_{k+2}). \quad (9.23)$$

The first term on the right hand side of eq. (9.22) represents the detrainment of cloud air into the layer; the second term represents adiabatic warming due to the subsidence in the environment. At present we assume that the temperature change does not exceed 1.5 K per step.

From (9.21) and (9.23), we obtain

$$\frac{\Delta p_{k+2}}{g} \frac{\partial h_{k+2}}{\partial t} = \eta (h_{k+1} - h_{k+2}), \quad (9.24)$$

and from (9.22)

$$\frac{\Delta p_k}{g} \frac{\partial h_k^*}{\partial t} = \eta [h_{k+2} - h_k^* + (1 + \gamma_k) (s_k - s_{k+1})], \quad (9.25)$$

with the aid of

$$\frac{\partial h_k^*}{\partial t} = (1 + \gamma_k) \frac{\partial s_k}{\partial t}. \quad (9.26)$$

From (9.24) and (9.25),

$$\frac{\partial}{\partial t} (h_{k+2} - h_k^*) = \eta g \left[ \frac{1}{\Delta p_{k+2}} (h_{k+1} - h_{k+2}) - \frac{1}{\Delta p_k} \{ (h_{k+2} - h_k^*) + (1 + \gamma_k) (s_k - s_{k+1}) \} \right].$$

(9.27)

If we assume an adjustment time  $\tau$ , mass flux becomes

$$\eta = \frac{1}{\tau g} \frac{h_{k+2} - h_k^*}{\frac{1}{\Delta p_{k+2}}(h_{k+1} - h_{k+2}) + \frac{1}{\Delta p_k} \{ (h_{k+2} - h_k^*) + (1 + \gamma_k)(s_k - s_{k+1}) \}} \quad (9.28)$$

Currently we use  $\tau = \Delta t_d = 60$  minutes. Finally from (9.20) and (9.21), precipitation due to middle level convection is given by

$$P_{ML} = \eta (q_{k+2} - (q_c)_k) \Delta t_d \quad (9.29)$$

### 9.4 Large-scale condensation

Large-scale condensation occurs if the grid cell is supersaturated, *i.e.*,  $q_k$  is greater than  $q_k^*$  where  $q_k$  is the water vapor mixing ratio and  $q_k^*$  is the saturation mixing ratio at the temperature  $T_k$  and the pressure  $p_k$  (Fig. 9.5).

This condensation removes moisture from the atmosphere and warms the atmosphere by releasing latent heat, with the warming in turn modifying the saturation mixing ratio. The condensation proceeds until  $q_k = q_k^*(T_k)$  at the new temperature. When condensation occurs in a layer which is not the lowermost layer of the model, the condensed water is brought into the next lower layer, and is forced to evaporate. This process is repeated until the lowest layer is reached. When the lowest layer is saturated, the condensed water precipitates onto the ground either as rain or snow according to the surface air temperature.

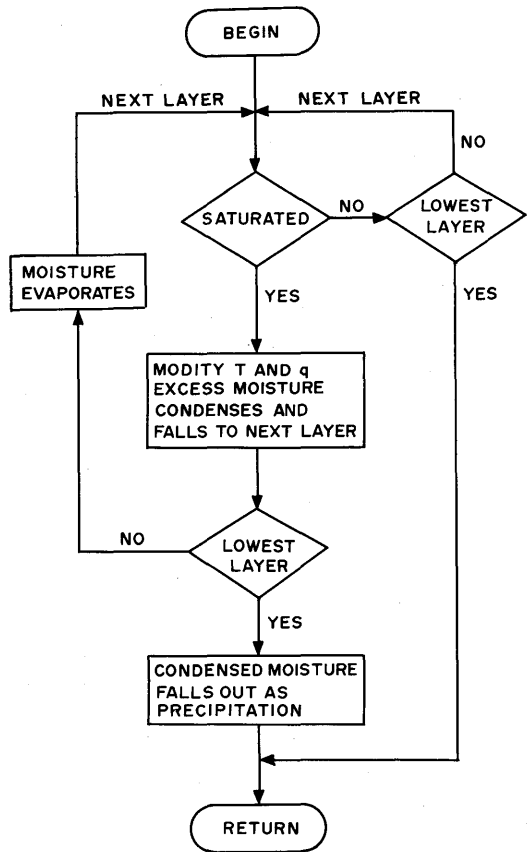


Fig. 9.5 Flow diagram of large-scale condensation.

Let  $C\Delta t$  denote the amount of condensation at level  $k$  per unit mass of dry air, when  $q_k > q_k^*$ . Then

$$q'_k = q_k - C\Delta t \tag{9.30}$$

$$T'_k = T_k + \frac{L}{c_p} C\Delta t, \tag{9.31}$$

$$q'_k = q^*(T = T'_k, p = p_k). \tag{9.32}$$

where the primes denote the modified values due to condensation. (9.32) describes the saturation condition for the modified moisture and temperature. From these three equations, we may obtain an equation for the modified temperatures;

$$q_k - \frac{c_p}{L}(T'_k - T_k) = q^*(T = T'_k, p = p_k). \tag{9.33}$$

With  $q_k, T_k, p_k$  and the functional form of  $q^*(T, p)$  given, the transcendental equation (9.33) can be solved iteratively for  $T'_k$  by Newton's method. After  $T'_k$  is obtained, we can calculate  $C\Delta t$  and  $q'_k$  from (9.30) and (9.31).

Fig. 9.6 schematically shows that the saturation mixing ratio  $q^*$  as a function of temperature denoted by

$$q = q^*(T) \tag{9.34}$$

and also a segment of the line,

$$q = q_0 - \frac{c_p}{L}(T - T_0) \tag{9.35}$$

which passes the point  $A_0(T_0, q_0)$  in the  $(T, p)$  plane. The intersection of the saturation curve,  $q = q^*(T)$ , and the line given by (9.35) gives the solution of (9.33). This point is denoted by  $A(T'_k, q'_k)$  in the figure.

We may obtain the intersection point approximately by the iterative method. Let  $A_1, A_2, \dots$  be a sequence of points whose coordinates in the  $(T, q)$  plane are, respectively,  $(T_1, q_1), (T_2, q_2), \dots$ . Such a sequence can be generated by the use of tangential lines to the saturation curve at  $T_\nu$ , for  $\nu = 0, 1, 2, \dots$ ,

$$q = q^*(T_\nu) + \left(\frac{\partial q^*}{\partial T}\right)_{T=T_\nu}(T - T_\nu). \tag{9.36}$$

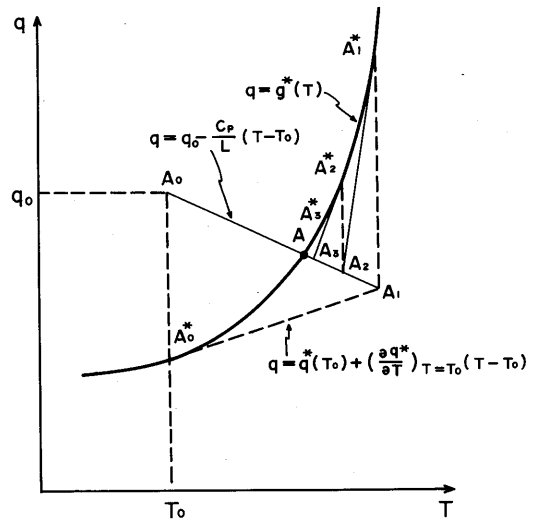


Fig. 9.6 Schematical explanation of adjustment in large-scale condensation.

Choosing

$$T_0 = T_k \text{ and } q_0 = q_k, (\nu = 0), \quad (9.37)$$

we determine  $(T_{\nu+1}, q_{\nu+1})$  recursively by

$$q_{\nu+1} = q^*(T_\nu) + \left(\frac{\partial q^*}{\partial T}\right)_{T=T_\nu} (T_{\nu+1} - T_\nu), \quad (9.38)$$

$$q_{\nu+1} = q_\nu - \frac{C_p}{L} (T_{\nu+1} - T_\nu), \quad (9.39)$$

for  $\nu \geq 0$ . From the slope of the saturation curve, we see that the point  $A_\nu$  uniformly approaches  $A$  as  $\nu$  increases, and that for ever  $\nu \geq 1$ ,

$$q_\nu < q^*(T_\nu). \quad (9.40)$$

Thus, even the first iteration leads to an unsaturated condition and higher accuracy is obtained with increasing  $\nu$ . At present, we take

$$\nu_{\max} = 1 \quad \text{for the upper layers,}$$

$$\nu_{\max} = 3 \quad \text{for the lowest layer and for the E- and the P- layer}$$

where  $\nu_{\max}$  is the maximum number of iteration in the layer.

From (9.38) and (9.39),

$$C_{\nu+1} \Delta t = \frac{C_p}{L} (T_{\nu+1} - T_\nu) = \frac{q_\nu - q^*(T_\nu)}{1 + \frac{L}{C_p} \left(\frac{\partial q^*}{\partial T}\right)_{T=T_\nu}}, \quad (9.41)$$

$$T_{\nu+1} = T_\nu + \frac{L}{C_p} C_{\nu+1} \Delta t, \quad (9.42)$$

$$q_{\nu+1} = q_\nu - C_{\nu+1} \Delta t. \quad (9.43)$$

In summary,

$$T'_k = T_k + \frac{L}{C_p} \sum_{\nu=1}^{\nu_{\max}} C_\nu \Delta t, \quad (9.44)$$

$$q'_k = q_k - \sum_{\nu=1}^{\nu_{\max}} C_\nu \Delta t, \quad (9.45)$$

$$T'_{k+2} = T_{k+2} - \frac{L}{C_p} \sum_{\nu=1}^{\nu_{\max}} C_\nu \Delta t \Pi_k \Delta \sigma_k / (\Pi_{k+2} \Delta \sigma_{k+2}), \quad (9.46)$$

$$q'_{k+2} = q_{k+2} + \sum_{\nu=1}^{\nu_{\max}} C_\nu \Delta t \Pi_k \Delta \sigma_k / (\Pi_{k+2} \Delta \sigma_{k+2}), \quad (9.47)$$

where  $C_\nu$  is determined by (9.41), (9.42), (9.43). At the lowest layer the condensation reaches the earth's surface and the large-scale precipitation per unit area becomes

$$P_{LS} = \frac{\Pi}{g} \sum_{\nu=1}^{\nu_{\max}} C_{\nu} \Delta t \cdot \Delta \delta_k \quad (9.48)$$

where  $\Delta \delta_k$  is the depth of the lowest layer in  $\delta$ -coordinate,  $\Pi = p_s - p_1$ ,  $p_s$  is the pressure at the earth's surface and  $p_1 = 100\text{mb}$ .

## 10. Ground hydrology and thermodynamics\*

### 10.1 Types of the earth's surface and related constants

In the model, the earth's surface is prescribed either as open ocean, sea ice, glacial ice, lake or land. The prescribed surface type is dependent on the model simulated time. The distribution of open ocean, sea ice and lake is determined once a month according to climatological data. Snow on the ground is a prognostic variable. The model predicts the surface temperature of either sea ice, glacial ice, land or snow. The sea ice has a depth of 3 m at both the Arctic and the Antarctic. The model also predicts interstitial moisture (so-called ground wetness) and interstitial ice. The lake is treated as land which is always saturated. The parameterization is based on Katayama (see AM).

#### 10.1.1 Roughness

Surface roughness ( $z_0$ ) is specified as follows according to the types of the surface;

$$\begin{aligned} z_0 &= 0.0002\text{m, for ocean} \\ &= 0.0001\text{m, for sea ice} \\ &= 0.005\text{m, for glacial ice} \\ &= 0.45\text{m, otherwise.} \end{aligned} \tag{10.1}$$

#### 10.1.2 Thermal conductivity

The thermal conductivities for ice, snow and soil are

$$\begin{aligned} k_{\text{ice}} &= 2.2 \text{ J/m/sec/deg,} \\ k_{\text{snow}} &= 0.34 \text{ J/m/sec/deg,} \\ k_{\text{soil}} &= 4.16 \times 0.2 \times (1 + w' + 0.25w_i) \text{ J/m/sec/deg,} \end{aligned} \tag{10.2}$$

respectively, where  $w'$  is the interstitial moisture (or ground wetness) and is given by

$$w' = W/W_m \tag{10.3}$$

where  $W$  is the amount of water stored in the ground and  $W_m$  is the prescribed maximum amount of  $W$  which the ground can absorb (the prescribed maximum amount of water per unit area,  $\rho W_m h$ , is assumed to be  $1.5 \text{ kg m}^{-2}$ ); and  $w_i$  is the interstitial ice, *i.e.*, the part of  $w'$  which is in the ice phase.

---

\* This chapter is prepared by A. Kitoh.

### 10.1.3 Heat capacity

The heat capacities for ice, snow and soil are

$$\begin{aligned} C_{\text{ice}} &= 4.16 \times 10^6 \times 0.51 \text{ J/m}^3/\text{deg}, \\ C_{\text{snow}} &= 4.16 \times 10^6 \times 0.23 \text{ J/m}^3/\text{deg}, \\ C_{\text{soil}} &= 4.16 \times 10^6 \times \{ 0.276 + (0.11 + 0.15w') (1. - 0.5w_i/w') \} \text{ J/m}^3/\text{deg}, \end{aligned} \quad (10.4)$$

respectively. Here the heat capacity of soil depends on interstitial moisture and ice.

### 10.1.4 Bulk heat capacity

Bulk heat capacity of the ground depends on the ground condition and is given by

$$C = ch, \quad (10.5)$$

where  $h$  is the characteristic decay depth. For both ice and snow,  $h$  is assigned to the value 0.1 m, and thus

$$\begin{aligned} C_{\text{ice}} &= 5.1 \times 4.16 \times 10^4 \text{ J/m}^2/\text{deg}, \\ C_{\text{snow}} &= 2.3 \times 4.16 \times 10^4 \text{ J/m}^2/\text{deg}. \end{aligned} \quad (10.6)$$

The bulk heat capacity of snow is assumed to be independent of the depth of the snow. For the soil, the characteristic depth of the diurnal variation is given by

$$h = \sqrt{D/\omega}. \quad (10.7)$$

where  $D = k/c$  is the thermal diffusivity and  $\omega = 2\pi$  radians/day. From (10.5) and (10.7)

$$C = ch = c \sqrt{D/\omega} = c \sqrt{k/c\omega} = \sqrt{ck/\omega}. \quad (10.8)$$

From above relations the bulk heat capacity for the soil is given by

$$\begin{aligned} C_{\text{soil}} &= 4.16 \times 10^4 \times \sqrt{\{0.276 + (0.11 + 0.15w') (1. - 0.5w_i/w')\}} \\ &\quad \times \sqrt{(1. + w' + 0.25w_i) \times 0.002/\omega}. \end{aligned} \quad (10.9)$$

## 10.2 Land surface temperature and heat balance

The ground temperature is obtained from

$$C \frac{\partial T_g}{\partial t} = H_A, \quad (10.10)$$

where  $T_g$  is the ground temperature,  $C$  is the bulk heat capacity and  $H_A$  is the net surface heating rate. The net surface heating rate is given by

$$H_A = - (F_h)_s - R_6 + S_6 + H_1, \quad (10.11)$$

where  $(F_h)_s$  is the heat flux (sensible plus latent heat flux) from the ground to the atmosphere,  $R_6$  is the net long wave flux from the ground to the atmosphere,  $S_6$  is the solar flux absorbed

at the earth's surface, and  $H_1$  is the heat conduction from below to the ground surface. For both land and glacial ice, we assume  $H_1=0$ . For sea ice, whether covered by snow or not,

$$H_1 = k_{ice}(T_1 - T_g) / h_1, \quad (10.12)$$

where  $T_1$  is the melting (or freezing) temperature of sea ice ( $=273.1\text{K}$  in the model), and  $h_1$  is the thickness of the sea ice. At present, we assume  $h_1$  to be constant ( $=3\text{m}$ ) regardless of the season.

In the implementation of (10.10),  $R_6$  is treated implicitly. Thus,

$$C \frac{\Delta T_g}{\Delta t} = S_6 + H_1 - (F_h)_s - R_6(T_g + \Delta T_g). \quad (10.13)$$

Using the first-order approximation

$$R_6(T_g + \Delta T_g)^4 \simeq \sigma T_g^4 + 4\sigma T_g^3 \Delta T_g, \quad (10.14)$$

the change of the ground temperature is given by

$$T_{g,new} - T_{g,old} = \Delta T_g = \frac{\Delta t \{ S_6 - R_6(T_{g,old}) + H_1 - (F_h)_s \}}{C + 4\sigma T_{g,old}^3 \Delta t}. \quad (10.15)$$

### 10.3 Surface hydrology and soil water budget

See Fig. 10.1 for the flow of the computation of ground hydrology.

#### 10.3.1 Surface evapotranspiration

The surface evapotranspiration is given by

$$E_s = \kappa (q_g - q_m)_e, \quad (10.16)$$

where  $(q_g - q_m)_e = \beta (q_g^* - q_m)$  is the effective ground-air total mixing ratio difference, and  $q$  is the mixing ratio, subscript  $g$  indicates a ground value, and subscript  $m$  indicates a mean value in the PBL and is defined by

$$( )_m = \frac{1}{p_s - p_B} \int_{p_B}^{p_s} ( ) dp, \quad (10.17)$$

and asterisk denotes the saturated value. The quantity  $\beta$  is the efficiency factor of evapotranspiration and is given by

$$\begin{aligned} \beta &= 1 && \text{when } w' \geq 0.5 \\ &= 2 \cdot w' && \text{when } w' \leq 0.5. \end{aligned} \quad (10.18)$$

When  $q_g < q_m$  (dew is being deposited), or if fog occurs, we assume that the ground has been wetted and  $\beta = 1$ .

$\kappa$  is the ventilation factor and is given by

$$\alpha = \rho |v_m| C_D C_H, \quad (10.19)$$

where  $\rho$  is the density,  $v_m$  is the representative velocity within the PBL and  $C_D$ ,  $C_H$  are transfer coefficients (see Fig. 8. 3). Negative evapotranspiration is able to occur, representing the condensation on the surface.

### 10.3.2 Snow

Precipitation results from large-scale supersaturation of the lowest model layer and/or from cumulus convection (middle level and penetrative). When precipitation occurs, it is counted either for rainfall ( $P_r$ ) or for snowfall ( $P_s$ ) depending upon the surface air temperature  $T_s$ , i.e.,

i) when  $T_s > T_i$ , rainfall occurs  
and

$$P_r = P, P_s = 0, \quad (10.20a)$$

ii) when  $T_s \leq T_i$ , snowfall occurs  
and

$$P_s = P, P_r = 0, \quad (10.20b)$$

where  $P$  is the rate of precipitation.

The snow mass is a prognostic variable in the model except for open ocean and is given by

$$\frac{\partial S}{\partial t} = P_s - E_s \{1 - \delta(S)\} - M_s, \quad (10.21)$$

where  $S$  is snow mass per unit area,  $E_s$  is evapotranspiration,  $M_s$  is snowmelt per unit area and

$$\begin{aligned} \delta(S) &= 1 \text{ if } S = 0, \\ &= 0 \text{ if } S \neq 0. \end{aligned} \quad (10.22)$$

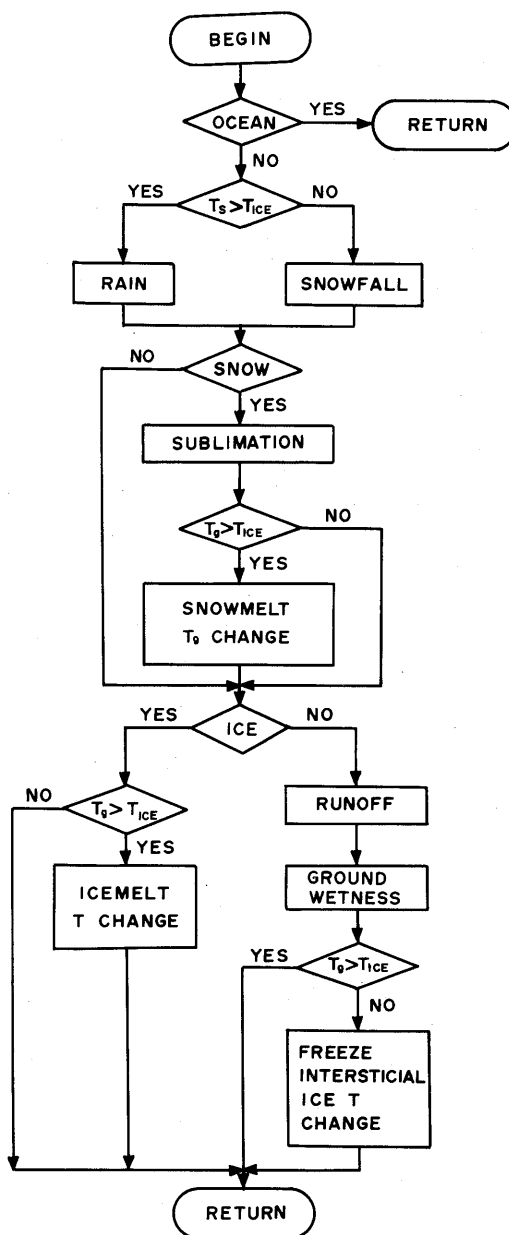


Fig. 10.1 Flow diagram of ground hydrology process.

Snowmelt occurs when model computed ground temperature  $T_g$  is greater than  $T_i$

$$\begin{aligned} \text{i) } T_g &\leq T_i, M_s = 0, \\ \text{ii) } T_g &> T_i, M_s \Delta t = \min\left(\frac{C_s}{L_i}(T_g - T_i), S\right), \end{aligned} \quad (10.23)$$

where  $C_s$  is bulk heat capacity of snow and  $L_i$  is latent heat of melting.

### 10.3.3 Interstitial moisture and interstitial ice

The interstitial moisture ( $w'$ ) and the interstitial ice ( $w_i$ ) are governed by

$$W_m \rho h \frac{\partial w'}{\partial t} = P_r - R - E_s \delta(S) + M_s + C_T, \quad (10.24)$$

$$W_m \rho h \frac{\partial w_i}{\partial t} = F_i \delta(S), \quad (10.25)$$

where  $\rho$  is the density of the ground,  $R$  is runoff,  $C_T$  is capillary transport of water into the soil layer, and  $F_i$  is the mass of interstitial moisture which freezes or melts per unit area and time. We assume that the maximum available water, per unit area of the soil layer,  $W_m \rho h$ , is a constant (15 gr/cm<sup>2</sup>).

Usually we assume  $C_T = 0$ , but when the predicted interstitial moisture without capillary pumping becomes either negative or greater than unity, we allow a value of  $C_T$  such that it restores the interstitial moisture to zero or unity, respectively.

### 10.3.4 Runoff

The rainfall-runoff relation we are using is

$$R = (P_r^3 + D^3)^{1/3} - D, \quad (10.26)$$

where the deficiency of water,  $D$ , is defined by

$$D = (1 - w') W_m \rho h. \quad (10.27)$$

If rainfall amount is zero, runoff is also zero. When  $D \neq 0$ , runoff increases with rainfall. When soil is saturated ( $D = 0$ ), all the rainfall becomes runoff. The runoff is discarded instantly out of the model.

## 11. Vertical and horizontal sub-grid-scale transports\*

### 11.1 Cumulus transport of momentum

The momentum change owing to the cumulus convection is divided into the following three components.

- (1) The loss due to momentum entrainment into the cloud. These momentum are released from the cloud into the environment above that level.
- (2) The gain due to momentum detrainment from the cloud.
- (3) The momentum change due to the cumulus subsidence.

The time rate of change in momentum due to cumulus convection is written as

$$\frac{\partial}{\partial t} \rho \mathbf{V} = -E\mathbf{V} + D\hat{\mathbf{V}} + \frac{\partial}{\partial z} (M_c \mathbf{V}), \quad (11.1)$$

where  $\rho$  is the density of the air,  $\mathbf{V}$  is the horizontal velocity of the air in the environment,  $\hat{\mathbf{V}}$  is the horizontal velocity of the air which is detraining from cumulus clouds,  $E$  is the total entrainment per unit depth,  $D$  is the total detrainment per unit depth, and  $M_c$  is the total vertical mass flux of the clouds.  $E$ ,  $D$  and  $M_c$  satisfy the mass budget equation,

$$-\frac{\partial M_c}{\partial z} + E - D = 0. \quad (11.2)$$

The total momentum is conserved by the redistribution of momentum due to cumulus convection. And

$$\int_{z_B}^{z_{\max}} D(z) \hat{\mathbf{V}}(z) dz = \int_{z_B}^{z_{\max}} E(z) \mathbf{V}(z) dz + \mathbf{V}_B M_c(z_B), \quad (11.3)$$

where  $z_B$  is the cloud base,  $z_{\max}$  is the detrainment level of the deepest cloud, and  $\mathbf{V}_B$  is the horizontal velocity of the air in the environment at  $z_B$ . See Chapter 7 and Fig. 11.1.

In a finite difference form, (11.1) at odd level  $k$  may be written as

$$\begin{aligned} \frac{\partial}{\partial t} \rho \mathbf{V}_k \Delta z_k = & - \sum_{i=k_{\min}}^{k-2} \mathbf{V}_k m_{B_i} e_{k,i} \Delta z_k \\ & + \sum_{k'=k+2}^{KN-1} \mathbf{V}_{k'} m_{B_k} e_{k',k} \Delta z_k + m_{B_k} \mathbf{V}_{KB} \\ & + (M_c)_{k-1} \mathbf{V}_{k-1} - (M_c)_{k+1} \mathbf{V}_{k+1}, \end{aligned} \quad (11.4)$$

---

\* This chapter is prepared by A. Kitoh.

where  $\Sigma'$  is the summation on odd levels only,  $i$  is the type of cloud which has the detrainment level at the odd level  $i$  (type- $i$  cloud in Chapter 7),  $k_{min}$  is the index for the odd level at which the deepest clouds detrain,  $m_{Bi}$  is the sub-ensemble vertical mass flux at level  $KN$ ,  $e_{k,i}$  is the normalized entrainment of type- $i$  cloud at level  $k$ ,  $\Delta z_k$  is the depth of layer  $k$ ,  $KN$  is the index of the even level immediately above the top of the planetary boundary layer,  $KB$  is the index of the odd level in which the top of the planetary boundary layer exists.  $(M_c)_{k-1}$  is the total vertical mass flux at level  $k-1$  and is given by

$$(M_c)_{k-1} = \sum_{i=k_{min}}^{k-2} \eta_{k-1,i} M_{Bi}, \tag{11.5}$$

where  $\eta$  is the normalized mass flux of type- $i$  cloud at level  $k$ . Entrainment and mass flux have the following relation

$$e_{k,i} \Delta z_k = \eta_{k-1,i} - \eta_{k+1,i}, \tag{11.6}$$

(see Fig. 11.2).

The first term on the right hand side of (11.4) represents the loss due to the momentum entrainment into the cloud which detrains above  $z_{k-1}$ . This term occurs because there is deeper cloud which has its top of the cloud above that level and this cloud entrains the environmental air into the cloud. The terms in the second line represent the gain due to the momentum detrainment. The detrained air at level  $k$  consists of the entrained air into type- $k$  cloud. These entrainment occurs at the odd levels below that level and at the top of the planetary boundary layer (cloud base flux). The third

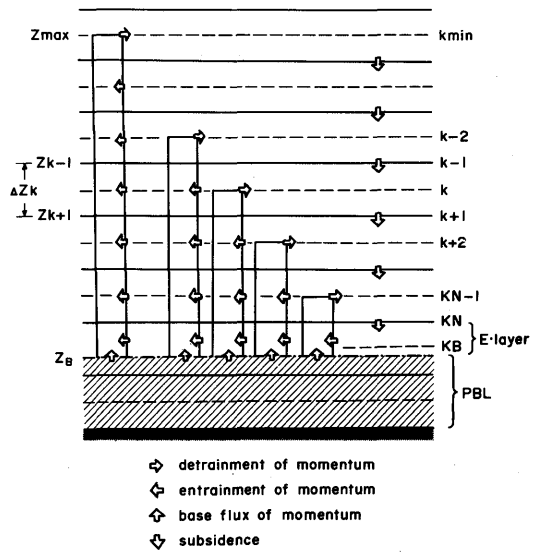


Fig. 11.1 Momentum budget of cumulus ensemble.

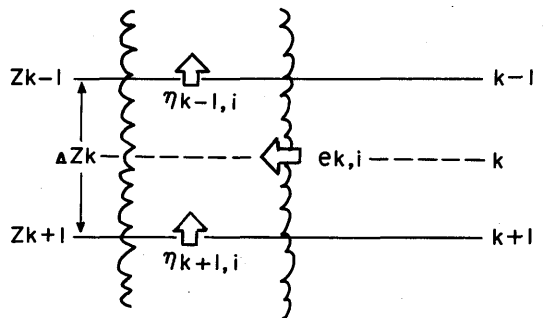


Fig. 11.2 Mass budget of type- $i$  cloud at level  $k$ .

line represents the momentum change due to the cumulus subsidence.

### 11.2 Vertical diffusion

Currently no vertical diffusions are included in any equations.

### 11.3 Horizontal Diffusion

In the model horizontal sub-grid-scale transport is introduced in momentum equations in terms of the horizontal non-linear eddy diffusion described in Holloway and Manabe (1971). The horizontal diffusion terms are expressed as follows ;

$$\frac{\partial}{\partial t}(\Pi_{i+\frac{1}{2},j}^{(u)} u_{i+\frac{1}{2},j}) + \dots = \left(\frac{m}{\Delta\xi}\right)_j (\tau_{i+1,j}^{\lambda\lambda} - \tau_{i,j}^{\lambda\lambda}) + \left(\frac{nm^2}{\Delta\eta}\right)_j \left\{ \left(\frac{\tau^{\lambda\phi}}{m^2}\right)_{i+\frac{1}{2},j+\frac{1}{2}} - \left(\frac{\tau^{\lambda\phi}}{m^2}\right)_{i+\frac{1}{2},j-\frac{1}{2}} \right\} \quad (11.7)$$

$$\frac{\partial}{\partial t}(\Pi_{i,j+\frac{1}{2}}^{(v)} v_{i,j+\frac{1}{2}}) + \dots = \left(\frac{m}{\Delta\xi}\right)_{j+\frac{1}{2}} (\tau_{i+\frac{1}{2},j+\frac{1}{2}}^{\lambda\phi} - \tau_{i-\frac{1}{2},j+\frac{1}{2}}^{\lambda\phi}) - \left(\frac{nm^2}{\Delta\eta}\right)_{j+\frac{1}{2}} \left\{ \left(\frac{\tau^{\lambda\lambda}}{m^2}\right)_{i,j+1} - \left(\frac{\tau^{\lambda\lambda}}{m^2}\right)_{i,j} \right\} \quad (11.8)$$

$$\tau_{i,j}^{\lambda\lambda} = \frac{1}{2} \left\{ (\Pi K_H)_{i+\frac{1}{2},j} + (\Pi K_H)_{i-\frac{1}{2},j} \right\} \cdot (D_T)_{i,j} \quad (11.9)$$

$$(D_T)_{i,j} = \left(\frac{m}{\Delta\xi}\right)_j (u_{i+\frac{1}{2},j} - u_{i-\frac{1}{2},j}) - \left(\frac{n}{m\Delta\eta}\right)_j \left\{ (vm)_{i,j+\frac{1}{2}} - (vm)_{i,j-\frac{1}{2}} \right\} \quad (11.10)$$

$$\tau_{i+\frac{1}{2},j+\frac{1}{2}}^{\lambda\phi} = \frac{1}{2} \left\{ (\Pi K_H)_{i+\frac{1}{2},j+1} + (\Pi K_H)_{i+\frac{1}{2},j} \right\} \cdot (D_S)_{i+\frac{1}{2},j+\frac{1}{2}} \quad (11.11)$$

$$(D_S)_{i+\frac{1}{2},j+\frac{1}{2}} = \left(\frac{m}{\Delta\xi}\right)_{j+\frac{1}{2}} (v_{i+1,j+\frac{1}{2}} - v_{i,j+\frac{1}{2}}) + \left(\frac{n}{m\Delta\eta}\right)_{j+\frac{1}{2}} \left\{ (um)_{i+\frac{1}{2},j+1} - (um)_{i+\frac{1}{2},j} \right\} \quad (11.12)$$

$$(K_H)_{i+\frac{1}{2},j} = \left(\frac{\Delta\xi\Delta\eta}{mn}\right)_j \cdot \min \left[ k_0^2 \left[ \frac{1}{2} \left\{ (D_T)_{i,j}^2 + (D_T)_{i+1,j}^2 + (D_S)_{i+\frac{1}{2},j+\frac{1}{2}}^2 + (D_S)_{i+\frac{1}{2},j-\frac{1}{2}}^2 \right\} \right]^{\frac{1}{2}}, D_{comax} \right] \quad (11.13)$$

The notations used in the above are the same as those used in Chapter 3. The reason for

keeping  $K_H$  less than  $D_{\text{comax}} \left( \frac{\Delta \xi \Delta \eta}{mn} \right)$  is to avoid linear instability due to diffusion terms, and  $D_{\text{comax}}$  is set to  $1 / \left\{ 4(\Delta t)_d \cdot \left( \frac{m}{\Delta \xi} \frac{\Delta \eta}{n} \right)_j \right\}$ , where  $(\Delta t)_d$  is the time interval of evaluating diffusion terms (see Fig. 5.1). The constant  $k_0$  is assigned the value 0.2.

In other equations, *i.e.* the thermodynamic equation, moisture equation and ozone equation, no horizontal diffusion terms are included.

## 12. Ozone photochemistry and surface destruction\*

The ozone photochemical process in the stratosphere and the ozone destruction by heterogeneous chemical reactions in the planetary boundary layer are parameterized following Cunnold *et al.* (1975), and Schlesinger and Mintz (1979). (see also Schlesinger, 1976)

### 12.1 Photochemical reactions

The photochemical production and destruction of ozone in the stratosphere is comprised of both the Chapman reactions



and the NO–NO<sub>2</sub> catalytic cycle



The chemical reaction rates  $k_i$  are

$$\begin{aligned} k_1 &= 1.1 \times 10^{-46} \exp(520/T) & \text{m}^6\text{s}^{-1}, \\ k_2 &= 1.9 \times 10^{-17} \exp(-2300/T) & \text{m}^3\text{s}^{-1}, \\ k_3 &= 2.1 \times 10^{-18} \exp(-1450/T) & \text{m}^3\text{s}^{-1}, \\ k_4 &= 9.1 \times 10^{-18} & \text{m}^3\text{s}^{-1}, \end{aligned} \quad (12.8)$$

and the photodissociation rate  $j_n(p)$  of species  $n$  at pressure  $p$  is given by

$$j_n(p) = \int_0^\infty \alpha_n(\lambda) I_0(\lambda) \exp\left[-M_F \sum_{m=1}^2 \alpha_m(\lambda) U_m(p)\right] d\lambda \quad (12.9)$$

Here  $\alpha_n(\lambda)$  is the absorption cross section of species  $n$  (1 : O<sub>2</sub>, 2 : O<sub>3</sub>, 3 : NO<sub>2</sub>) at wave length

---

\* This chapter is prepared by I. Yagai; Forecast Research Division

$\lambda$ ,  $I_0(\lambda)$  is the extraterrestrial monochromatic photon flux per unit wave length.  $M_F$  is a magnification factor to account for the departure from the plane parallel atmosphere, which will be defined by (13.51) in Chapter 13, and  $U_m$  is the absorber amount of species  $m$  ( $1 : O_2$ ,  $2 : O_3$ ) in a vertical column above pressure  $p$ , and the summation extends over all species  $m$ . To calculate photodissociation rates  $j_n(p)$ , the values of  $\alpha_1(\lambda)$ ,  $\alpha_2(\lambda)$  and  $I_0(\lambda)$  are taken from Ackermann (1971), Kockarts (1971), and  $\alpha_3(\lambda)$  from the data of The Natural Stratosphere of 1974, CIAP Monograph 1. Currently  $j_n(p)$  is computed by a linear bivariate interpolation of precomputed values of  $j_n(p)$  as a function of  $U_1$  and  $U_2$  to save CPU time.

## 12.2 Governing equations for the photochemical reactions

The equations governing the time change rates of the concentration of O,  $O_2$ ,  $O_3$ , NO, and  $NO_2$  given by reactions (12.1)–(12.7) are

$$\frac{\partial [O]}{\partial t} = 2j_1[O_2] - k_1[O][O_2][M] + j_2[O_3] - k_2[O][O_3] - k_4[O][NO_2] + j_3[NO_2], \quad (12.10)$$

$$\begin{aligned} \frac{\partial [O_2]}{\partial t} = & -j_1[O_2] - k_1[O][O_2][M] + j_2[O_3] + 2k_2[O][O_3] + k_3[NO][O_3] \\ & + k_4[NO_2][O], \end{aligned} \quad (12.11)$$

$$\frac{\partial [O_3]}{\partial t} = k_1[O][O_2][M] - j_2[O_3] - k_2[O][O_3] - k_3[NO][O_3], \quad (12.12)$$

$$\frac{\partial [NO]}{\partial t} = -k_3[NO][O_3] + k_4[NO_2][O] + j_3[NO_2], \quad (12.13)$$

$$\frac{\partial [NO_2]}{\partial t} = k_3[NO][O_3] - k_4[NO_2][O] - j_3[NO_2], \quad (12.14)$$

where  $[X]$  denotes the concentration of species  $X$  in molecules  $m^{-3}$  and  $M$  represents that of air.

The equilibrium concentrations of atomic oxygen O and nitric monoxide NO are calculated by (12.10) and (12.13),

$$[O]_e = \frac{2j_1[O_2] + j_2[O_3] + j_3[NO_2]}{k_1[O_2][M] + k_2[O_3] + k_4[NO_2]}, \quad (12.15)$$

$$[NO]_e = \frac{k_4[NO_2][O] + j_3[NO_2]}{k_3[O_3]}, \quad (12.16)$$

the relaxation times are approximately given by  $\tau_0 \approx (k_1[O_2][M])^{-1}$  and  $\tau_{NO} \approx (k_3[O_3])^{-1}$ ; their representative values are order 1 minute and 10 minutes, respectively. Then, it can be assumed that O and NO are in equilibrium with other constituents, and we can approximate  $[O]_e$  and  $[NO]_e$  instead of  $[O]$  and  $[NO]$ .

Substituting (12.15) and (12.16) into (12.12) gives

$$\frac{\partial [O_3]}{\partial t} = A - B[O_3] - C[O_3]^2 \quad (12.17)$$

where

$$A = 2 \frac{k_1 j_1 [O_2]^2 [M] - k_4 j_1 [O_2] [NO_2] - k_4 j_3 [NO_2]^2}{k_1 [O_2] [M] + k_2 [O_3] + k_4 [NO_2]}$$

$$B = 2 \frac{k_2 j_1 [O_2] + (k_2 j_3 + k_4 j_2) [NO_2]}{k_1 [O_2] [M] + k_2 [O_3] + k_4 [NO_2]}$$

$$C = 2 \frac{k_2 j_2}{k_1 [O_2] [M] + k_2 [O_3] + k_4 [NO_2]}$$

$[O_2]$  can be given as  $[O_2] = 0.21[M]$ , and  $[NO_2]$  is prescribed to vary only in the vertical with the relation

$$[NO_2](z) = \beta [NO_2]_{McElroy}(z) \quad (12.18)$$

where  $[NO_2]_{McElroy}(z)$  is the one-dimensional profile calculated by McElroy *et al.* (1974), and  $\beta$  is an empirical constant to adjust the simulated  $O_3$  mixing ratio to the observed value at 10 mb in the tropics. Currently  $\beta$  is set to 1.62.

### 12.3 Vertical distribution of absorber amounts

The integrated absorber amount of species  $m$  in a vertical column above pressure  $p$  is defined by

$$U_m(p) = \frac{1}{g} \int_0^p [ ]_m(p) \frac{dp}{\rho} \quad (12.19)$$

where  $[ ]_m$  is the concentration of species  $m$  in molecules  $m^{-3}$ . We assume that molecular oxygen is well-mixed throughout the atmosphere,  $[O_2] = 0.21[M]$ ; then for molecular oxygen

$$U_1(p) = \frac{0.21 a p}{g m} \quad (12.20)$$

where  $a$  is Avogadro's number, and  $m$  is the molecular weight of air. For ozone, it is assumed that the number density  $[O_3(z)]$  above the midlevel of layer 1 decays exponentially

with altitude following Krueger (1973). Thus

$$[O_3(z)] = [O_3(z_1)] \exp\left(-\frac{z-z_1}{H}\right) \quad z \geq z_1 \quad (12.21)$$

where  $[O_3(z_1)]$  is the GCM predicted ozone number density for layer 1, and H is the scale height for ozone (=4.45km). Then (12.19) can be written as

$$U_2(p) = \int_{z_1}^{\infty} [O_3(z)] dz + \frac{a}{gM_{O_3}} \int_{P_1}^P q_{O_3}(p) dp \quad (12.22)$$

where  $M_{O_3}$  is the molecular weight of ozone.

#### 12.4 Ozone destruction at the earth's surface

Ozone is destroyed at the earth's surface by heterogeneous chemical reactions. The rate of destruction  $D_{O_3}$  may be expressed as

$$D_{O_3} = \rho K (q_{O_3})_s \quad (12.23)$$

where  $\rho$  is the air density, K the reaction rate constant,  $(q_{O_3})_s$  the surface ozone mixing ratio. We assume that the destruction  $D_{O_3}$  is approximately compensated by the downward ozone flux at the top of the planetary boundary layer (PBL),  $(F_{O_3})_B$  which may be approximated as

$$(F_{O_3})_B = \rho D \frac{\partial q_{O_3}}{\partial Z} = \rho D \frac{(q_{O_3})_{LM} - (q_{O_3})_s}{Z_{LM} - Z_s} \quad (12.24)$$

where D is the eddy diffusivity at the top of the PBL, Z the altitude, and subscript LM denotes the midlevel of the lowest layer.  $(q_{O_3})_s$  is determined by equating (12.23) with (12.24) as

$$(q_{O_3})_s = \frac{D}{D + K(Z_{LM} - Z_s)} (q_{O_3})_{LM} \quad (12.25)$$

The constants K and D are currently assigned to  $0.0008 \text{ m sec}^{-1}$  and  $10 \text{ m}^2\text{sec}^{-1}$  after Cunnold *et al.* (1975).

## 13. Radiation\*

### 13.1 Introduction

The radiation calculation scheme adopted in the MRI-GCM-I closely follows the one described in Arakawa and Mintz (1974).

The solar radiation incident on the top of the model atmosphere has both seasonal and diurnal variations. In the MRI-GCM-I, the solar flux under cloudless conditions is depleted by ozone absorption, water vapor absorption and Rayleigh scattering. The model forms interactive clouds, such as clouds by large scale condensation and cirrus. They influence the radiational heating fields strongly by absorption and reflection. The albedo of the earth's surface is determined diagnostically by the model as a simple function of surface conditions.

The parameterization of the solar radiation is based on Katayama (1972). The solar radiation is divided into two parts at the wave length  $\lambda = \lambda_c = 0.9\mu$ .

i) The part  $\lambda < \lambda_c$  is called "scattered" part. Rayleigh scattering is considered in this wave length region below 200 mb.

ii) The part  $\lambda > \lambda_c$  is called "absorbed" part, where absorption by water vapor is considered, while Rayleigh scattering is neglected.

For the long wave radiation, we adopt a hybrid scheme proposed by Schlesinger (1976); the scheme consists of two different methods which are connected with each other at 30 km level.

i) From the surface up to the 30 km level, we use the method developed by Katayama (1972); weighted mean transmission functions defined for the entire band are used to calculate long wave radiation flux and its flux divergence. Water vapor, carbon dioxide and ozone are treated as absorbers.

ii) Above the 30 km level, we adopt the long wave radiative cooling parameterization developed by Dickinson (1973).

Usually radiation model is a time-consuming part of the GCM. This is one of the reasons for neglecting diurnal variations in the radiative flux calculation in many GCMs. It is pointed out that diurnal variations are taken account of in the current radiation model, which is realized by an adoption of an economical scheme for long wave radiation developed by

---

\* This chapter is prepared by I. Yagai.

Katayama (1972). Therefore various prognostic variables especially those associated with the planetary boundary layer undergo their diurnal variations.

## 13.2 Terrestrial radiation

### 13.2.1 Basic equations

The upward and the downward fluxes of terrestrial radiation,  $R_z^\uparrow$ , and  $R_z^\downarrow$ , are given by ;

$$R_z^\uparrow = \int_0^\infty \pi B_\nu(T_z) d\nu + \int_0^\infty d\nu \int_{T_z}^{T_g} \pi \frac{dB_\nu(T)}{dT} \tau_t \{ \ell_\nu (u_z - u) \} dT \quad (13.1)$$

$$R_z^\downarrow = \int_0^\infty \pi B_\nu(T_z) d\nu + \int_0^\infty d\nu \int_{T_z}^{T_T} \pi \frac{dB_\nu(T)}{dT} \tau_t \{ \ell_\nu (u - u_z) \} dT - \int_0^\infty \pi B_\nu(T_T) \tau_t \{ \ell_\nu (u_\infty - u_z) \} d\nu \quad (13.2)$$

where  $u_z = u(T_z)$  is the effective amount of absorbing medium (water vapor, carbon dioxide and ozone) in the vertical air column from the earth's surface to the level  $z$ ,  $T_z$  the temperature at level  $z$ ,  $T_g$  the ground temperature,  $B_\nu$  the Planck's radiation function expressed in terms of frequency  $\nu$ ,  $\ell_\nu$  the absorption coefficient,  $\tau_t$  the transmission function of a slab at frequency  $\nu$ ,  $T_T$  the temperature of the effective lid of the atmosphere. In the 12 layer version of the MRI-GCM-I, the long wave flux is calculated up to the 10 mb level, therefore  $T_T$  is defined as the vertical mean temperature above 10 mb. As for the tropospheric version of the MRI-GCM-I,  $T_T$  is assigned the value shown in Fig. 13.1 based on the annually averaged temperature in the lower stratosphere.

The net upward flux  $R_z$  is defined as

$$R_z = R_z^\uparrow - R_z^\downarrow \quad (13.3)$$

The heating rate is given by

$$\left( \frac{\partial T}{\partial t} \right)_{tr} = \frac{g}{c_p} \frac{\partial R_z}{\partial p} \quad (13.4)$$

where  $g$  is the acceleration due to gravity and  $c_p$  is the specific heat of air at constant pressure.

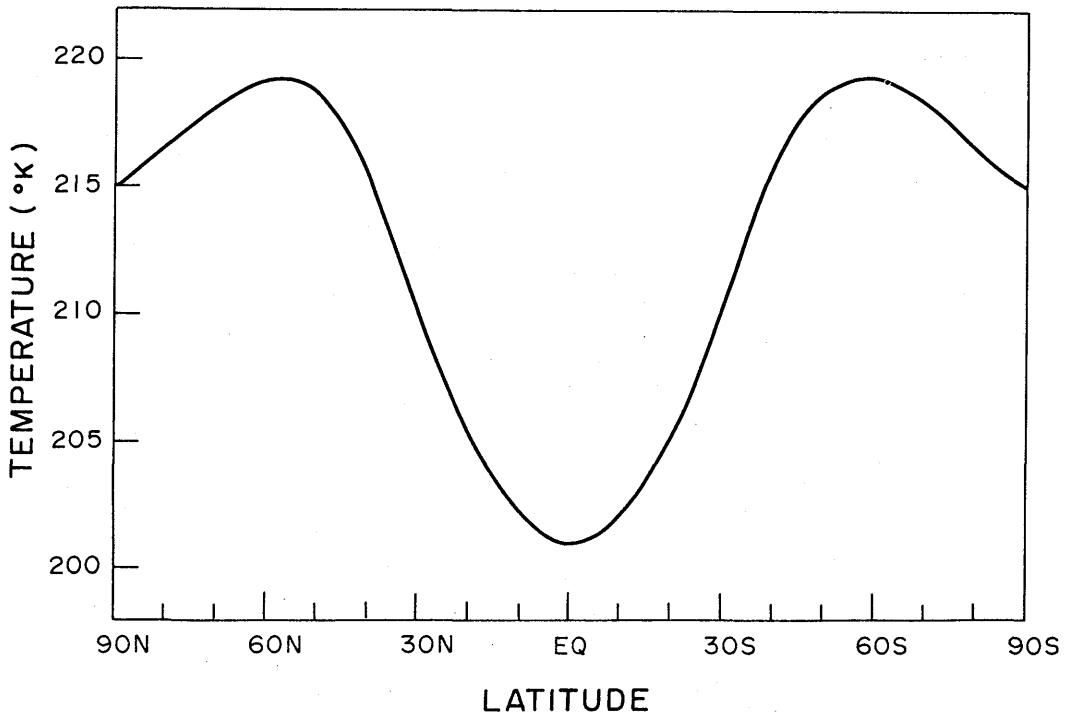


Fig. 13.1 Latitudinal variation of  $T_T$ , the temperature of the effective lid adopted in the tropospheric version of the MRI-GCM-I.  $T_T$  is based on the annually averaged temperature in the lower stratosphere.

### 13.2.2 Simplification : Weighted mean transmission functions

In order to simplify the computation of equations (13.1) and (13.2), Yamamoto (1952) introduced the following weighted mean transmission functions.

$$\tau(u^*, T) \equiv \left[ \pi \frac{dB(T)}{dT} \right]^{-1} \int_0^\infty \pi \frac{dB_\nu(T)}{dT} \tau_\tau(\ell_{\nu_0} u^*) d\nu \quad (13.5)$$

and

$$\tilde{\alpha}(u^*, T) \equiv [\pi B(T)]^{-1} \int_0^\infty \pi B_\nu(T) \tau_\tau(\ell_{\nu_0} u^*) d\nu \quad (13.6)$$

where

$$\pi B(T) = \int_0^\infty \pi B_\nu(T) d\nu = \sigma T^4$$

$$\ell_{\nu_0} u^* = \ell_\nu u$$

and  $\sigma$  is the Stefan - Boltzman constant,  $\ell_{\nu_0}$  the absorption coefficient at the standard

pressure  $p_0$ . The effective absorber amount  $u^*$  is given by

$$u_n^*(p) = \frac{1}{g} \int_p^{p_s} q_n(p') \left(\frac{p'}{p_0}\right)^{\alpha_n} dp' \quad (13.7)$$

where  $p_s$  is the surface pressure,  $q_n$  the absorber mixing ratio, and  $n$  a symbol of either  $H_2O$ ,  $CO_2$ , or  $O_3$ . Pressure scaling factor  $\alpha_n$  is given in Table 13.1.

Yamamoto found for water vapor that the dependence of  $\tau(u^*, T)$  on temperature is weak in between  $210^\circ K$  and  $320^\circ K$ . Furthermore, according to Schlesinger (1976), the temperature dependence of  $\tau$  on carbon dioxide and ozone is weak in between  $190^\circ K$  and  $310^\circ K$ . Therefore, we introduce the following approximation

$$\tau(u^*, T) \doteq \tau(u^*, \bar{T}) \quad \text{for } T \geq T_c = 220^\circ K \quad (13.8)$$

where  $\bar{T} = 260^\circ K$ .

With the use of (13.8), equations (13.1) and (13.2) are transformed into the following form

$$R_z^\downarrow = \pi B_z - \pi B_c \tilde{\tau}(u_\infty^* - u_z^*, T_c) - (\pi B_T - \pi B_c) \tau(u_\infty^* - u_z^*, \bar{T}) + \int_{\pi B_z}^{\pi B_T} \tau(u^* - u_z^*, \bar{T}) d(\pi B) \quad (13.9)$$

and

$$R_z^\uparrow = \pi B_z + \int_{\pi B_z}^{\pi B_c} \tau(u_z^* - u^*, \bar{T}) d(\pi B) \quad (13.10)$$

where  $B_z = B(T_z)$ ,  $B_c = B(T_c)$ ,  $B_T = B(T_T)$ . Following Yamamoto (1952), the transmission functions of a mixture of water vapor, carbon dioxide, and ozone may be approximated by the product of their respective transmission functions, i.e.,

$$\tau(u^*, \bar{T}) = \tau_{H_2O}(u_{H_2O}^*, \bar{T}) \tau_{CO_2}(\bar{T}) \tau_{O_3}(u_{O_3}^*, \bar{T}) \quad (13.11)$$

and

$$\tilde{\tau}(u^*, T_c) = \tilde{\tau}_{H_2O}(u_{H_2O}^*, T_c) \tilde{\tau}_{CO_2}(T_c) \tilde{\tau}_{O_3}(u_{O_3}^*, T_c) \quad (13.12)$$

### 13.2.3 Cloudless atmosphere

The vertical discretization of the atmosphere and the vertical index are shown in Fig. 13.

2. With use of the notation

$$\begin{aligned} \tilde{\tau}_\ell &= \tilde{\tau}_\ell(u_\infty^* - u_\ell^* - u_\ell^*, T_c) \\ \tau_\ell &= \tau_\ell(u_\infty^* - u_\ell^*, \bar{T}) \\ \tau_{\ell, \ell} &= \tau(|u_\ell^* - u_\ell^*|, \bar{T}) \equiv \tau_{\ell, \ell} \end{aligned} \quad (13.13)$$

Eqs. (13.9) and (13.10) may be expressed respectively as

$$R_{\ell}^{\downarrow} = \pi B_{\ell} - \pi B_c \tilde{\tau}_{\ell} - (\pi B_T - \pi B_c) \tau_{\ell} + \int_{\pi B_{\ell}}^{\pi B_T} \tau(u^* - u_{\ell}^*, \bar{T}) d(\pi B) \quad (13.14)$$

and

$$R_{\ell}^{\uparrow} = \pi B_{\ell} + \int_{\pi B_{\ell}}^{\pi B_{LM+1}} \tau(u_{\ell}^* - u^*, \bar{T}) d(\pi B) + (\pi B_g - \pi B_{LM+1}) \tau_{\ell, LM+1} \quad (13.15)$$

Let  $C_{\ell', \ell}$  represent the contribution to the flux at the upper level of layey  $\ell$  from the layer  $\ell'$ , then  $C_{\ell', \ell}$  can be evaluated by the trapezoidal low,

$$C_{\ell', \ell} = \int_{\pi B_{\ell'}}^{\pi B_{\ell'+1}} \tau(|u^* - u_{\ell}^*|, \bar{T}) d(\pi B) = \frac{1}{2} (\tau_{\ell'+1, \ell} + \tau_{\ell', \ell}) (\pi B_{\ell'+1} - \pi B_{\ell'}) \quad (13.16)$$

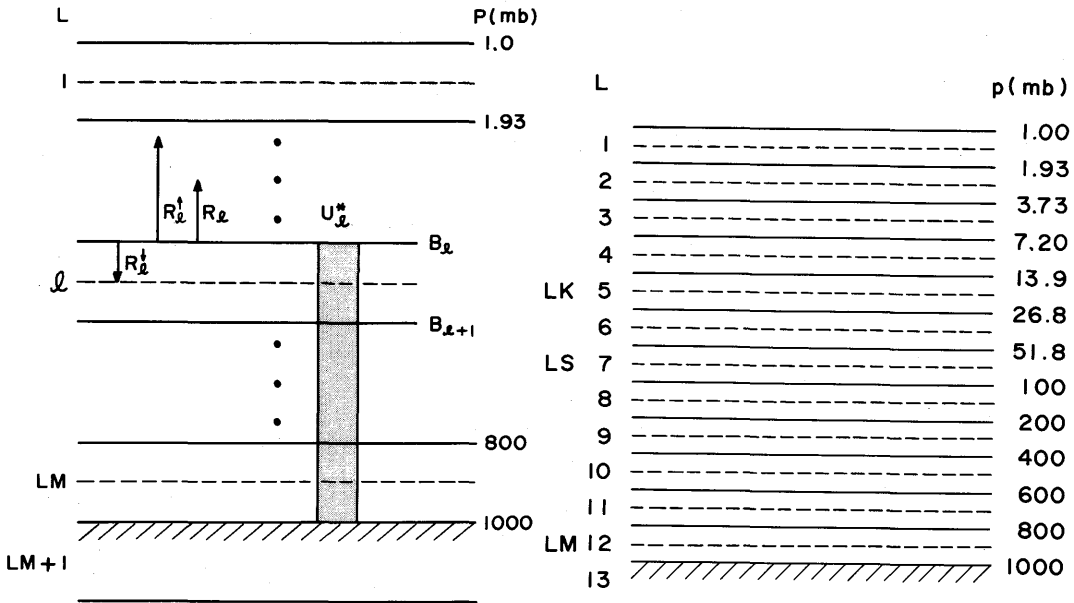


Fig. 13.2 (a) Indexing scheme for the long wave radiation calculation. The effective absorber amount  $u_{\ell}^*$  is defined between the earth's surface and the top level of layer  $\ell$ , (see eq. (13.7)). (b) Vertical discretization of the 12-layer MRI • GCM-I. The lowest five layers are same as that of the tropospheric version of the MRI • GCM-I. LM is the index of the middle level of the lowest layer and LS is that of the lowest stratospheric layer. LK defines the level above which we use Dickinson (1973)'s longwave parameterization. Currently we adopt the value LM=12, LS=7 and LK=5 for the 12-layer model, and LM=5 and LS=0 for the 5-layer model.

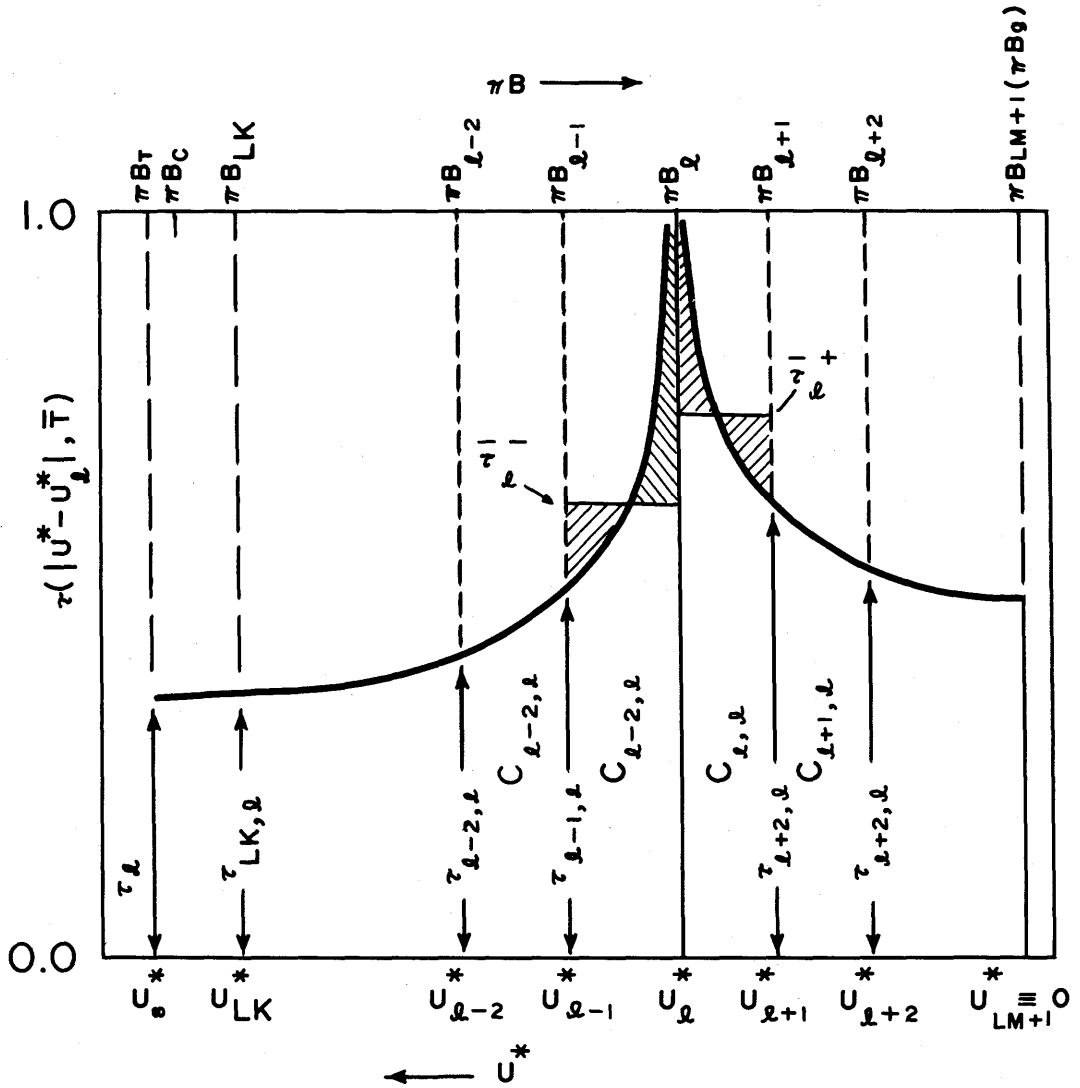


Fig. 13.3 Schematic representation of the transmission functions  $\tau(|u^* - u_l^*|, \bar{T})$  and  $\bar{\tau}_l^\pm$  at layer  $l$ .

This form is approximately valid except when  $l' = l + 1$  and  $l' = l$ . When the two layers are adjacent to each other,  $\tau$  does not vary linearly with  $\pi B$ . Therefore, following Katayama (1972), two bulk transmission functions  $\bar{\tau}_l^\pm$  are defined as follows,

$$\bar{\tau}_l^- \equiv (\pi B_l - \pi B_{l-1})^{-1} C_{l-1,l} \tag{13.17}$$

$$\bar{\tau}_l^+ \equiv (\pi B_{l+1} - \pi B_l)^{-1} C_{l,l} \tag{13.18}$$

Fig. 13.3 shows a schematic representation of  $\tau(|u^* - u_l^*|, \bar{T})$  and  $\bar{\tau}_l^\pm$ .

Substituting (13.16), (13.17) and (13.18) into (13.14) and (13.15), we obtain

$$R_{\ell}^{\downarrow} = \pi B_{\ell} - (\pi B_{\ell} - \pi B_{\ell-1}) \bar{\tau}_{\ell}^{-} - \frac{1}{2} \sum_{\ell'=\ell-2}^{\text{LK}} (\tau_{\ell'+1,\ell} + \tau_{\ell',\ell} - \pi B_{\ell'}) - (\pi B_{\text{LK}} - \pi B_{\text{T}}) \tau_{\text{LK},\ell} - (\pi B_{\text{T}} - \pi B_{\text{C}}) \tau_{\ell} - \pi B_{\text{C}} \bar{\tau}_{\ell} \quad (13.19)$$

and

$$R_{\ell}^{\uparrow} = \pi B_{\ell} + (\pi B_{\ell+1} - \pi B_{\ell}) \bar{\tau}_{\ell}^{+} + \frac{1}{2} \sum_{\ell'=\ell+1}^{\text{LM}} (\tau_{\ell'+1,\ell} + \tau_{\ell',\ell}) (\pi B_{\ell'+1} - \pi B_{\ell'}) + (\pi B_{\text{g}} - \pi B_{\text{LM}+1}) \tau_{\ell,\text{LM}+1} \quad (13.20)$$

Currently LK=5 and LM=12 in the 12-L model. Above the level LK, we use Dickinson (1973)'s parameterization of long wave radiative cooling described in section 13.7. In the 5-L model, LK=1 and LM=5.

### 13.2.4 Cloudy atmosphere

Five types of clouds are identified currently. They are schematically shown in Fig. 13.4 and are classified as 1) clouds associated with large-scale condensation, 2) cirrus associated with sub-grid-scale deep cumulus convection, 3) sub-grid-scale penetrative cumulus convection, 4) clouds associated with middle level convection, and 5) stratus clouds associated with supersaturation within the planetary boundary layer. Currently only the first two types of clouds explicitly interact with radiation. Clouds are treated as black body radiators with a fractional cloudiness  $CL_{\ell}$  equals to unity, except when the cloud layers are above 400 mb or colder than  $-40^{\circ}\text{C}$ . In the latter case, clouds are considered to be in ice phase (*i.e.*, cirrus), and the fractional cloudiness  $CL_{\ell}$  is assigned the value 0.5. Thus, for a cloudy atmosphere (13.19) and (13.20) are modified to

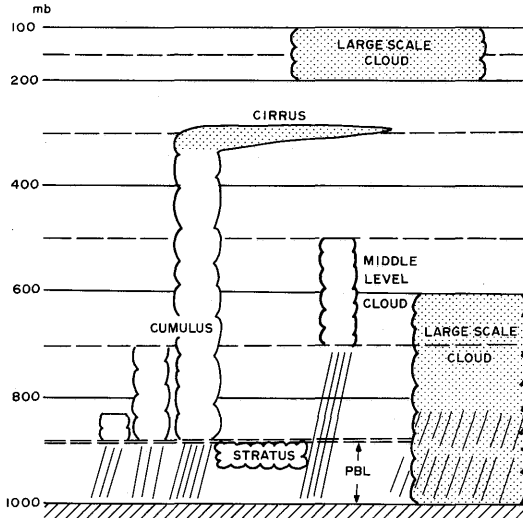


Fig. 13.4 Various types of clouds identified in the MRI-GCM-I. Radiatively interactive clouds are shaded.

for a cloudy atmosphere (13.19) and (13.20) are modified to

$$\begin{aligned}
 R_{\downarrow}^{\downarrow} &= \pi B_{\ell} - (\pi B_{\ell} - \pi B_{\ell-1}) \bar{\tau}_{\ell}^{-} (1 - CL_{\ell-1}) \\
 &\quad - \frac{1}{2} \sum_{\ell'=\ell-2}^{LK} (\tau_{\ell'+1,\ell}) (\pi B_{\ell'+1} - \pi B_{\ell'}) \prod_{k=\ell-1}^{\ell'} (1 - CL_k) \\
 &\quad - [(\pi B_{LK} - \pi B_T) \tau_{LK,\ell} + (\pi B_T - \pi B_c) \tau_{\ell} + \pi B_c \tilde{\tau}_{\ell}] \prod_{k=\ell-1}^{LK} (1 - CL_k) \quad (13.21)
 \end{aligned}$$

$$\begin{aligned}
 R_{\downarrow}^{\uparrow} &= \pi B_{\ell} + (\pi B_{\ell+1} - \pi B_{\ell}) \bar{\tau}_{\ell}^{-} (1 - CL_{\ell}) \\
 &\quad + \frac{1}{2} \sum_{\ell'=\ell+1}^{LM} (\tau_{\ell'+1,\ell} + \tau_{\ell',\ell}) (\pi B_{\ell'+1} - \pi B_{\ell'}) \prod_{k=\ell}^{\ell'} (1 - CL_k) \\
 &\quad + (\pi B_g - \pi B_{LM+1}) \tau_{\ell,LM+1} \prod_{k=\ell}^{LM} (1 - CL_k) \quad (13.22)
 \end{aligned}$$

### 13.2.5 Effective absorber amounts

#### 13.2.5.a Water vapor

The effective absorber amount  $u^*$  is given by (13.7). The water vapor mixing ratio  $q_{H_2O}(p)$  is a prognostic variable which is calculated by the way described in Chapters 6, 7 and 9. Pressure scaling laws were originally incorporated to replace an inhomogeneous optical path with an equivalent homogeneous optical path. Since this is an empirical method, there is some uncertainty in the value of the pressure scaling factor  $\alpha_{H_2O}$ . In Table 13.1 the values of  $\alpha_{H_2O}$  which is adopted by various authors are tabulated. Currently  $\alpha_{H_2O}$  is assumed to be 0.9 after McClatchey *et al.* (1972), who found a best fit to laboratory and theoretical data for that value.

Table 13.1 Pressure scaling factor for water vapor adopted by various authors.

	MANABE <i>et al.</i> (1967)	SASAMORI (1968)	KATAYAMA (1972)	McCLATCHEY <i>et al.</i> (1972)
$\alpha_{H_2O}$	0.7	1.0	0.6	0.9

#### 13.2.5.b Carbon dioxide

For carbon dioxide, (13.7) is slightly modified as

$$u^*_{CO_2}(p) = \frac{1}{g \rho_{CO_2,NTP}} \int_P^{PS} q_{CO_2}(p') \left(\frac{p'}{p_0}\right) \alpha^{CO_2} dp' \quad (13.23)$$

where  $\rho_{CO_2,NTP} = 1.977 \text{ kg m}^{-3}$  is the carbon dioxide density at NTP. The mixing ratio of  $CO_2$

is assumed to be constant both in space and time, and is assigned the value 0.0489 percent by weight ( $q_{CO_2} = 4.89 \times 10^{-4}$ ), or 0.032 percent by volume (320PPM). Thus

$$u^*_{CO_2}(p) = \frac{252}{\alpha_{CO_2} + 1} \left[ \left( \frac{p_s}{p_o} \right)^{\alpha_{CO_2} + 1} - \left( \frac{p}{p_o} \right)^{\alpha_{CO_2} + 1} \right] \quad (13.24)$$

Following Manabe and Möller (1961),  $\alpha_{CO_2}$  is taken as 0.86.

### 13.2.5.c Ozone

The ozone mixing ratio  $q_{O_3}(p)$  is predicted in a way described in Chapters 6 and 12. The predicted amount is used for the radiation calculation. The effective absorber amount of ozone is also given by (13.23) by replcing  $\rho_{CO_2,NTP}$  and  $\alpha_{CO_2}$  with  $\rho_{O_3,NTP} = 2.144 \text{ kg m}^{-3}$  and  $\alpha_{O_3} = 0.3$  respectively, after Manabe and Möller (1961).

Thus,

$$u^*_{O_3,\ell} = \frac{1}{\rho_{O_3,NTP}} \sum_{\ell'=\ell}^{LM} q_{O_3,\ell'} \int_{p_{\ell'}}^{p_{\ell'+1}} \left( \frac{p'}{p_o} \right)^{\alpha_{O_3}} dp' \quad (13.25)$$

## 13.2.6 Empirical transmission function equations

### 13.2.6.a Water vapor

Total transmission function of a mixture of gases is given by (13.11) and (13.12). Yamamoto (1952) calculated  $\tau$  and  $\tilde{\tau}$  for water vapor from experimental laboratory data. Katayama (1972) obtained the empirical transmission functions for  $\tau_{H_2O}(u^*_{H_2O}, \bar{T})$  by taking an average of  $\tau$  given by Yamamoto (1952) for  $T = 220^\circ\text{K}$ ,  $260^\circ\text{K}$ , and  $300^\circ\text{K}$ , *i.e.*,

$$\tau_{H_2O}(u^*, T) = \begin{cases} 0.373 - 0.274Z + 0.035Z^2, & (u^* \geq 1) \\ 0.373 - 0.2595Z - 0.0275Z^2, & (10^{-4} \leq u^* < 1) \\ F(298.7, 1.0), & (u^* < 10^{-4}) \end{cases} \quad (13.26)$$

where  $F(a,b) = 1/(1+au^{*b})$  and  $Z = \log_{10} u^*$ .

And for  $\tilde{\tau}_{H_2O}(u^*, T_c)$

$$\tilde{\tau}_{H_2O}(u^*, 220^\circ\text{K}) = \begin{cases} 0.254 - 0.1985Z + 0.0205Z^2, & (u^* \geq 0.1) \\ 0.216 - 0.2827Z - 0.0258Z^2, & (10^{-4} \leq u^* < 0.1) \\ F(2.56, 0.39), & (u^* < 10^{-4}) \end{cases} \quad (13.27)$$

### 13.2.6.b Carbon dioxide and ozone

We adopt empirical transmission function equations derived by Schlesinger (1976) both for  $15\mu$  band of carbon dioxide and for  $9.6\mu$  band of ozone based on the experimental

laboratory measurements by Elsasser (1960).

$$\tau_{\text{CO}_2}(u_{\text{CO}_2}^*, T) = 0.924 - 0.0390Z - 0.00466Z^2 \quad (13.28)$$

$$\tau_{\text{O}_3}(u_{\text{O}_3}^*, T) = 0.919 - 0.0252Z - 0.000998Z^2 \quad (13.29)$$

where  $Z$  equals to  $\log_{10} u_{\text{CO}_2}^*$  for (13.28) and  $\log_{10} u_{\text{O}_3}^*$  for (13.29).  $\tau_{\text{CO}_2}(u_{\text{CO}_2}^*, \bar{T})$  and  $\tau_{\text{O}_3}(u_{\text{O}_3}^*, \bar{T})$  are defined as the arithmetic mean of  $\tau_{\text{CO}_2}$  and  $\tau_{\text{O}_3}$  over  $-80^\circ\text{C}$  to  $40^\circ\text{C}$ .

### 13.2.6.c Bulk transmission functions

Katayama (1972) introduced the bulk transmission functions  $\bar{\tau}_\ell^\pm$  by (13.17) and (13.18) which are evaluated by linear interpolation between  $\bar{\tau}_\ell^\pm = 1$  for  $|u^* - u_\ell^*| = 0$  and  $\bar{\tau}_\ell^\pm = \bar{\tau}_{\ell \pm 1, \ell}$  as,

$$\bar{\tau}_\ell^\pm = (1 + m_\ell^\pm \tau_{\ell \pm 1, \ell}) / (1 + m_\ell^\pm) \quad (13.30)$$

The linear interpolation factors  $m_\ell^\pm$  must be determined by the physical parameters of the adjacent layers. Katayama (1972) determined  $m_\ell^\pm$  once and for all by numerical experiments in which trapezoidal integration scheme (13.17) was evaluated numerically by subdividing the layer under consideration into thin sublayers of 10 mb thickness. In this calculation, the vertical distribution of the water vapor mixing ratio  $q$  and the temperature  $T$  in an adjacent layer are assumed to be

$$q = q_\ell (p/p_\ell)^{k_\ell} \quad (13.31)$$

$$T = T_\ell + \gamma_\ell (p - p_\ell)$$

We follow Katayama's (1972) numerical experiment. He could express  $m_\ell^\pm$  approximately as a linear function of  $\Delta p$ , the depth of layer in mb, when the remaining parameters are fixed. Thus,

$$m_\ell^\pm = a_\ell^\pm + b_\ell^\pm \Delta p / 100. \quad (13.32)$$

$a_\ell^\pm$  and  $b_\ell^\pm$  are obtained empirically,

$$a_\ell^+ = L_a^+(p_\ell) + F_a^+(z_\ell) \quad (13.33)$$

$$b_\ell^+ = L_b^+(p_\ell) + F_b^+(z_\ell) + \left(\frac{\partial b}{\partial k}\right)^+ \Delta k_\ell + \left(\frac{\partial b}{\partial \gamma}\right)^+ \Delta \gamma_\ell$$

where  $\Delta k = k_\ell - 3$ ,  $\Delta \gamma_\ell = \gamma_\ell - 10$  ( $^\circ\text{K}/100$  mb), and

$$L_a^+(p_\ell) = -1.66 + 1.76 \log_{10} p_\ell, \quad (13.34)$$

$$L_b^+(p_\ell) = -0.197 + 0.0002 p_\ell,$$

$$F_a^+(Z_\ell) = 0.30 Z_\ell + 0.28 Z_\ell^2 + 0.04 Z_\ell^3, \quad (13.35)$$

$$F_b^+(Z_\ell) = 0.0812 Z_1 - 0.045 Z_1^2 + 0.02334 Z_1^3,$$

$$\left(\frac{\partial b}{\partial k}\right)^+ = \text{Min}(-0.041 + 0.021 Z_{\ell} - 0.006) < 0, \quad (13.36)$$

$$\left(\frac{\partial b}{\partial \gamma}\right)^+ = \text{Max}(0.01225 + 0.007 Z_{\ell}, 0.0093) > 0,$$

$$a_{\ell}^- = -0.09L_{\bar{a}}^-(p_{\ell}) + F_{\bar{a}}^+(Z_{\ell} - 0.105L_{\bar{a}}^-(p_{\ell})), \quad (13.37)$$

$$b_{\ell}^- = -0.09L_{\bar{b}}^-(p_{\ell}) + F_{\bar{b}}^-(Z_{\ell} - 0.105L_{\bar{b}}^-(p_{\ell})) + \left(\frac{\partial b}{\partial k}\right)^- \Delta k_{\ell} + \left(\frac{\partial b}{\partial \gamma}\right)^- \Delta \gamma_{\ell} \\ L_{\bar{a}}^-(p_{\ell}) = \text{Max}(61.86 - 22.92 \log_{10} p_{\ell}, 76.63 - 28.39 \log_{10} p_{\ell}), \quad (13.38)$$

$$L_{\bar{b}}^-(p_{\ell}) = \text{Min}(-42.59 + 15.78 \log_{10} p_{\ell}, -60.81 + 22.53 \log_{10} p_{\ell}), \\ F_{\bar{a}}^-(X) = 2.57 + 0.233 X + 0.18 X^2 + 0.027 X^3, \quad (13.39)$$

$$F_{\bar{b}}^-(X) = 1.42 + 0.48 X + 0.16 X^2 + 0.011 X^3, \\ \left(\frac{\partial b}{\partial k}\right)^- = 0.08 + (0.371 - 0.102 \log_{10} p_{\ell})(Z_{\ell} + 2.1) > 0, \quad (13.40)$$

$$\left(\frac{\partial b}{\partial r}\right)^- = \text{Min}(-0.0325 - 0.005 Z_{\ell}, -0.0275) < 0,$$

In the above  $Z_{\ell} = \log_{10} q_{\ell}$ ,  $Z_1 = |Z_{\ell} + 2.5|$ , and X is a dummy variable.

Recall that  $\bar{\tau}_{\ell}^{\pm}$  were introduced due to the failure of the trapezoidal integration scheme for the layers adjacent to the level under consideration.  $\tau$  varies more rapidly with  $\pi B$  than a linear relationship within these layers. This nonlinear character of  $\tau$  is most pronounced in the troposphere where water vapor is abundant. However in the stratosphere where water vapor is less important,  $\pi B$  is more uniform (Schlesinger, 1976). Thus,

$$m_{\ell}^{\pm} = 1 \quad \ell \leq \text{LS} \quad (13.41)$$

is assumed above 100 mb level.

### 13.2.7 Long wave radiative cooling in the upper stratosphere

Although Katayama's method of using mean transmission functions (13.5) and (13.6) is good in the troposphere and also in the lower stratosphere, it is less so in the upper stratosphere where unisotropy of radiative flux dominates. As a substitute of Katayama's method, we adopt Dickinson (1973)'s long wave radiative cooling parameterization in the upper stratosphere (*i. e.* the region above 13.9 mb in the current 12 layer version. See Fig. 13.2).

That is

$$\left(\frac{\partial T_{\ell}}{\partial t}\right)_{\text{tr}} = -C_{o,\ell} - a_{o,\ell}(T_{\ell} - T_{o,\ell})\beta_{\ell} \quad (13.42)$$

where

$$\beta_{\ell} = \begin{cases} 1, & \text{if } |T_{\ell} - T_{o,\ell}| \leq 5^{\circ}\text{K} \\ 1 + \frac{0.0033(T_{\ell} - T_{o,\ell})}{T_{o,\ell} - 135} & \text{if } |T - T_{o,\ell}| > 5^{\circ}\text{K and } T_{\ell} \geq 130^{\circ}\text{K} \\ \frac{e^{-960/T_{\ell}} - e^{-960/T_{o,\ell}}}{960e^{-960/T_{o,\ell}}(T_{\ell} - T_{o,\ell})} T_{o,\ell}^2 & \text{if } |T_{\ell} - T_{o,\ell}| > 5^{\circ}\text{K and } T_{\ell} < 130^{\circ}\text{K} \end{cases} \quad (13.43)$$

$C_{o,\ell}$  is the cooling rate expected for the reference temperature profile  $T_{o,\ell}$ , and  $a_{o,\ell}$  is a Newtonian cooling coefficient. As for a reference temperature  $T_{o,\ell}$ , the 1962 standard atmosphere profile is adopted.  $\beta_{\ell}$  is a modification factor introduced by Dickinson and revised by Schlesinger (1976).

The values of  $T_{o,\ell}$ ,  $C_{o,\ell}$  and  $a_{o,\ell}$  for the upper four layers are presented in Table 13.2.

Table 13.2 Values used in the Dickinson's long wave cooling parameterization.

k	p (mb)	$T_{o,\ell}$ (K)	$C_{o,\ell}$ (K DAY <sup>-1</sup> )	$a_{o,\ell}$ (DAY <sup>-1</sup> )
1	1.39	265.73	9.47	0.180
2	2.68	251.81	6.14	0.127
3	5.18	238.57	4.17	0.0993
4	10.0	227.72	2.62	0.0755

### 13.3 Solar radiation

#### 13.3.1 Basic quantities

The extraterrestrial solar flux incident on a horizontal surface is given by

$$S = \bar{S}_o \left( \frac{\bar{\gamma}_E}{\gamma_E} \right)^2 \cos \zeta \quad (13.44)$$

where

$$\cos \zeta = \sin \phi \sin \delta + \cos \phi \cos \delta \cos h, \quad (13.45)$$

$S_o = 1345 \text{ watt m}^{-2}$  is the solar constant at one astronomical unit  $\bar{\gamma}_E$ ,  $\gamma_E$  is the earth-sun distance,  $\zeta$  is the solar zenith angle,  $\phi$  is the latitude,  $\delta$  is the solar declination and  $h$  is the hour angle of the sun. As shown in Appendix A13.1,  $\delta$  and  $\gamma_E$  can be determined by a perturbation of Kepler's second law. The hour angle at each grid point is updated at every

adiabatic time step, and the solar declination and earth-sun distance are updated once a simulated day.

In the solar radiation parameterization developed by Katayama (1972) and Schlesinger (1976), the solar flux under cloudless conditions is depleted only by water vapor and ozone absorption and Rayleigh scattering. The effective absorption bands of water vapor for the solar spectrum exist in the wave length range  $\lambda > 0.9\mu$ . As the amount of Rayleigh scattering varies as  $\lambda^{-4}$ , the scattering in that range can be neglected. As for ozone, the absorption bands exist in the wavelength range  $\lambda < 0.8\mu$ . Because the amount of Rayleigh scattering increases exponentially with pressure, and because the heating by ozone absorption below 200 mb is negligible compared to the heating by water vapor absorption, we can neglect the effect of Rayleigh scattering on ozone absorption above 200 mb and also neglect the effect of ozone absorption on Rayleigh scattering below 200 mb.

Following Joseph (1966, 70) and based upon above considerations, the solar radiation is divided into two parts. One is "the scattered part",

$$S_0^s = 0.634 S_0 \cos \xi \quad 0.9\mu > \lambda \quad (13.46)$$

and the other "the absorbed part",

$$S_0^a = 0.366 S_0 \cos \xi \quad \lambda > 0.9\mu \quad (13.47)$$

### 13.3.2 Absorptivity of water vapor

Schlesinger (1976) calculated water vapor absorptivity  $A_{H_2O}$  from the data of McClatchey *et al.* (1972) and approximated the absorptivity piecewisely by quadratic polynomials;

$$A'_{H_2O}(X) = a_i + b_i X + c_i X^2 \quad X_{i-1} \leq X < X_i \quad (13.48)$$

$$A_{H_2O}(X) = A'_{H_2O}(X)/0.366 \quad (13.49)$$

$$X = u^* M \quad (13.50)$$

where the effective water vapor amount  $u^*$  is given by (13.7),

$$M = 35 \sec \xi / \sqrt{1224 + \sec^2 \xi} \quad (13.51)$$

is the magnification factor after Rodgers (1967), with sphericity.  $A_{H_2O}(X)$  is the absorptivity for the "absorbed" part, and  $A'_{H_2O}(X)$  is the absorptivity for the total solar spectrum. The coefficients  $a_i$ ,  $b_i$ , and  $c_i$  are presented in Appedix A13.2.

By letting  $y = A'_{H_2O}(X)$ , the inverse function  $X = A'^{-1}_{H_2O}(y)$  was fitted into quadratic polynomials;

$$X = A'^{-1}_{H_2O}(y) = d_j + e_j y + f_j y^2, \quad y_{j-1} < y \leq y_j \quad (13.52)$$

The coefficients  $d_j$ ,  $e_j$ , and  $f_j$  are also presented in Appendix A13.2.

### 13.3.3 Absorptivity of ozone

The absorptivity function of ozone for the total solar spectrum was calculated by Schlesinger (1976) and was fitted by quadratic polynomials;

$$A'_{O_3}(X) = a_i + b_i X + c_i X^2 \quad X_{i-1} < X \leq X_i \quad (13.53)$$

$$A_{O_3}(X) = A'_{O_3}(X)/0.634 \quad (13.54)$$

where  $A_{O_3}(X)$  is absorptivity for the "scattered" part,  $A'_{O_3}(X)$  is the absorptivity for the entire solar spectrum and

$$X = u_{O_3}^* M$$

The coefficients  $a_j$ ,  $b_j$ , and  $c_j$  are tabulated in Appendix A13.3.

The effective ozone amount  $u_{O_3}^*$  is calculated by, (cf. eq. (13.21))

$$u_{O_3}^* = \frac{1}{\rho_{O_3,NTP}} \int_0^z \rho_{O_3}(z) dz = \frac{1}{g\rho_{O_3,NTP}} \int_0^p p_{O_3}(p') dp' \quad (13.55)$$

where  $\rho_{O_3}$  is the ozone density,  $q_{O_3}$  is the ozone mixing ratio and  $\rho_{O_3,NTP} = 2.144 \text{ kg m}^{-3}$  is the ozone density at NTP. In a discrete case, (13.55) can be written as,

$$u_{O_3,\ell}^* + \frac{1}{g\rho_{O_3,NTP}} \sum_{\ell'=1}^{\ell} q_{O_3,\ell'} (p_{\ell'+1} - p_{\ell'}) \quad (13.56)$$

where  $p_{\ell'}$  is the pressure at the upper surface of layer  $\ell'$ ,  $q_{O_3,\ell'}$  the predicted ozone mixing ratio for layer  $\ell'$ , and

$$u_{O_3,\ell}^* = \frac{1}{\rho_{O_3,NTP}} \int_{z_{0.5}}^{\infty} \rho_{O_3}(z) dz \quad (13.57)$$

In calculating (13.57), we assume that ozone number density  $n_{O_3}(z)$  above the top level of the model  $z_{0.5}$  decays exponentially with altitude following the mean ozone distribution by Krueger (1973). Thus,

$$n_{O_3}^*(z) = n_{O_3}(z_1) \exp\left(\frac{z - z_1}{H}\right) \quad z \geq z_1 \quad (13.58)$$

where  $z_1$  is the altitude of the midlevel of layer 1, and  $H = 4.35 \text{ km}$ . Substituting (13.58) into (13.57) gives

$$u_{O_3,\ell}^* = \frac{H \exp\left(-\frac{z_{0.5} - z_1}{H}\right) q_{O_3,\ell} p_{1.5}}{\rho_{O_3,NTP} R T_1} \quad (13.59)$$

Where  $p_{1.5}$  and  $T_1$  are pressure and temperature at the midlevel of layer 1 respectively, and

R is gas constant.

### 13.3.4 Cloudless atmosphere

#### 13.3.4.a "Absorbed" part

The "absorbed" part of the solar radiation  $S_0^s$  is absorbed only by the water vapor in the troposphere and at the earth's surface. The other absorption can be neglected. (e.g. The absorption by the water vapor in the stratosphere can be neglected in comparison to the "scattered" part absorption by ozone.)

After neglecting the absorption by water vapor on the radiation reflected by the earth's surface, the net downward flux of the "absorbed" part at the upper surface of layer  $\ell$ ,  $S_{a,\ell}$ , is

$$S_{a,\ell} = S_0^a \quad \ell = 1, \dots, LS \quad (13.60)$$

$$S_{a,\ell} = S_0^a \{1 - A_{H_2O} [(u_{H_2O,\infty}^* - u_{H_2O,\ell}^*)M]\} \quad \ell = LS+1, \dots, LM+1$$

where  $A_{H_2O}$  was given by (13.48) and (13.49). The absorption of solar radiation by water vapor in layer  $\ell$ ,  $AS_{a,\ell}$ , is therefore

$$AS_{a,\ell} = 0.0, \quad \ell = 1, \dots, LS \quad (13.61)$$

$$AS_{a,\ell} = S_{a,\ell} - S_{a,\ell+1}, \quad \ell = LS+1, \dots, LM$$

The absorption of the solar radiation that is absorbed at the earth's surface is

$$AS_{a,LM+1} = (1 - \alpha_s) S_{a,LM+1} \quad (13.62)$$

where  $\alpha_s$  is the albedo of the surface, which is given in Table 13.3.

#### 13.3.4.b "Scattered" part

By neglecting the effect of Rayleigh scattering on ozone absorption above 200 mb, the downward flux and the absorption of the downward flux of the scattered part are

$$S_{s,\ell}^{\downarrow} = S_0^s \{1 - A_{O_3}(u_{O_3,\ell}^* M)\} \quad (13.63)$$

$$AS_{s,\ell}^{\downarrow} = S_{s,\ell}^{\downarrow} - S_{s,\ell+1}^{\downarrow}, \quad \ell = 1, \dots, LS+1$$

$$AS_{s,\ell}^{\downarrow} = 0.0, \quad \ell = LS+2, \dots, LM \quad (13.64)$$

where the effective ozone amount  $u_{O_3,\ell}^*$ , is given by (13.56) and (13.59).

By neglecting the effect of ozone absorption on Rayleigh scattering below 200 mb, the downward flux of the "scattered" part at the earth's surface,  $S_{s,LM+1}^{\downarrow}$  is

$$S_{s,LM+1}^{\downarrow} = S_{s,LS+2}^{\downarrow} (1 - \alpha_o) / (1 - \alpha_o \alpha_s) \quad (13.65)$$

where

Table 13.3 Surface albedo adopted in the MRI-GCM- I .

Surface condition	Albedo
open ocean	0.07
bare land	0.14
frozen land	0.3
permanent land ice and snow	Min (0.85, 0.7 + 0.15 h) where h is height in km
bare sea ice	0.4
snow on sea ice	0.7
melting snow	0.5

$$\alpha_o = 0.085 - 0.247 \log_{10} \left( \frac{P_s}{1000} \cos \xi \right) \quad (13.66)$$

is the albedo due to Rayleigh scattering. (Coulson, 1959)

The "scattered" part of the solar radiation that is absorbed at the earth's surface is

$$AS_{s,LM+1}^\downarrow = (1 - \alpha_s) S_{s,LM+1}^\downarrow \quad (13.67)$$

The upward flux of the "scattered" part at LS+2,  $S_{s,LS+2}^\uparrow$ , is

$$\begin{aligned} S_{s,LS+2}^\uparrow &= S_{s,LS+2}^\downarrow - AS_{s,LM+1}^\downarrow \\ &= S_{s,LS+2}^\downarrow \{1 - (1 - \alpha_s)(1 - \alpha_o)/(1 - \alpha_o \alpha_s)\} \end{aligned} \quad (13.68)$$

By neglecting the effect of Rayleigh scattering on ozone absorption above 200 mb, the absorption of upward flux of the "scattered" part in layer  $\ell$ ,  $AS_{a,\ell}$  is

$$\begin{aligned} AS_{s,\ell}^\uparrow &= S_{s,LS+2}^\uparrow \{A_{O_3}(u_{O_3,LS+2}^* M + 1.9(u_{O_3,LS+2}^* - u_{O_3,\ell}^*)) \\ &\quad - A_{O_3}(u_{O_3,LS+2}^* M + 1.9(u_{O_3,LS+2}^* - u_{O_3,\ell+1}^*))\}, \ell = 1, \dots, LS+1 \end{aligned} \quad (13.69)$$

$$AS_{s,\ell}^\uparrow = 0.0 \quad , \quad \ell = LS+2, \dots, LM$$

where the factor 1.9 is an average magnification factor for the diffuse upward radiation. (Lacis and Hansen, 1974)

The heating rate due to absorption of solar radiation at layer  $\ell$  is given by

$$\left( \frac{\partial T}{\partial t} \right)_{sr,\ell} = \frac{g(AS_{a,\ell} + AS_{s,\ell}^\downarrow + AS_{s,\ell}^\uparrow)}{c_p(p_{\ell+1} - p_\ell)} \quad (13.70)$$

where  $p_\ell$  is the pressure at the upper surface of layer  $\ell$ . (cf. (13.4))

### 13.3.5 Cloudy atmosphere

#### 13.3.5.a Single cloud

Consider a single cloud located in layer L as shown in Fig. 13.5. The flux of the "absorbed" part at the upper surface of layer  $\ell \leq L$ ,  $S_{a,\ell}$ , is given by (13.60) as

$$S_{a,\ell} = S_0^a \{ 1 - A_{H_2O} \{ (u_{H_2O,\infty}^* - u_{H_2O,\ell}^*) M \} \} \quad (13.71)$$

By letting  $A_{c,L}$  and  $R_{c,L}$  denote the absorptivity per unit pressure thickness and the reflectivity of cloud layer L, the flux of the "absorbed" part at the upper surface of layer L+1,  $S_{a,L+1}$ , is given by

$$S_{a,L+1} = \{ 1 - R_{c,L} - A_{c,L}(p_{L+1} - p_L) \} S_{a,L} \quad (13.72)$$

where the quantity in brackets represents the transmissivity of cloud layer L. In order to calculate the fluxes beneath the cloud by (13.71), the total optical thickness from the top of the atmosphere to the upper surface of the layer under consideration is required. Katayama (1972) defined the equivalent total optical thickness of water vapor from the top of the atmosphere to the base of the cloud layer L,  $\Gamma_{L+1}$ , by

$$(1 - R_{c,L}) S_0^a \{ 1 - A_{H_2O}(\Gamma_{L+1}) \} = S_{a,L+1}, \quad (13.73)$$

hence

$$\Gamma_{L+1} = A_{H_2O}^{-1} \left( 1 - \frac{S_{a,L+1}}{(1 - R_{c,L}) S_0^a} \right) \quad (13.74)$$

where  $A_{H_2O}^{-1}$  is the inverse of the water vapor absorptivity function given by (13.52). The flux across the upper surface of any layer beneath the cloud base is, then, given by

$$S_{a,\ell} = (1 - R_{c,L}) S_0^a \{ 1 - A_{H_2O} \{ \Gamma_{L+1} + 1.66(u_{H_2O,L+1}^* - u_{H_2O,\ell}^*) \} \} \quad (13.75)$$

where 1.66 is the diffusivity factor for diffuse radiation beneath the cloud. The absorption of solar radiation is

$$AS_{a,\ell} = \begin{cases} S_{a,\ell} - S_{a,\ell+1} & , \ell = LS+1, \dots, LM \text{ except } \ell = L \\ (1 - R_{c,L}) S_{a,L} - S_{a,L+1} & , \ell = L \end{cases} \quad (13.76)$$

where  $R_{c,L}$  is the reflectivity of cloud layer L for the "absorbed" part, and  $S_{a,L}$ , the solar radiations reflected from the cloud layer. The absorption of radiation reflected from the

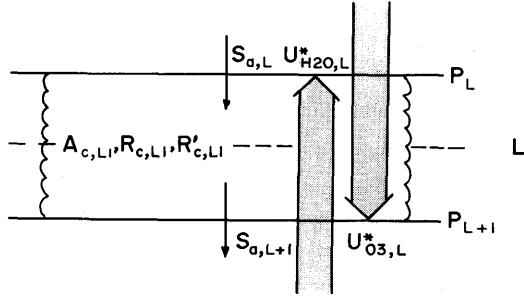


Fig. 13.5 A single cloud layer.  $u_{H_2O,\ell}^*$  follows the definition of eq. (13.7), while  $u_{H_2O,\ell}^*$  defined as the effective ozone absorber amount between the bottom level of layer  $\ell$  and top of the atmosphere.

cloud layer is neglected. The "absorbed" part of the solar radiation that is absorbed at the earth's surface is given by (13.62).

In the case of "scattered" part of the solar radiation, equations (13.63), (13.64), (13.67), and (13.69) are unchanged. In equations (13.65) and (13.68),  $\alpha_0$  is replaced by  $\alpha_c$ , the albedo of the cloudy atmosphere for the "scattered" part,

$$\alpha_c = 1 - (1 - R'_{c,L})(1 - \alpha_0) \quad (13.77)$$

where  $R'_{c,L}$  is the reflectivity of cloud layer L for the "scattered" part.

### 13.3.5.b Two or more contiguous cloud layers, and multiple clouds

In the model, each cloud layer within two or more contiguous cloud layers is treated as a separate cloud for the solar radiation calculation like one of multiple clouds.

#### (A) "Absorbed" part

For simplicity, consider two clouds each consisting of a single layer. The cloud 1 lies in the layer  $L1$  and the cloud 2 in the layer  $L2$  (see Fig. 13.6). For layers  $\ell \leq L1$ ,  $S_{a,\ell}$  is given by (13.60),

$$S_{a,\ell} = S_0^a \{1 - A_{H_2O} \{ (u_{H_2O,\infty}^* - u_{H_2O,\ell}^*)$$

M)\}

$$\ell = LS+1, \dots, LM+1 \quad (13.78)$$

By (13.72),  $S_{a,L1+1}$  is

$$S_{a,L1+1} = (1 - \bar{R}_{c,L1} - A_{c,L1}(P_{L1+1} - P_{L1})) S_{a,L1} \quad (13.79)$$

By (13.74), the equivalent total optical thickness from the top of the atmosphere to the base of cloud 1,  $\Gamma_{L1}$ , is

$$\Gamma_{L1} = A_{H_2O}^{-1} \left( 1 - \frac{S_{a,L1+1}}{(1 - \bar{R}_{c,1}) S_0^a} \right) \quad (13.80)$$

The flux across the upper surface of layers  $L1+2 \leq \ell < L2$  is given by (13.75)

$$S_{a,\ell} = (1 - \bar{R}_{c,1}) S_0^a A_{H_2O} \{ 1 - \{ \Gamma_{L1} + 1.66(u_{H_2O,L1+1}^* - u_{H_2O,\ell}^*) \} \} \quad (13.81)$$

$S_{a,L2+1}$  is given by

$$S_{a,L2+1} = (1 - \bar{R}_{c,L2} - A_{c,L2}(P_{L2+1} - P_{L2})) S_{a,L2} \quad (13.82)$$

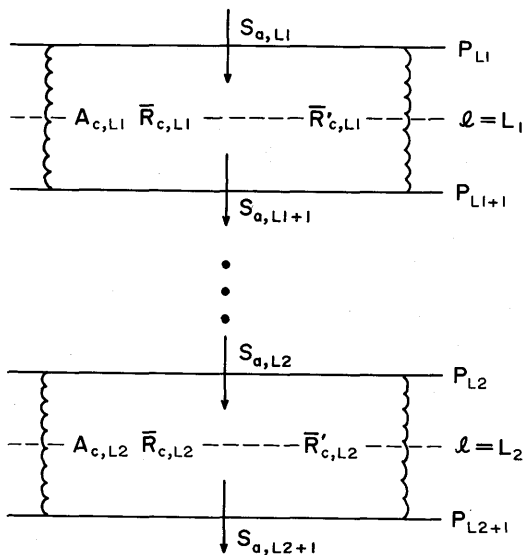


Fig. 13.6 Two separated cloud layers.

where use has been made of (13.72). The equivalent total optical thickness from the top of the atmosphere to the base of cloud 2,  $\Gamma_{L2}$ , is

$$\Gamma_{L2} = A_{H_2O}^{-1} \left\{ 1 - \left( \frac{S_{a,L2+1}}{(1-\bar{R}_{c,1})(1-\bar{R}_{c,2})S_0^a} \right) \right\} \quad (13.83)$$

The solar flux incident on the lower cloud 2,  $S_{a,L2}$ , is affected by the existence of cloud 1 (see (13.79)). Then, from (13.82) and (13.83)  $\Gamma_{L2}$  differs from what it would be if cloud 1 did not exist; that is, the equivalent total optical thickness is a function of the overlying cloud cover.

The flux across the upper surface of layers  $\ell \geq L2+2$  is

$$S_{a,\ell} = (1-\bar{R}_{c,2})(1-\bar{R}_{c,1})S_0^a \left\{ 1 - A_{H_2O} \left[ \Gamma_{L2} + 1.66(u_{L2+1}^* - u_{\ell}^*) \right] \right\} \\ \ell = L2+2, \dots, LM+1 \quad (13.84)$$

The absorption of solar radiation,  $AS_{\ell}$ , is

$$AS_{a,\ell} = \begin{cases} S_{a,\ell} - S_{a,\ell+1} & \ell = LS+1, \dots, LM \\ \text{but } \ell \neq L1 \text{ or } L2 \\ (1-\bar{R}_{c,j})S_{a,Lj} - S_{a,Lj+1}, & \ell = L1 \text{ and } L2 \end{cases} \quad (13.85)$$

The direct solar radiation in the "absorbed" part that reaches the earth's surface,  $S_{a,LM+1}^d$  is

$$S_{a,LM+1}^d = (1-\bar{R}_{c,2})(1-\bar{R}_{c,1})S_0^a \left\{ 1 - A_{H_2O} \left[ \Gamma_{L2} + 1.66u_{H_2O,L2+1}^* \right] \right\} \quad (13.86)$$

The indirect solar radiation in the "absorbed" part that reaches the earth's surface due to multiple reflections between the two clouds,  $S_{a,LM+1}^i$ , is

$$S_{a,LM+1}^i = (\bar{R}_{c,2}S_{a,L2}) \left( \frac{\bar{R}_{c,1}}{1-\bar{R}_{c,1}\bar{R}_{c,2}} \right) (1-\bar{R}_{c,2}) \left( \frac{1}{1-\alpha_s\bar{R}_{c,1,2}} \right) \quad (13.87)$$

$$\bar{R}_{c,1,2} = 1 - \left( \frac{(1-\bar{R}_{c,1})(1-\bar{R}_{c,2})}{1-\bar{R}_{c,1}\bar{R}_{c,2}} \right) \quad (13.88)$$

is the albedo of the two clouds (neglecting atmospheric absorption of the reflected radiation).

The total solar radiation in the "absorbed" part reaching the earth's surface  $S_{a,LM+1}$ , is

$$S_{a,LM+1} = S_{a,LM+1}^d + S_{a,LM+1}^i \quad (13.89)$$

and the absorption by the earth's surface is given by (13.62).

The above equations may be generalized in a straightforward manner to the case of an arbitrary number of cloud layers.

(B) "Scattered" part

The treatment is the same as that described in subsection 13.3.5 but  $\bar{R}'_{c,L}$  in (13.77) is replaced by  $\bar{R}'_{c,1,2}$  which is given by (13.88) with  $\bar{R}_{c,j}$  replaced by  $\bar{R}'_{c,j}$ .

### 13.3.6 The reflectivity and absorptivity of clouds

The reflectivities of the "absorbed" part  $R_c$ , and that of the "scattered" part  $R'_c$ , and the absorptivity per unit pressure thickness of the "absorbed" part  $A_c$ , and that of the "scattered" part  $A'_c$ , for cloud layer are assumed to be characterized by the respective properties of low, middle, or high clouds following Rodgers (1967) and Katayama (1972). That is

$$R_{c,\ell}(R'_{c,\ell}) = \begin{cases} 0.19(0.21), & \text{for } 100 \text{ mb} \leq p_\ell < 400 \text{ mb cirrus} \\ 0.46(0.54), & \text{for } 400 \text{ mb} \leq p_\ell < 800 \text{ mb and not cirrus} \\ 0.50(0.66), & \text{for } 800 \text{ mb} \leq p_\ell \text{ and not cirrus} \end{cases}$$

$$A_{c,\ell} = A'_{c,\ell} = \begin{cases} 0.05/300 \text{ mb}, & \text{for } 100 \text{ mb} \leq p_\ell < 400 \text{ mb cirrus} \\ 0.20/400 \text{ mb}, & \text{for } 400 \text{ mb} \leq p_\ell < 800 \text{ mb} \\ 0.30/200 \text{ mb}, & \text{for } 800 \text{ mb} \leq p_\ell \text{ and not cirrus} \end{cases}$$

where  $p_\ell$  is the pressure of the upper surface of layer  $\ell$ .

## Appendix A13.1 Calculation of earth-sun distance and solar zenith angle

### A13.1.1 Earth-sun distance

Although the earth's orbit around the sun is elliptic, the eccentricity of the earth's orbit is so small ( $e=0.01672$ ) that the orbit is in fact very nearly circular. Therefore the earth-sun distance  $\gamma_E$  and the angular position of the sun  $\omega(t)$  can be expressed as an asymptotic series in terms of mean angular position  $M(t)$  measured by a constant angular velocity with the periodicity of one year,

$$M(t) = \frac{2\pi}{T}(t - t_0), \quad (\text{A13.1.1})$$

where  $T$  is 365 days,  $t_0$  the time of perigee. The date of perigee adopted in the MRI-GCM-I is January 3.36 which is the mean date of perigee from 1950 through 1972. Therefore,  $M(t)$  is expressed as

$$M(t) = 0.0172142(t - 2.36), \quad (\text{A13.1.2})$$

where  $t$  is the time in days counted from January 1. Then, from Kepler's second law

$$\gamma_E(t)/\bar{\gamma}_E = A_0 - A_1 \cos M - A_2 \cos 2M - A_3 \cos 3M - \dots, \quad (\text{A13.1.3})$$

$$\omega(t) = M + B_1 \sin M + B_2 \sin 2M + B_3 \sin 3M + \dots,$$

where

$$A_0 = 1 + e^2 = 1.00027956,$$

$$A_1 = e - e^3 - e^5 - \dots \approx 0.01671825,$$

$$A_2 = e^2 - e^4 - \dots \approx 0.00013975,$$

$$A_3 = e^3 - e^5 - \dots \approx 0.00000175,$$

$$B_1 = 2e - e^3 + e^5 - \dots \approx 0.0334388,$$

$$B_2 = e^2 - e^4 + \dots \approx 0.0003494,$$

$$B_3 = e^3 - e^5 + \dots \approx 0.00000506,$$

and  $\bar{\gamma}_e$  is one astronomical unit.

### A13.1.2 Solar zenith angle

The cosine of the solar zenith angle is given by (13.45) ; the hour angle  $h$  is counted from the midday position and changes  $15^\circ$  per hour. Thus,

$$h(t) = \lambda + \frac{2\pi}{24}(t - t_G) \quad (\text{A13.1.4})$$

where  $\lambda$  is the longitude,  $t_G$  the midday time at Greenwich.

As for the solar declination  $\delta$ , it is given by

$$\delta(t) = \sin^{-1}(\sin \epsilon \sin \ell) \quad (\text{A13.1.5})$$

where  $\ell(t) = \omega(t) + \ell_0$  is ecliptic longitude of the sun,  $\ell_0$  the ecliptic longitude at perigee ( $= -1.3550737$  rad or  $-77.64^\circ$ ),  $\epsilon$  the inclinations of the earth's orbit ( $= 23^\circ 27'$ ).

**Appendix A13.2** Water vapor absorptivity function for the total solar spectrum,  $A'_{H_2O}(X)$ .  
E-5 means  $10^{-5}$

x (g cm <sup>-2</sup> )	A' <sub>H<sub>2</sub>O</sub> (x)	A <sub>H<sub>2</sub>O</sub> (X)=a+bx+cx <sup>2</sup>			x=d+eA' <sub>H<sub>2</sub>O</sub> +fA' <sub>H<sub>2</sub>O</sub> <sup>2</sup>		
		a	b	c	d	e	f
1E-5	3.19E-4						
2	5.46						
3	7.43	8.61E-5	2.47E1	-9.92E4			
4	9.13						
5	1.07E-3				-1.17E-6	2.94E-2	1.172E1
6	1.22						
7	1.35						
8	1.48						
9	1.60	4.57E-4	1.37E1	-1.23E4			
1E-4	1.72						
2	2.69						
3	3.47						
4	4.12						
5	4.69						
6	5.22				-2.23E-6	3.20E-2	1.60E1
7	5.70	1.41E-3	7.52E0	-1.96E3			
8	6.15						
9	6.58						
1E-3	6.98						

Table (Continued)

x (g cm <sup>-2</sup> )	A' <sub>H<sub>2</sub>O</sub> (x)	A <sub>H<sub>2</sub>O</sub> (X)=a+bx+cx <sup>2</sup>			x=d+eA' <sub>H<sub>2</sub>O</sub> +fA' <sub>H<sub>2</sub>O</sub> <sup>2</sup>		
		a	b	c	d	e	f
2E-3	1.01E-2	3.82E-3	3.47E0	-1.97E2	4.61E-4	-7.53E-2	2.22E1
3	1.25						
4	1.44						
5	1.61						
6	1.76						
7	1.90						
8	2.02	1.06E-2	1.32E0	-1.62E1	1.32E-2	-1.20E0	4.69E1
9	2.13						
1E-2	2.24						
2	3.03	2.25E-2	5.02E-1	-1.79E0	9.31E-2	-5.18E0	9.66E1
3	3.57						
4	3.99						
5	4.32						
6	4.62						
7	4.87						
8	5.10						
9	5.30						
1E-1	5.49						
2	6.80	4.23E-2	1.44E-1	-1.04E-1	6.29E-1	-2.33E1	2.49E2
3	7.64						
4	8.26						
5	8.75						
6	9.17						

Table (Continued)

x (g cm <sup>-2</sup> )	A' <sub>H<sub>2</sub>O</sub> (x)	A <sub>H<sub>2</sub>O</sub> (X)=a+bx+cx <sup>2</sup>			x=d+eA' <sub>H<sub>2</sub>O</sub> +fA' <sub>H<sub>2</sub>O</sub> <sup>2</sup>		
		a	b	c	d	e	f
7E-1	9.53E-2	7.76E-2	2.82E-2	-3.14E-3	4.59E0	-1.12E2	7.45E2
8	9.85						
9	1.01E-1						
1E0	1.04						
2	1.22	1.25E-1	-5.04E-3	-8.30E-5	2.96E1	-5.12E2	2.35E3
3	1.32						
4	1.41						
5	1.47						
6	1.52						
7	1.57						
8	1.61						
9	1.64						
1E1	1.68	1.82E-1	8.01E-4	-2.00E-6	6.08E2	-6.70E3	1.90E4
2	1.89						
3	2.02						
4	2.11						
5	2.18						
6	2.24						
7	2.29						
8	2.33						
9	2.37	2.60E3	-2.40E4	5.68E4			
1E2	2.40						
2	2.62						

Table (Continued)

x (g cm <sup>-2</sup> )	A' <sub>H<sub>2</sub>O</sub> (x)	A <sub>H<sub>2</sub>O</sub> (X)=a+bx+cx <sup>2</sup>			x=d+eA' <sub>H<sub>2</sub>O</sub> +fA' <sub>H<sub>2</sub>O</sub> <sup>2</sup>		
		a	b	c	d	e	f
3E2	2.75E-1	2.41E-1	1.29E-4	-5.99E-8	1.30E4	-1.03E5	2.05E5
4	2.84				6.57E4	-4.56E5	7.98E5
4	2.91						
6	2.96						
7	3.00						
8	3.04						
9	3.08						
1E3	3.10	2.94E-1	1.98E-5	-1.62E-9	3.57E5	-2.22E6	3.46E6
2	3.29				1.13E6	-6.58E6	9.62E6
3	3.39						
4	3.46						
5	3.51						
6	3.55						
7	3.59						
8	3.61	3.27E-1	5.98E-6	-2.02E-10	1.13E6	-6.58E6	9.62E6
9	3.64						
1E4	3.66						

**Appendix A13.3** Ozone absorptivity function for the total solar spectrum,  $A'_{O_3}(X)$ .  
E-5 means  $10^{-5}$

x (cm-NTP)	$A'_{O_3}(x)$	$A'_{O_3}(x) = a + bx + cx^2$		
		a	b	c
1E-5	1.48E-5	2.62E-7	1.47E0	-1.22E2
2	2.95			
3	4.42			
4	5.89			
5	7.35			
6	8.82			
7	1.03E-4			
8	1.17			
9	1.32			
1E-4	1.46	1.82E-4	1.25E0	-5.79E1
2	2.90			
3	4.31			
4	5.70			
5	7.06			
6	8.39			
7	9.71			
8	1.10E-3			
9	1.23			
1E-3	1.35	3.24E-3	4.74E-1	-6.30E0
2	2.48			
3	3.44			
4	4.26			
5	4.97			
6	5.59			
7	6.14			
8	6.63			
9	7.06			
1E-2	7.46	8.76E-3	1.16E-1	-2.26E-1
2	1.01E-2			
3	1.18			
4	1.31			
5	1.42			
6	1.51			
7	1.59			
8	1.66			
9	1.73			
1E-1	1.80E-2			

Table (Continued)

x (cm-NTP)	A'o <sub>o</sub> (x)	A'o <sub>o</sub> (x) = a + bx + cx <sup>2</sup>		
		a	b	c
2E-1	2.30E-2	1.54E-2	4.08E-2	-8.51E-3
3	2.70			
4	3.05			
5	3.37			
6	3.68			
7	3.97			
8	4.25			
9	4.52			
1E0	4.78			
2	7.15	2.51E-2	2.44E-2	-7.83E-4
3	9.21			
4	1.11E-1			
5	1.27			
6	1.43			
7	1.57			
8	1.70			
9	1.82			
1E1	1.93			
2	2.70	7.85E-2	1.32E-2	-1.79E-4
3	3.12			

**Appendix I. Tree diagram of the MRI-GCM-I**

The schematic structure of the program of the MRI-GCM-I is illustrated in Fig. AI.1. Names in the boxes indicate the subroutines. The functions of the subroutines are listed in Table AI. 1.

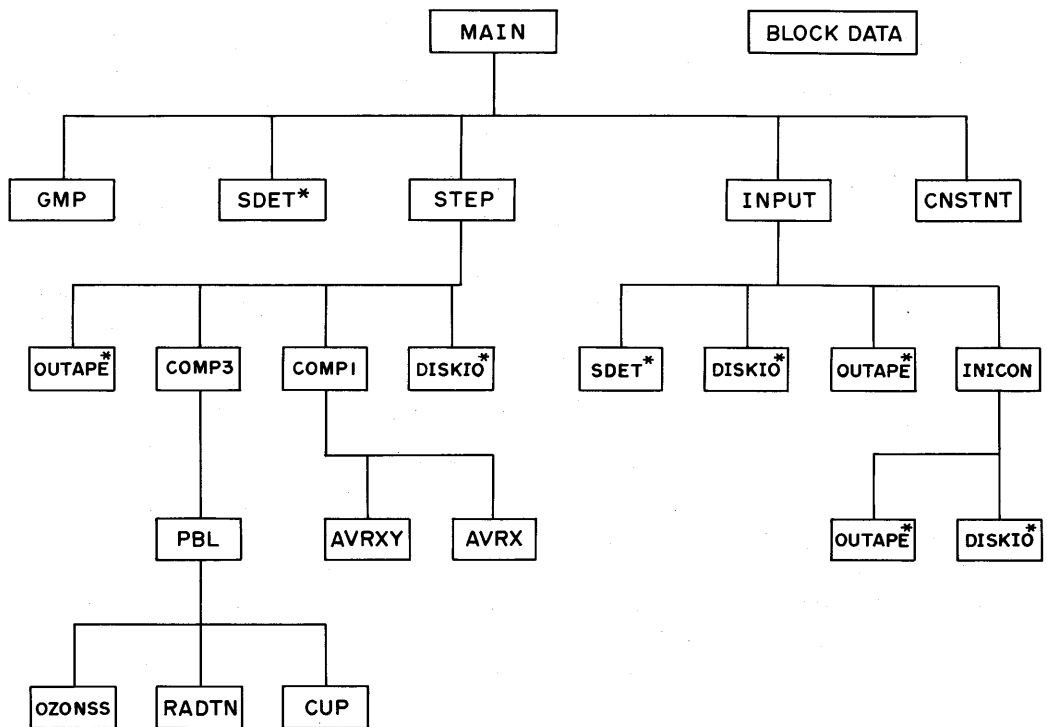


Fig. AI.1 Tree diagram of the MRI-GCM-I. Names in the boxes indicate subroutines. Subroutines with asterisk appear more than once in the diagram.

Table AI.1

subroutine	function
MAIN	Main program.
CNSTNT	Computing constant parameters once for all.
INPUT	Preparing initial data.
STEP	Doing time integration. Controlling data flow and advective and physical processes.
SDET	Computing astronomical parameters. Refer to Chapter 13.
GMP	Adjusting the global average surface pressure to its standard values once every 24 hours.*
INICON	Setting the initial condition when the previous history is not available.
OUTAPE	Dealing with the data exchange between "MSS" (Mass Strage System) and disk.
DISKIO	Dealing with the data exchange between global data and latitude strip data.
COMP1	Calculating the dynamical precesses. Refer to Chapters 1, 3 and 11.
COMP3	Calculating the physical processes. Refer to Chapters 2, 6, 9, 10 and 11.
AVRX	Smoothing the selected terms at $\Pi$ - and $u$ -points near the poles. Refer to Chapter 4.
AVRXY	Smoothing the selected terms at $v$ -points near the poles. Refer to Chapter 4.
PBL	Computing the PBL processes. Refer to Chapter 8.
CUP	Computing the processes of penetrative cumulus convection. Refer to Chapter 7.
RADTN	Computing the radiation processes. Refer to Chapter 13.
OZONSS	Computing the photochemical processes of ozone. Refer to Chapter 12.

\* Although the mass continuity equation in the finite difference form guarantees the conservation of mass in both the horizontal and vertical differencing, the globally integrated mass continues to decrease with time. This is related with the fact that the computer has the limit of at most 7 decimal digits in the single-precision calculation. This gives rise to a small loss of mass at each time step.

## Appendix II. Surface boundary conditions and numerical constants used in the MRI-GCM-I

### II.1 Surface boundary conditions.

Topography used in the MRI-GCM-I is shown in Fig. AII.1. Also shown are prescribed sea surface temperature and sea-ice distributions for January, April, July and October.

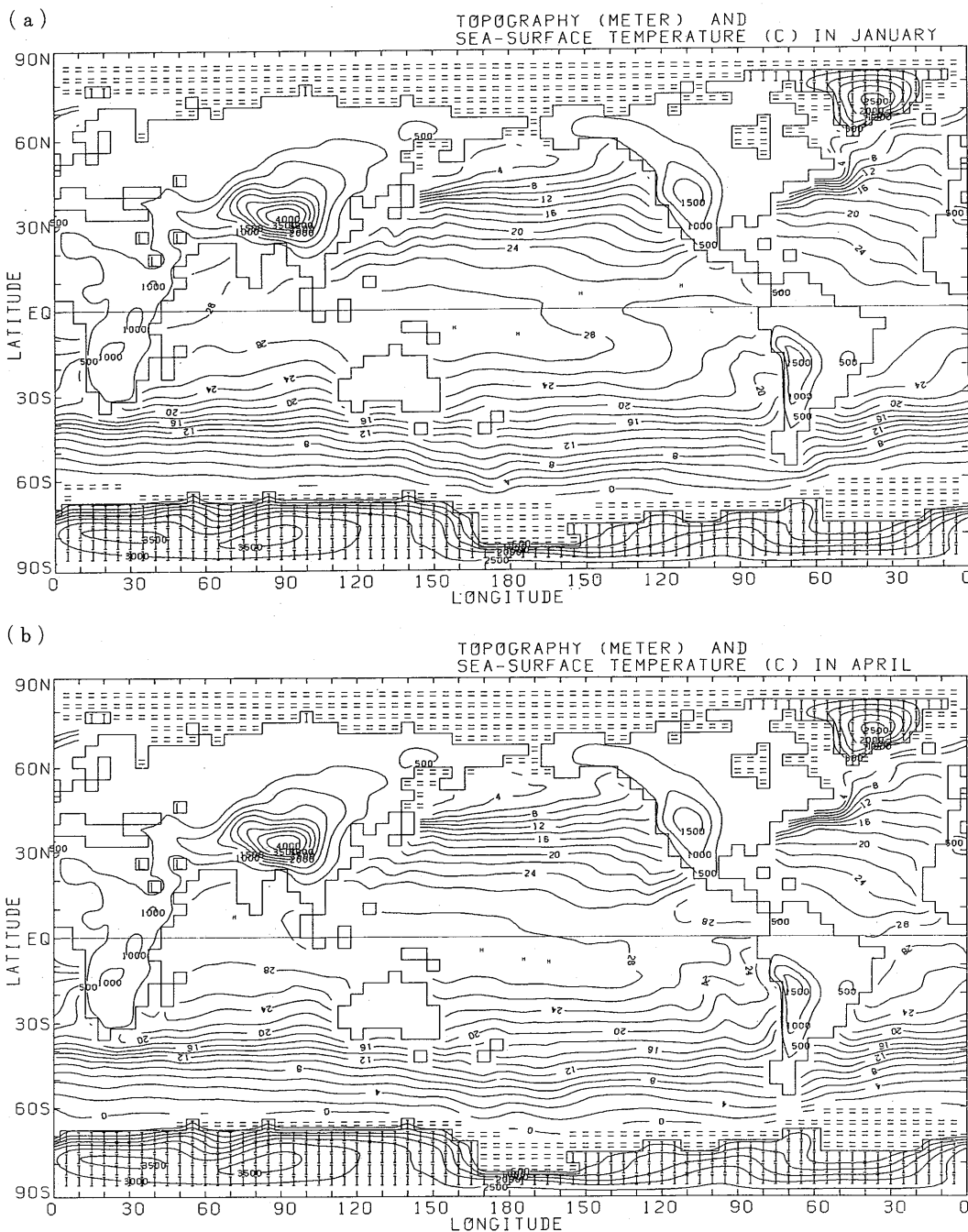


Fig. AII.1 Topography used in the MRI • GCM-I. The contour interval is 500 m. The sea surface temperature distributions are shown over the ocean for (a) January, (b) April, (c) July and (d) October, together with land ice distributions indicated with "I", and sea-ice distributions indicated with "=". The contour interval for sea surface temperature is 2°C. The grid points indicated with "L" are lake points.

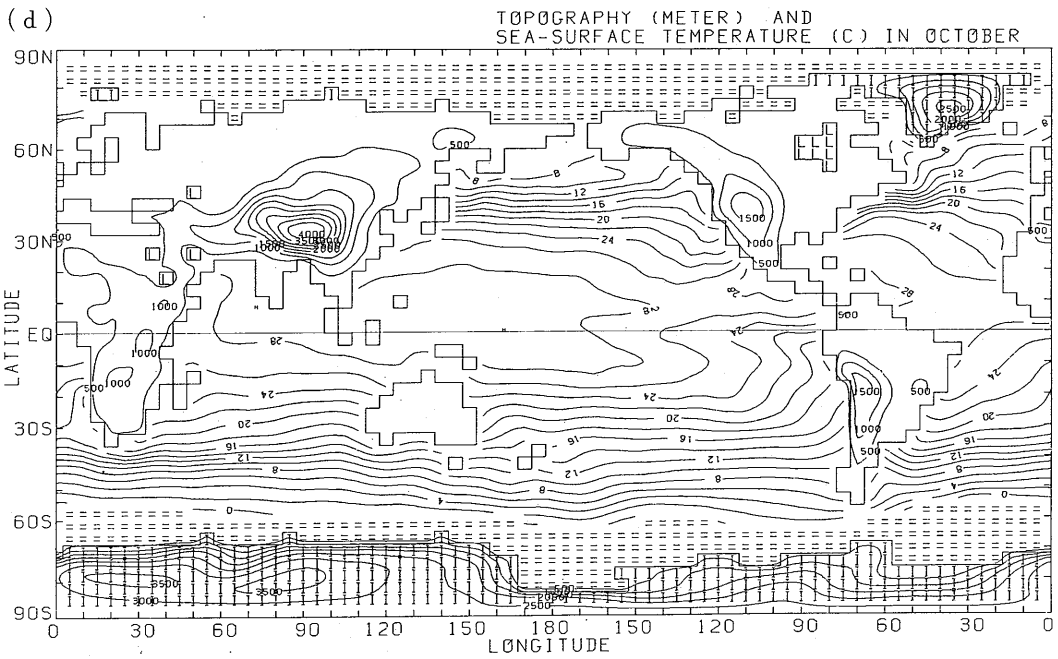
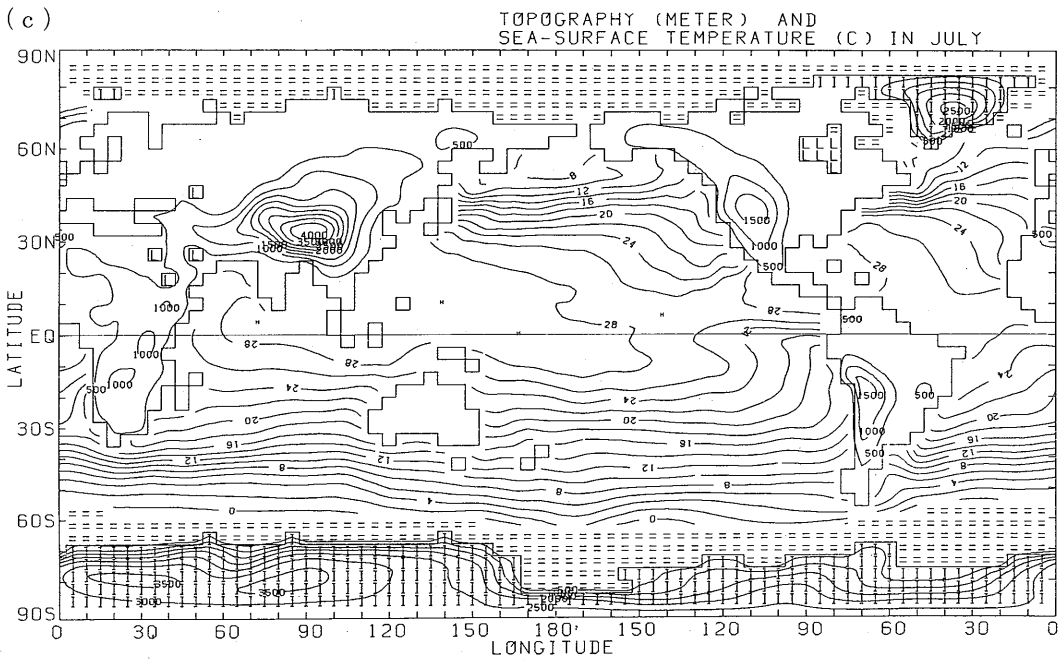


Fig. AII.1(continued)

## II.2 Numerical constants and functions used in the MRI-GCM-I

Numerical constants and functions used in the MRI-GCM-I are summarized in Tables All.1 and All.2. The names of constants are shown in the left column. Also the conventional symbols or symbols used in the text are shown in the parentheses. In the middle column the values are shown. When the values are derived from other variables in the program of the MRI-GCM-I, the relations are also shown. The first line of the right column shows the variable name used in the program, and the second line shows the subroutine where the variable is defined (see Fig. AI.1).

Tabel All.1 Fundamental numerical constants and functions

solar constant ( $S_0$ )	1345 W m <sup>-2</sup>	S0 COMP3
eccentricity of the earth's orbit ( $e$ )	0.01672	SDET
inclination of the earth's orbit	23° 27'	SDET
perihelion	January 3.36 (2.36 day)	SDET
1 year	365 days	DAYPYR BLOCK DATA
mean radius of the earth ( $a$ )	6375 km	RAD BLOCK DATA
acceleration of gravity ( $g$ )	9.81 m s <sup>-2</sup>	GRAV BLOCK DATA
gas constant for dry air ( $R$ )	287 J kg <sup>-1</sup> K <sup>-1</sup>	RGAS BLOCK DATA
latent heat of vaporization ( $L$ )	25.12 × 10 <sup>5</sup> J kg <sup>-1</sup>	HLTM BLOCK DATA
latent heat of sublimation ( $L_t$ )	28.48 × 10 <sup>5</sup> J kg <sup>-1</sup>	HLTF CUP
latent heat of melting ( $L_i$ )	3.36 × 10 <sup>5</sup> J kg <sup>-1</sup>	HLTI, HICE CUP, COMP3
ratio of gas constant to specific heat at constant pressure ( $\kappa$ )	0.286 ( $\kappa = R/c_p$ )	KAPA BLOCK DATA
specific heat capacity of dry air at constant pressure ( $c_p$ )	1003.5 J kg <sup>-1</sup> K <sup>-1</sup> $c_p = R/\kappa$	CP CNSTNT

mean surface pressure which determines total mass of the atmosphere on the earth	984 mb	PSF
		BLOCK DATA
Stefan-Boltzmann constant ( $\sigma$ )	$5.67 \times 10^{-8} \text{ J m}^{-2}\text{s}^{-1}\text{K}^{-4}$	STBO
		RADTN
melting point	273.1 K	TICE
		COMP3
angular velocity of rotation ( $\Omega$ )	$7.292 \times 10^{-5} \text{ s}^{-1}$	CNSTNT
		AVO
Avogadro's number	$6.022 \times 10^{26} \text{ k mol}^{-1}$	OZONSS
		(Inline development) related constant QSATEX, QSTIEX in MAIN
saturation mixing ratio of water vapor (Tetens' formula) $q^*(T, p)$	$e = 6.11 \times 10^{(7.5 \frac{T-273.2}{T-35.9})}$ on water	
	$e = 6.11 \times 10^{(9.5 \frac{T-273.2}{T-8.7})}$ on ice	
	$q^* = 0.622 \frac{e}{p-e}$	

Table All.2 Other numerical constants and functions

surface roughness ( $Z_0$ )	0.0002m for ocean 0.0001m for sea-ice 0.005 m for land ice 0.45 m otherwise	Z0
		PBL
surface albedo ( $\alpha_s$ )	0.07 for ocean 0.14 for bare land 0.3 for frozen land Min (0.85, 0.7+0.15×Z) for snow or ice where Z is height in km 0.4 for bare sea-ice 0.7 for snow on sea-ice 0.5 for melting snow	ALS
		RADTN
coefficient of horizontal non-linear eddy diffusion ( $K_0^2$ )	0.04	K0SQ
		COMP3
field capacity of soil ( $\rho W_m h$ )	1.5 kg m <sup>-2</sup>	FLDCAP
		COMP3

critical temperature of ice phase transition in cumulus clouds ( $T_{cr}$ )	253.1 K	TCR
		CUP
conversion coefficient from cloud water to rain water ( $C_o$ )	0.004 $m^{-1}$ at cloud top 0.002 $m^{-1}$ otherwise	C0, C1
		CUP
maximum sustainable cloud water ( $\ell_{cr}$ )	0.0	CRITL
		CUP
base line cloud work function ( $A_o(p_d)$ )	$2 \times (\delta p \times 0.01)^3$ J where $\delta p$ is cloud depth in mb	A0 (K)
		CUP
climatological mixing ratio of water vapor ( $H_2O$ ) in the stratosphere	$2.5 \times 10^{-6}$ (kg/kg)	QST
		RADTN
carbon dioxide density at NTP ( $\rho_{CO_2,NTP}$ )	1.977 $kg\ m^{-3}$	
		RADTN
ozone density at NTP ( $\rho_{O_3,NTP}$ )	2.144 $kg\ m^{-3}$	RO3NTP
		RADTN
ozone chemical reaction rates ( $k_n$ )	see Eqs. (12.2), (12.4), (12.5), (12.6) and (12.8)	RR (n)
		OZONSS
photodissociation rates ( $j_n(p)$ )	see Eq. (12.9)	PHOD (n)
		OZONSS
reaction rate for ozone surface destruction (K)	$8 \times 10^{-4}$ $ms^{-1}$	RC
		OZONSS
eddy diffusivity at the PBL top (D)	$10\ m^2\ s^{-1}$	ED
		OZONSS
entrainment rate across the PBL top (E)	see Eq. (8.24)	ENTRAN
		PBL
transfer coefficients of heat ( $C_H$ ) and momentum ( $C_D$ )	see Fig. 8.3	CT and CU
		PBL
bulk heat capacity for ice ( $C_{ice}$ ), snow ( $C_{snow}$ ) and soil ( $C_{soil}$ )	see Eqs. (10.6) and (10.9)	CZH
		COMP3
efficiency factor of evapo-transpiration ( $\beta$ )	see Eq. (10.18)	EVE
		PBL
functional form of runoff (R)	see Eq. (10.26)	RUNOFF
		COMP3

constant related to polytropic atmosphere (a)	0.2	AKAP
		BLOCK DATA
mixing ratio of carbon dioxide ( $q_{CO_2}$ )	$4.89 \times 10^{-4}$ (kg/kg) (=320ppm)	RADTN
pressure scaling factor ( $\alpha_{H_2O}, \alpha_{CO_2}, \alpha_{O_3}$ )	0.9 for water vapor 0.86 for carbon dioxide 0.3 for ozone	PEXP-1, ACO2, AO3
		RADTN
constants for the Dickinson's long wave cooling parameterization ( $C_o, a_o, \beta_o, T_o$ )	see Table 13.2	CSTD, ASTD, BC, TLSTD
		RADTN
diffusivity factor for the downward radiation	1.66	RADTN
diffusivity factor for the upward radiation	1.9	RADTN
reflectivity of clouds ( $R_c$ )	see Eq. (13.90)	TACA, TACS
		RADTN
absorptivity of clouds ( $A_c$ )	see Eq. (13.91)	DELABS
		RADTN

### II.3 Time steps and resolutions

Currently, we have three versions of the model, namely, coarse resolution 5-layer model (C5), coarse resolution 12-layer model (C12) and fine resolution 5-layer model (F5). C5 and F5 are the tropospheric models and exclude the process related to ozone and the sponge layer. Values of version dependent parameters are listed in Table AII.3. The time steps for physical process  $\Delta t_a$  is common to all the version and set to be 1 hour.

Table AII.3

version	time step for advective process $\Delta t$	resolution in latitude $\Delta \phi$	resolution in longitude $\Delta \lambda$	model's top $P_{top}$
C5	450 sec	4 degree	5 degree	100 mb
C12	450 sec	4 degree	5 degree	1 mb
F5	225 sec	2 degree	2.5 degree	100 mb

### Appendix III. Selected monthly mean fields produced by the MRI-GCM-I

Selected results taken from a simulation of annual cycle with 5 layer version of the MRI-GCM-I (see Fig. 1.2(a)) are shown in this appendix without any comments on the results. Discussions on them will be found in the forthcoming papers by Tokioka, Kitoh, Yagai and Yamazaki (1985), Kitoh and Tokioka (1985) and Tokioka and Kitoh (1985). The simulated results of the 12-layer MRI-GCM-I are not included here. Those who are interested in them, some preliminary results are found in Tokioka and Yagai (1984).

Horizontal resolution of the model is  $\Delta\lambda = 5^\circ$  and  $\Delta\phi = 4^\circ$ . As for the time increment,  $\Delta t = 7.5$  min and  $\Delta t_d = 60$  min are used.

Monthly mean maps are shown for January, April, July and October. For each month, the following fields are included ;

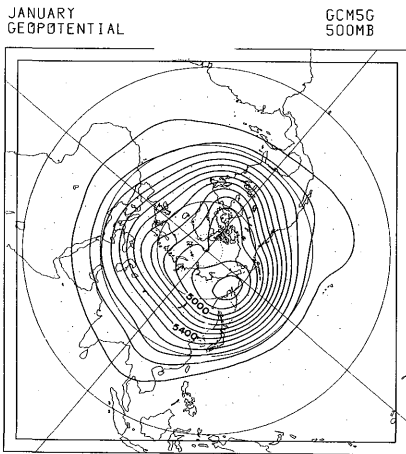
- i : Monthly mean sea level pressure. (a) model and (b) observation
- ii : Monthly mean geopotential field at 500 mb. (a) model and (b) observation
- iii : Monthly mean wind and stream lines at 900 mb. (a) model and (b) observation
- iv : Same as iii but for 200 mb
- v : Monthly mean velocity potential and divergent wind of the model at 200 mb.
- vi : Seasonal mean precipitation. (a) model and (b) observation
- vii : Monthly mean evaporation of the model.
- viii : Monthly mean sensible heat flux at the surface of the model.
- ix : Monthly mean net downward flux of solar radiation at the top of the atmosphere. (a) model and (b) observed value
- x : Monthly mean net upward flux of terrestrial radiation at the top of the atmosphere. (a) model and (b) observed value
- xi : Monthly mean net downward flux of radiation at the top of the atmosphere. (a) model and (b) observed value
- xii : Monthly mean net downward flux of solar radiation of the model at the surface.
- xiii : Monthly mean net upward flux of terrestrial radiation of the model at the surface.
- xiv : Monthly mean net downward flux of radiation of the model at the surface.
- xv : Monthly mean total heating of air column of the model.
- xvi : Monthly mean snow depth of the model.
- xvii : Monthly mean total cloudiness of the model.
- xviii : Monthly mean zonally averaged temperature. (a) model and (b) observation

xix : Monthly mean zonally averaged zonal wind. (a) model and (b) observation

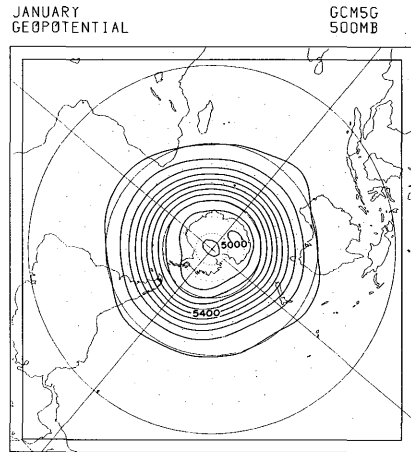
xx : Monthly mean meridional stream function. (a) model and (b) based on observation

xxi : Monthly mean zonally averaged total heating rate of the model.

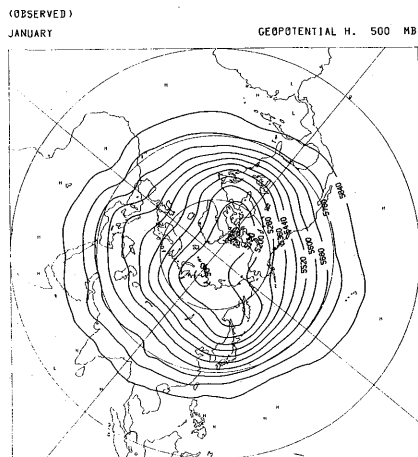
( a - 1 )



( a - 2 )



( b - 1 )



( b - 2 )

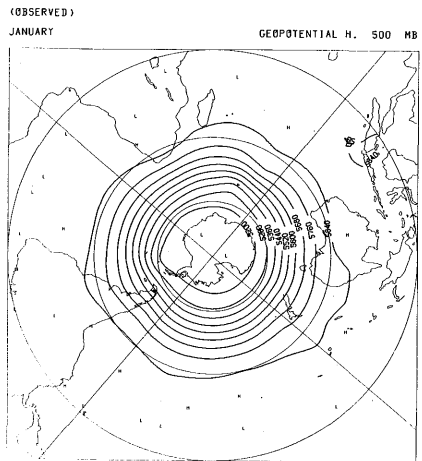


Fig. AIII.1.ii Monthly mean geopotential field at 500 mb for January. (a-1) model and (b-1) observation (Oort, 1983) for the northern hemisphere. (a-2) model and (b-2) observation (Oort, 1983) for the southern hemisphere. Contour interval is 80 gpm.

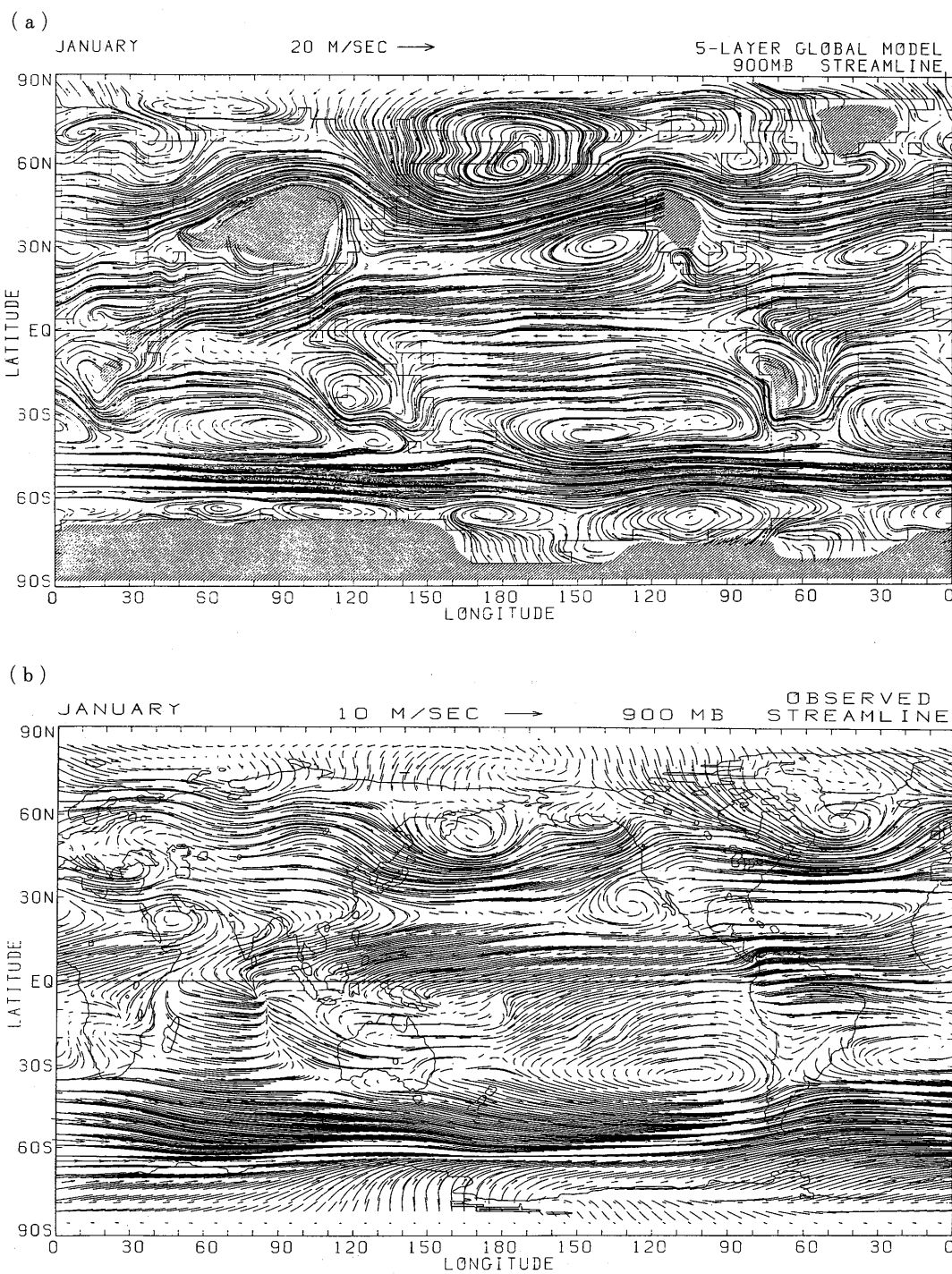


Fig. AIII.1.iii Global distribution of monthly mean wind and stream lines at 900 mb for January. (a) model and (b) observation (based on Oort (1983)).

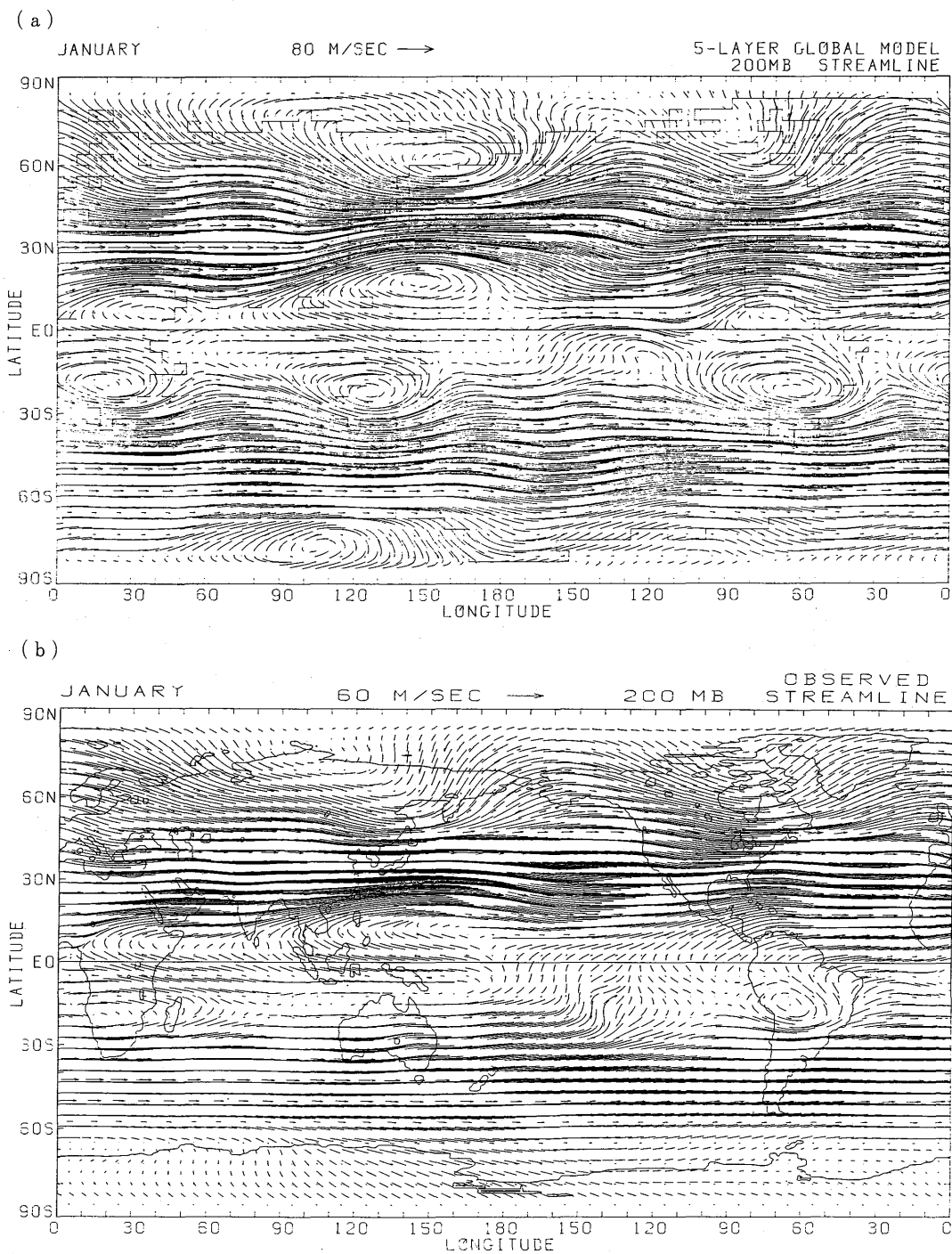


Fig. AIII.1.iv Same as in Fig. AIII.1.iii but for 200 mb.

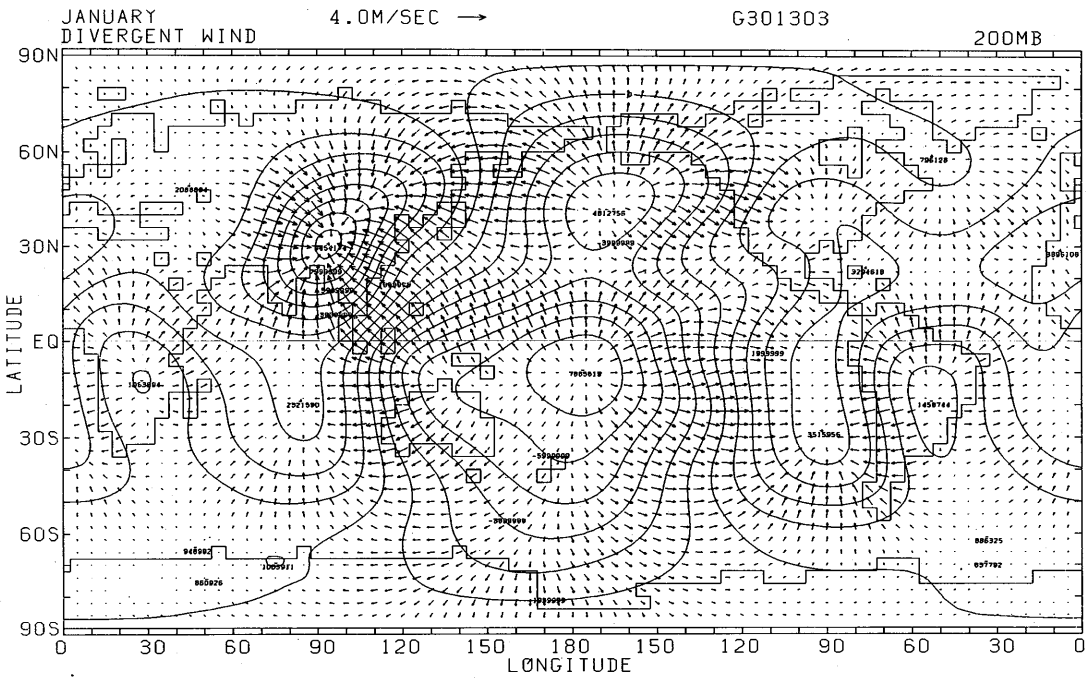


Fig. AIII.1.v Global distribution of monthly mean velocity potential and divergent wind of the model at 200 mb for January. Contour interval is  $10^6 \text{m}^2 \text{s}^{-1}$ .

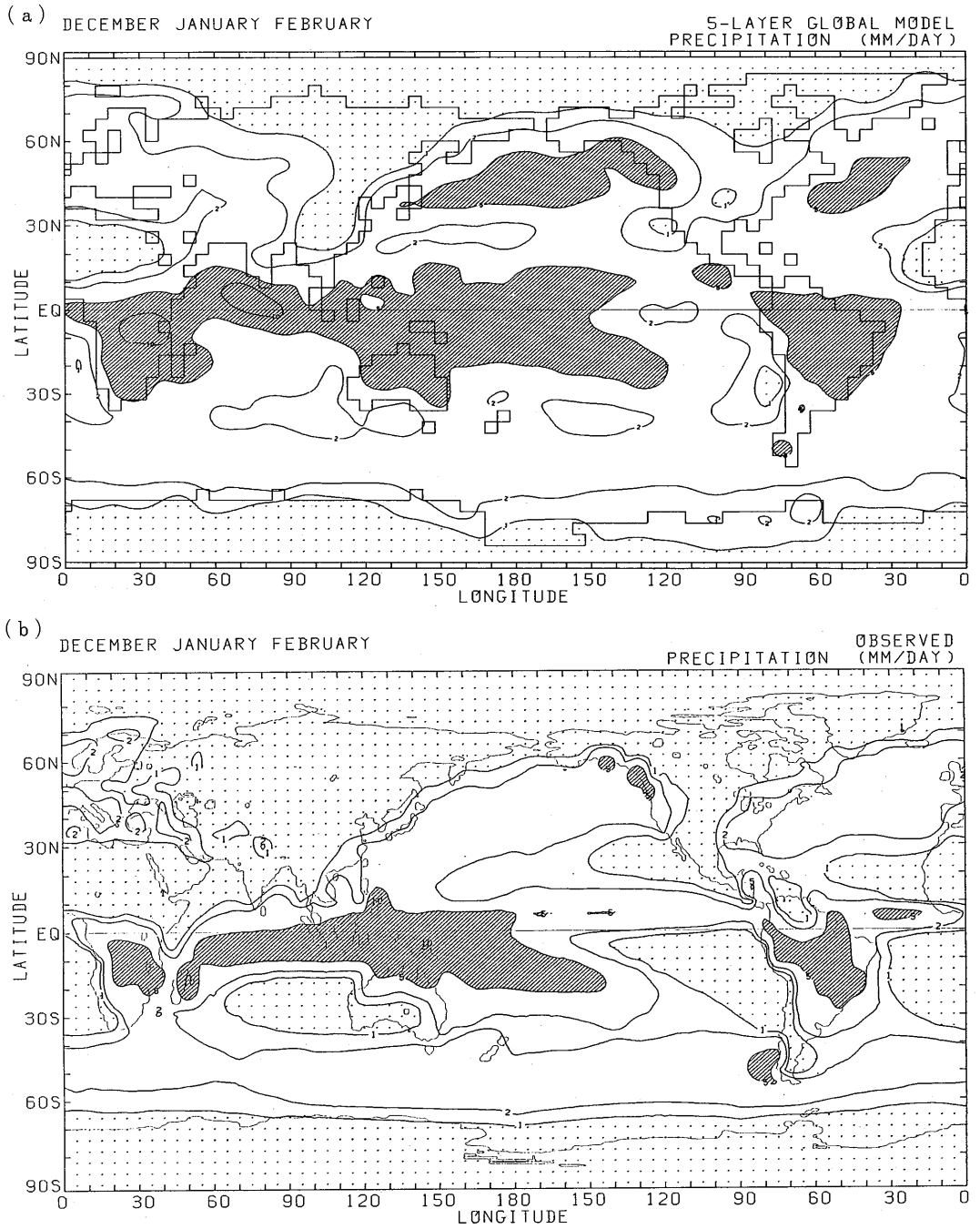


Fig. AIII.1.vi Global distribution of total precipitation for December, January and February. (a) model and (b) observation (Schutz and Gates, 1972). (unit : mm/d) Areas over 5mm/d and less than 1mm/d are covered with shades and dots, respectively.

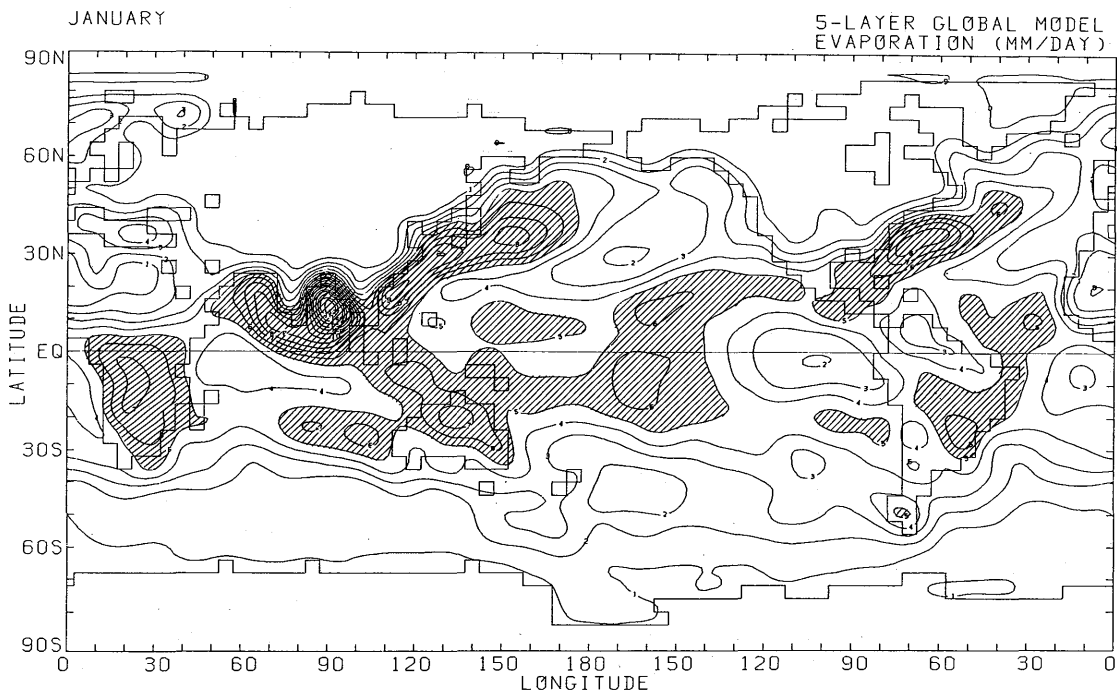


Fig. AIII.1.vii Global distribution of evaporation of the model at the surface for January. (unit : mm/d). Areas over 5mm/d are covered with shades.

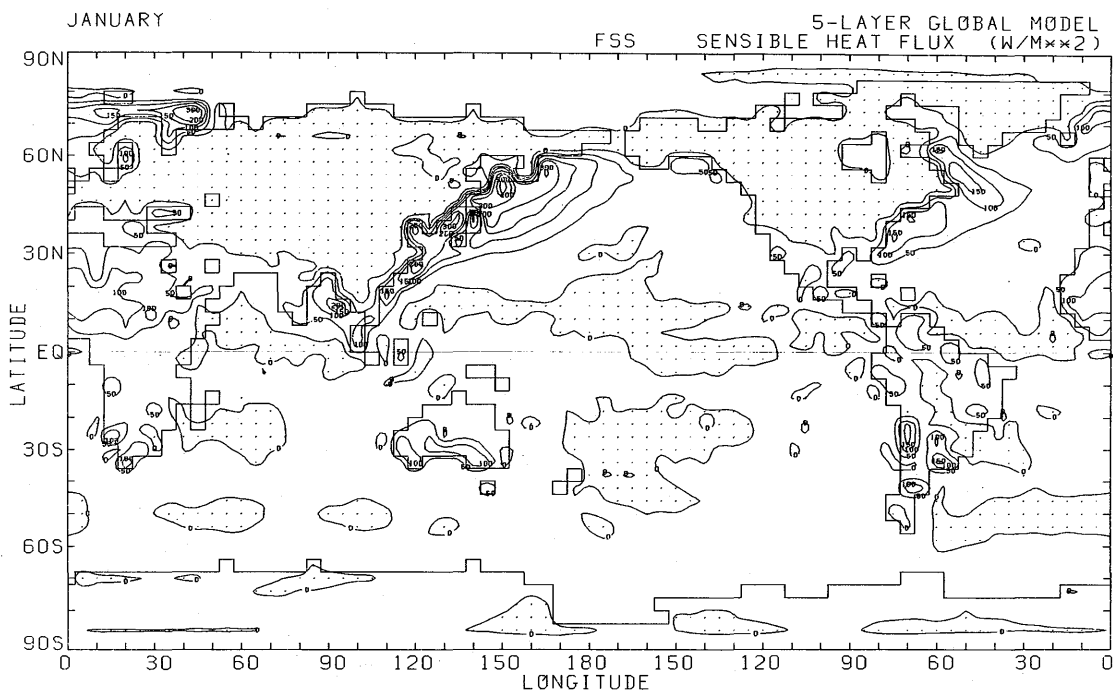


Fig. AIII.1.viii Global distribution of upward sensible heat flux of the model at the surface for January. Contour interval is  $50 \text{ W m}^{-2}$ . Negative areas are covered with dots.

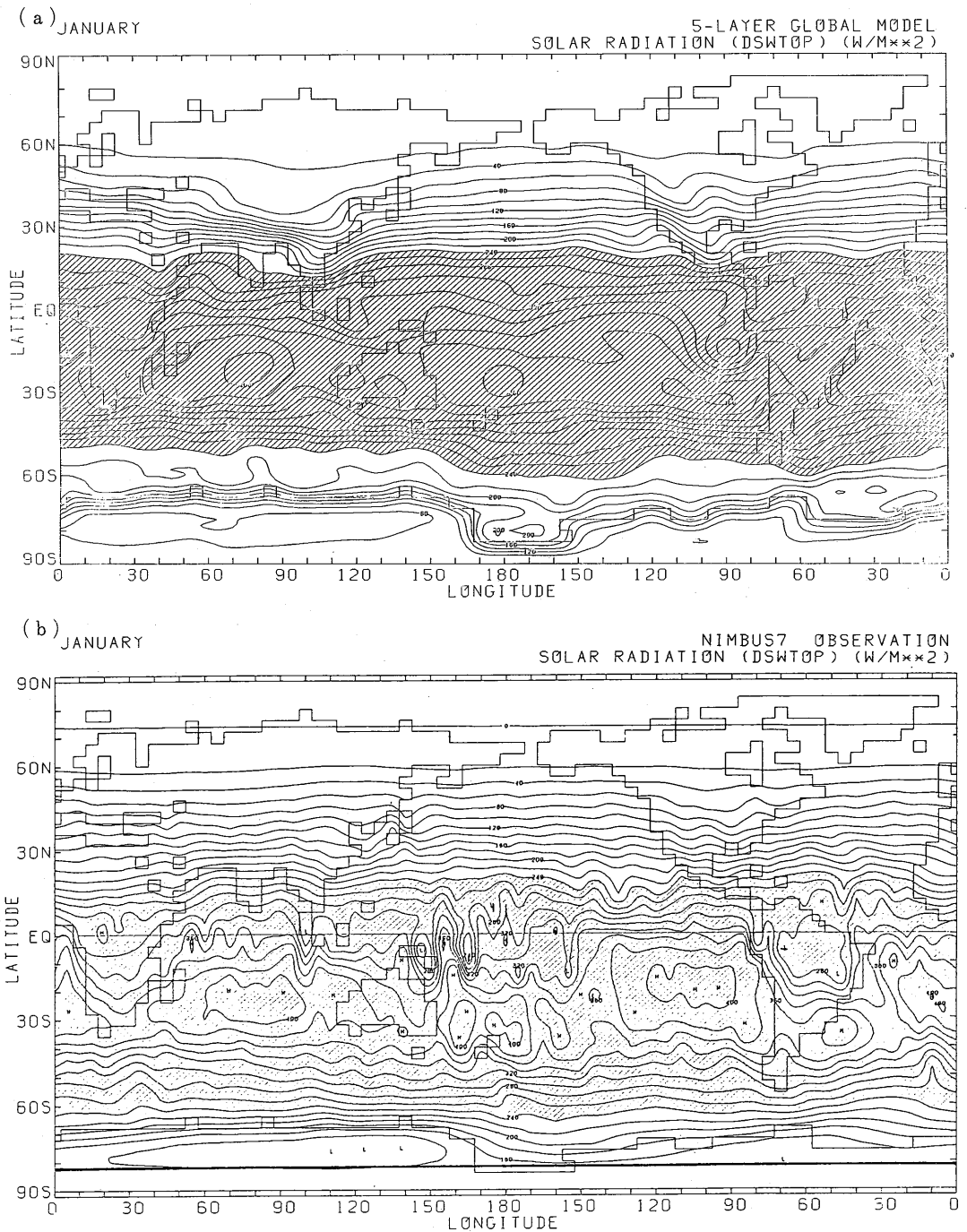


Fig. AIII.1.ix Global distribution of monthly mean net downward flux of solar radiation at the top of the atmosphere for January. (a) model and (b) observed value (Jacobowitz *et al.*, 1984). Contour interval is  $20 W m^{-2}$ . Areas over  $240 W m^{-2}$  are shaded.

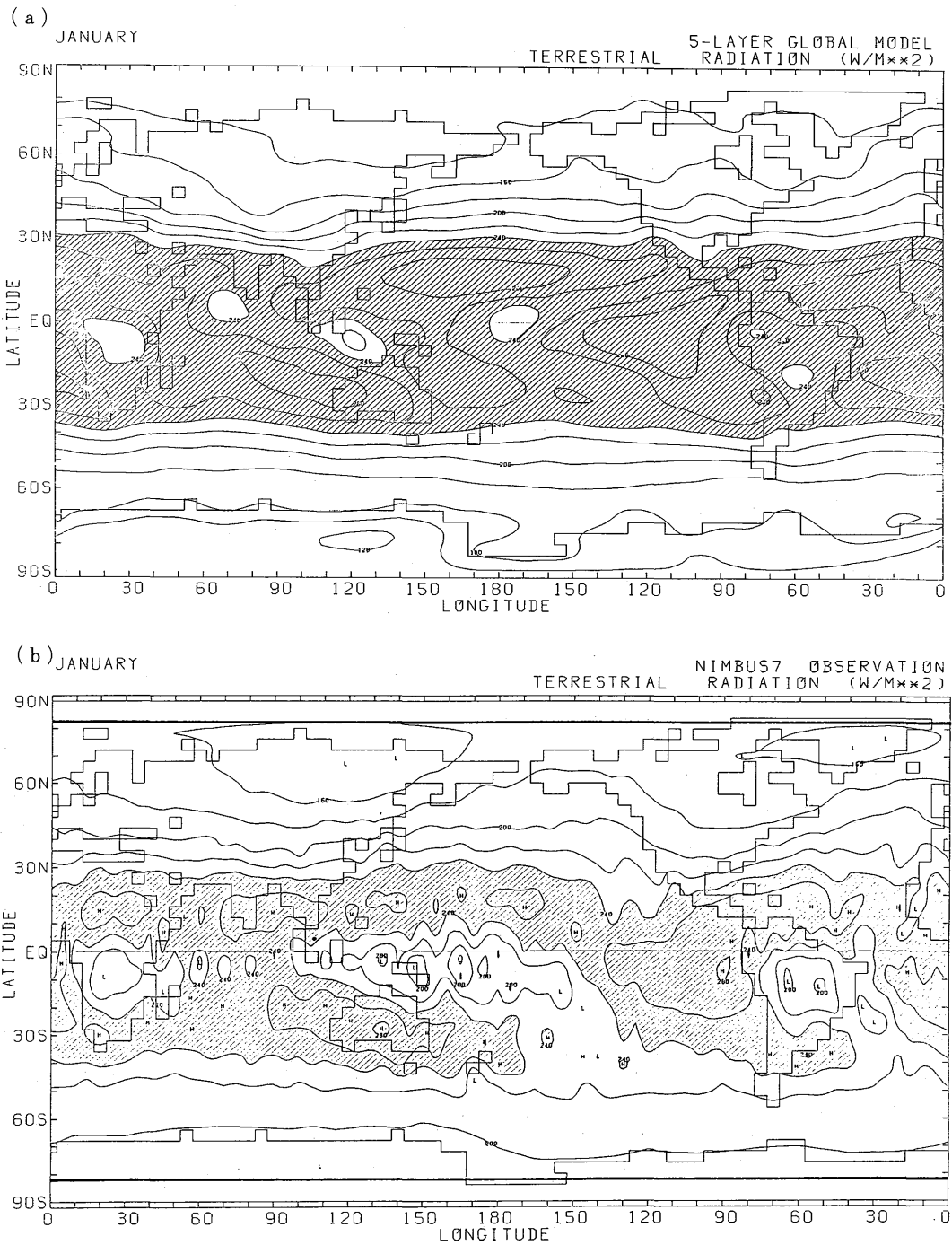


Fig. AIII.1.x Global distribution of monthly mean net upward flux of terrestrial radiation at the top of the atmosphere for January. (a) model and (b) observed value (Jacobowitz *et al.*, 1984). Contour interval is  $20 W m^{-2}$ . Areas over  $240 W m^{-2}$  are shaded.

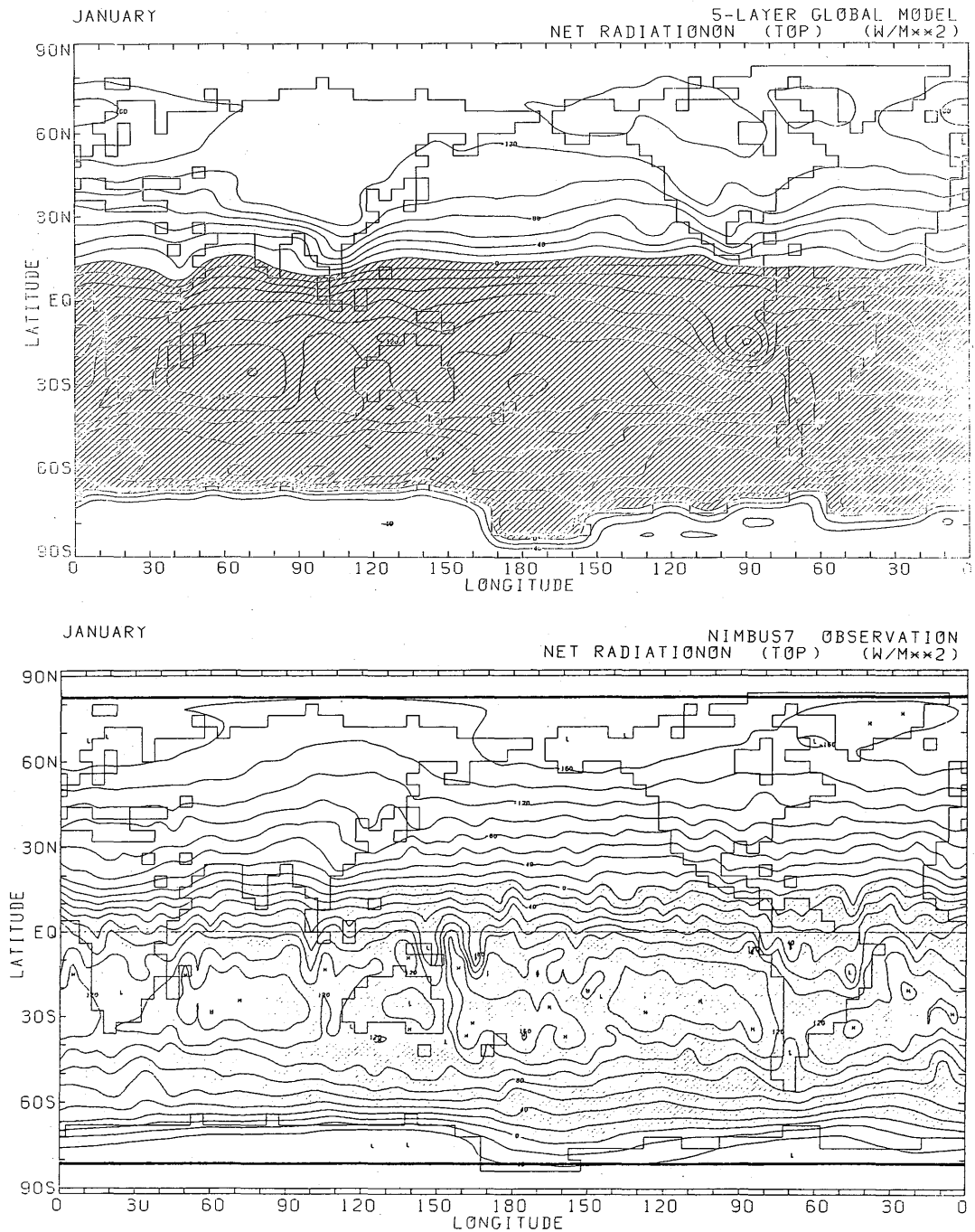


Fig. AIII.1.xi Global distribution of monthly mean net downward flux of radiation at the top of the atmosphere for January. (a) model and (b) observed value (Jacobowitz *et al.*, 1984). Contour interval is  $20 \text{ W m}^{-2}$ . Positive areas are shaded.

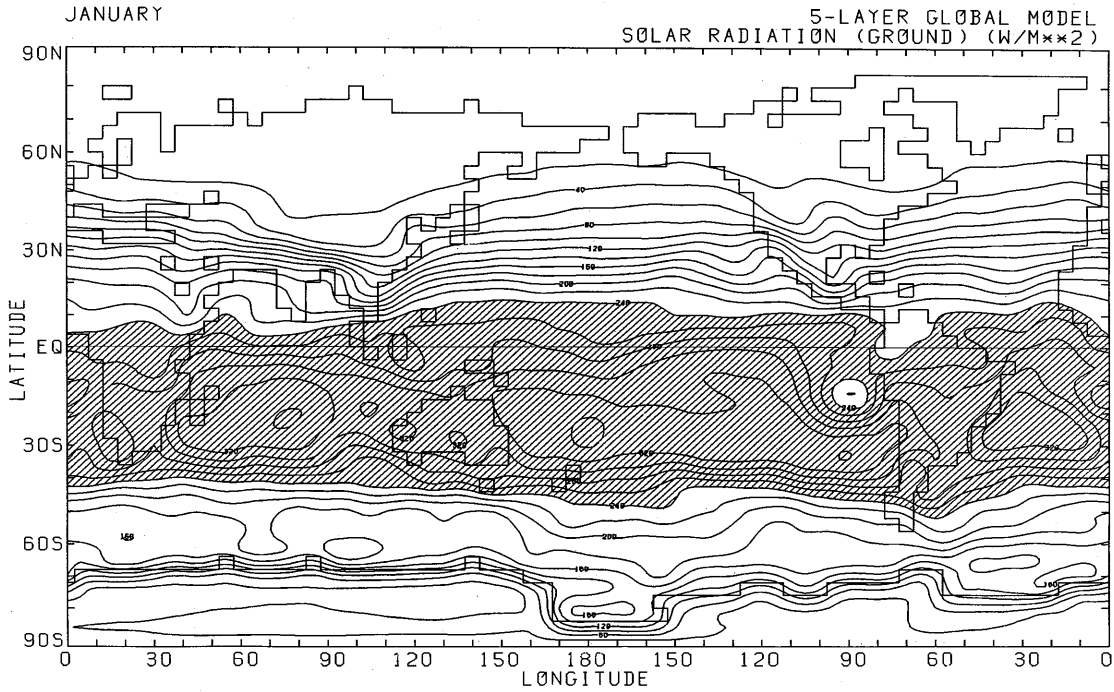


Fig. AIII.1.xii Global distribution of monthly mean net downward flux of solar radiation at the surface of the model for January. Contour interval is  $20 \text{ W m}^{-2}$ . Areas over  $240 \text{ W m}^{-2}$  are shaded.

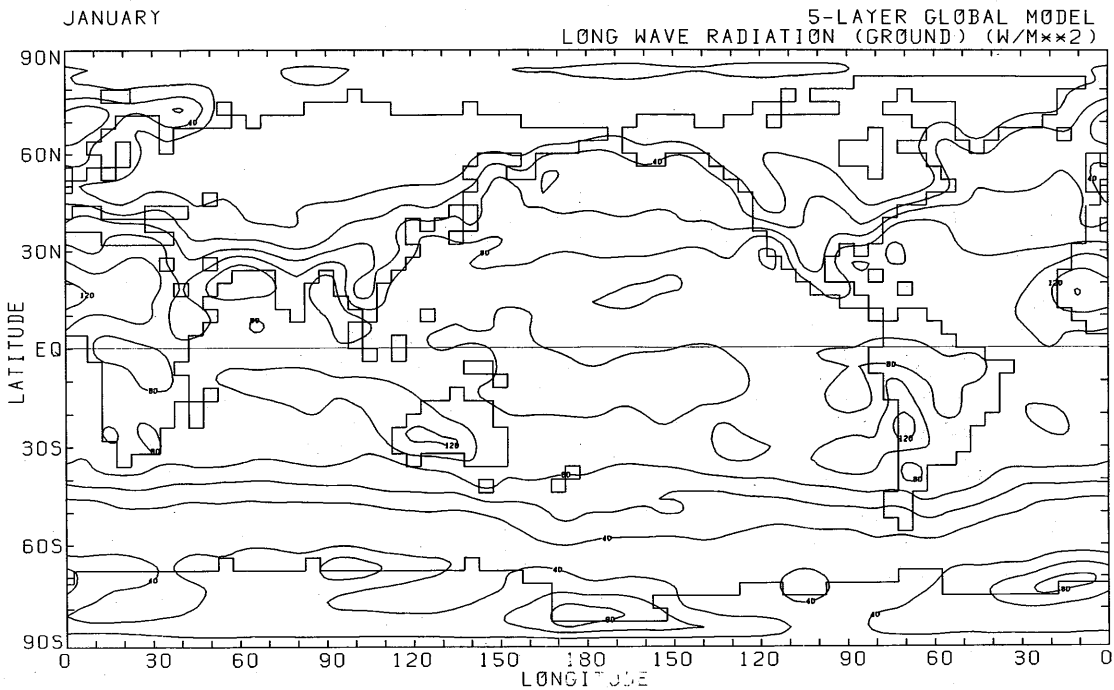


Fig. AIII.1.xiii Global distribution of monthly mean net upward flux of terrestrial radiation at the surface of the model for January. Contour interval is  $20 \text{ W m}^{-2}$ .

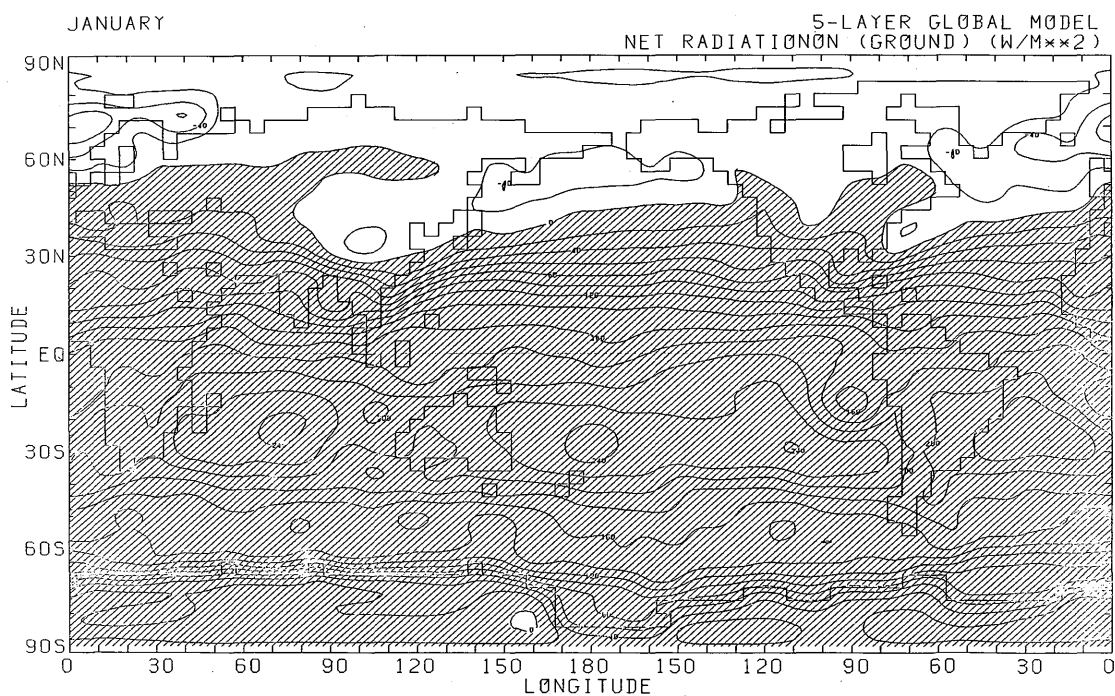


Fig. AIII.1.xiv Global distribution of monthly mean net downward flux of radiation at the surface of the model for January. Contour interval is 20 W m<sup>-2</sup>. Positive areas are shaded.

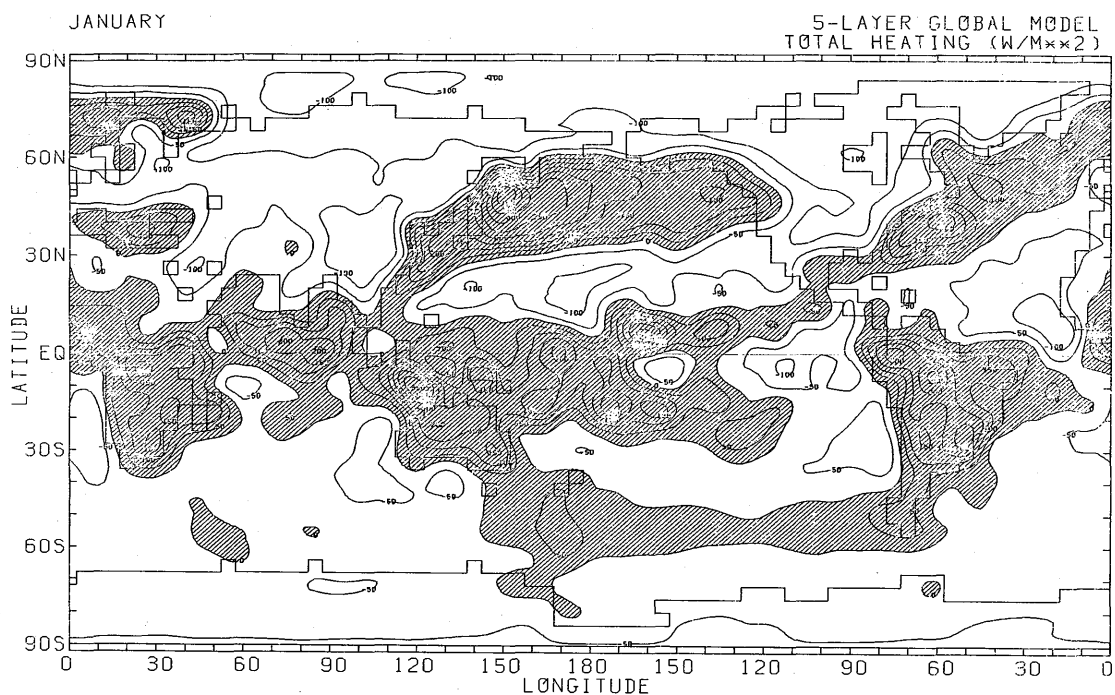


Fig. AIII.1.xv Global distribution of monthly mean total heating of air column of the model for January. Contour interval is 50 W m<sup>-2</sup>. Positive areas are covered with shades.

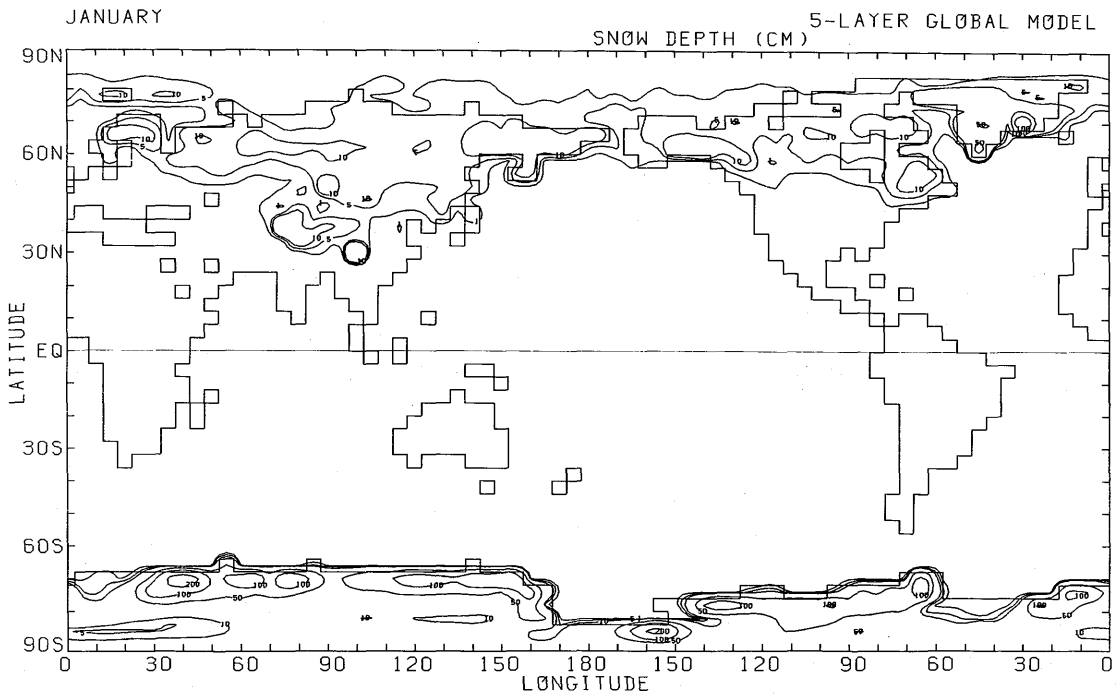


Fig. AIII.1.xvi Global distribution of monthly mean snow depth of the model for January. (unit : cm)

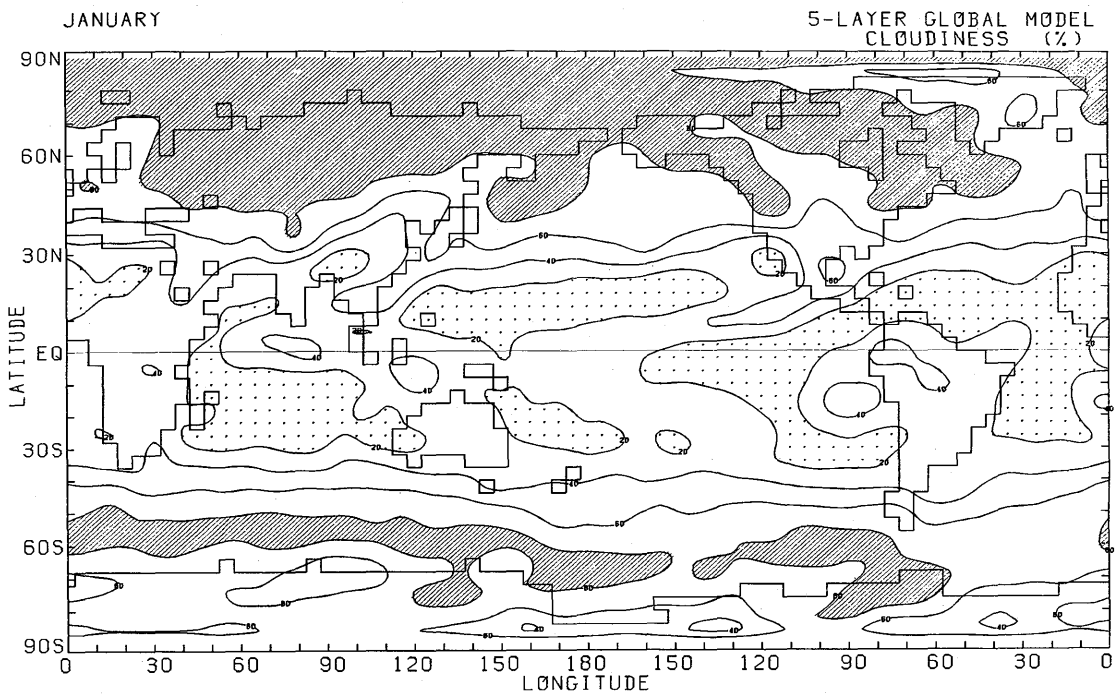


Fig. AIII.1.xvii Global distribution of monthly mean total cloudiness of the model for January. Areas over 80% and less than 20% cloudiness are covered with shades and dots, respectively.

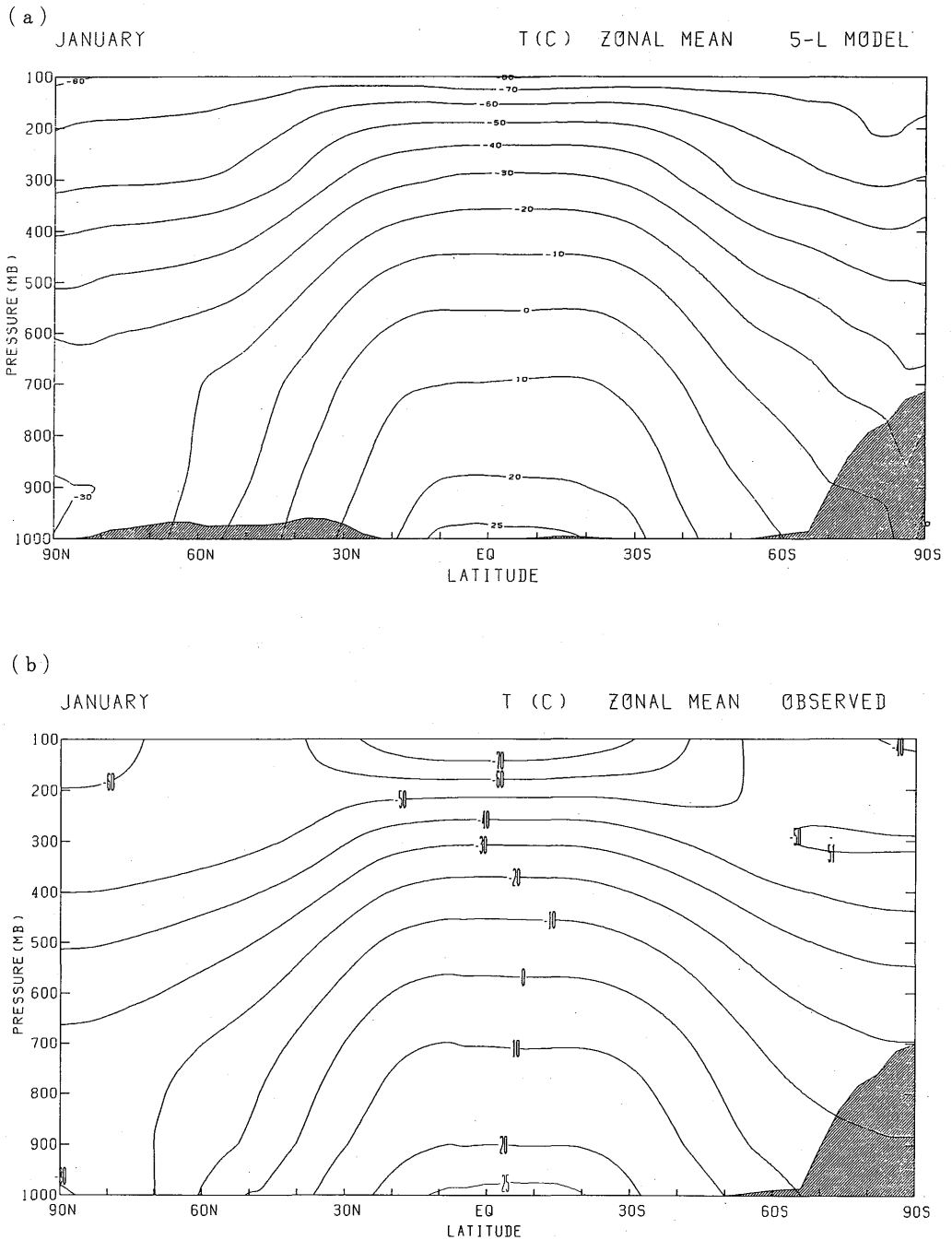


Fig. AIII.1.xviii Meridional distribution of monthly mean zonally averaged temperature for January. (a) model and (b) observation (Oort, 1983). Contour interval is 10C.

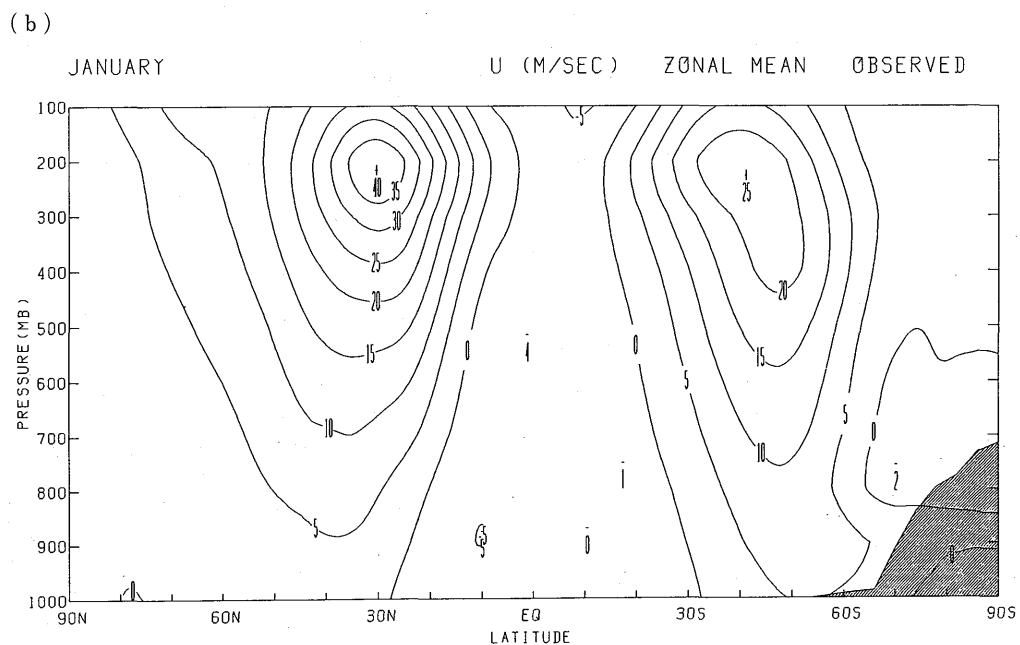
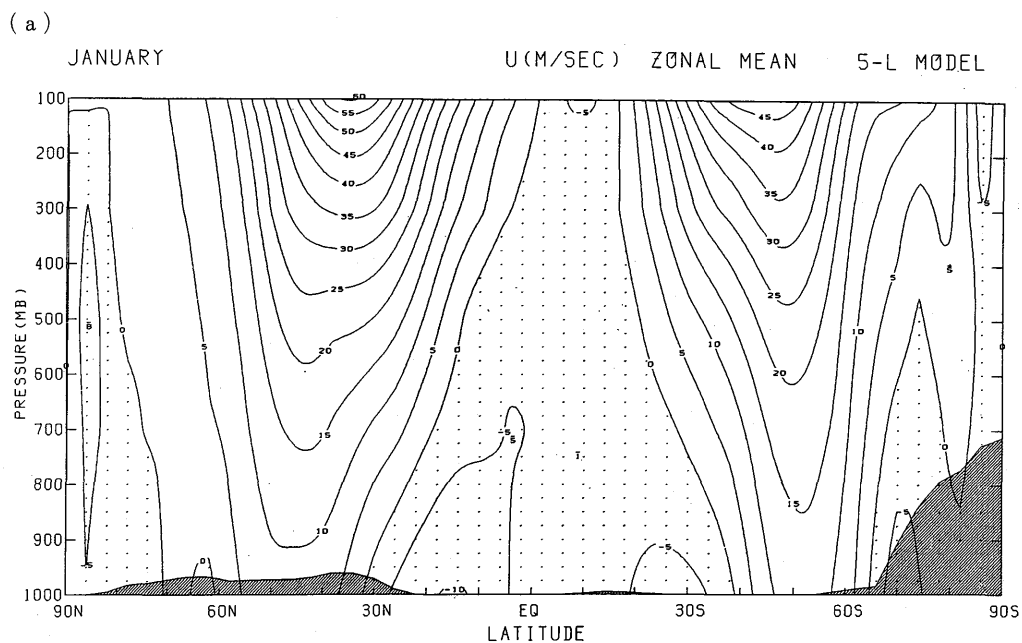


Fig. AIII.1.xix Meridional distribution of monthly mean zonally averaged zonal wind for January. (a) model and (b) observation (Oort, 1983). Contour interval is  $5 \text{ m s}^{-1}$ .



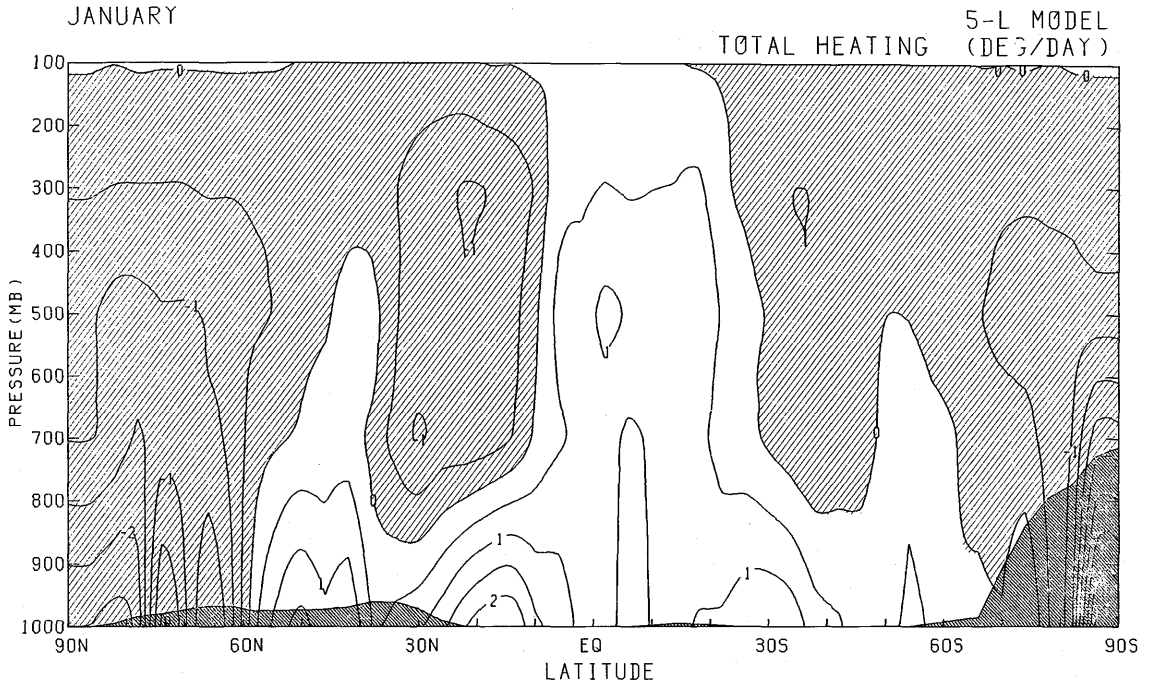


Fig. AIII.1.xxi Meridional distribution of monthly mean zonally averaged total heating rate of the model for January. Contour interval is  $0.5 \text{ K d}^{-1}$ . Cooling areas are covered with shades.

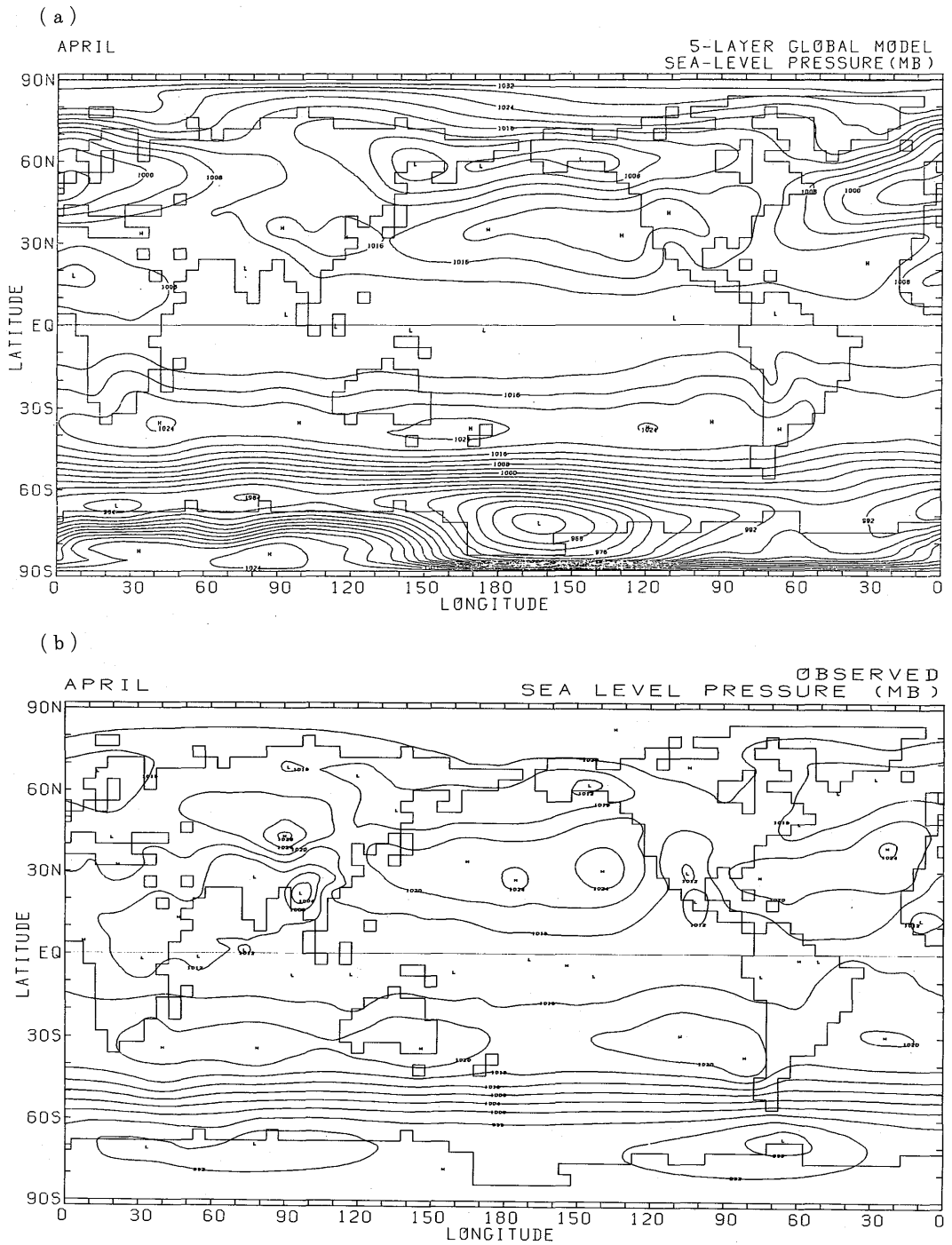
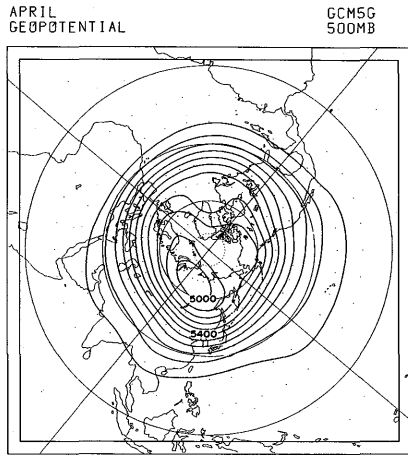
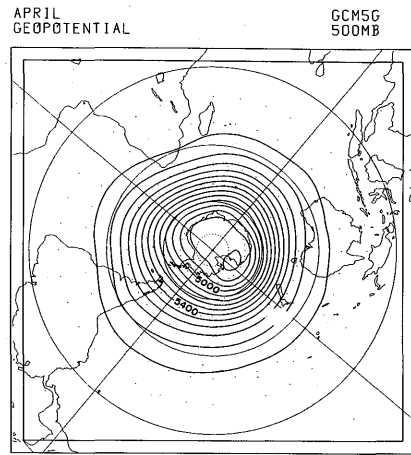


Fig. AIII.2.i Same as in Fig. AIII.1.i but for April.

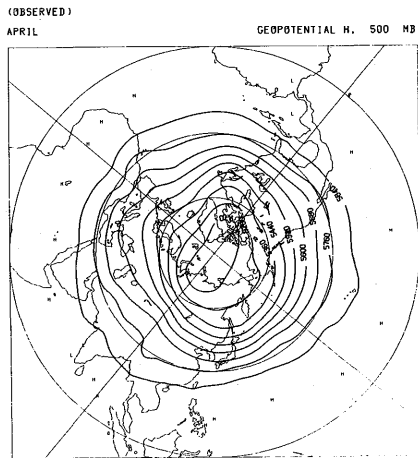
(a-1)



(a-2)



(b-1)



(b-2)

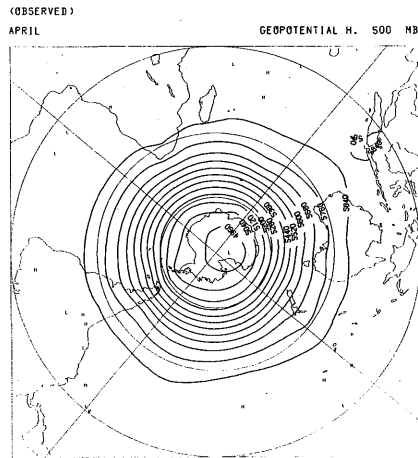


Fig. AIII.2.ii Same as in Fig. AIII.1.ii but for April.

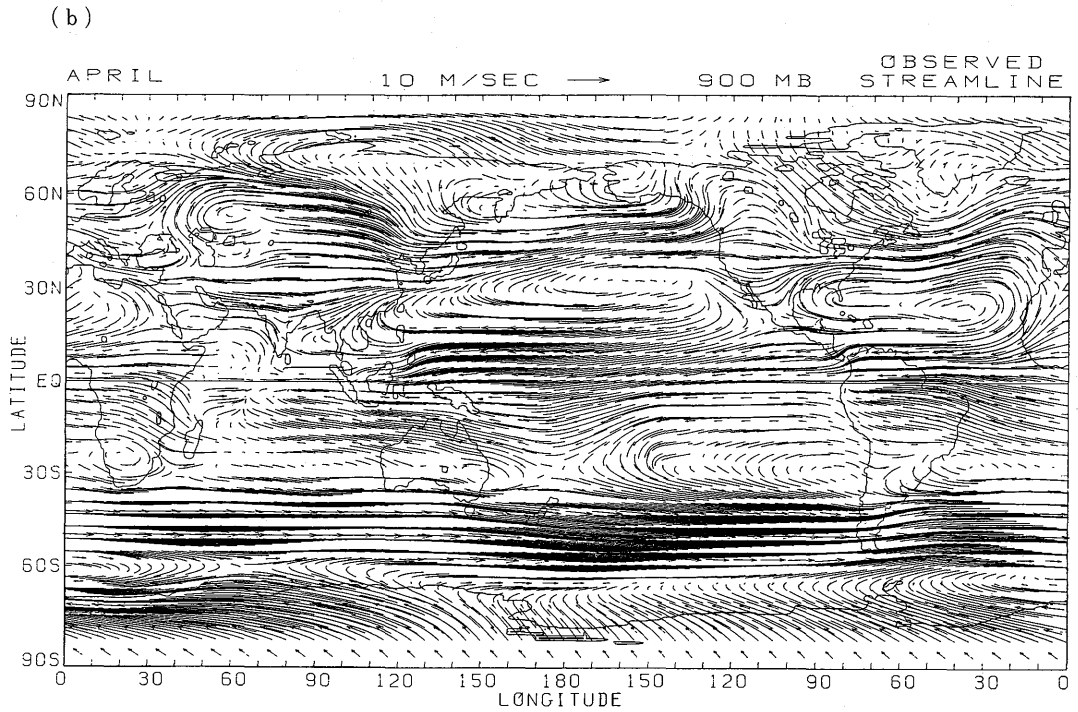
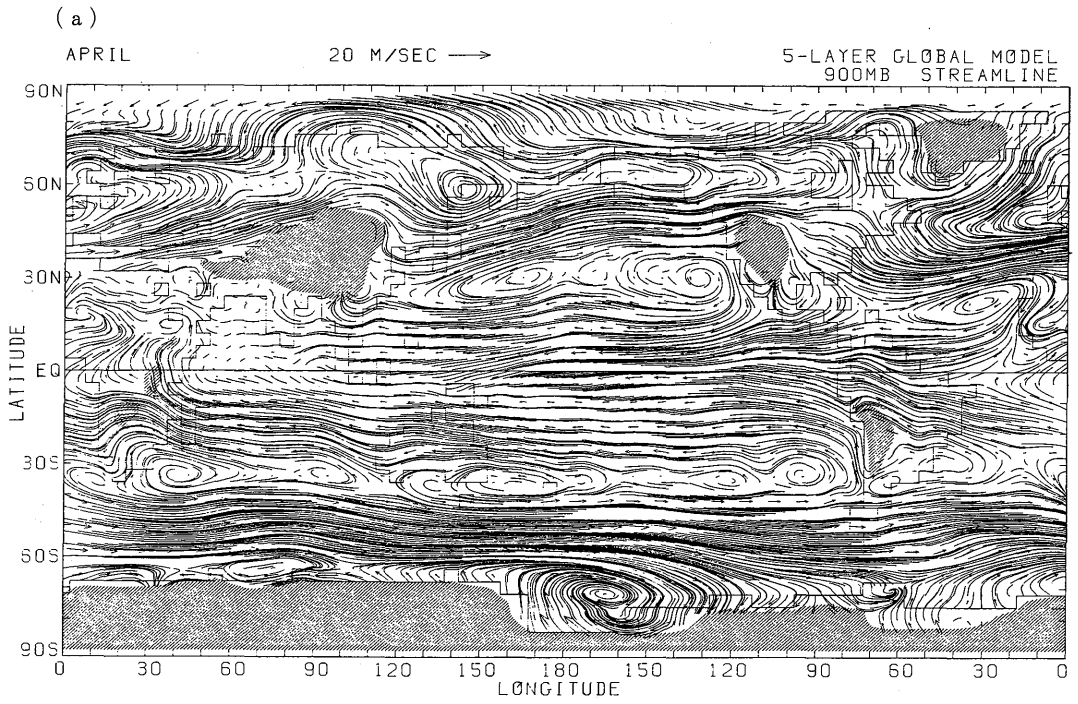


Fig. AIII.2.iii Same as in Fig. AIII.1.iii but for April.

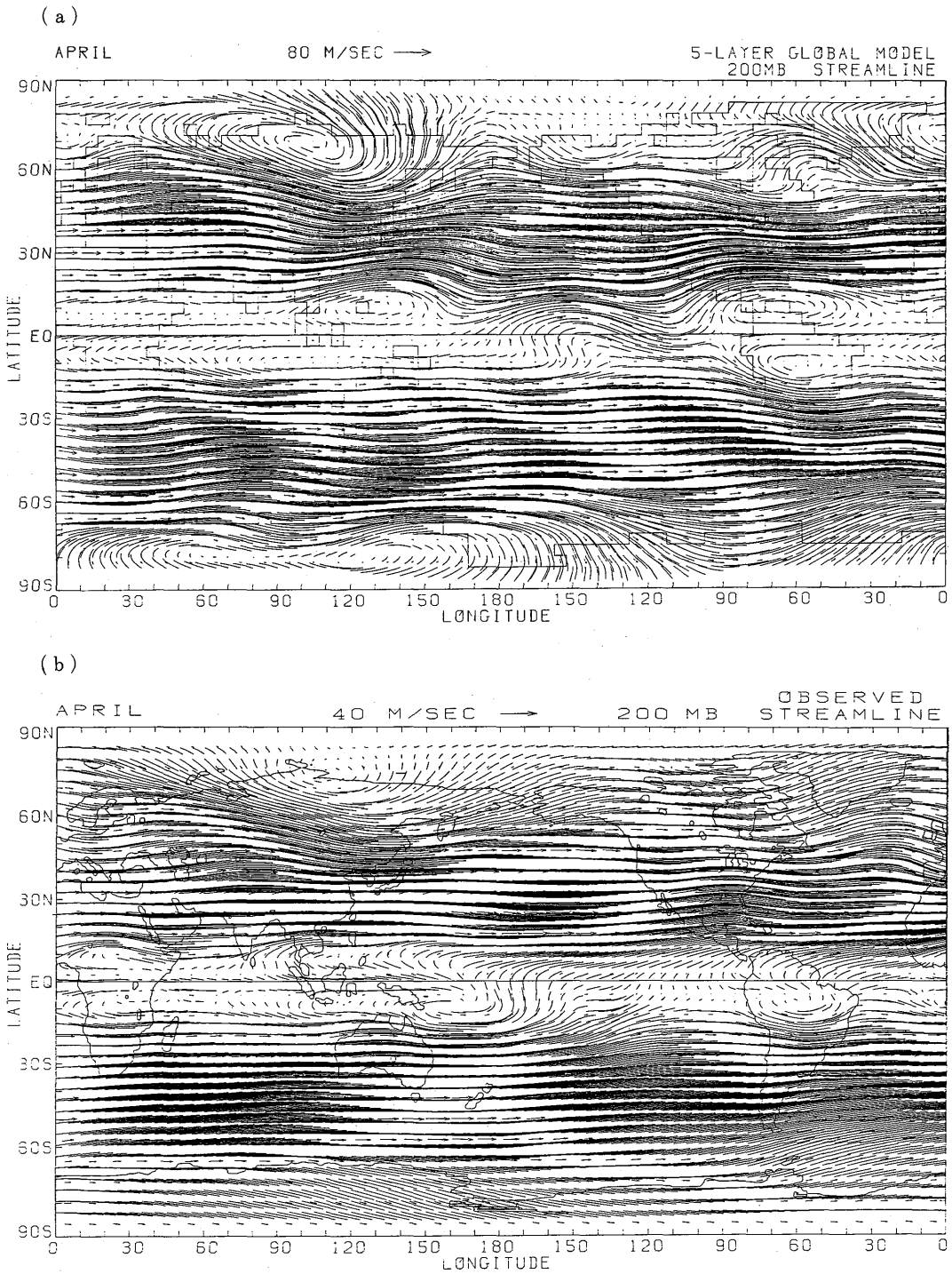


Fig. AIII.2.iv Same as in Fig. AIII.1.iv but for April.

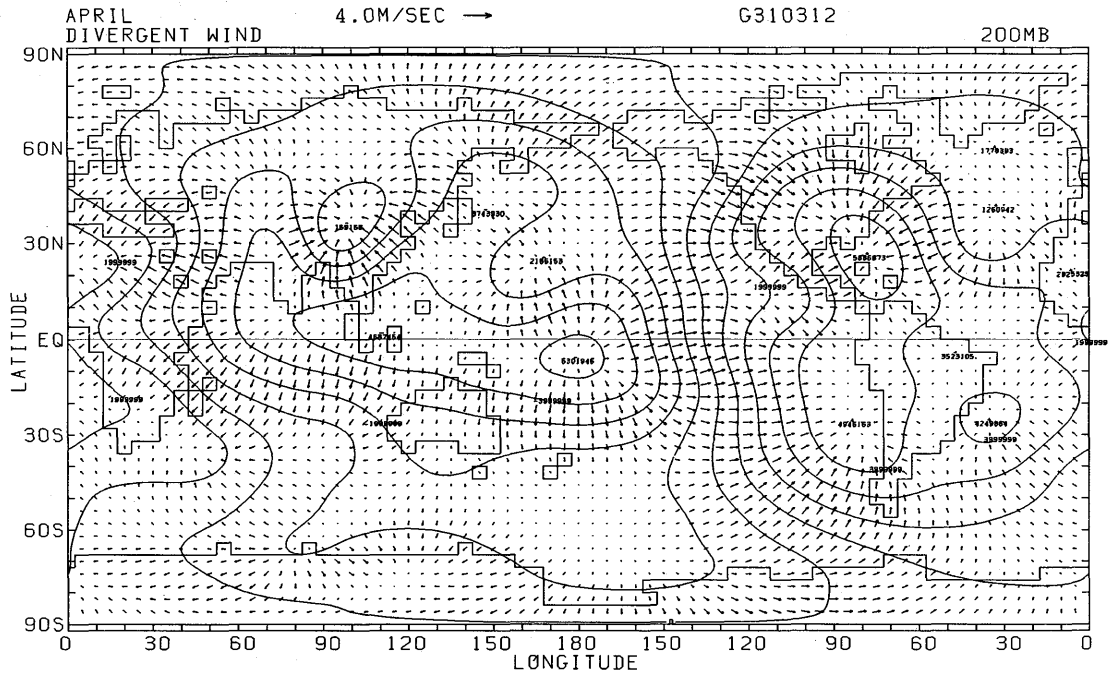


Fig. AIII.2.v Same as in Fig. AIII.1.v but for April.

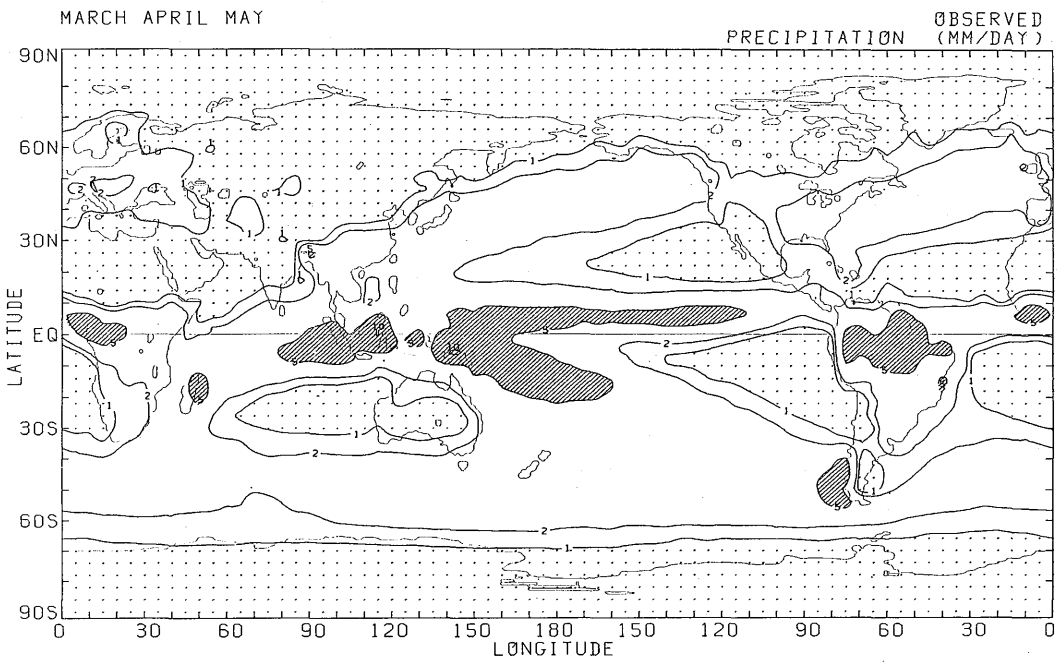
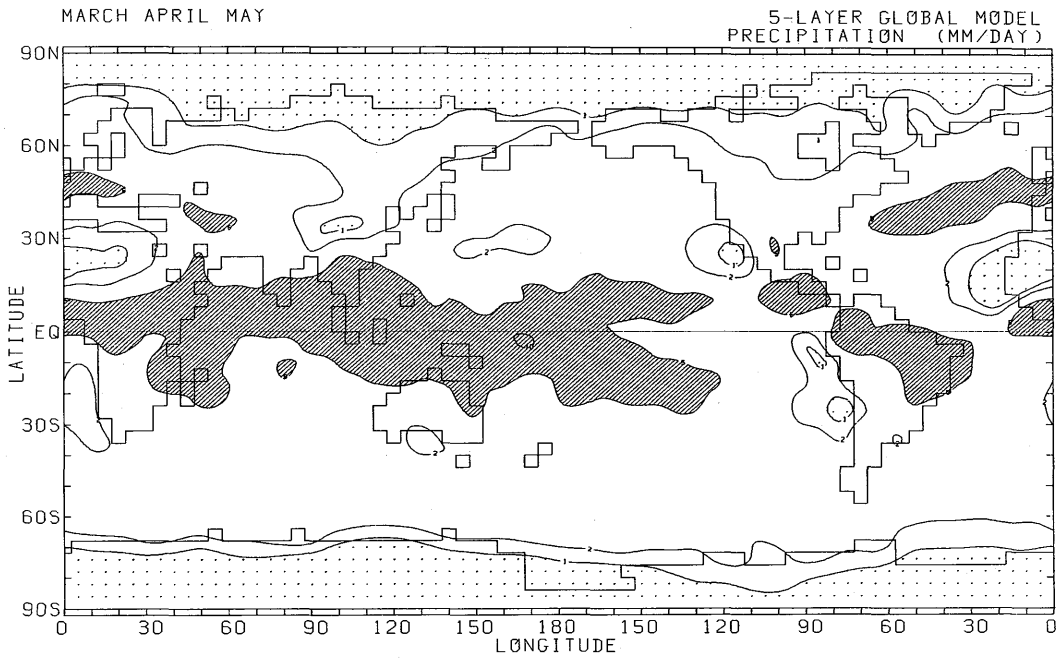


Fig. AIII.2.vi Same as in Fig. AIII.1.vi but for March, April and May.

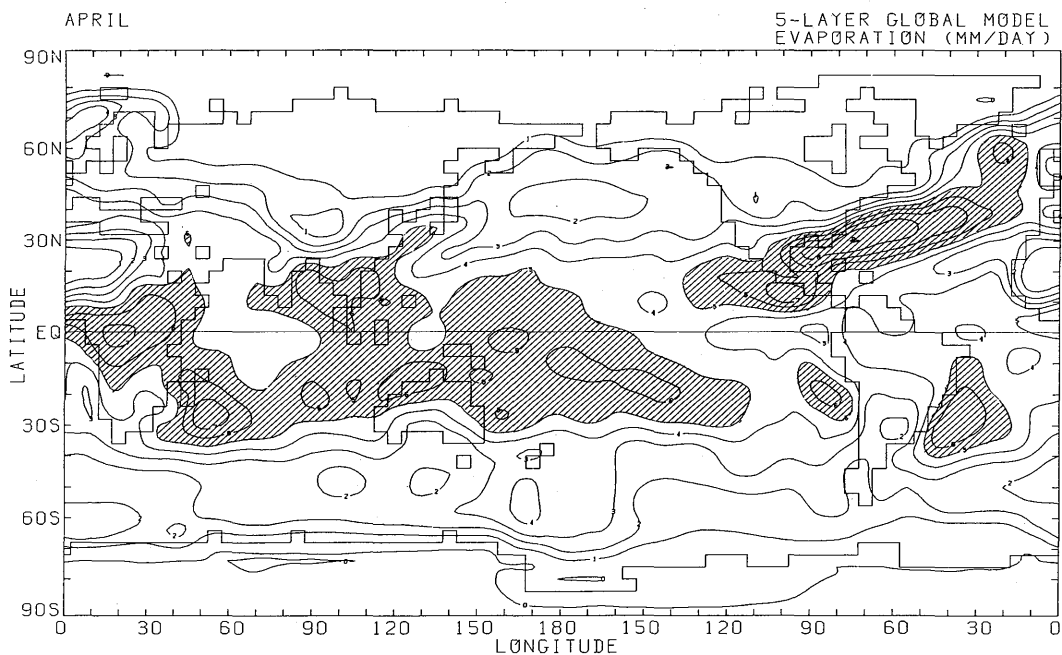


Fig. AIII.2.vii Same as in Fig. AIII.1.vii but for April.

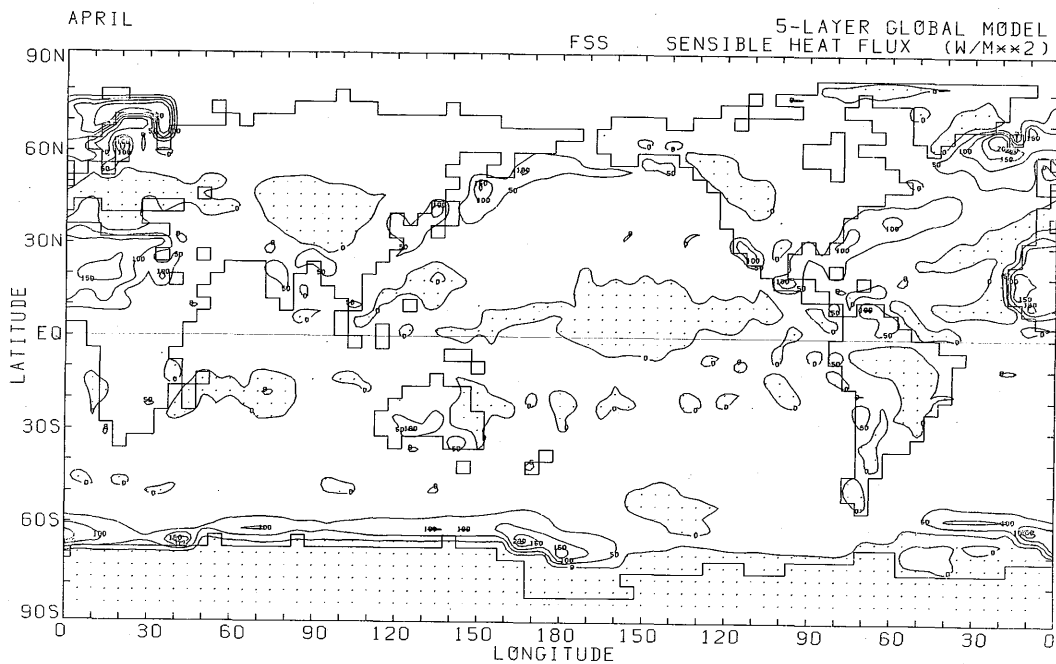


Fig. AIII.2.viii Same as in Fig. AIII.1.viii but for April.

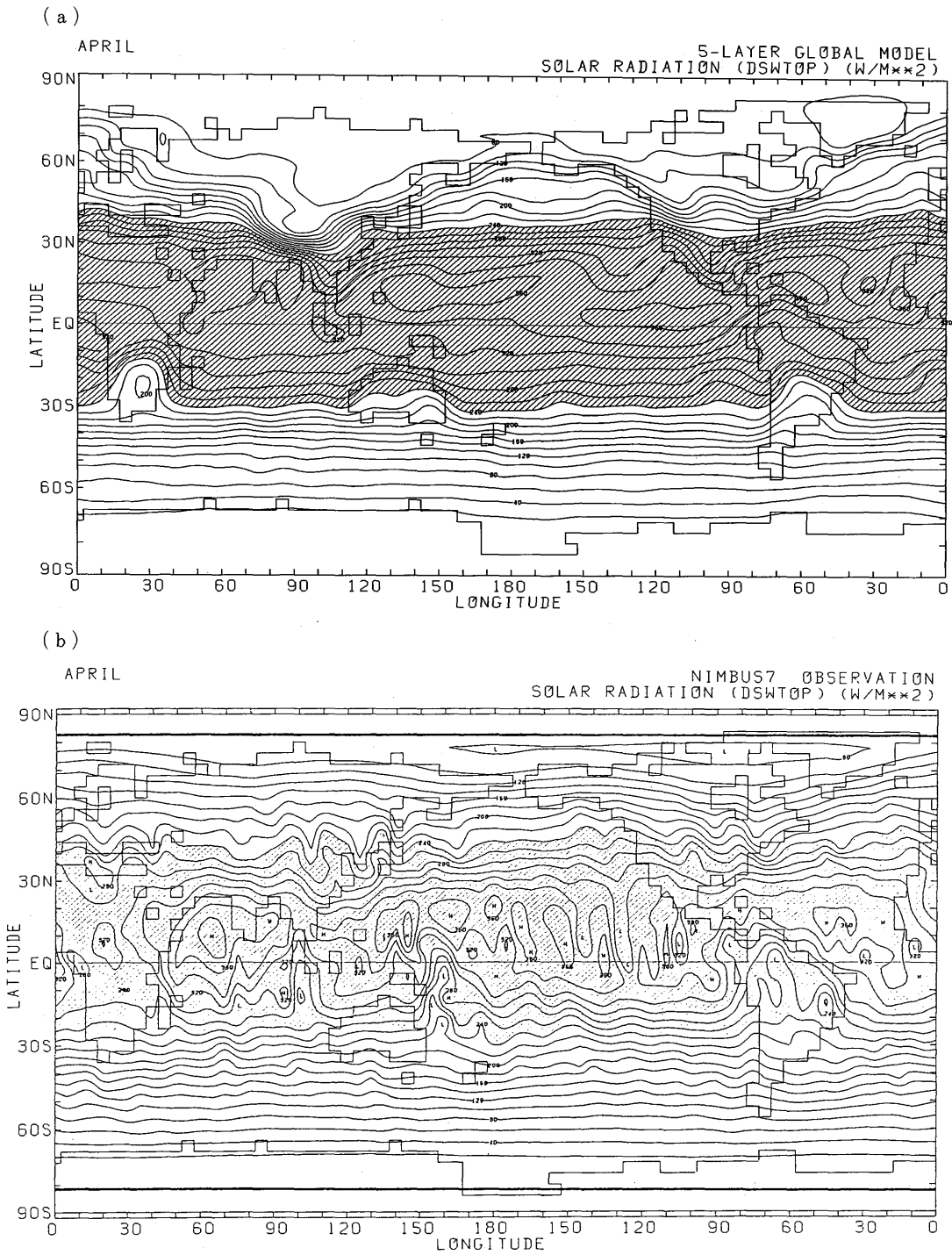


Fig. AIII.2.ix Same as in Fig. AIII.1.ix but for April.

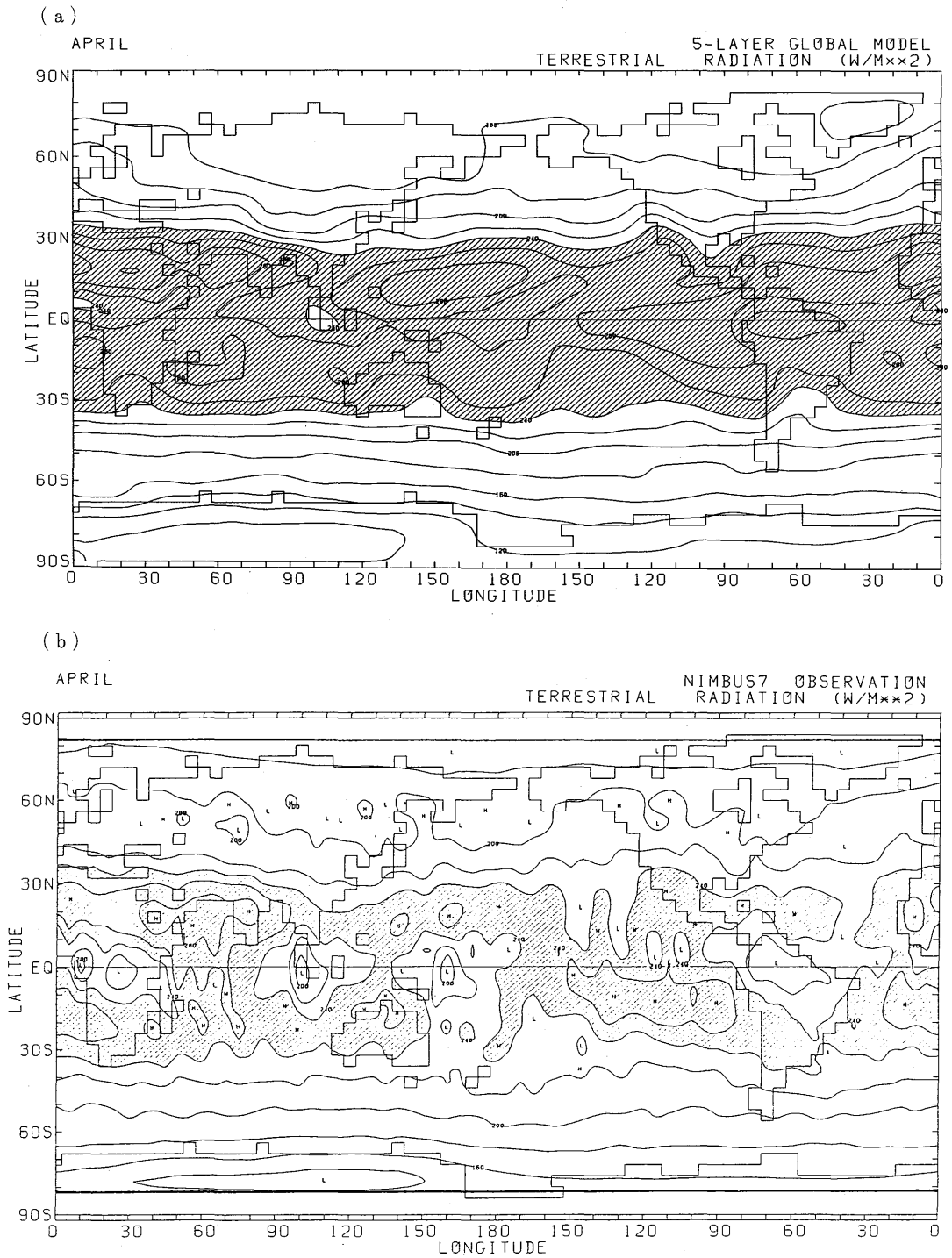


Fig. AIII.2.x Same as in Fig. AIII.1.x but for April.

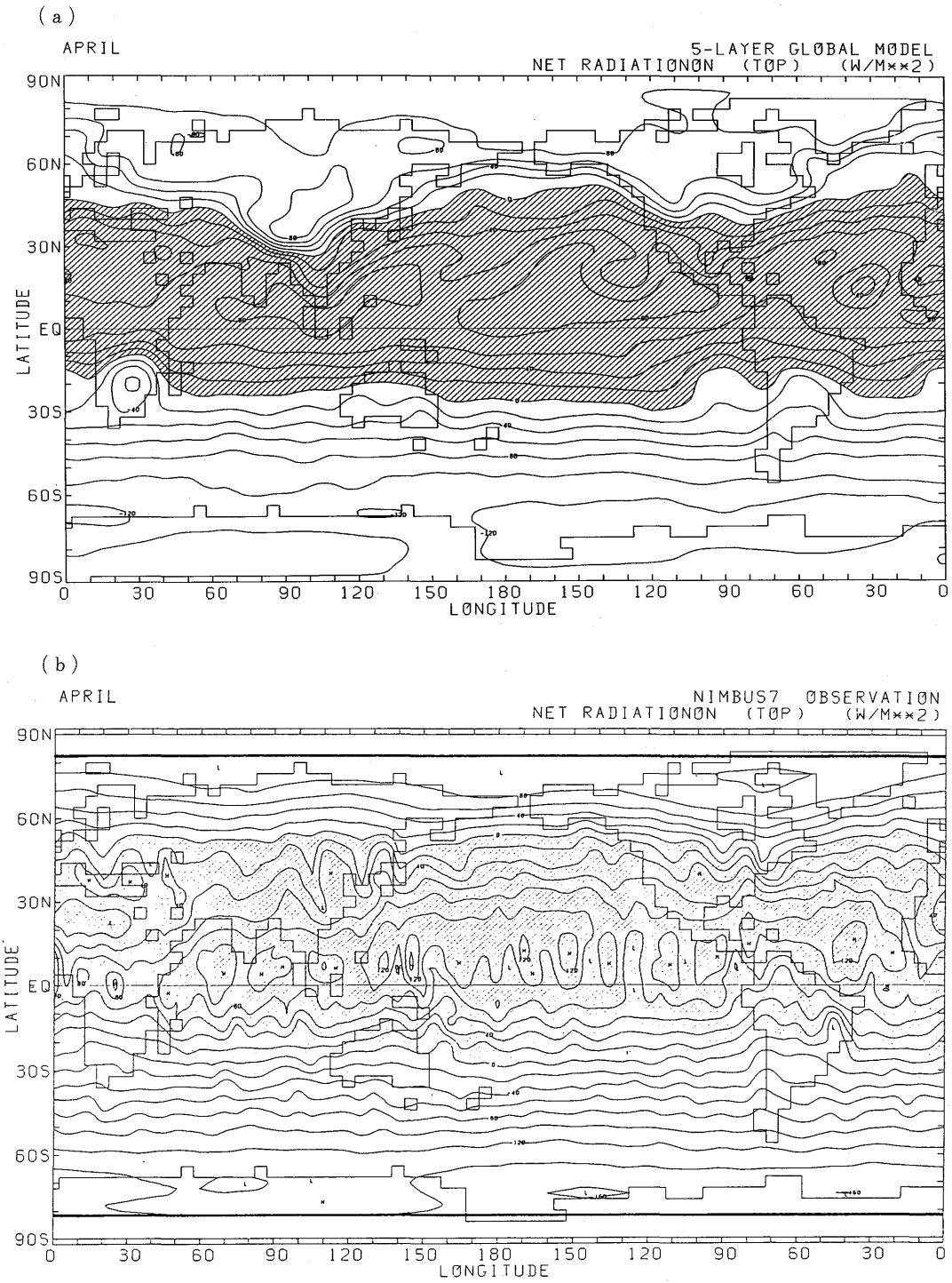


Fig. AIII.2.xi Same as in Fig. AIII.1.xi but for April.

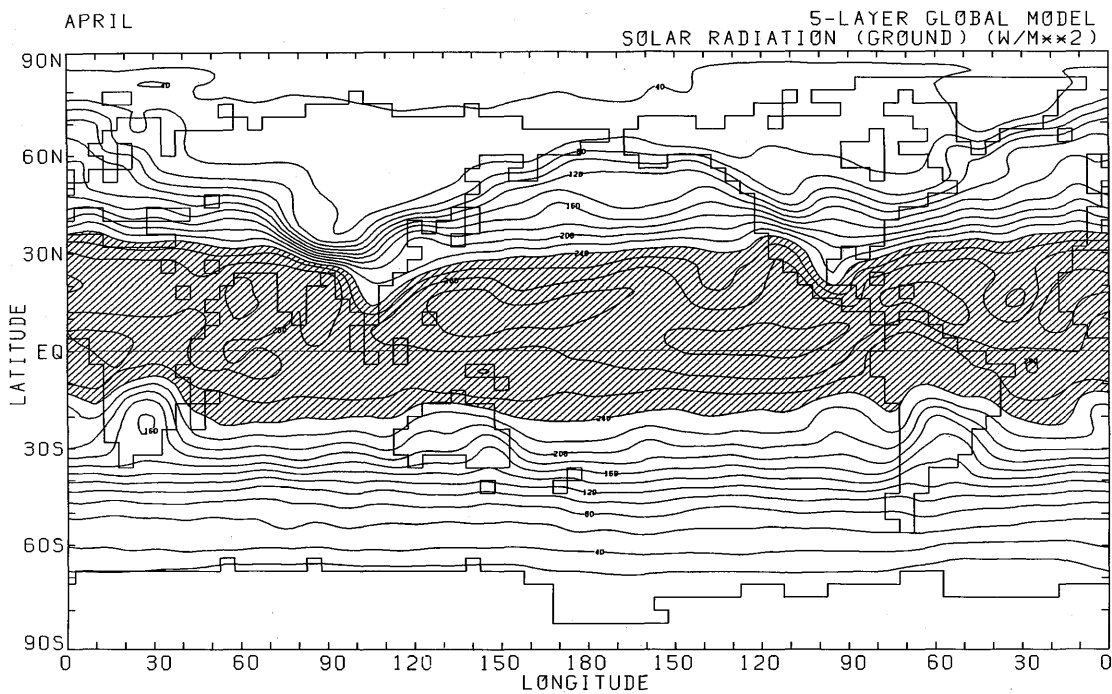


Fig. AIII.2.xii Same as in Fig. AIII.1.xii but for April.

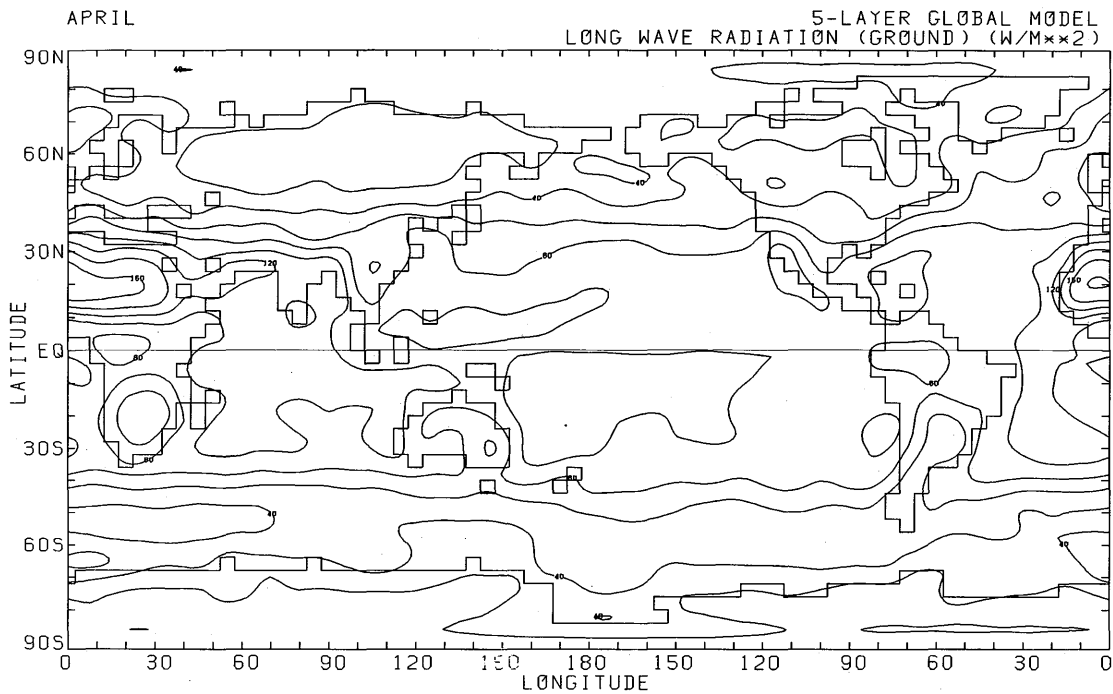


Fig. AIII.2.xiii Same as in Fig. AIII.1.xiii but for April.

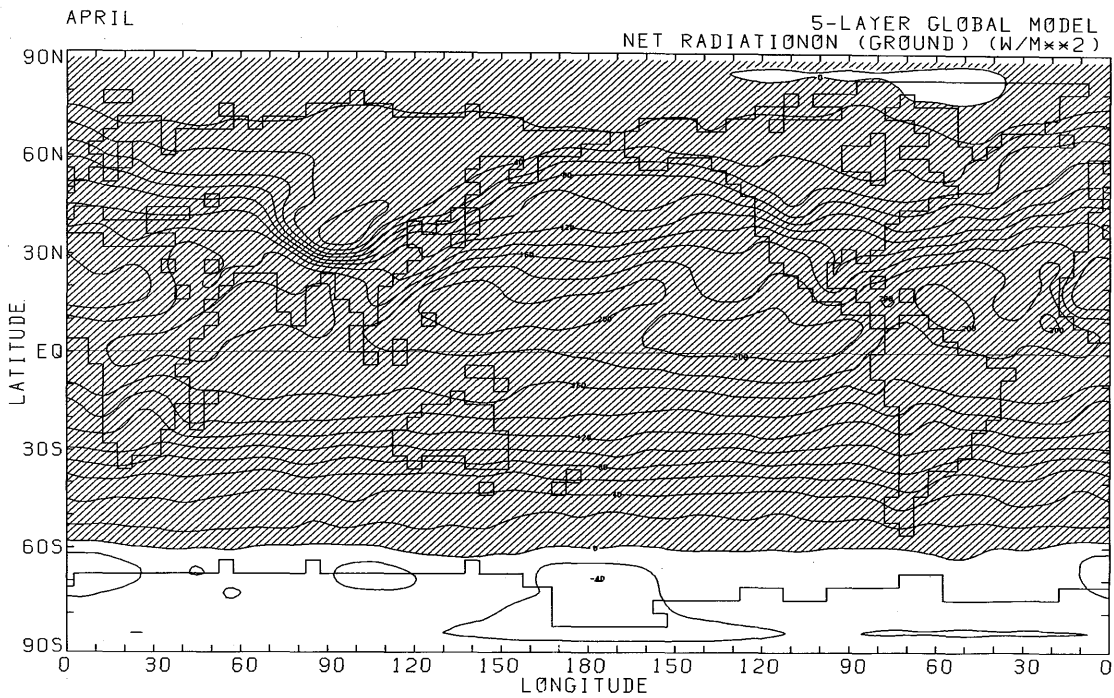


Fig. AIII.2.xiv Same as in Fig. AIII.1.xiv but for April.

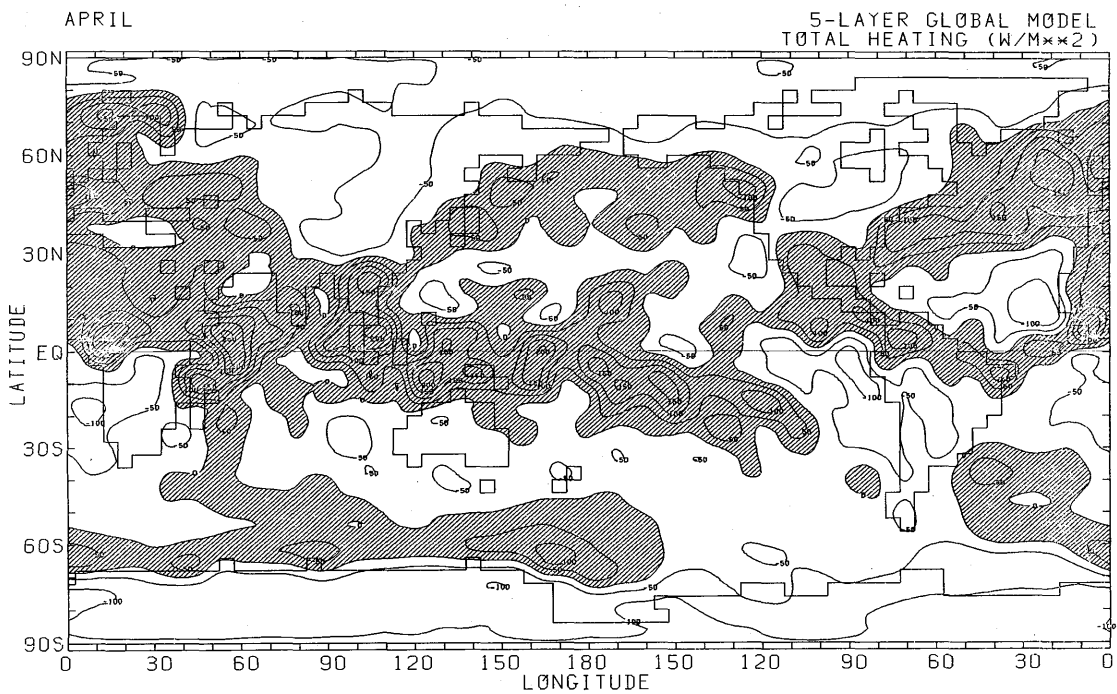


Fig. AIII.2.xv Same as in Fig. AIII.1.xv but for April.

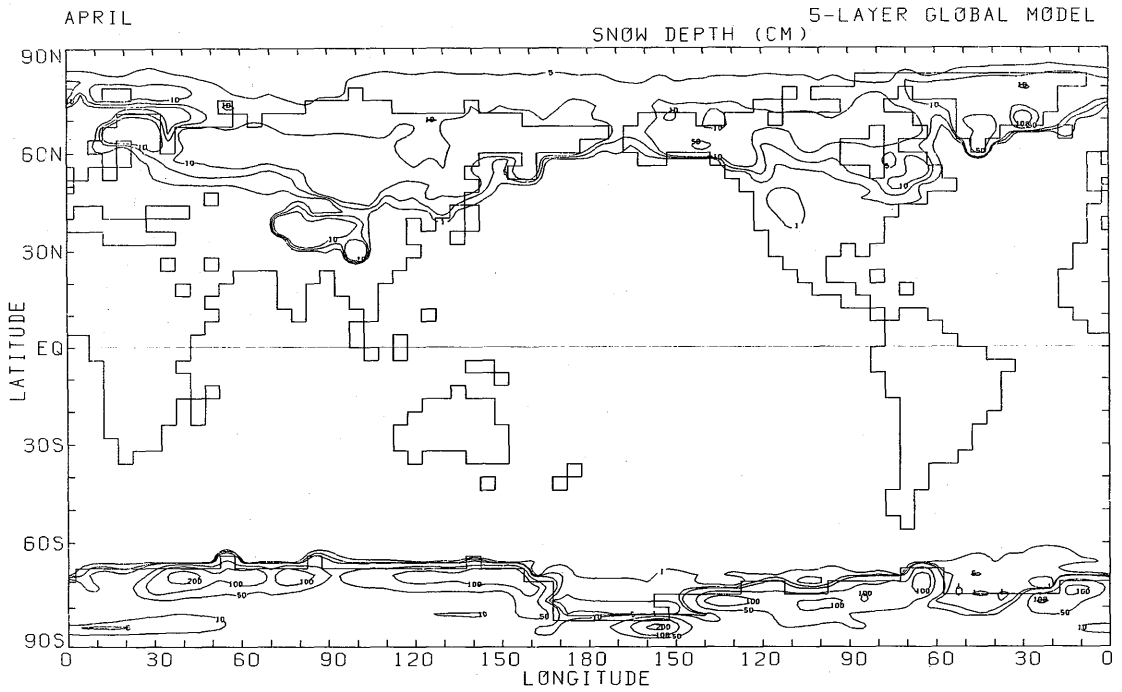


Fig. AIII.2.xvi Same as in Fig. AIII.1.xvi but for April.

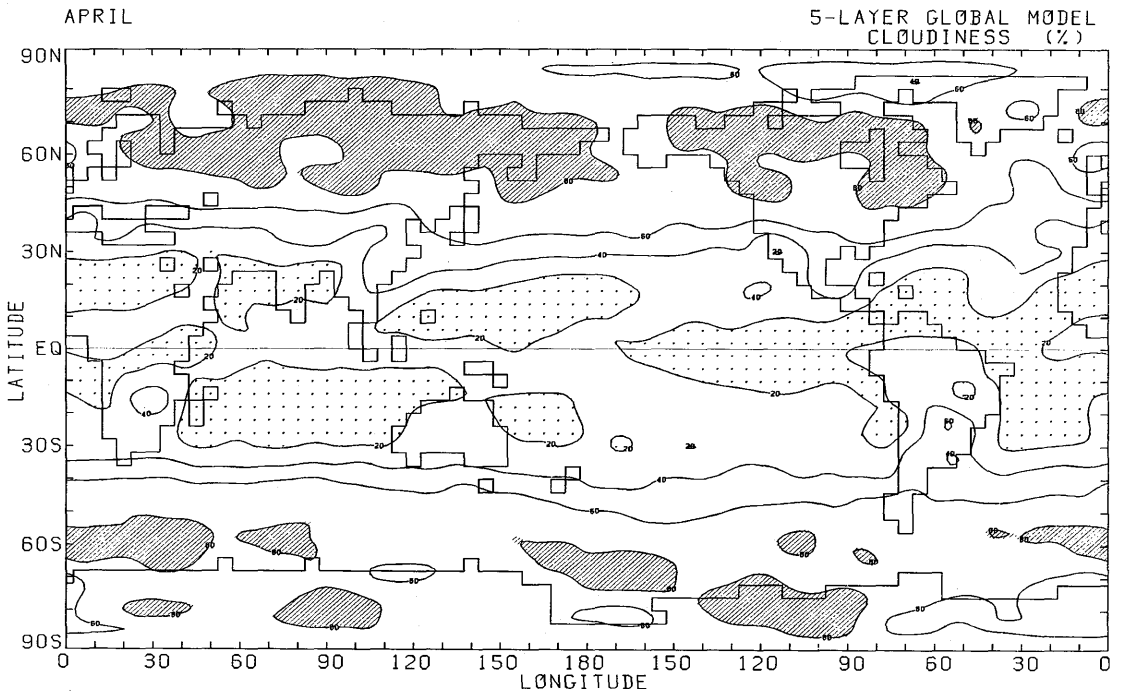


Fig. AIII.2.xvii Same as in Fig. AIII.1.xvii but for April.

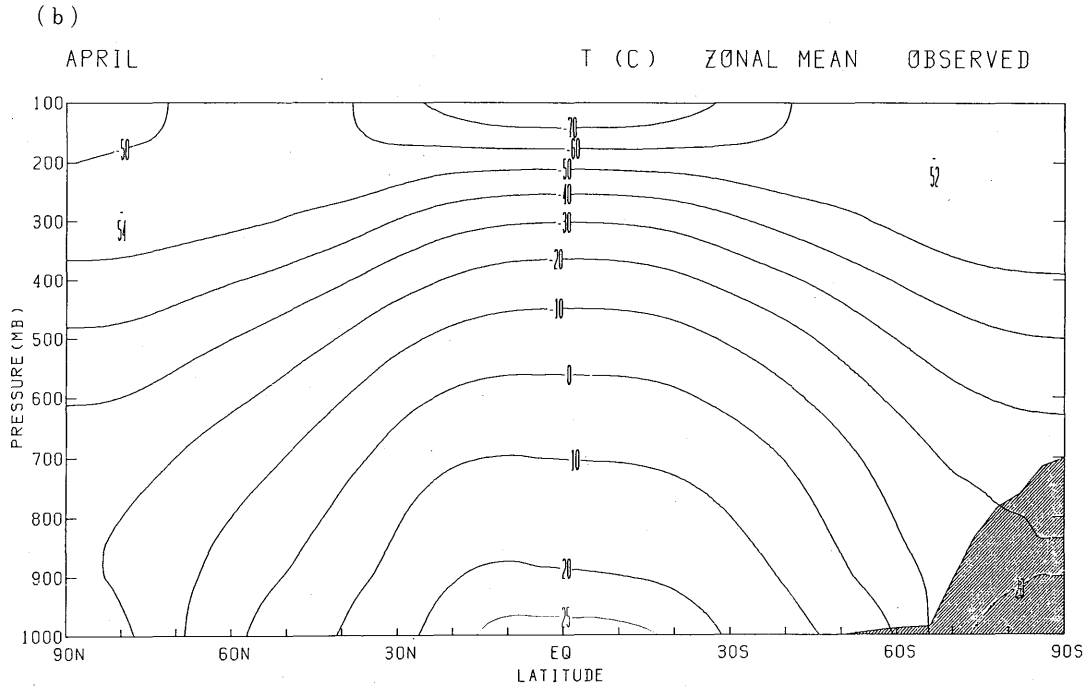
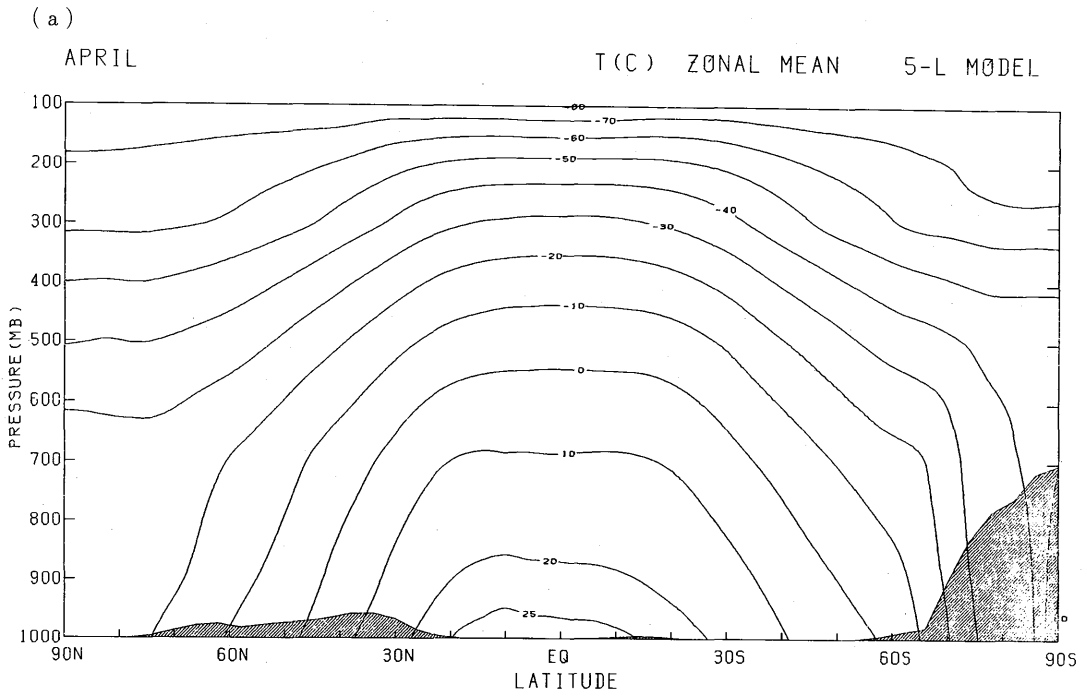


Fig. AIII.2.xviii Same as in Fig. AIII.1.xviii but for April.

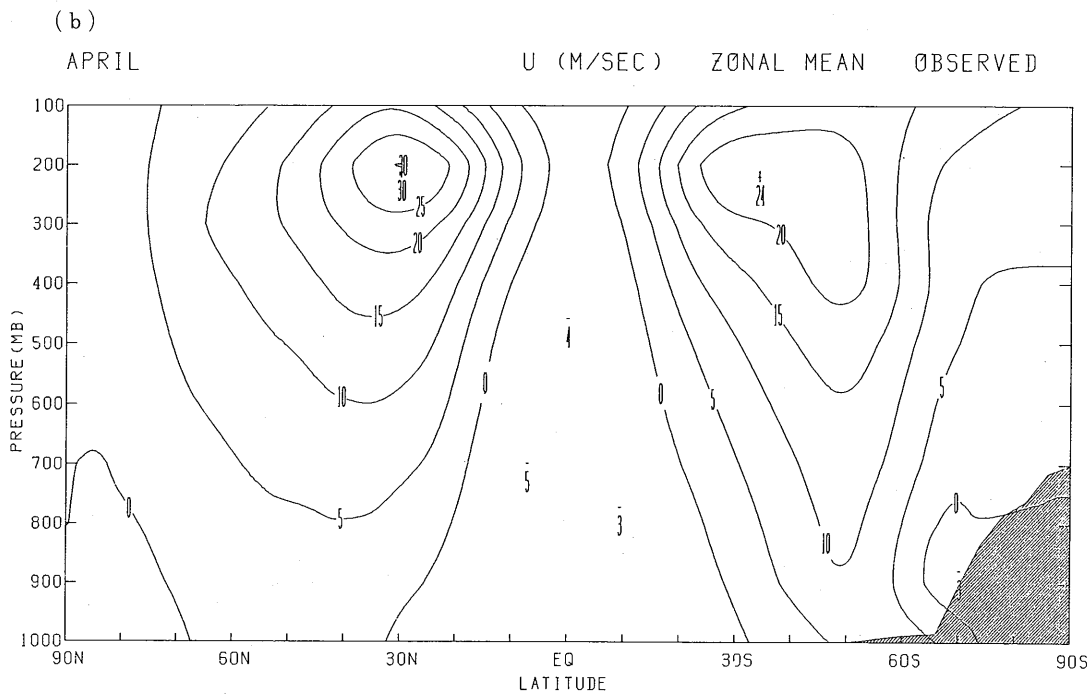
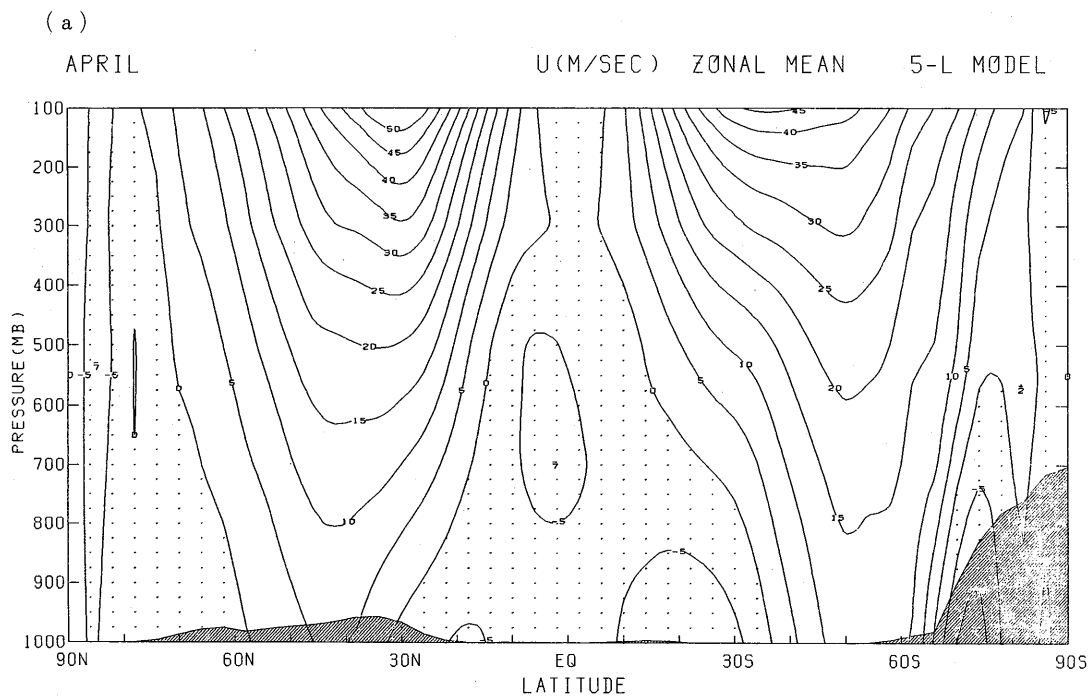


Fig. AIII.2.xix Same as in Fig. AIII.1.xix but for April.



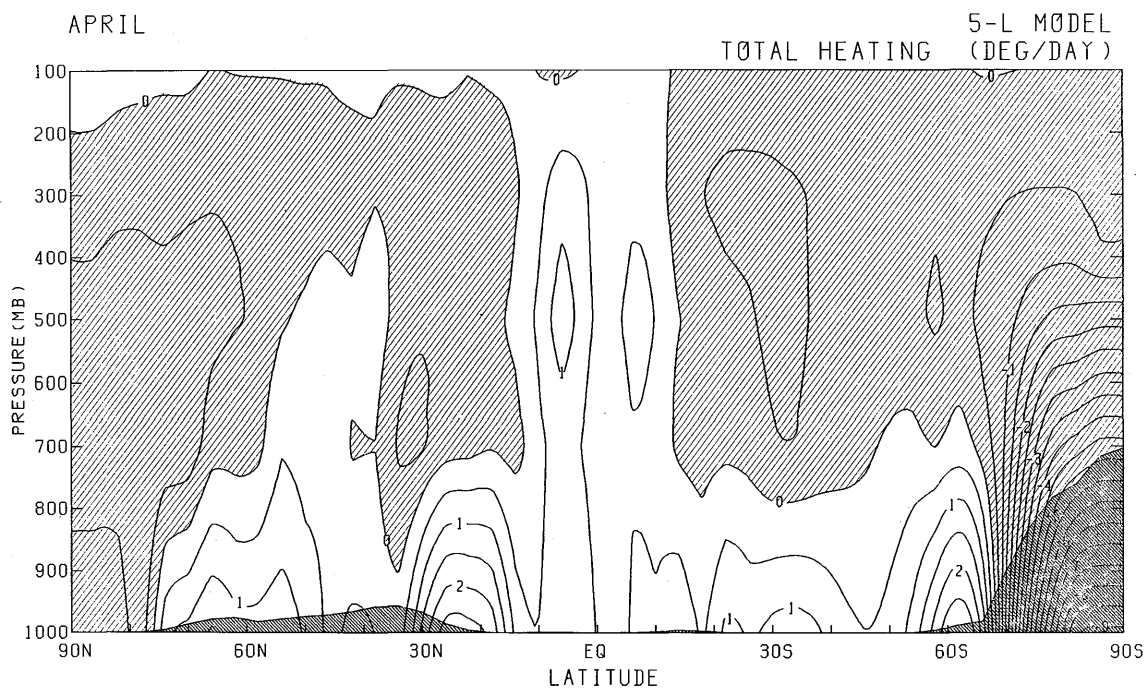


Fig. AIII.2.xxi Same as in Fig. AIII.1.xxi but for April.

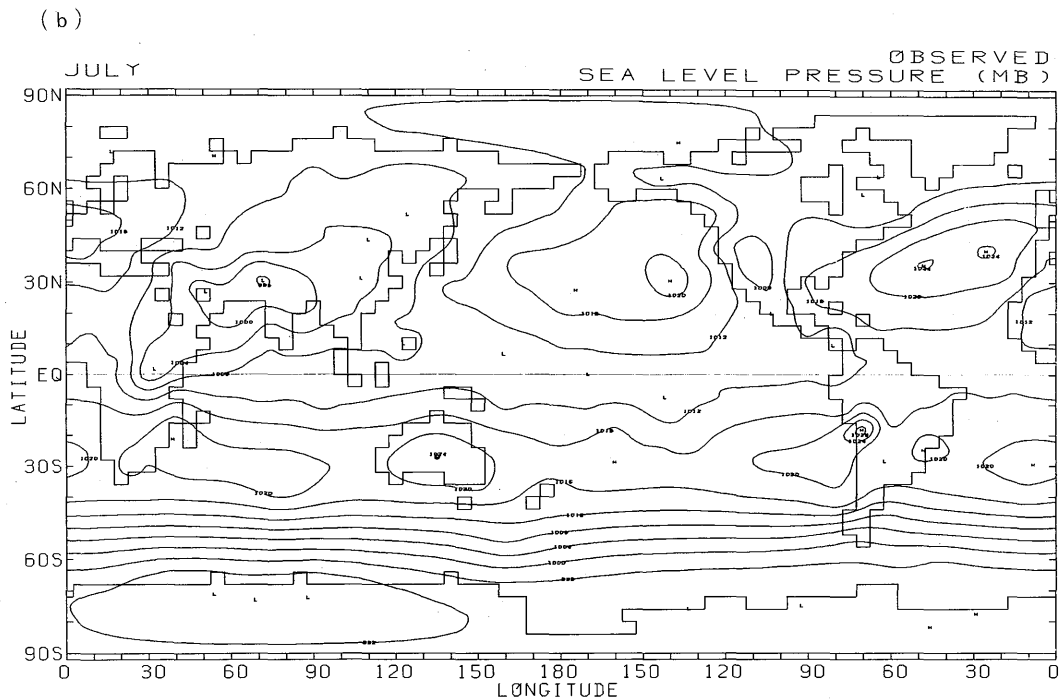
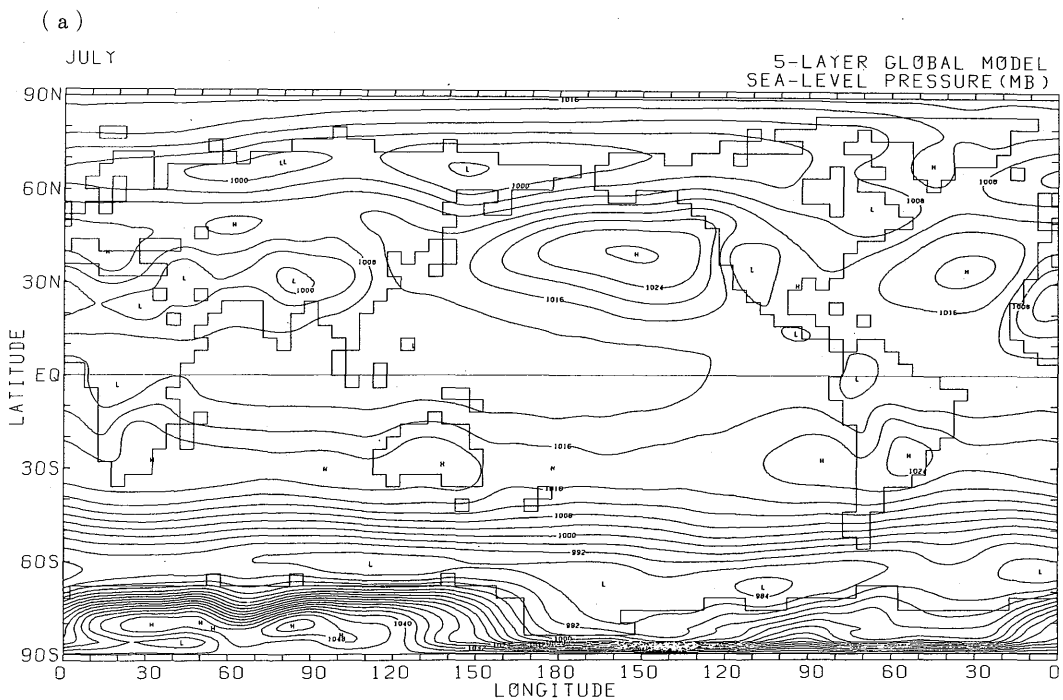
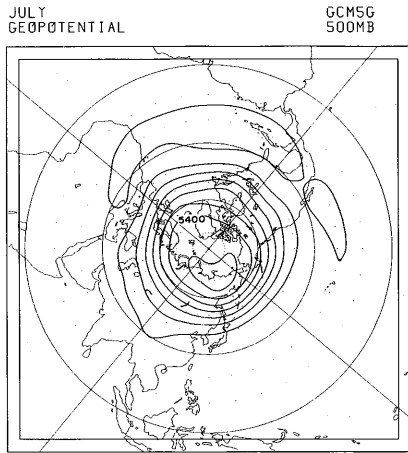
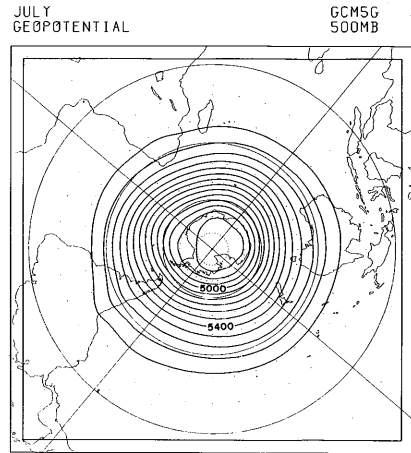


Fig. AIII.3.i Same as in Fig. AIII.1.i but for July.

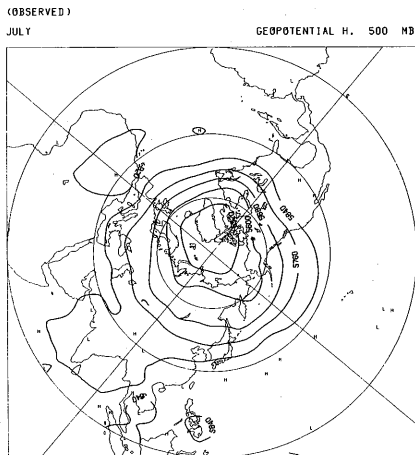
( a - 1 )



( a - 2 )



( b - 1 )



( b - 2 )

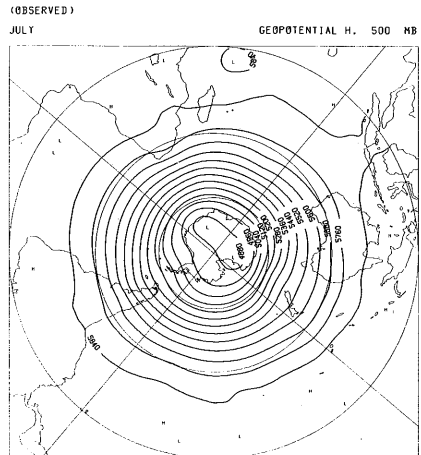


Fig. AIII.3.ii Same as in Fig. AIII.1.ii but for July.

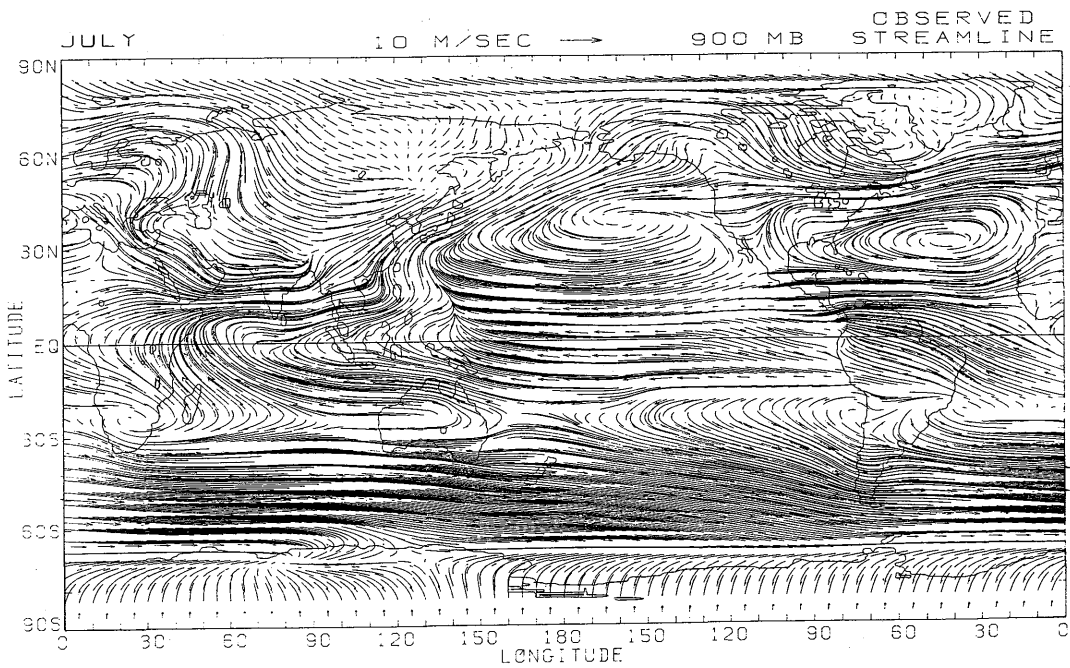
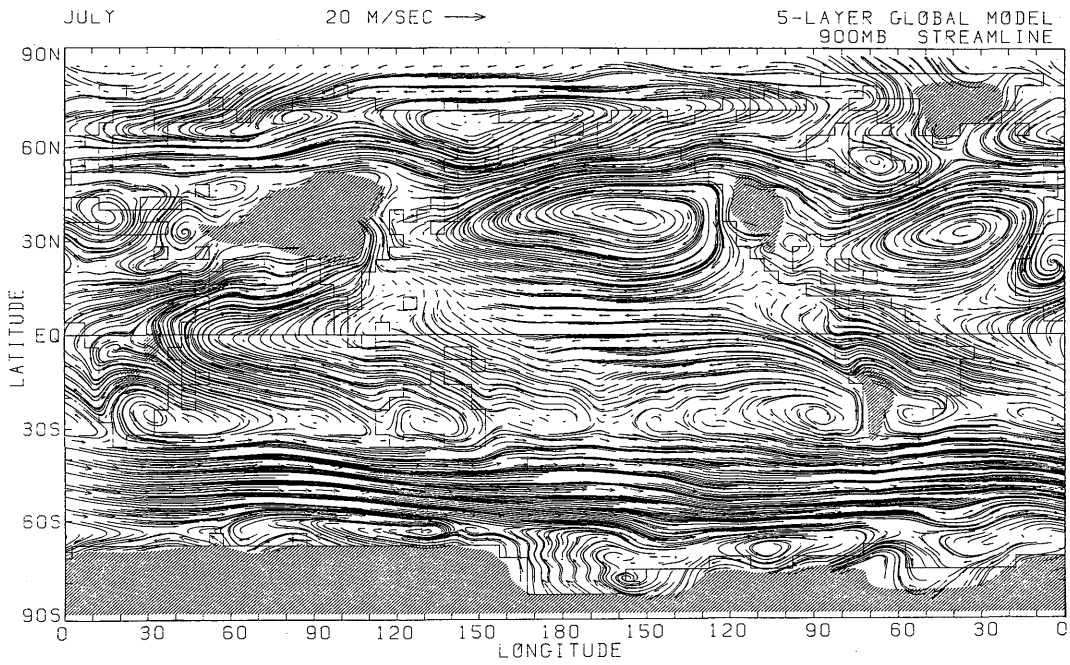


Fig. AIII.3.iii Same as in Fig. AIII.1.iii but for July.

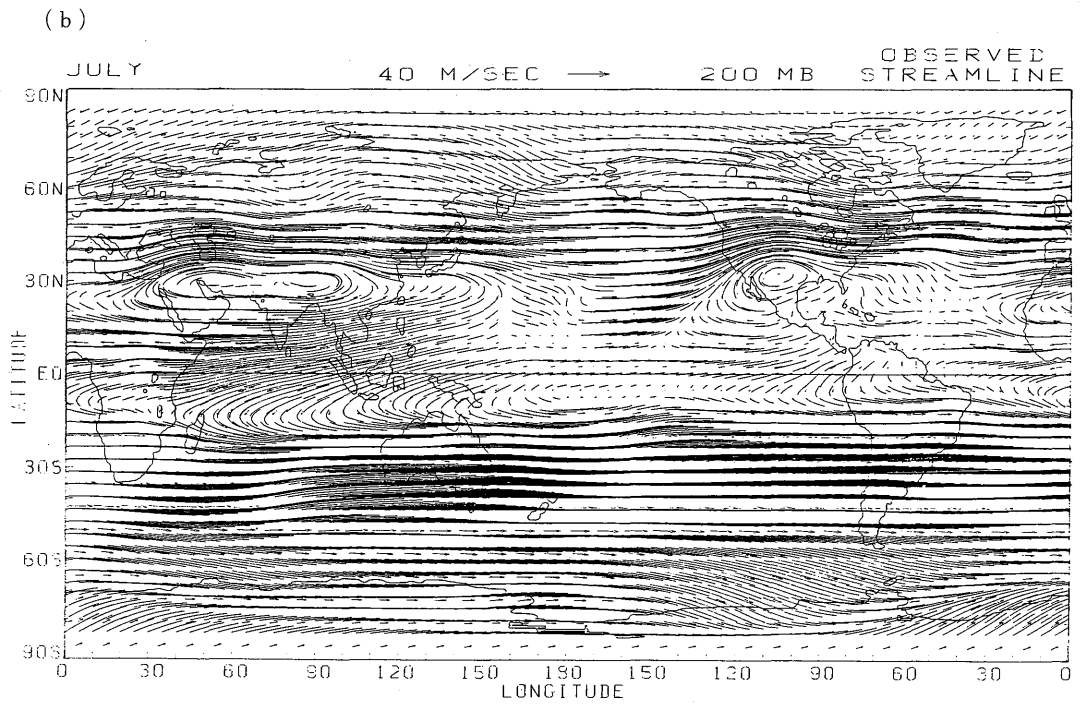
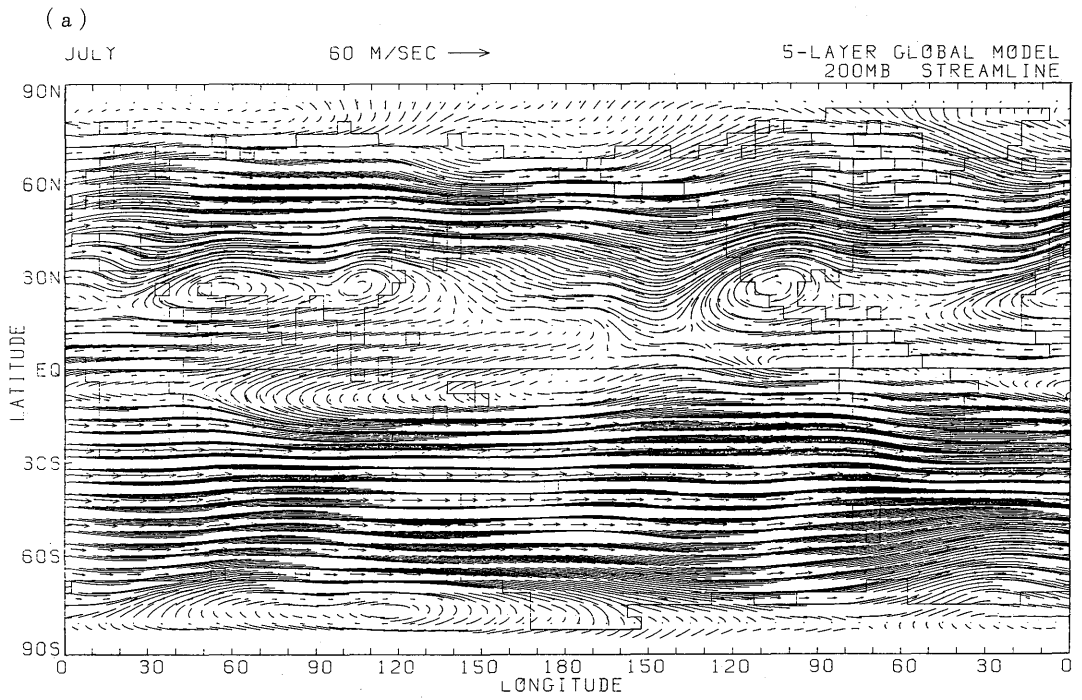


Fig. AIII.3.iv Same as in Fig. AIII.1.iv but for July.

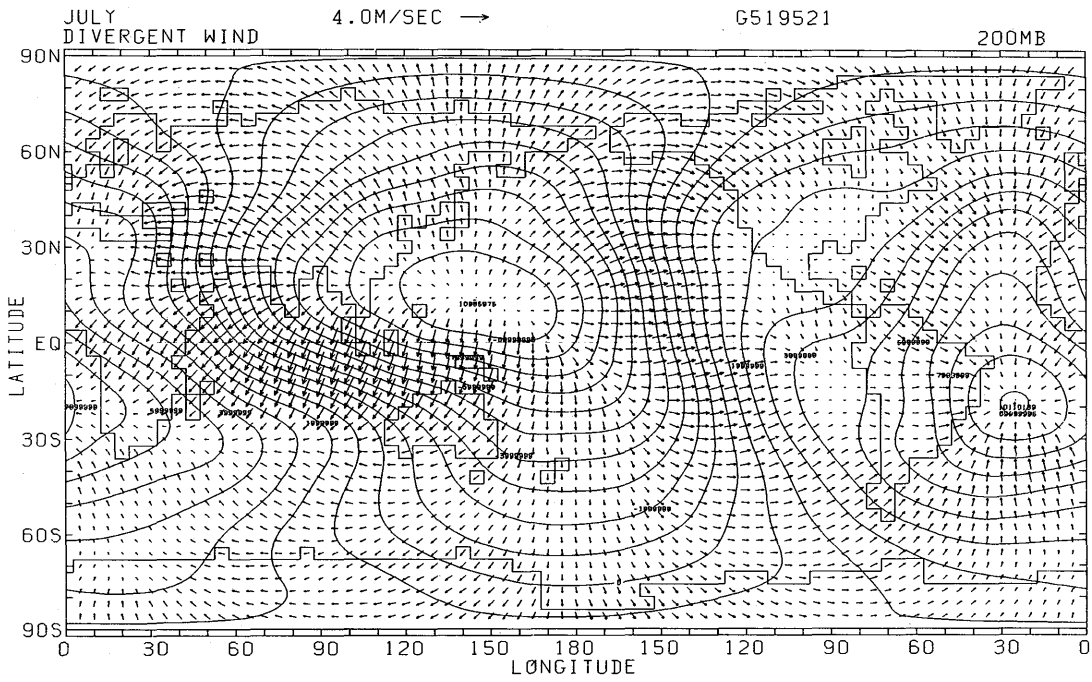


Fig. AIII.3.v Same as in Fig. AIII.1.v but for July.

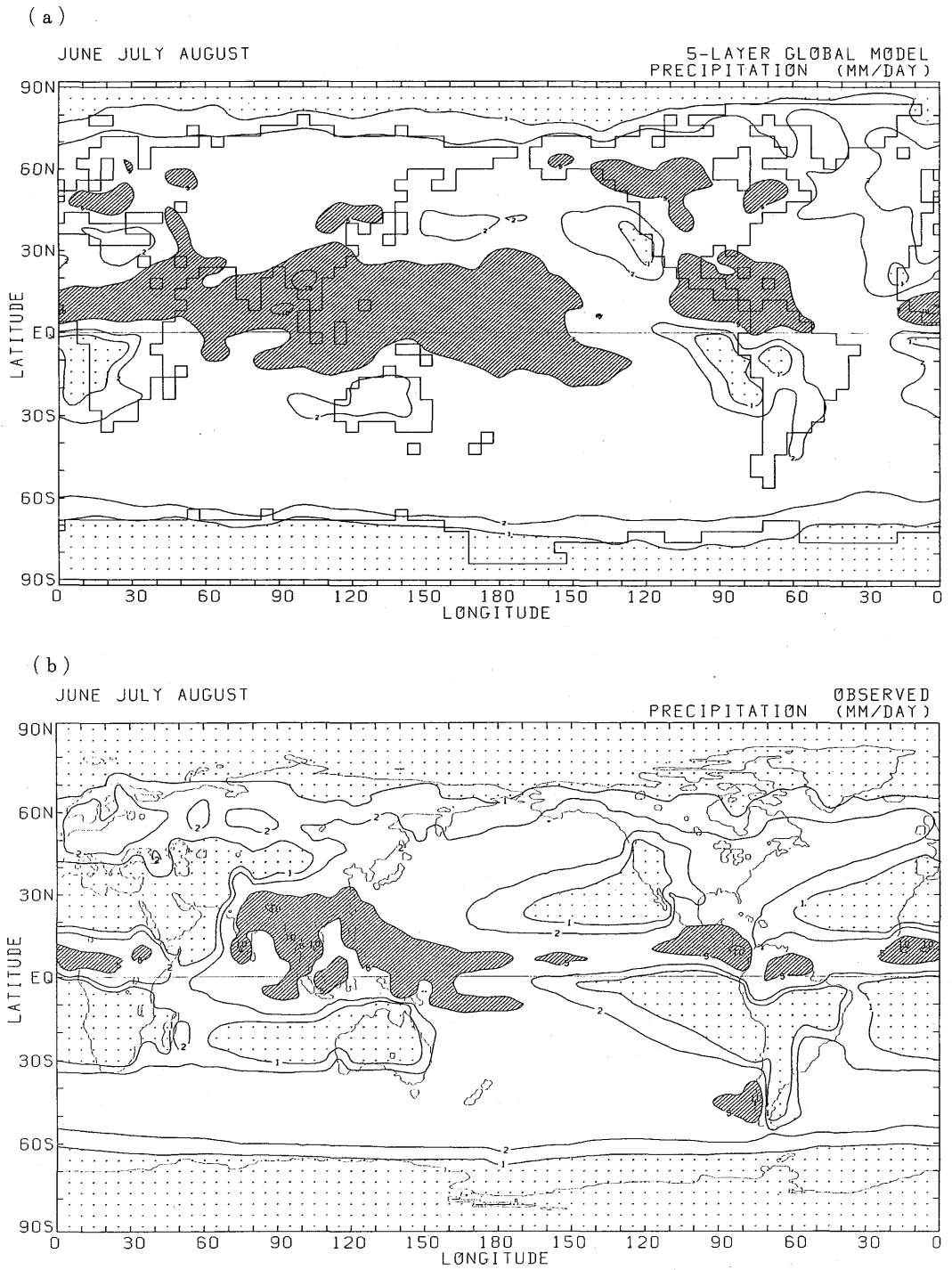


Fig. AIII.2.vi Same as in Fig. AIII.1.vi but for June, July and August.

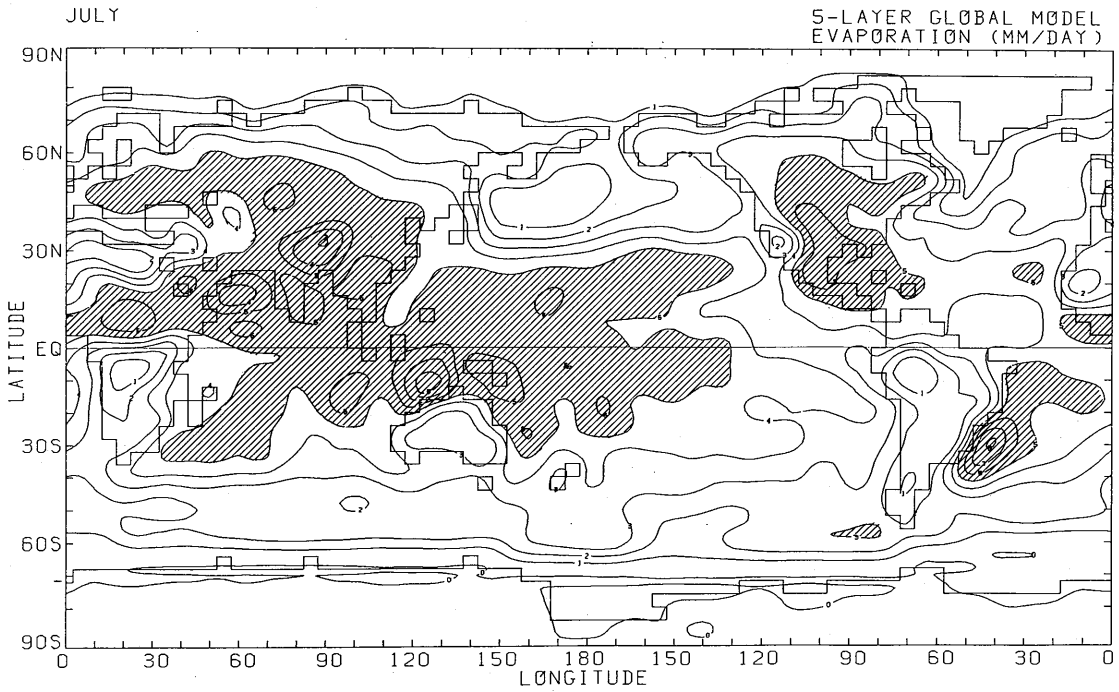


Fig. AIII.3.vii Same as in Fig. AIII.1.vii but for July.

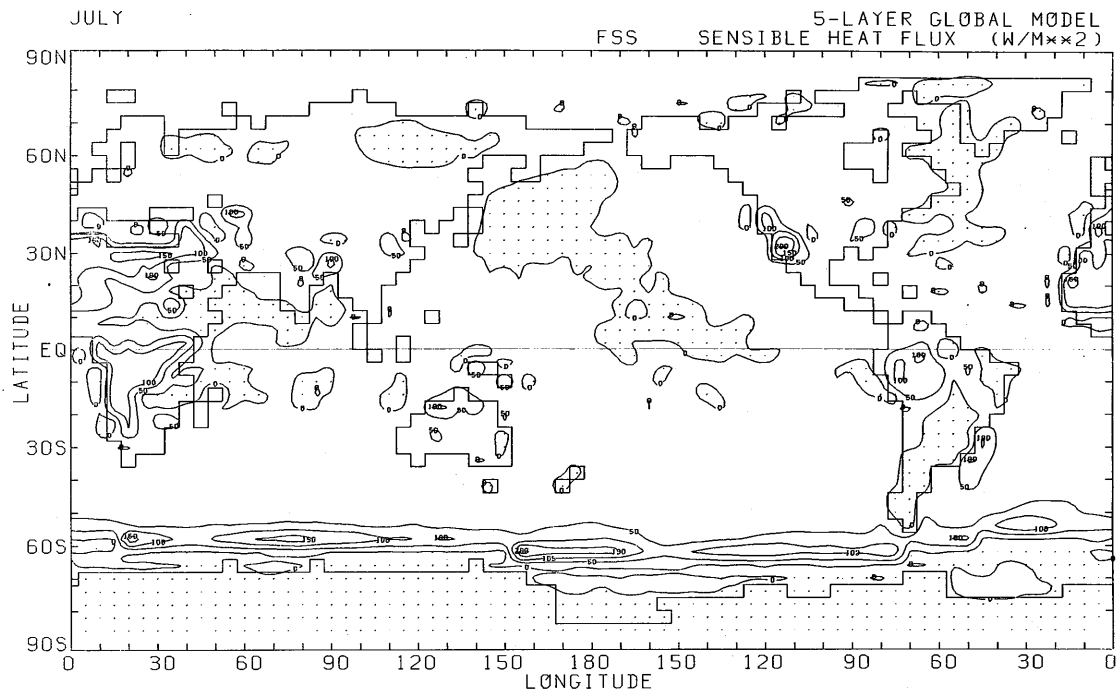


Fig. AIII.3.viii Same as in Fig. AIII.1.viii but for July.

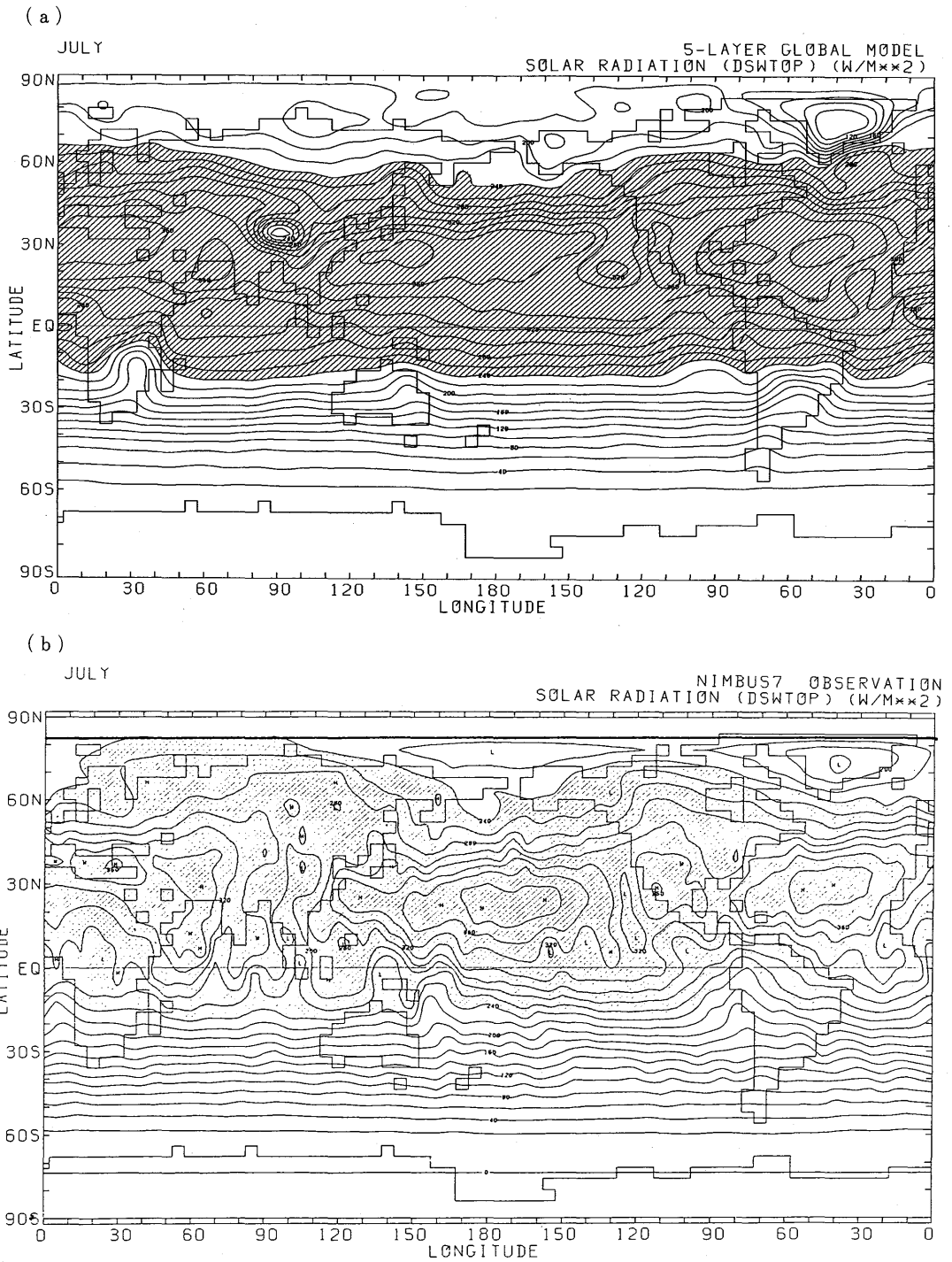


Fig. AIII.3.ix Same as in Fig. AIII.1.ix but for July.

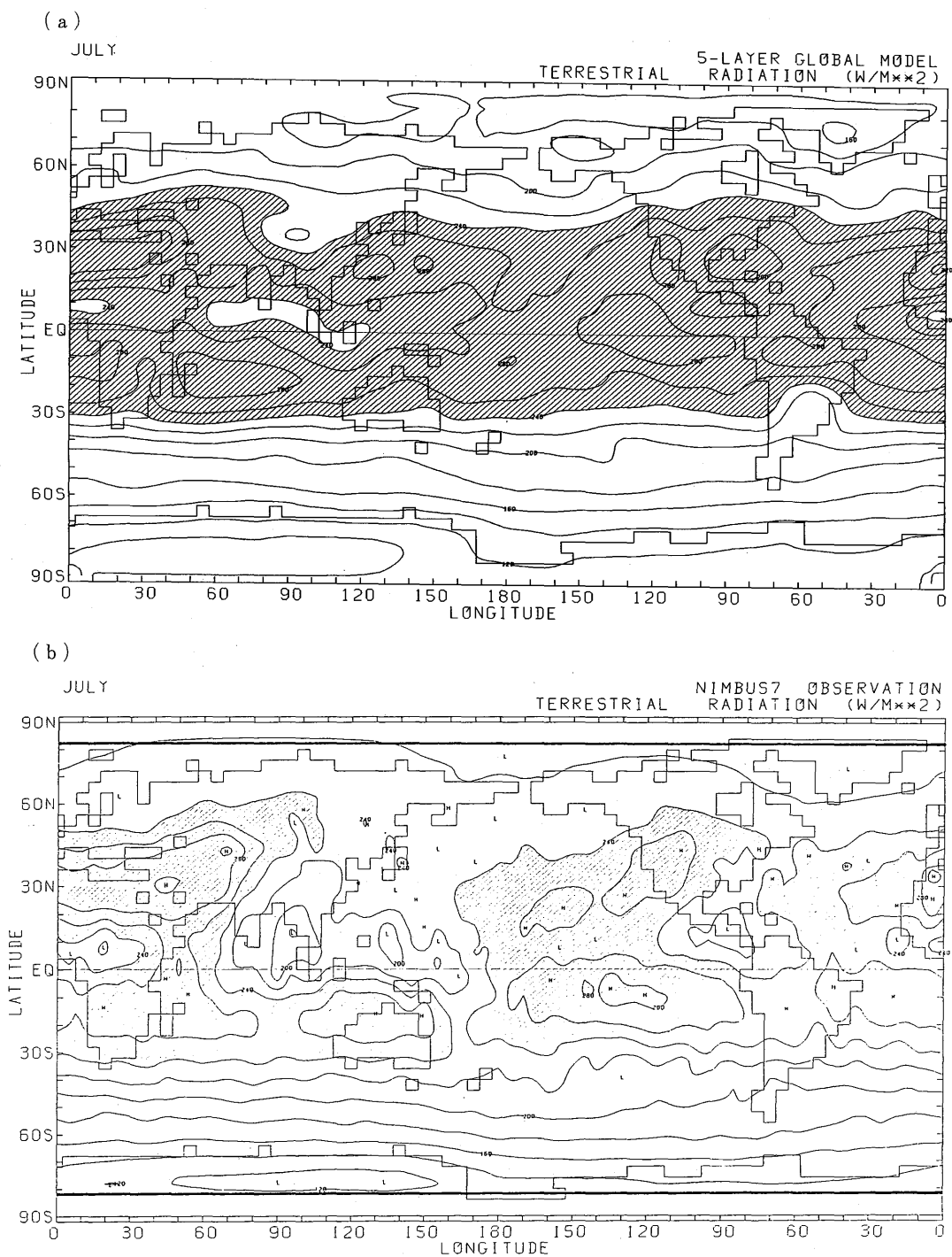


Fig. AIII.3.x Same as in Fig. AIII.1.x but for July.

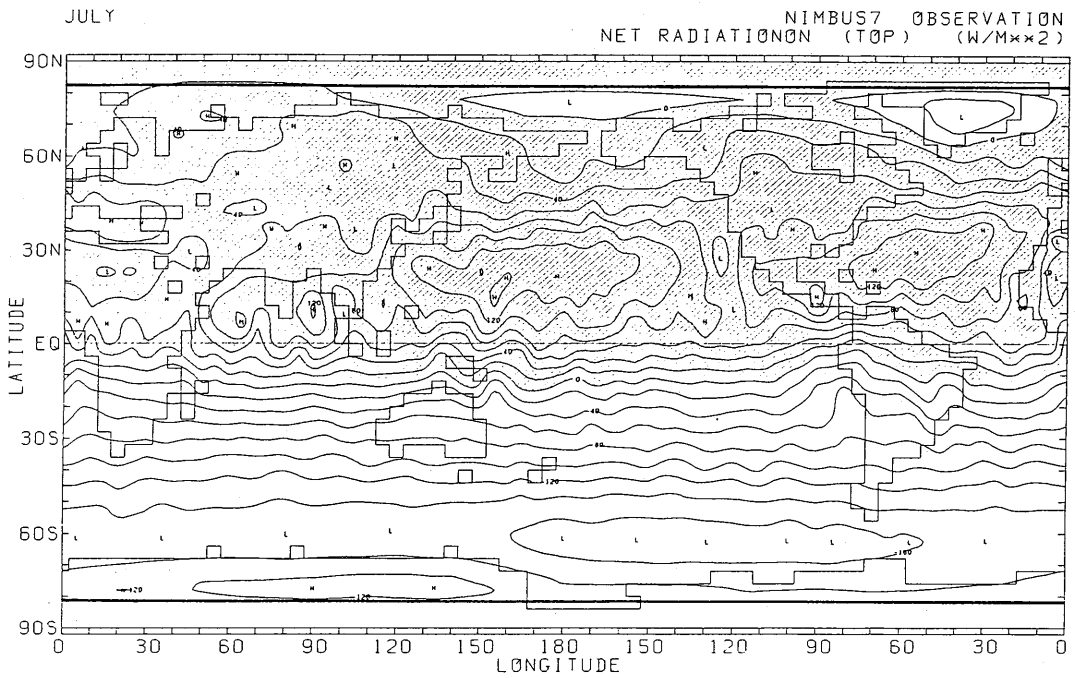
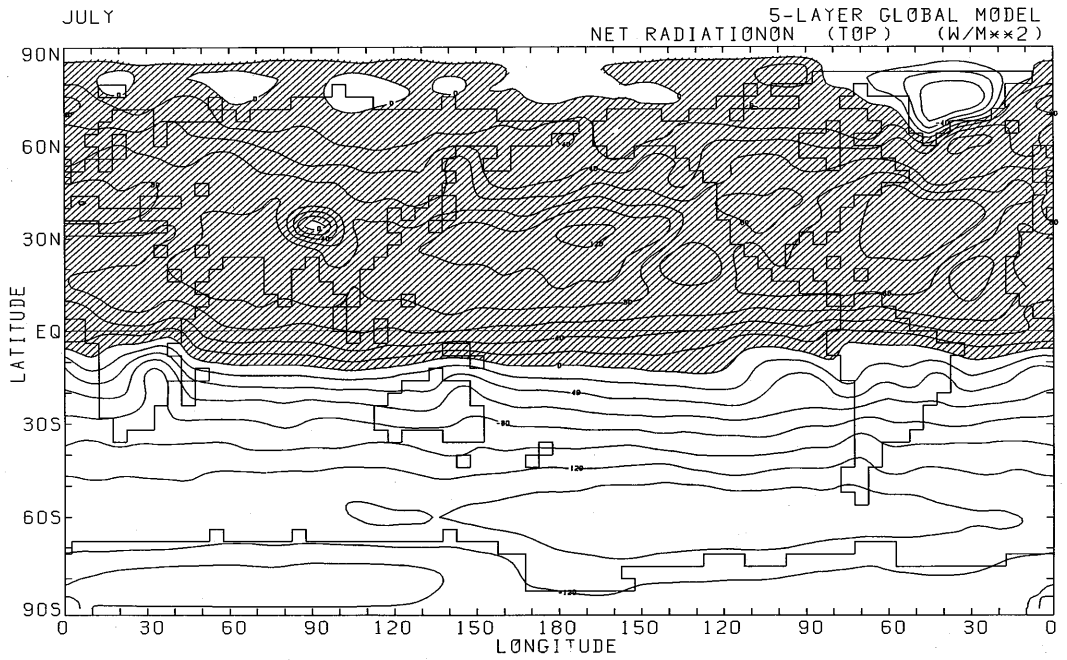


Fig. AIII.3.xi Same as in Fig. AIII.1.xi but for July.

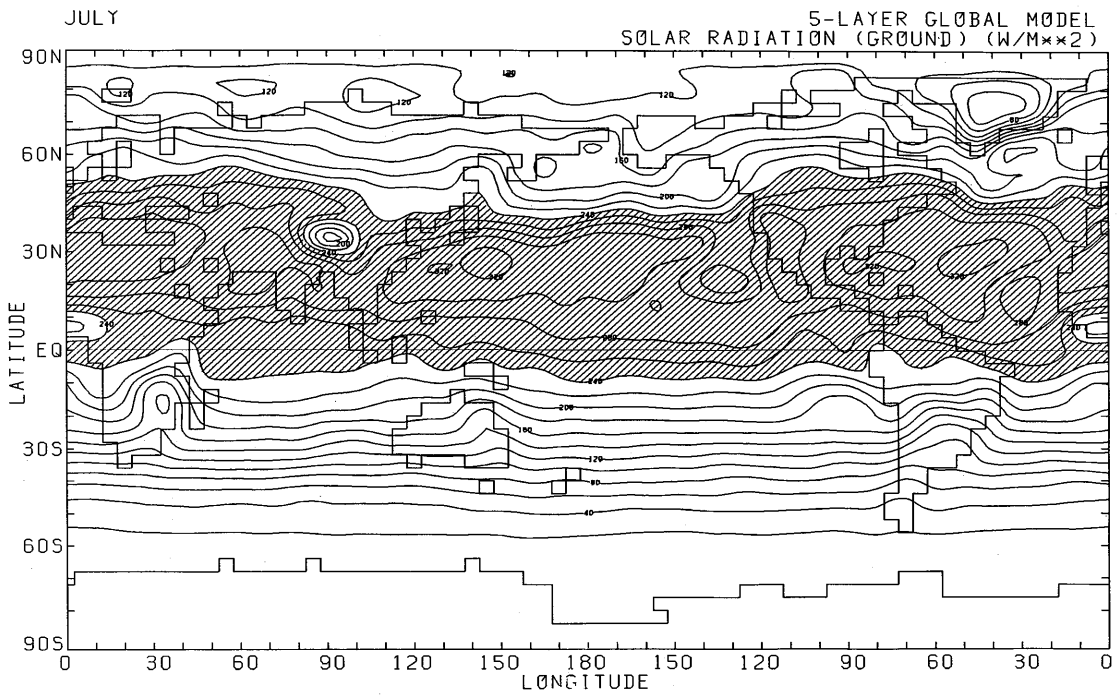


Fig. AIII.3.xii Same as in Fig. AIII.1.xii but for July.

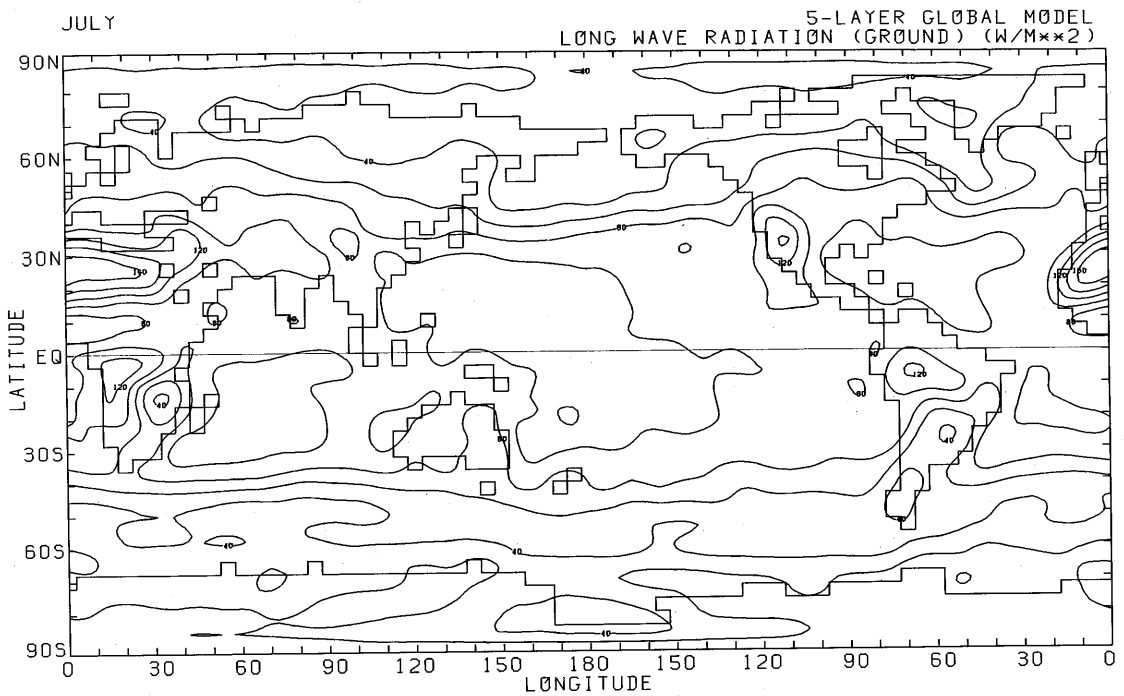


Fig. AIII.3.xiii Same as in Fig. AIII.1.xiii but for July.

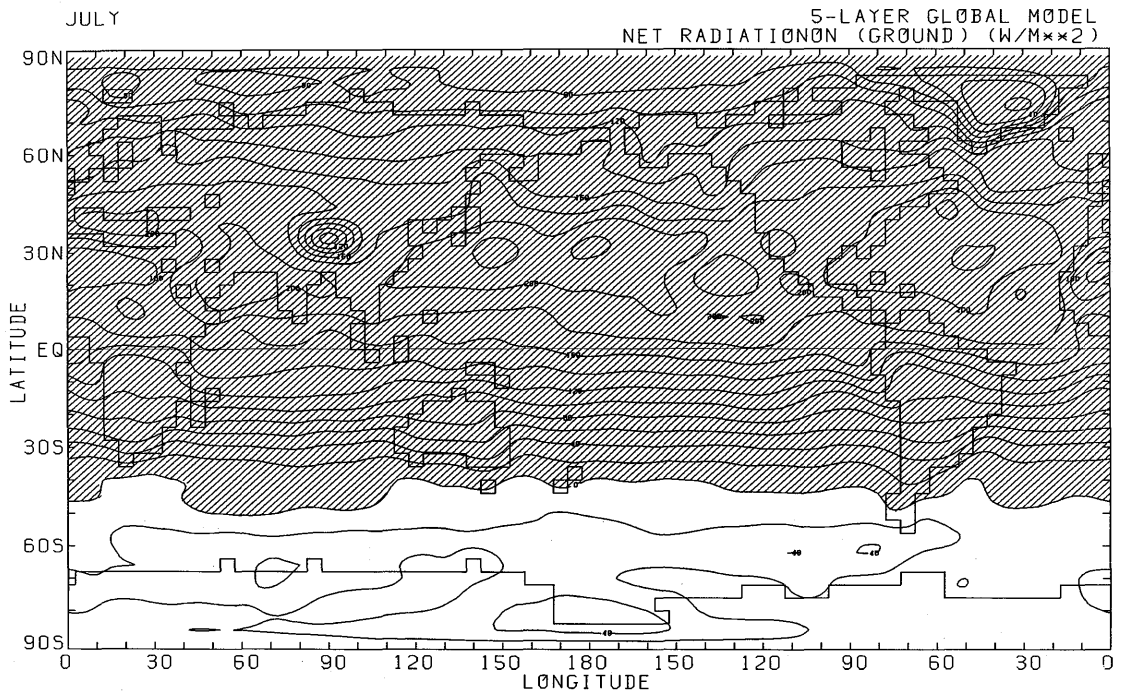


Fig. AIII.3.xiv Same as in Fig. AIII.1.xiv but for July.

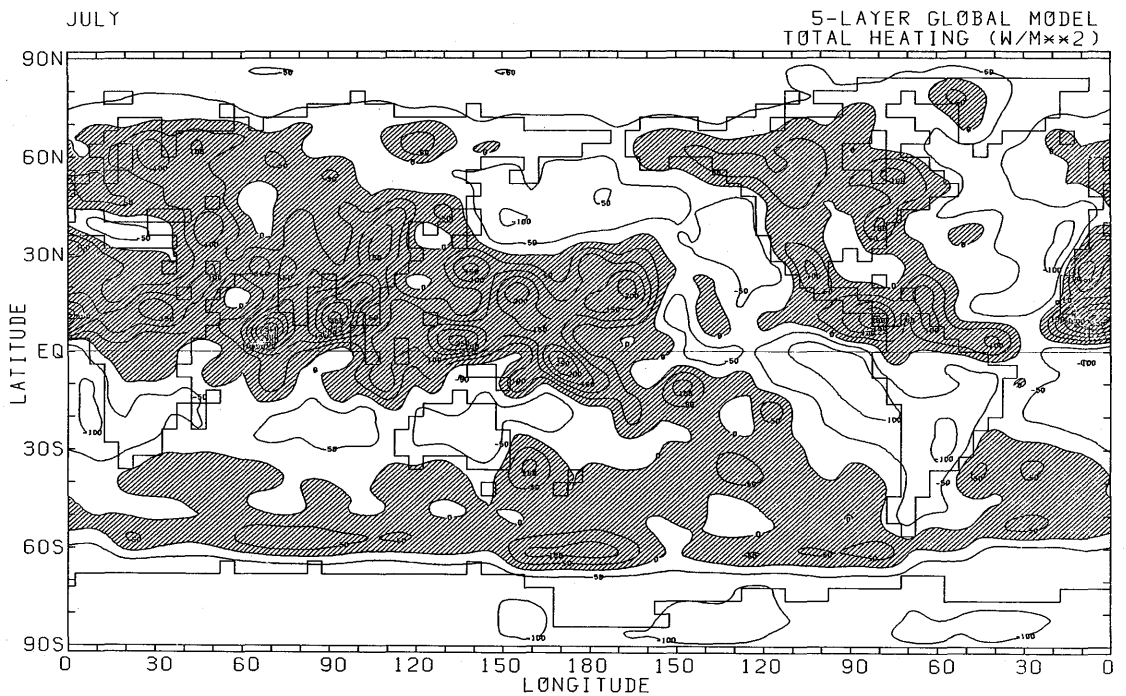


Fig. AIII.3.xv Same as in Fig. AIII.1.xv but for July.

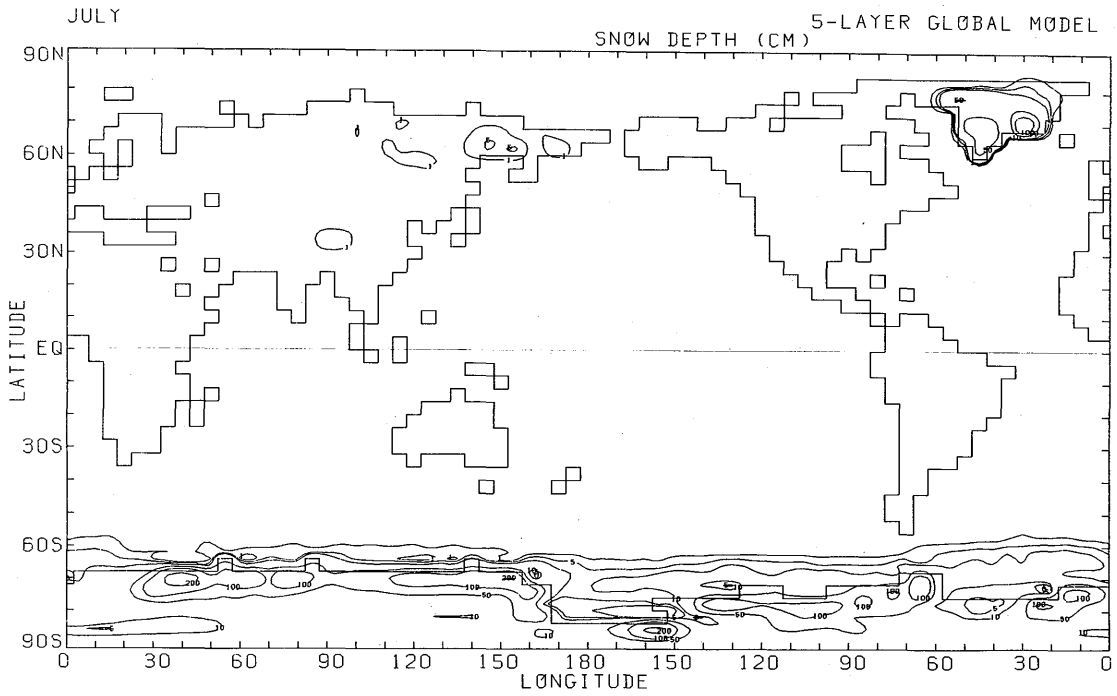


Fig. AIII.3.xvi Same as in Fig. AIII.1.xvi but for July.

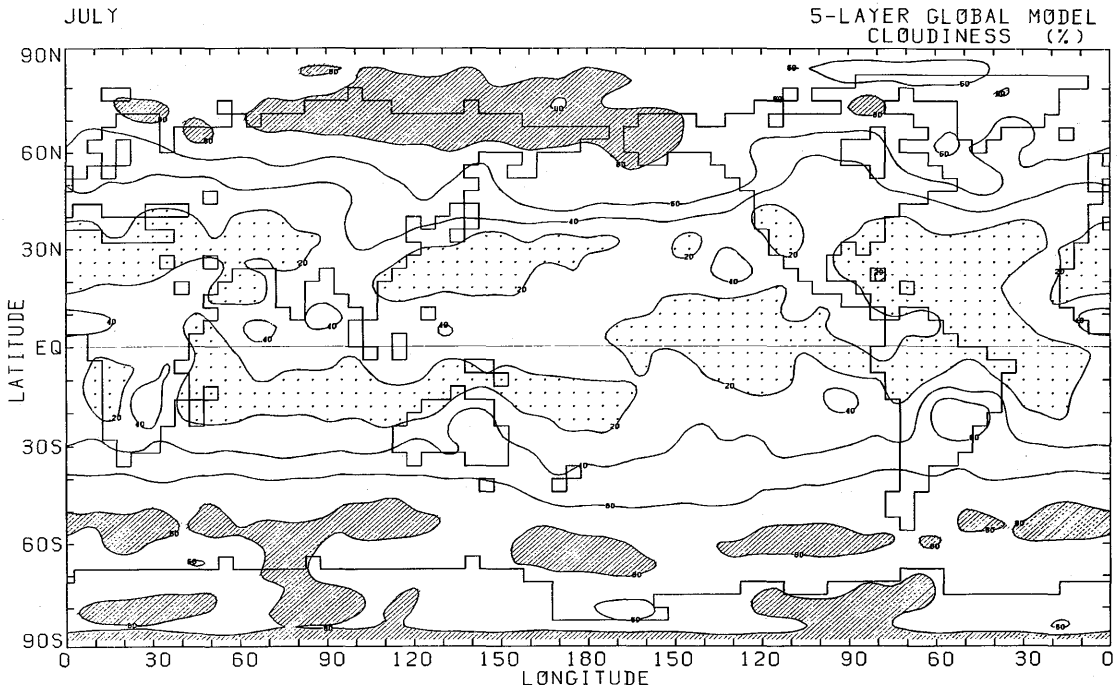


Fig. AIII.3.xvii Same as in Fig. AIII.1.xvii but for July.

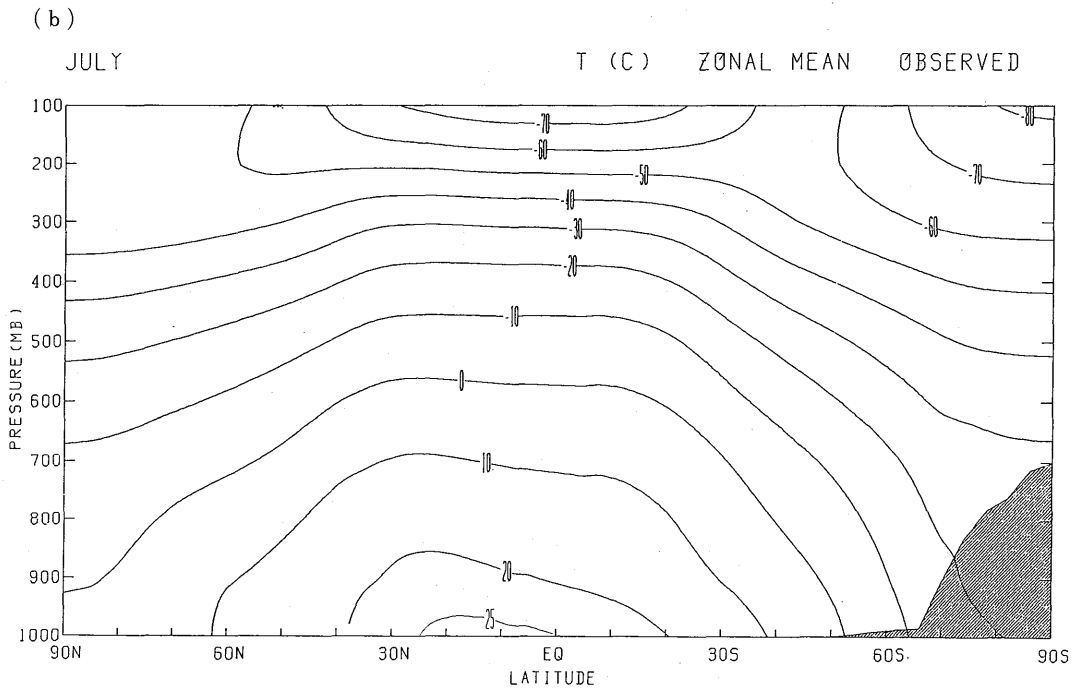
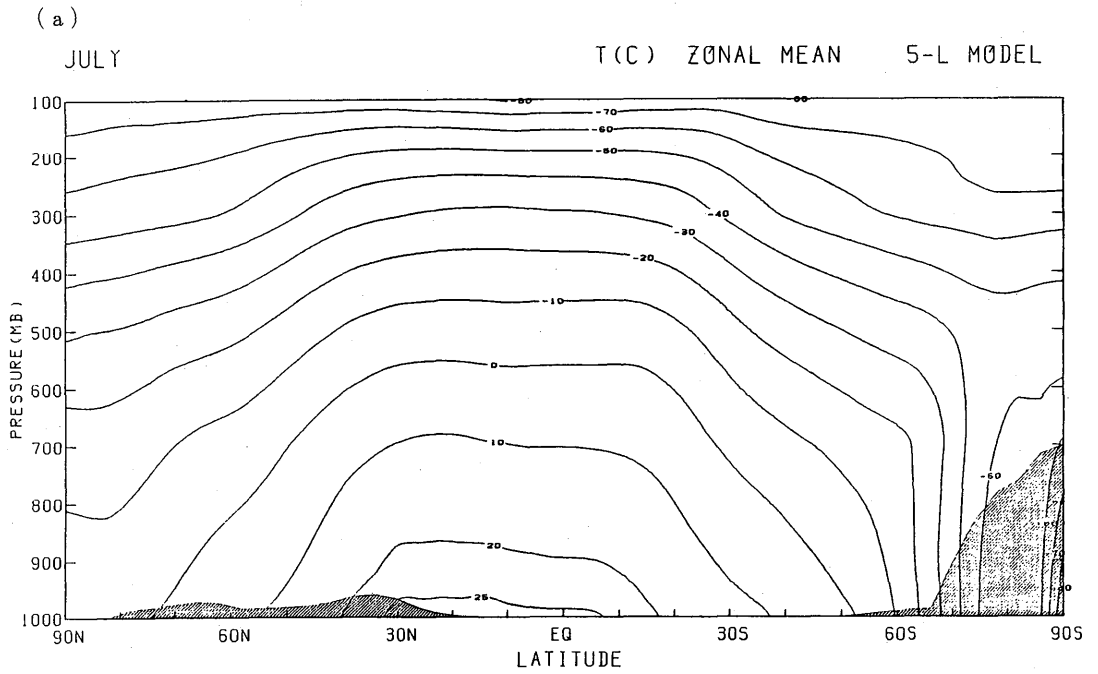


Fig. AIII.3.xviii Same as in Fig. AIII.1.xviii but for July.

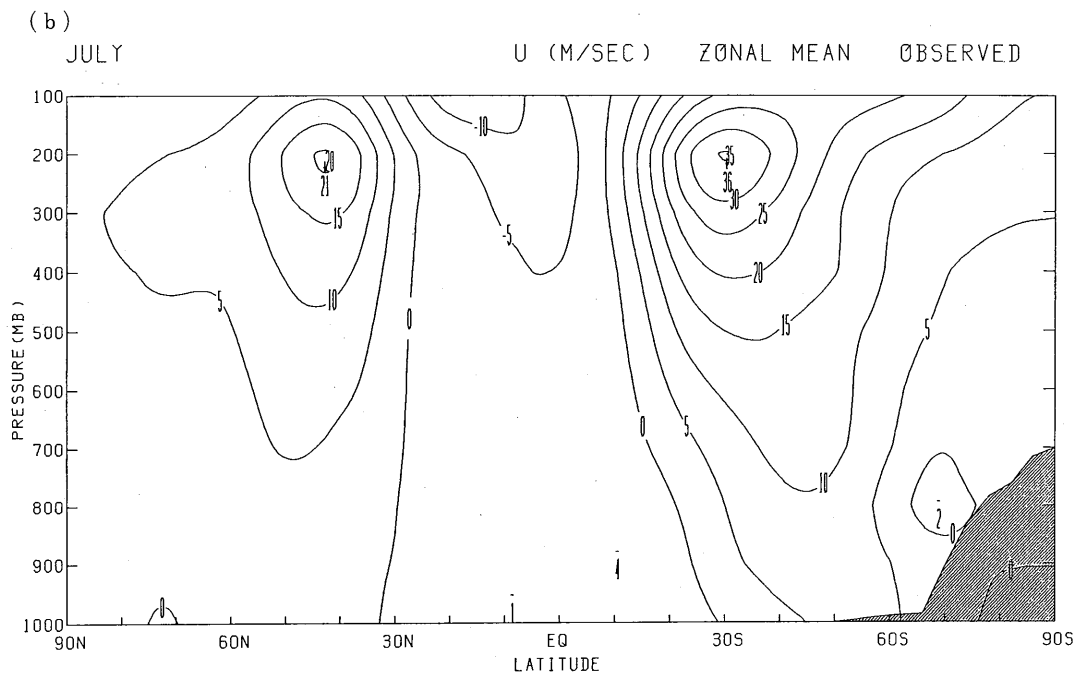
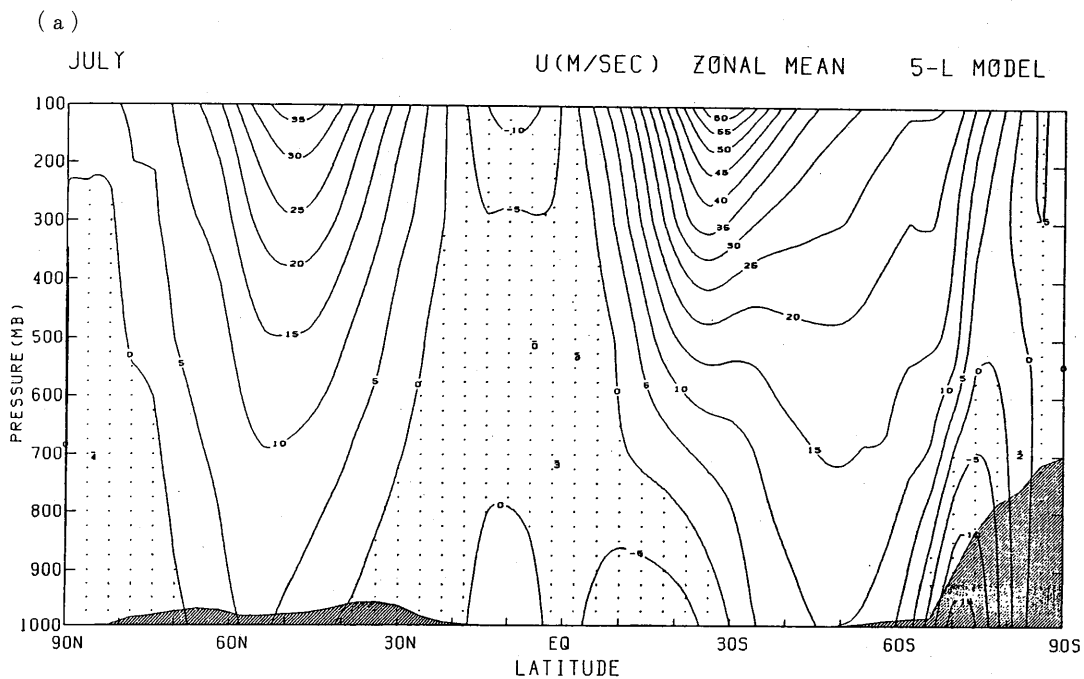


Fig. AIII.3.xix Same as in Fig. AIII.1.xix but for July.

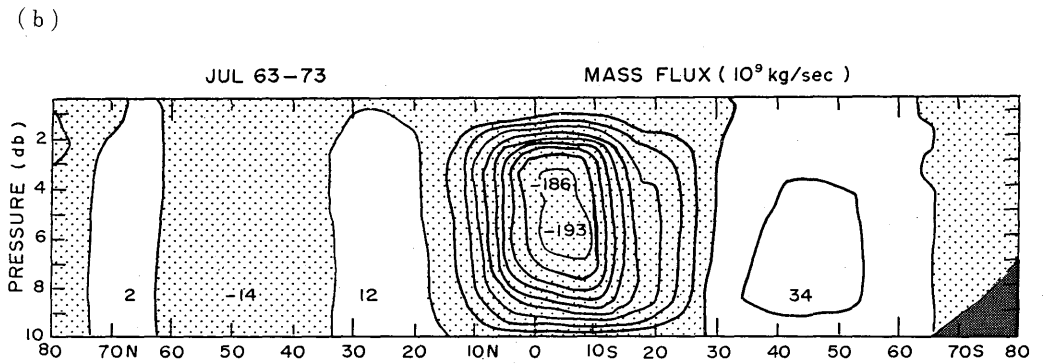
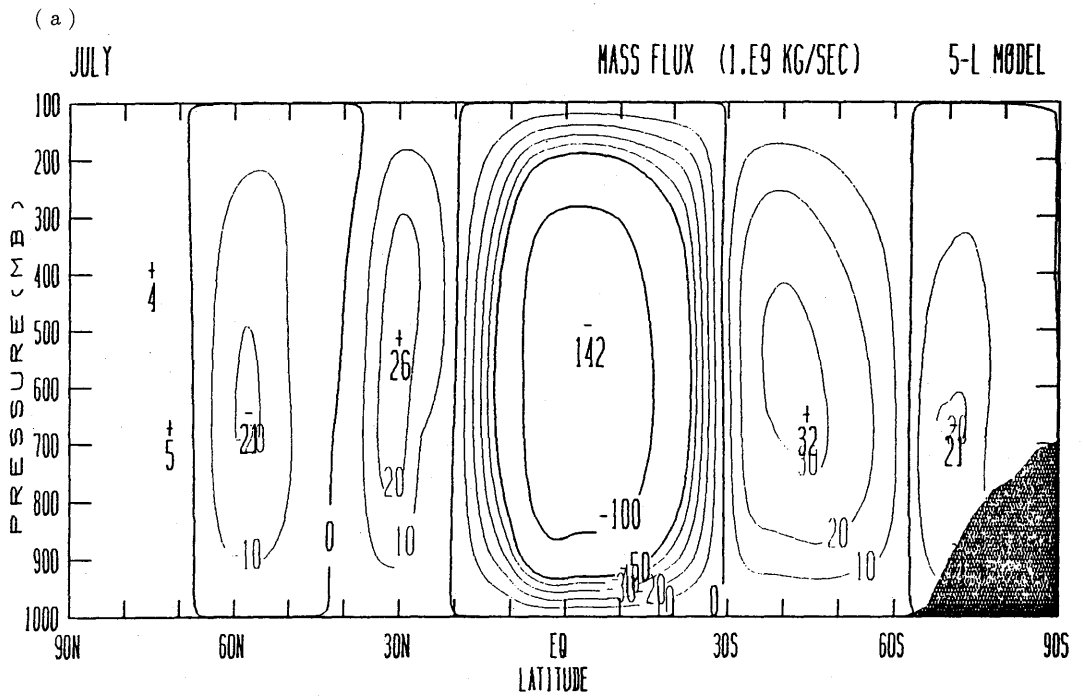


Fig. AIII.3.xx Same as in Fig. AIII.1.xx but for July.

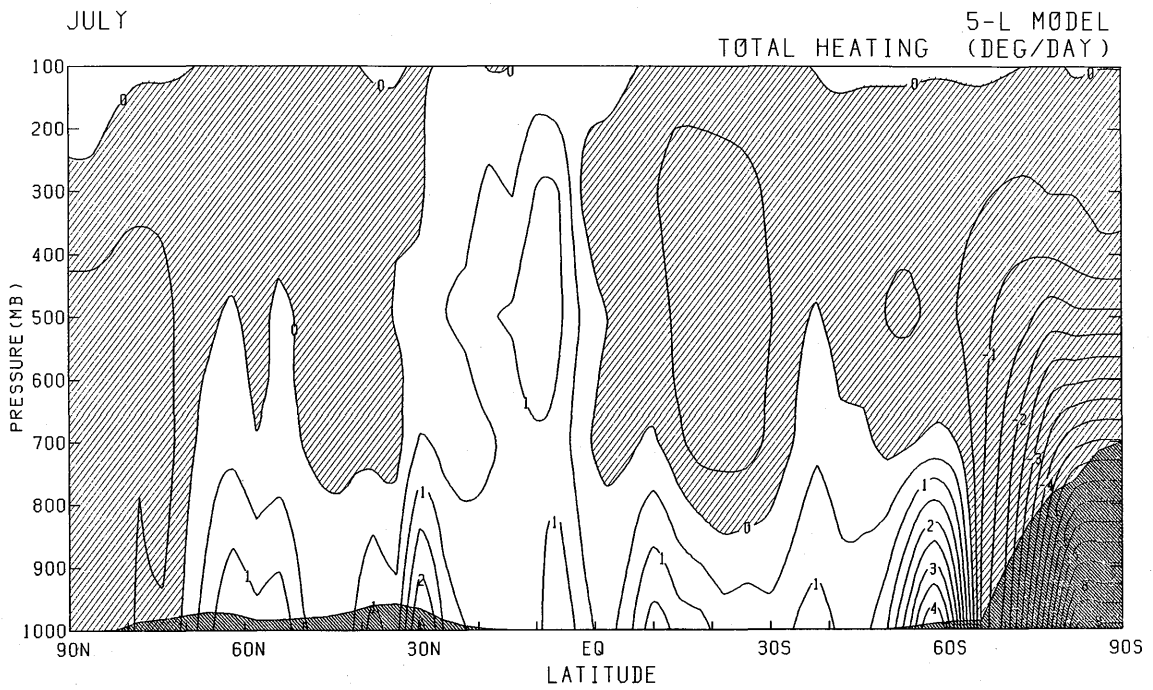


Fig. AIII.3.xxi Same as in Fig. AIII.1.xxi but for July.

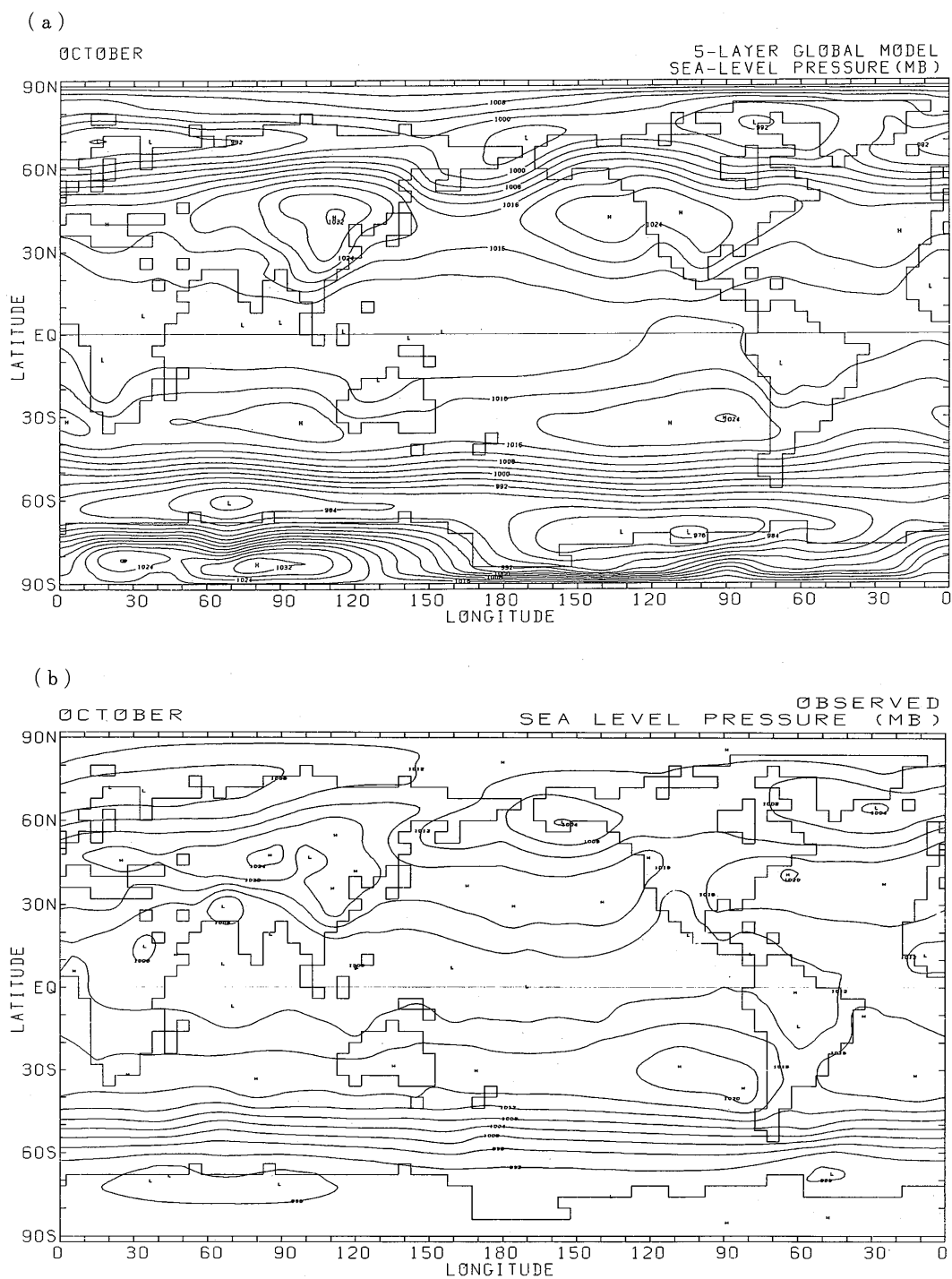
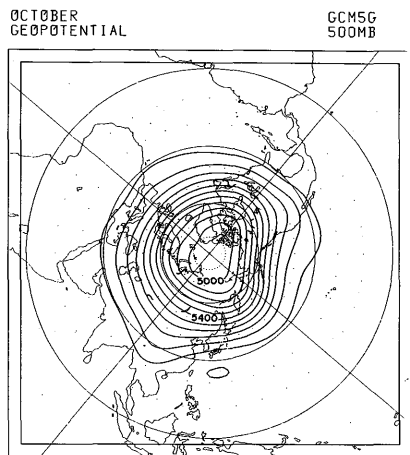
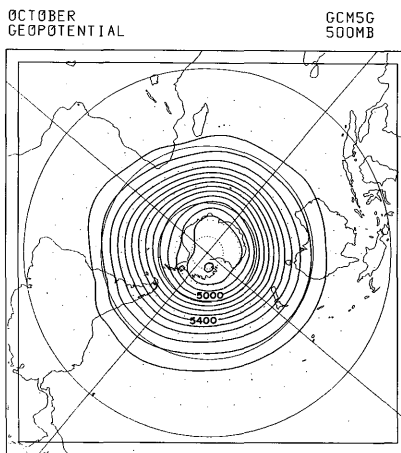


Fig. AIII.4.i Same as in Fig. AIII.1.i but for October.

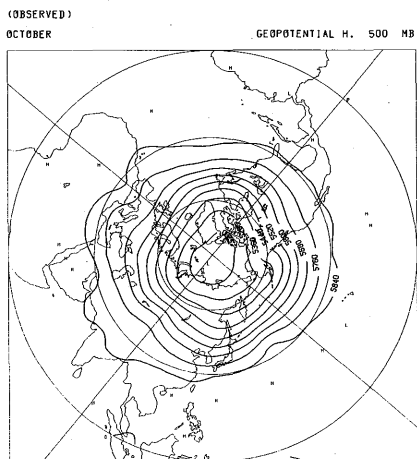
(a-1)



(a-2)



(b-1)



(b-2)

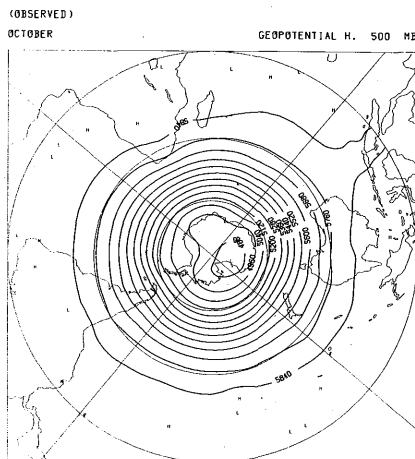


Fig. AIII.4.ii Same as in Fig. AIII.1.ii but for October.

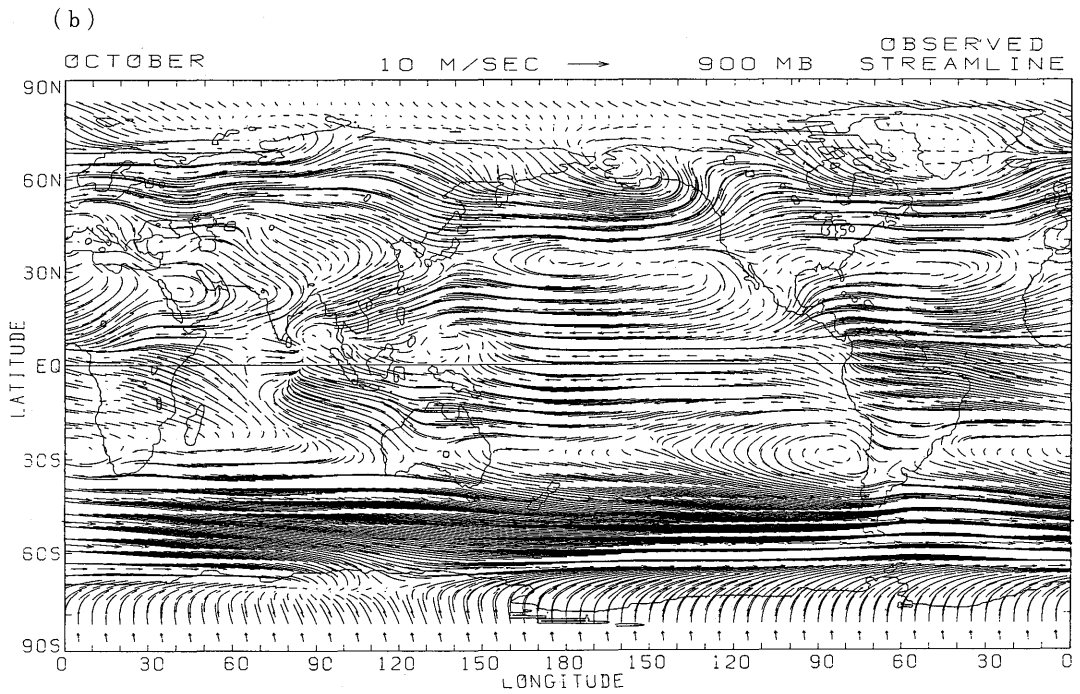
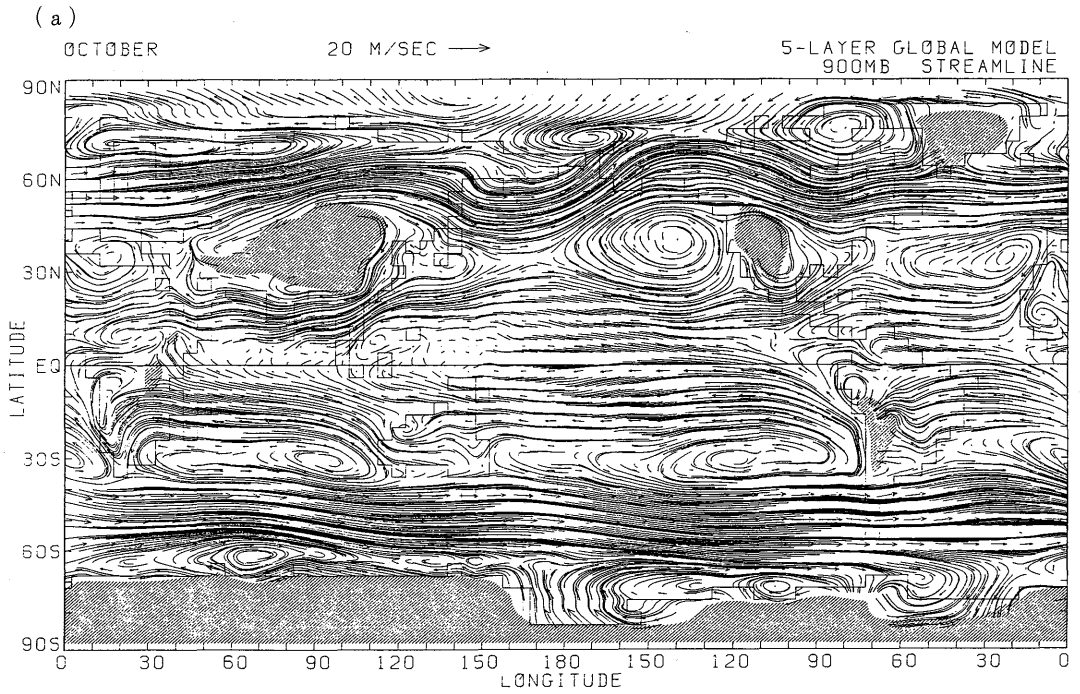


Fig. AIII.4.iii Same as in Fig. AIII.1.iii but for October.

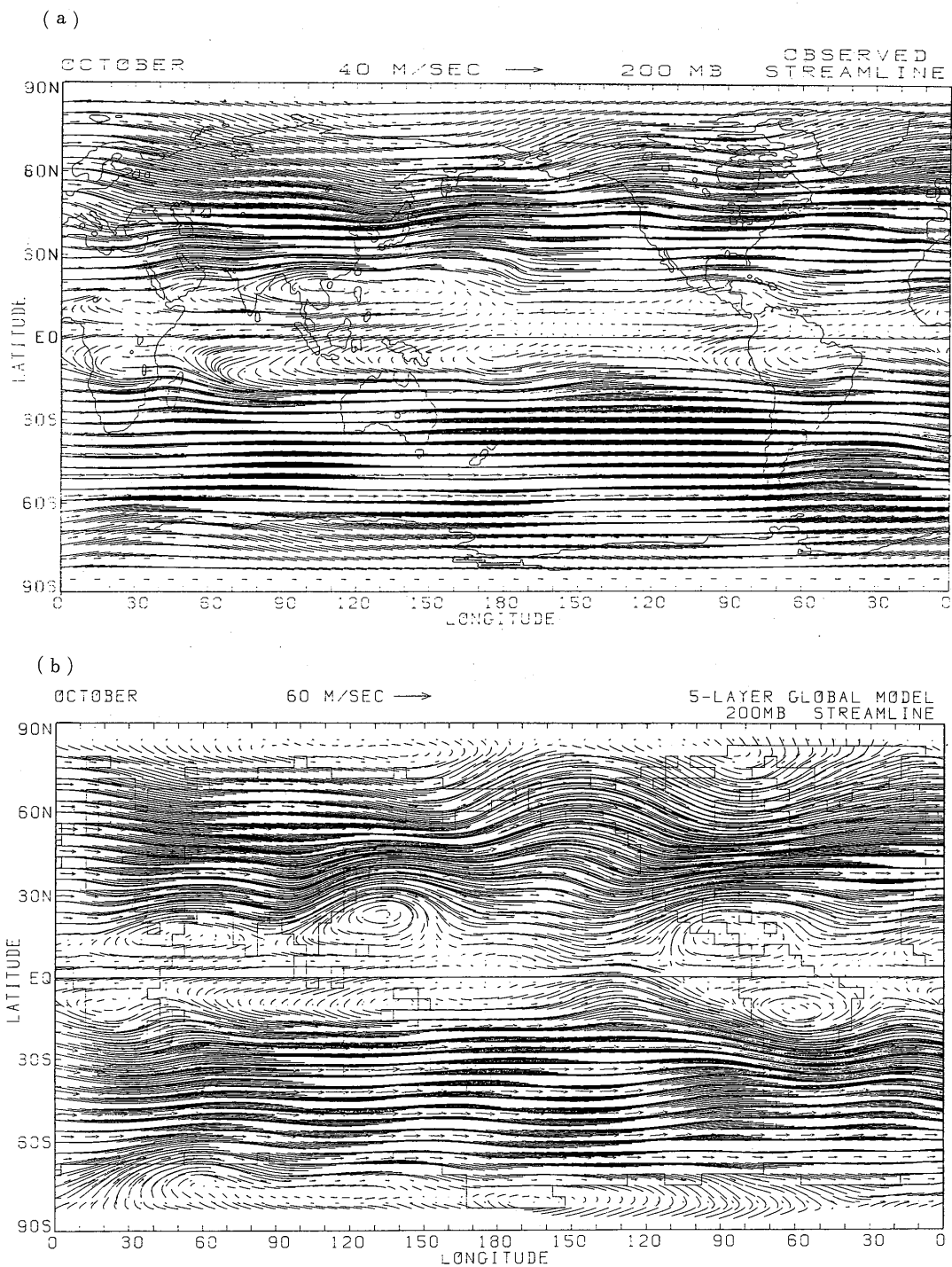


Fig. AIII.4.iv Same as in Fig. AIII.1.iv but for October.

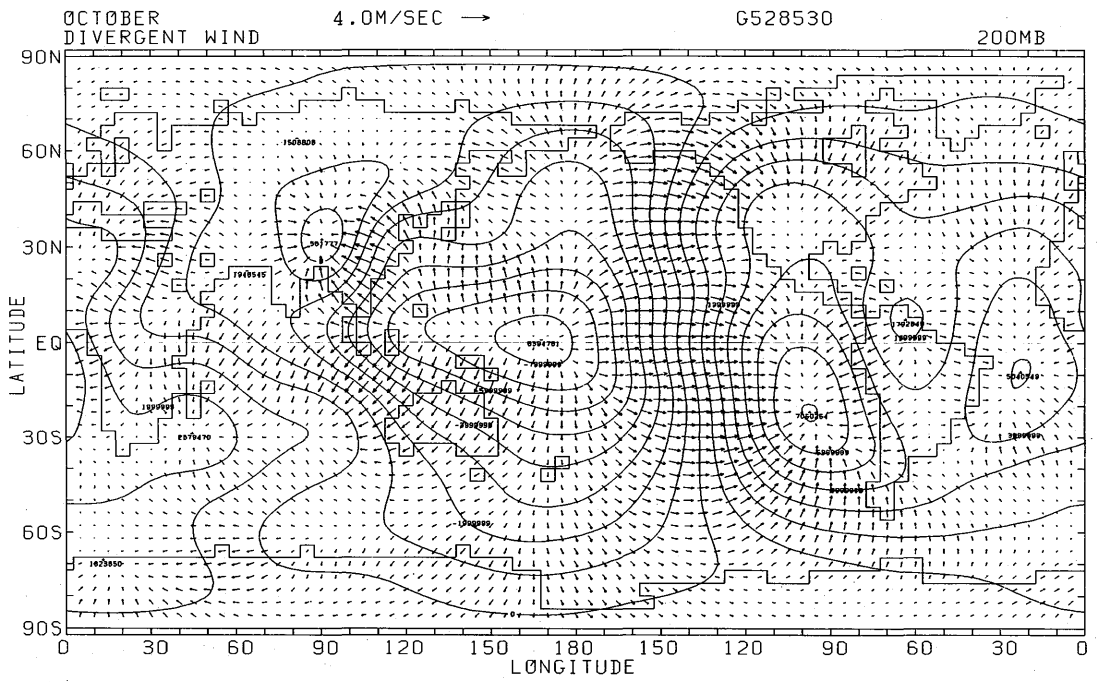


Fig. AIII.4.v Same as in Fig. AIII.1.v but for October.

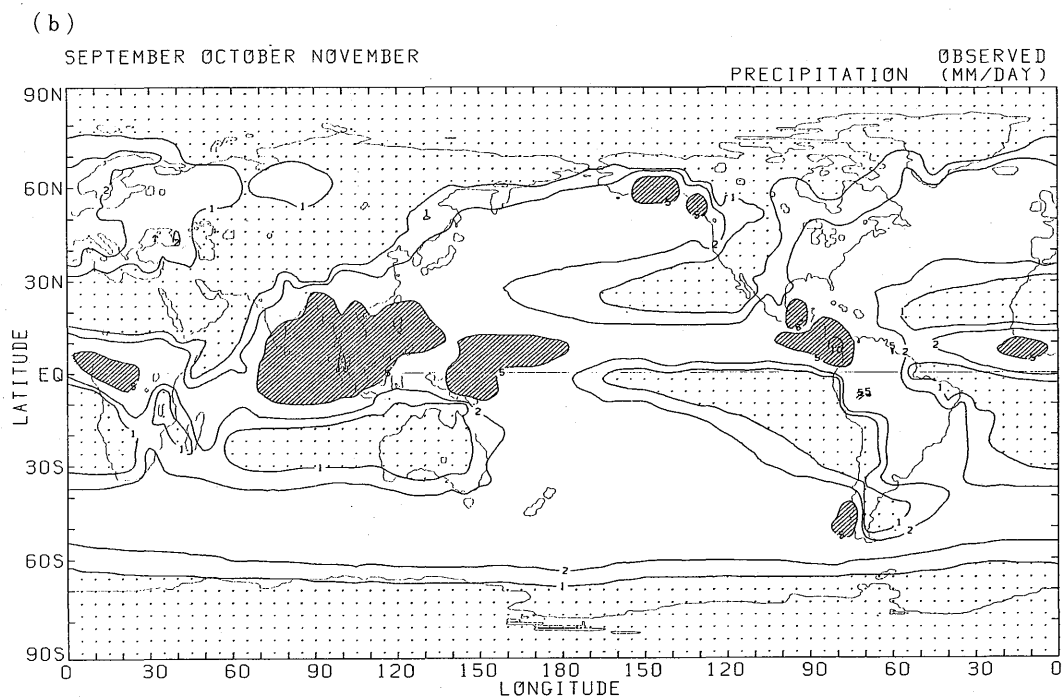
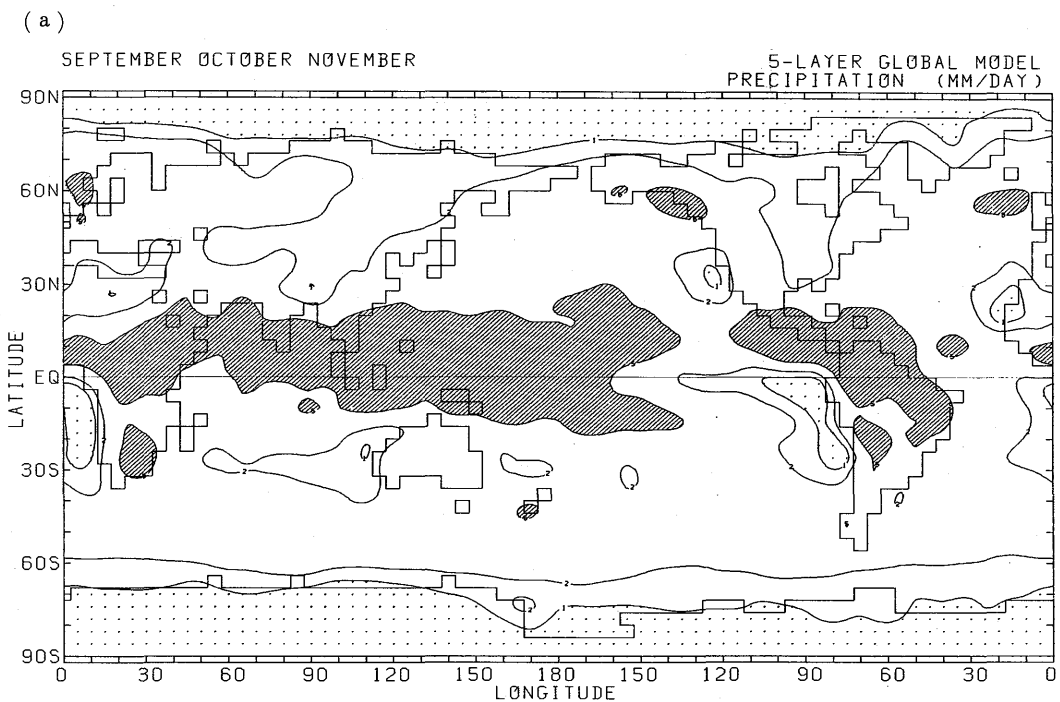


Fig. AIII.4.vi Same as in Fig. AIII.1.vi but for September, October and November.

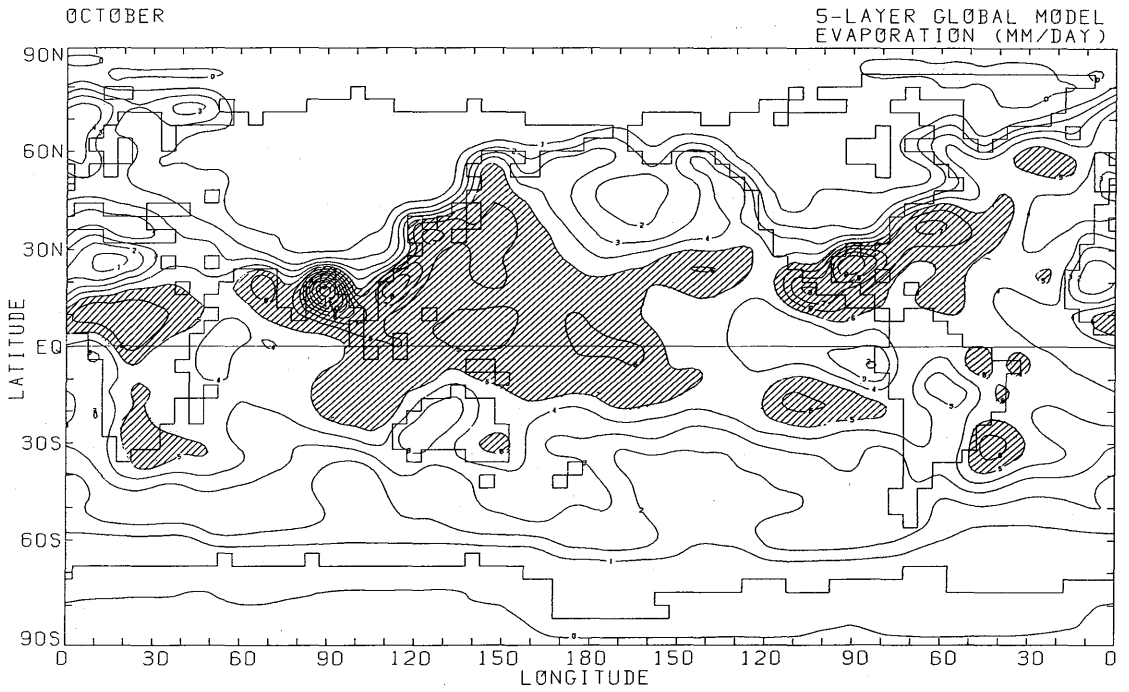


Fig. AIII.4.vii Same as in Fig. AIII.1.vii but for October.

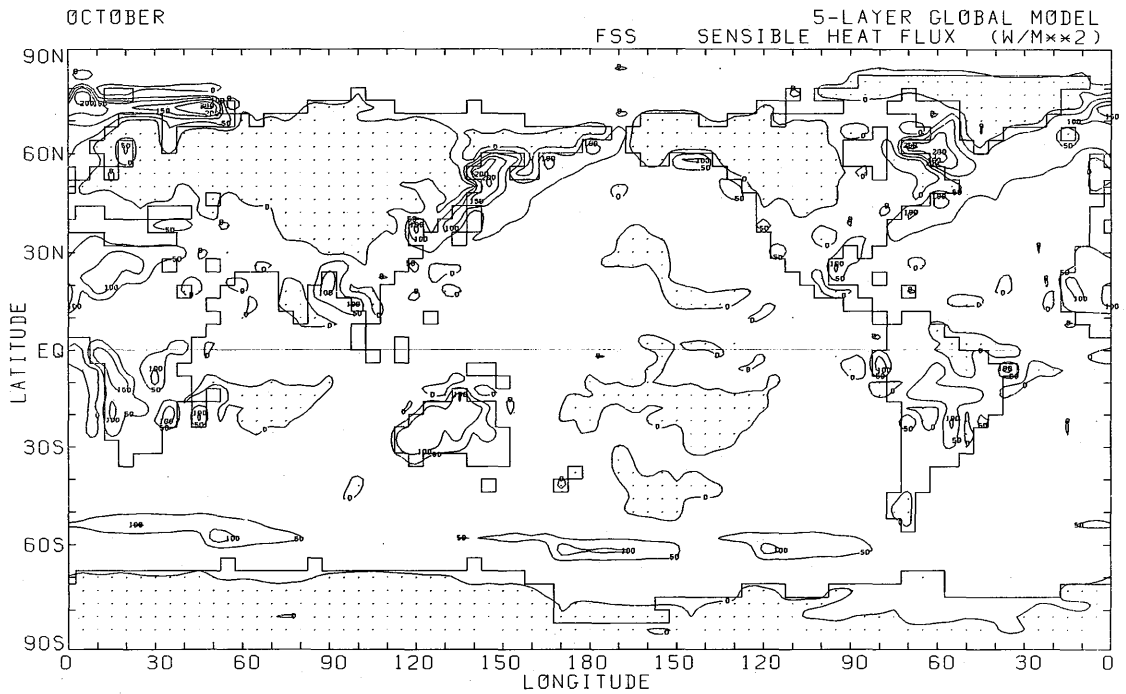


Fig. AIII.4.viii Same as in Fig. AIII.1.viii but for October.

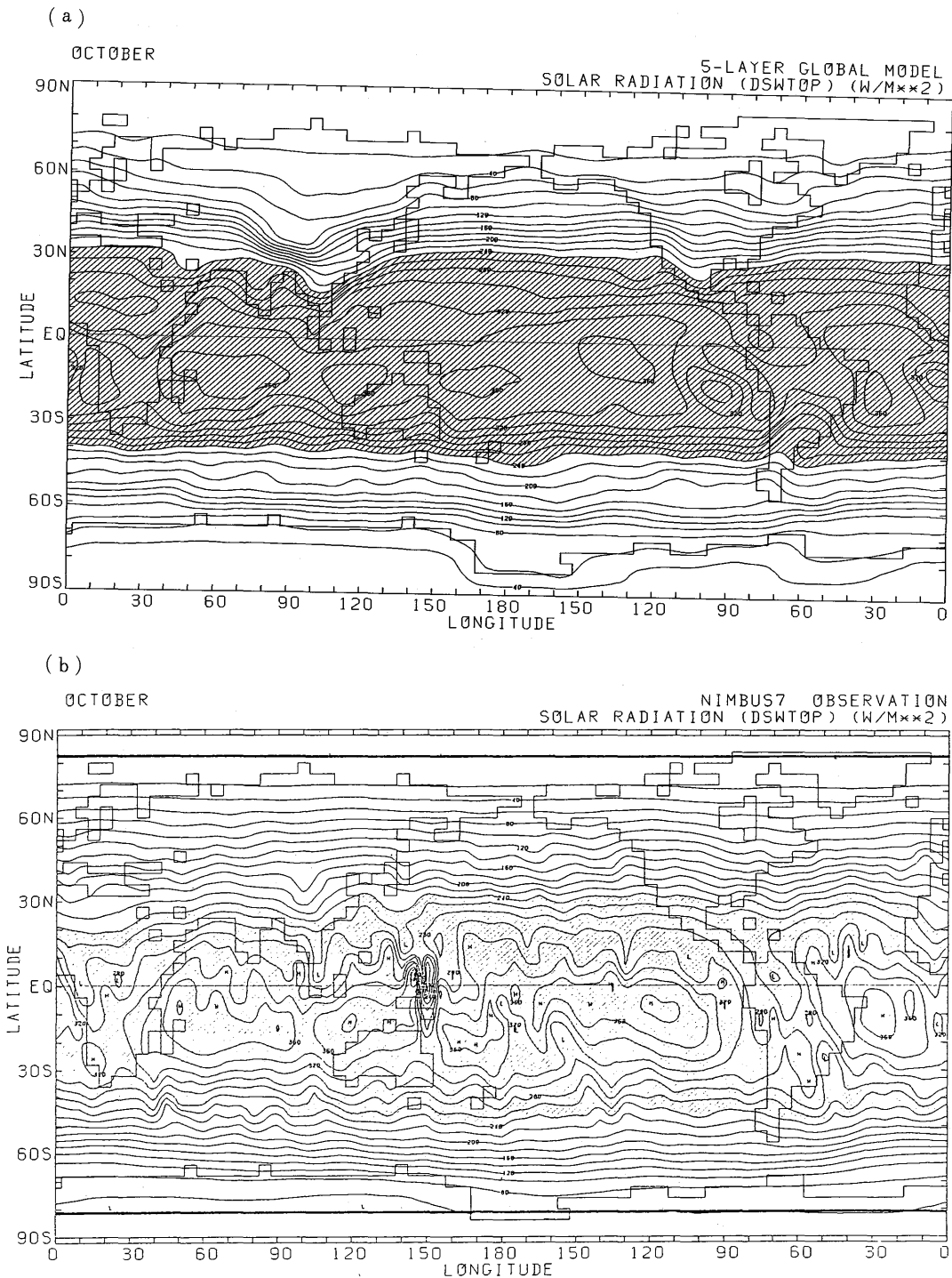


Fig. AIII.4.ix Same as in Fig. AIII.1.ix but for October.

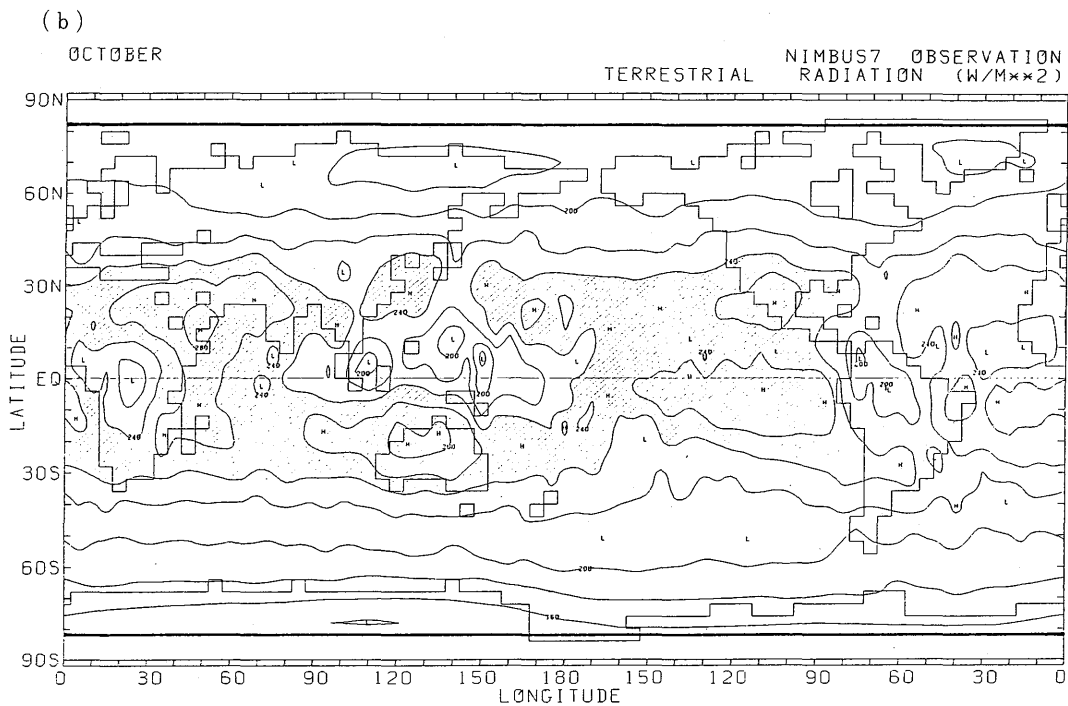
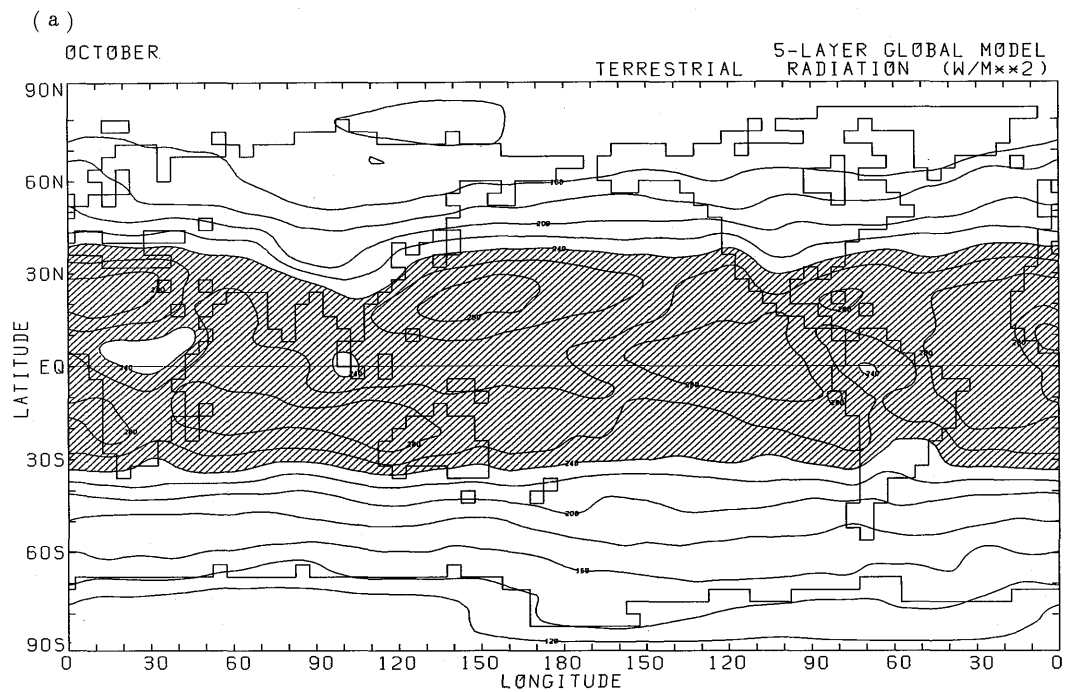
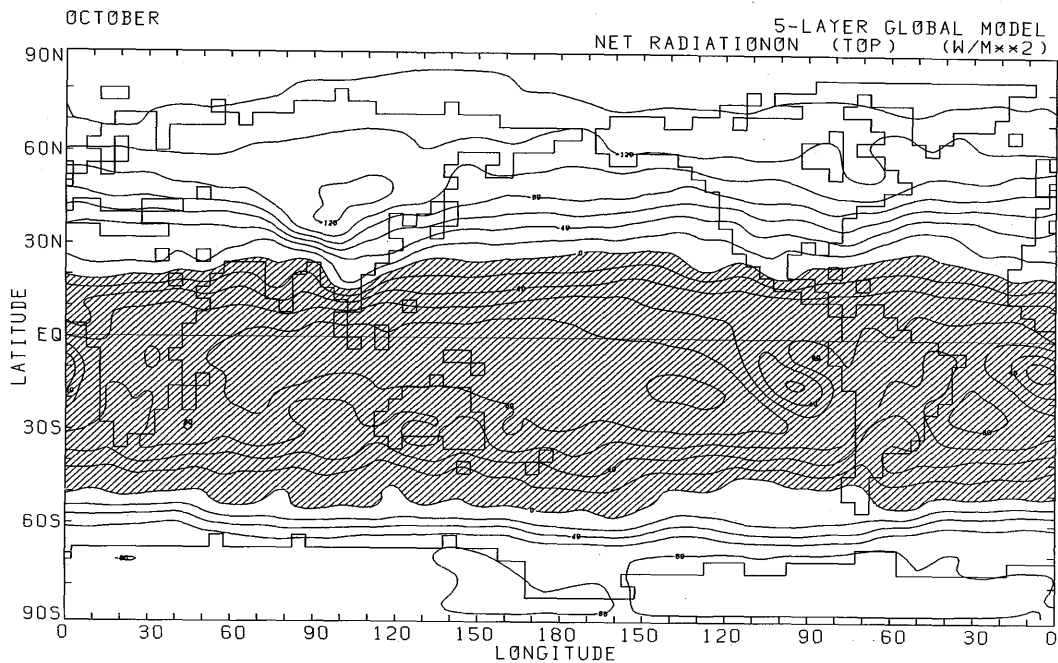


Fig. AIII.4.x Same as in Fig. AIII.1.x but for October.

(a)



(b)

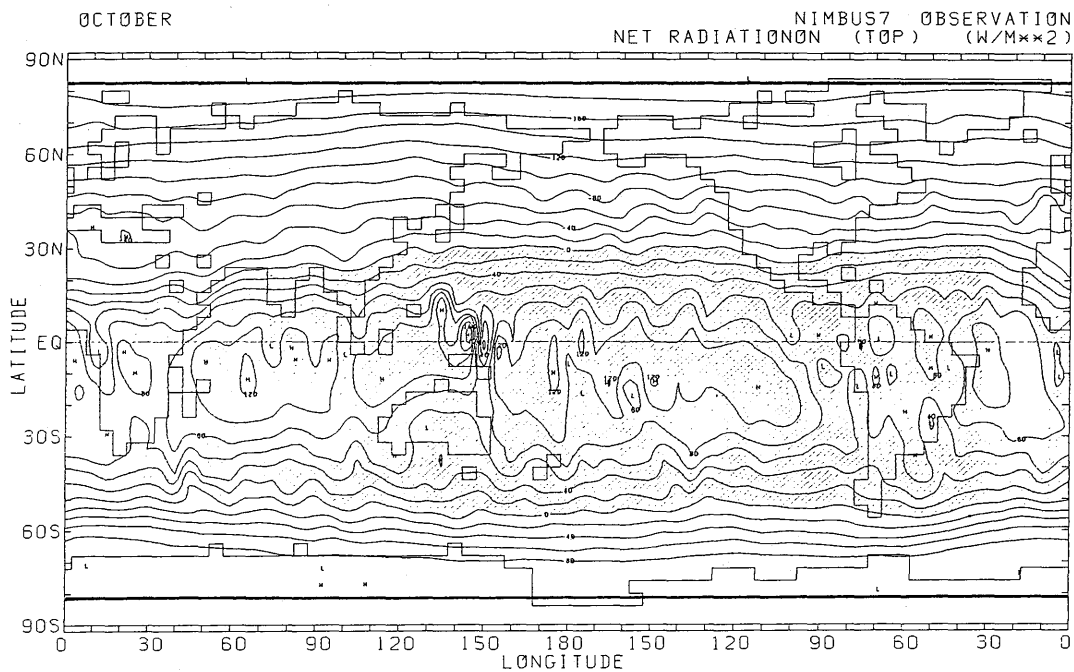


Fig. AIII.4.xi Same as in Fig. AIII.1.xi but for October.

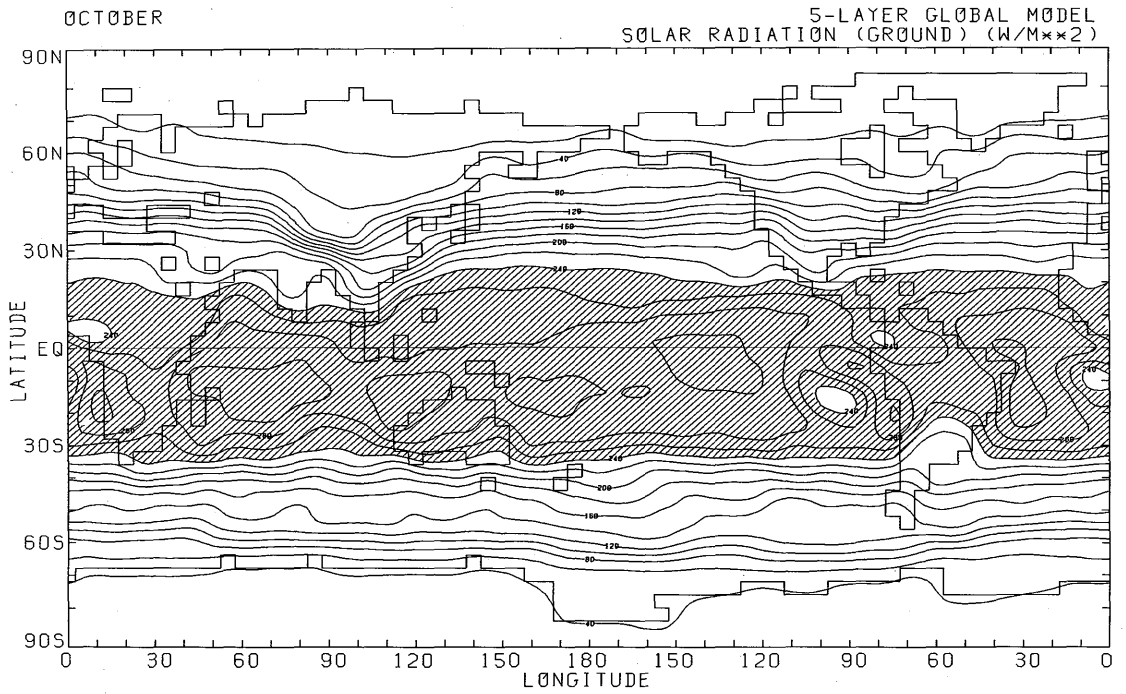


Fig. AIII.4.xii Same as in Fig. AIII.1.xii but for October.

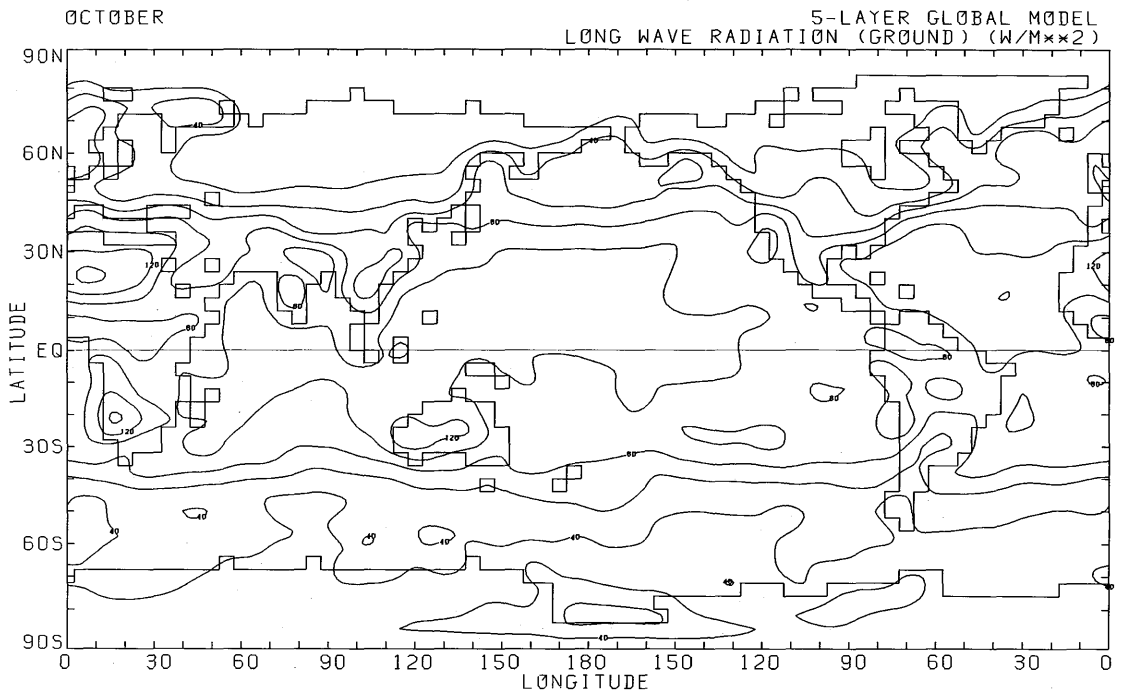


Fig. AIII.4.xiii Same as in Fig. AIII.1.xiii but for October.

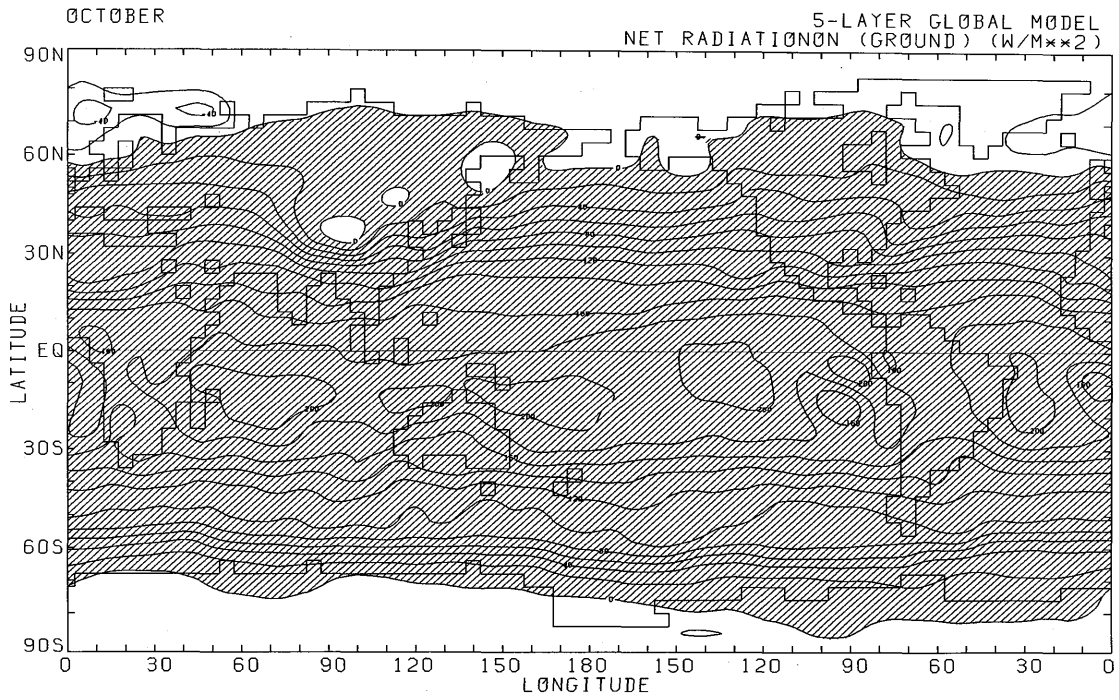


Fig. AIII.4.xiv Same as in Fig. AIII.1.xiv but for October.

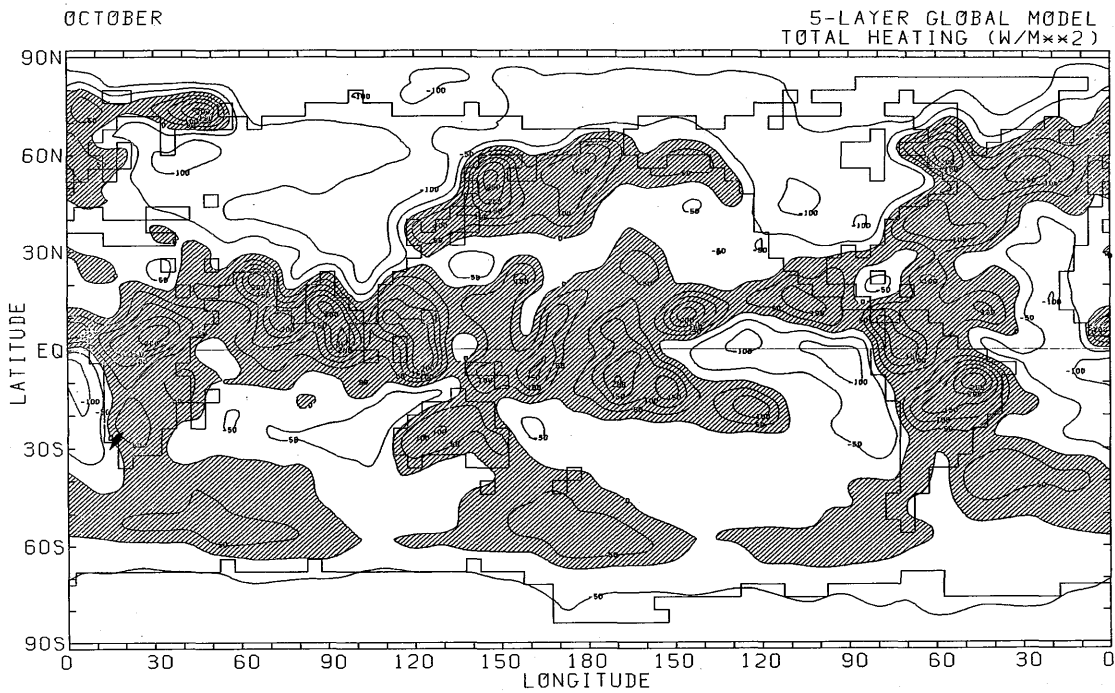


Fig. AIII.4.xv Same as in Fig. AIII.1.xv but for October.

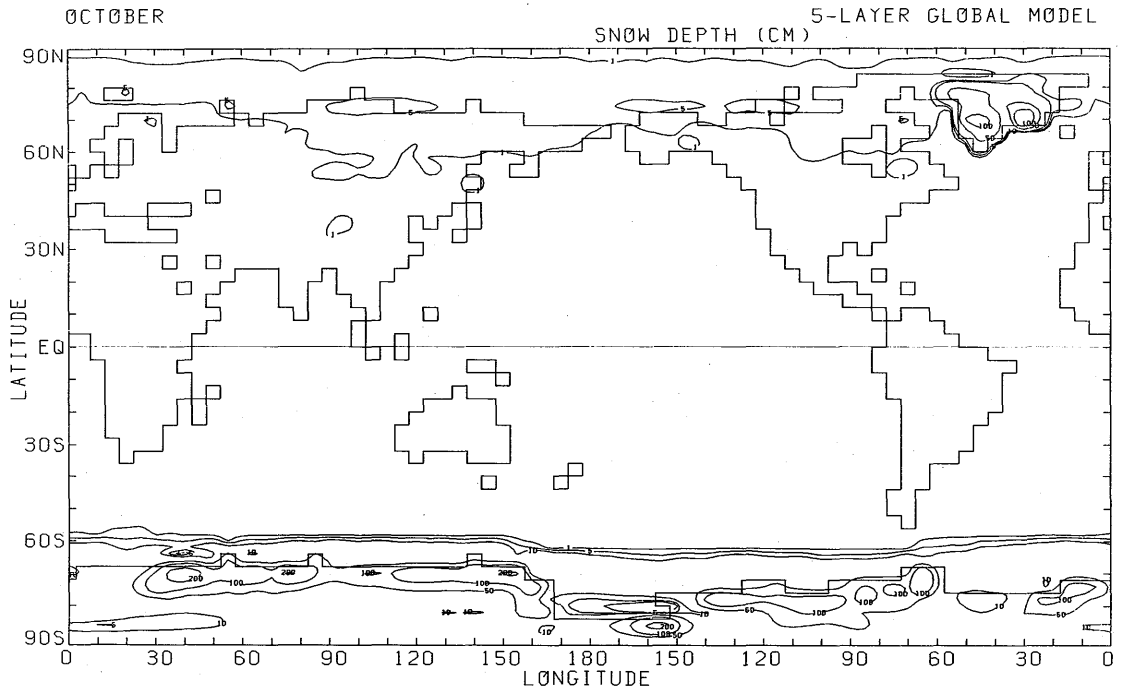


Fig. AIII.4.xvi Same as in Fig. AIII.1.xvi but for October.

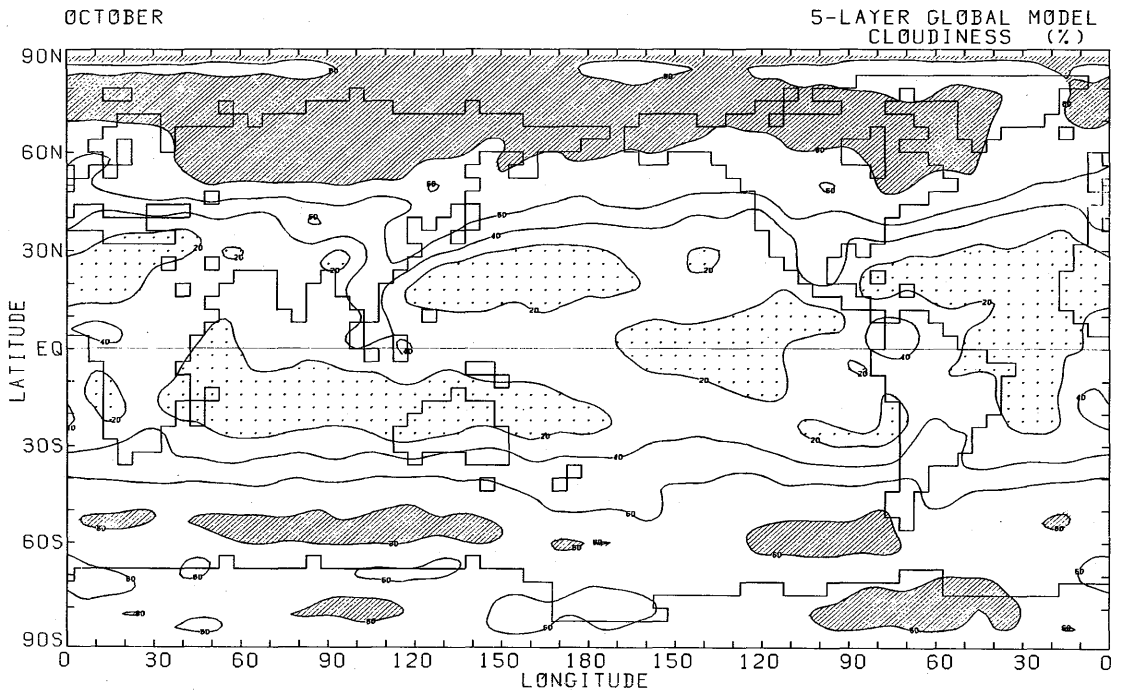


Fig. AIII.4.xvii Same as in Fig. AIII.1.xvii but for October.

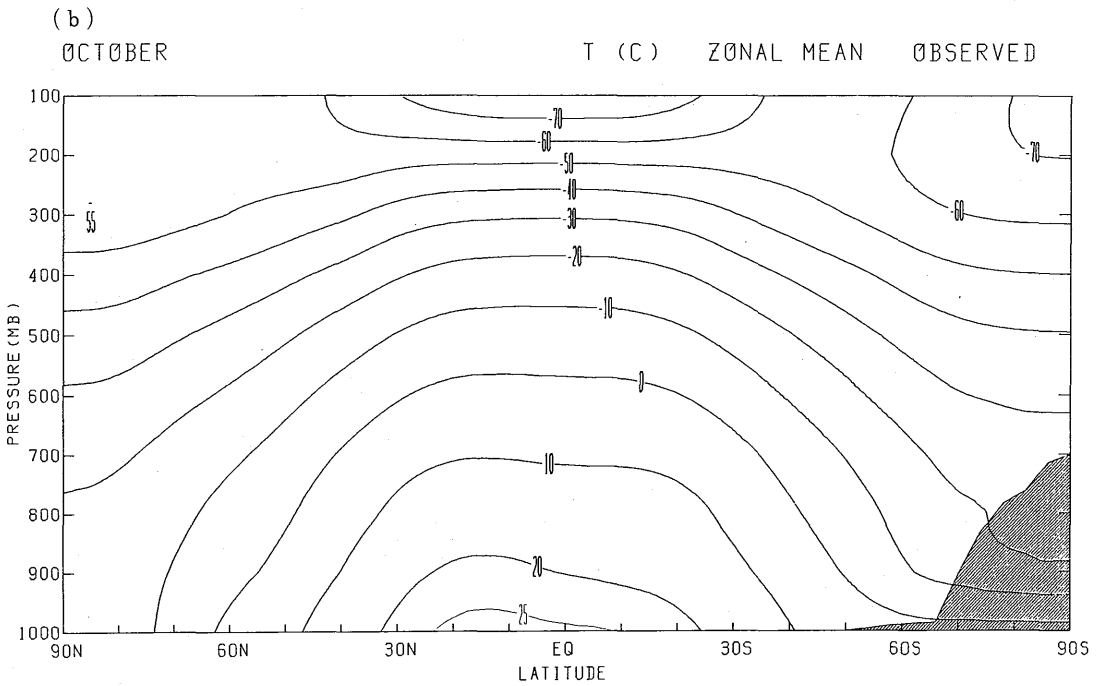
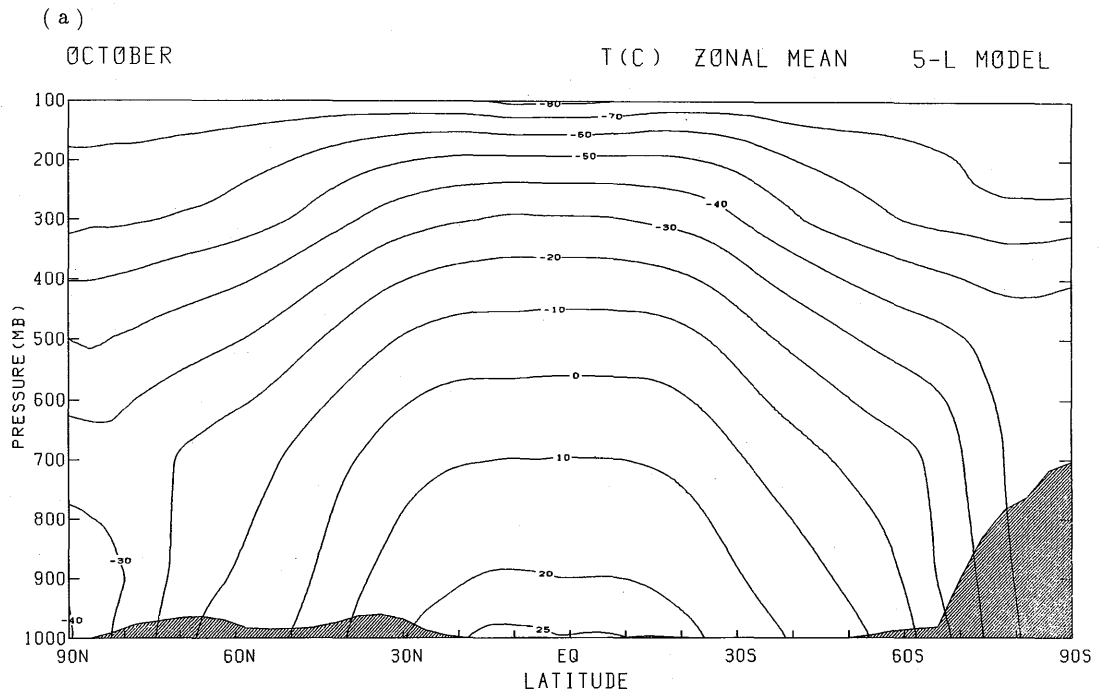


Fig. AIII.4.xviii Same as in Fig. AIII.1.xviii but for October.

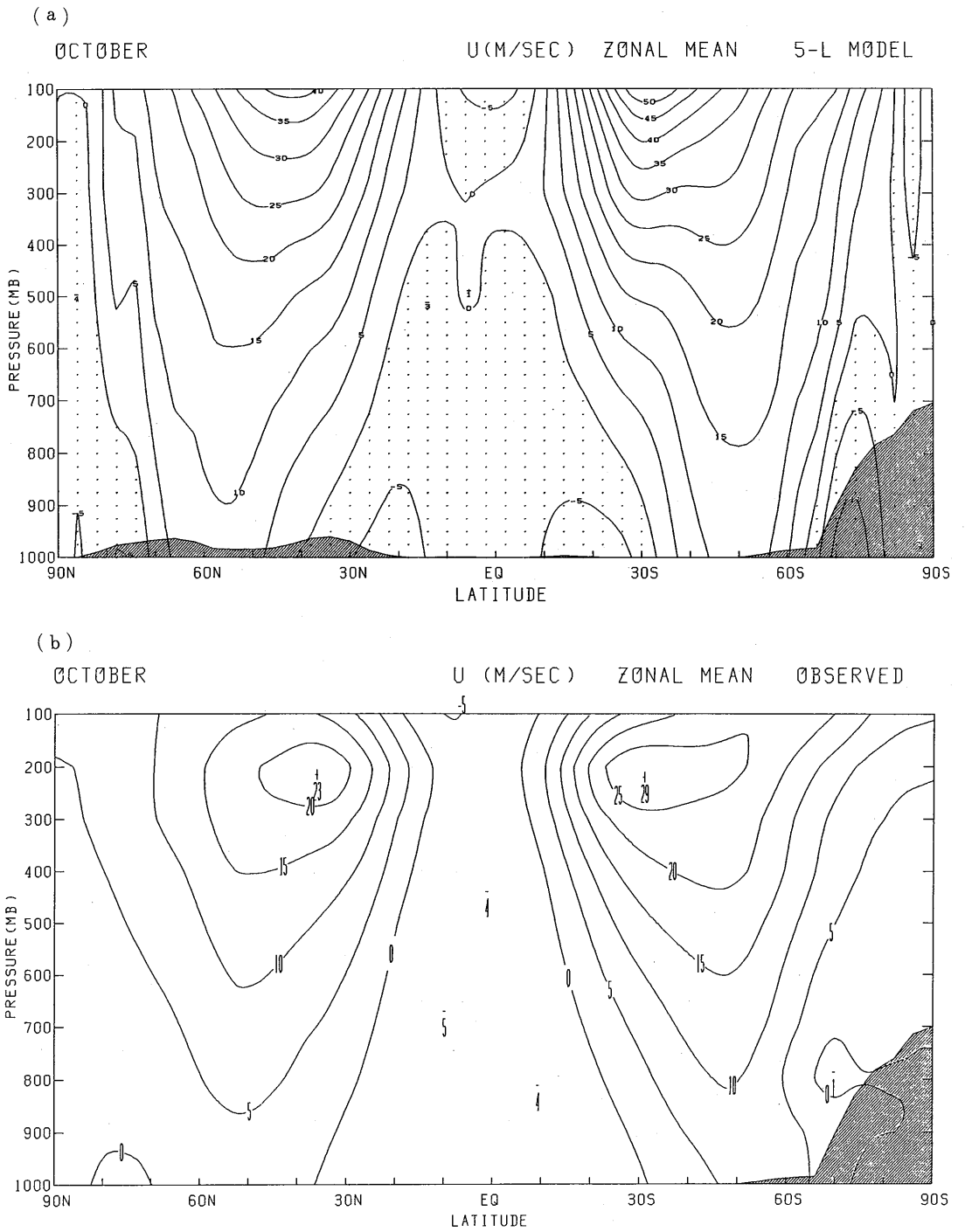


Fig. AIII.4.xix Same as in Fig. AIII.1.xix but for October.



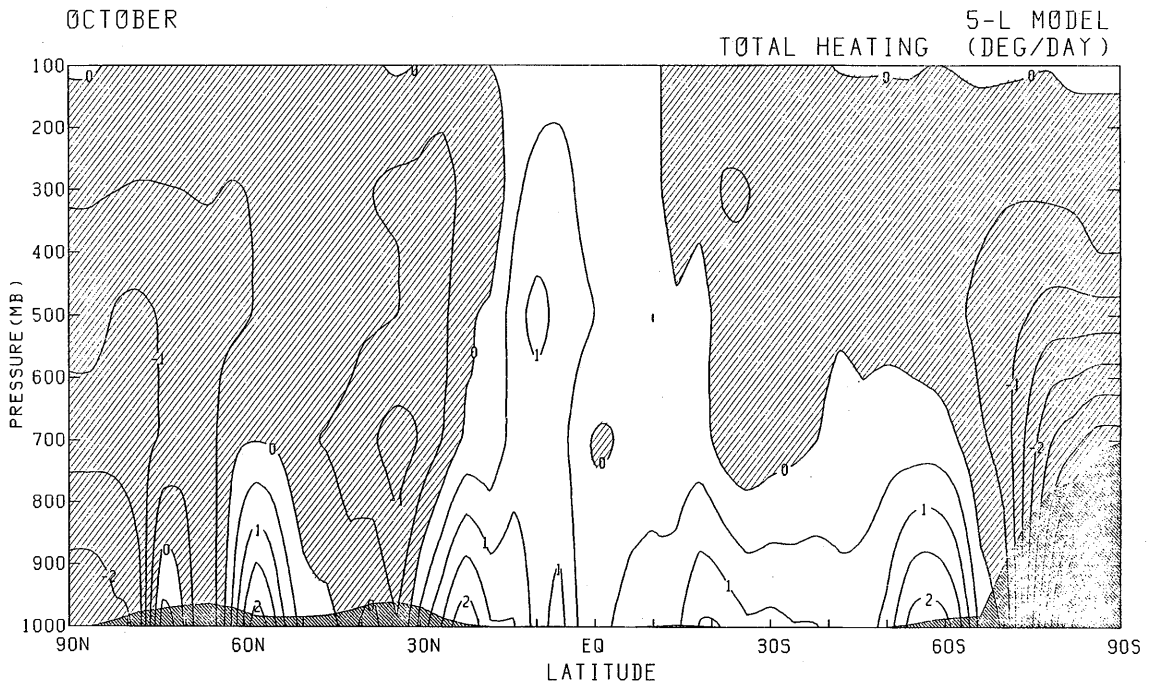


Fig. AIII.4.xxi Same as in Fig. AIII.1.xxi but for October.

References

- Ackerman, B., 1963 : Some observations of water contents in hurricanes. *J. Atmos. Sci.*, **20**, 238-298.
- Ackerman, M., 1971 : Ultraviolet solar radiation related to mesospheric processes, *Mesospheric Models and Related Experiments*. Ed. G. Fiocco, Reidel, Dordrecht-Holland, pp. 149-159.
- Arakawa, A., 1972 : Design of the UCLA general circulation model. Numerical Simulation of Weather and Climate. Tech. Rept. No. 7, Dept. of Meteorology, UCLA, 116 pp.
- \_\_\_\_\_, 1975 : Modelling clouds and cloud processes for use in climate models. GARP Publ. Ser. **16**, 183-197.
- \_\_\_\_\_, and V. Lamb, 1977 : Computational design of the basic dynamical processes of the UCLA general circulation model. *Methods in Computational Physics*, Advances in Research and Application, Vol. 17 : General circulation models of the atmosphere, Academic Press, Inc, 337 pp.
- \_\_\_\_\_, and Y. Mintz, 1974 : The UCLA atmospheric general circulation model. Notes distributed at the workshop 25 March-4 April 1974, Dept. of Meteorology, UCLA, 404 pp.
- \_\_\_\_\_, and W. H. Schubert, 1974 : Interaction of a cumulus ensemble with the large-scale environment, Part I. *J. Atmos. Sci.*, **31**, 674-701.
- Beland, M. and T. Warn, 1975 : The radiation condition for transient Rossby waves. *J. Atmos. Sci.*, **32**, 1873-1880.
- Betts, A. K., 1973 : Non-precipitating cumulus convection and its parameterization. *Quart. J. Roy. Met. Soc.*, **99**, 178-196.
- Businger, J. A., J. C. Wyngaard, Y. Izumi and E. F. Bradley, 1971 : Flux-profile relationships in the atmospheric surface layer. *J. Atmos. Sci.*, **28**, 181-189.
- Chapman, S. and R. S. Lindzen, 1970 : Atmospheric tides. Gordon and Breach Science Publishers, New York, 200pp.
- CIAP, 1974 : *The Natural Stratosphere of 1974, CIAP Monograph 1*. Ed. A. J. Grobecker, Department of Transportation, Climatic Impact Assessment Program, Washington, D. C, 1199 pp.
- Coulson, K. L., 1959 : Radiative flux from the top of a Rayleigh atmosphere. Ph. D. dissertation, Department of Meteorology, University of California, Los Angeles, 176 pp.
- Cunnold D., F. Alyea, N. Phillips and R. Prinn, 1975 : A three dimensional dynamical chemical model of atmospheric ozone. *J. Atmos. Sci.*, **32**, 170-194.
- Deardorff, J. W., 1972 : Parameterization of the planetary boundary layer for use in general circulation models. *Mon. Wea. Rev.*, **100**, 93-106.
- \_\_\_\_\_, 1976 : On the entrainment rate of a stratocumulus-topped mixed layer. *Quart. J. Roy. Meteor. Soc.*, **102**, 563-582.
- \_\_\_\_\_, 1980 : Cloud top entrainment instability. *J. Atmos. Sci.*, **37**, 131-147.
- Dickinson, R. E., 1973 : Method of parameterization for infrared cooling between the altitudes of 30 and 70 kilometers. *J. Geophys. Res.*, **78**, 4451-4457.
- Dopplick, T. G., 1970 : Global radiative heating of the earth's atmosphere. Rept. No. 24, Planet. Circ. Project, Dept. of Meteorology, MIT, 128 pp. (Nuclear Science Abstracts, Cumulative Report Number Index MIT-2241-58)
- \_\_\_\_\_, 1979 : Radiative heating of the global atmosphere : Corrigendum. *J. Atmos. Sci.*, **36**, 1812-1817.
- Elsasser, W. M., 1960 : Atmospheric radiation tables, *Meteorological Monographs*, vol. 4, No. 23, American Meteorol. Soc., Boston, 43 pp.
- Holloway, J. L. Jr., and S. Manabe, 1971 : Simulation of climate by a global circulation model : I. Hydrologic cycle and heat balance. *Mon. Wea. Rev.*, **99**, 335-370.

- Jacobowitz, H., and R. J. Tighe, and the NIMBUS 7 ERB Experiment Team, 1984 : The earth radiation budget derived from the NIMBUS 7 earth radiation budget experiment. *J. Geophys. Res.*, **89**, 4997-5010.
- Jordan, C. L., 1958 : Mean soundings for the West Indies area. *J. Meteor.*, **15**, 91-97.
- Joseph, J. H., 1966 : Calculation of radiative heating in numerical general circulation models. Technical Report No. 1, Department of Meteorology, University of California, Los Angeles, 60 pp.
- \_\_\_\_\_, 1970 : On the calculation of solar radiation fluxes in the troposphere. *Solar Energy*, **13**, 251-261.
- Katayama, A., 1972 : A simplified scheme for computing radiative transfer in the troposphere. Technical Report No. 6, Department of Meteorology, University of California, Los Angeles, 77 pp.
- Kato, H. and O. M. Phillips, 1969 : On the penetration of a turbulent layer into stratified fluid. *J. Fluid Mech.*, **37**, 643-655.
- Kim, J.-W., 1976 : A generalized bulk model of the oceanic mixed layer. *J. Phys. Oceanogr.*, **6**, 686-695.
- Kitoh, A. and T. Tokioka, 1985 : A simulation of the tropospheric general circulation with the MRI atmospheric general circulation model. Part II : July performance. (to be submitted)
- Kockarts, G., 1971 : Penetration of solar radiation in the Schuman Runge bands of molecular oxygen. *Mesospheric models and Related Experiments*, Ed. G. Fiocco, Reidel, Dordrecht-Holland, 160-176.
- Krueger, A. J., 1973 : The mean ozone distribution from several series of rocket soundings to 52 km at latitudes from 58°S to 64°N. *Pure and Appld. Geophys.*, **106-108**, 1254-1263.
- Lacis, A. A., and J. E. Hansen, 1974 : A parameterization for the absorption of solar radiation in the earth's atmosphere. *J. Atmos. Sci.*, **31**, 118-133.
- Lindzen, R. S., E. S. Batten and J.-W. Kim, 1968 : Oscillations in atmospheres with tops. *Mon. Wea. Rev.*, **96**, 133-140.
- Lord, S. J., 1982 : Interaction of a cumulus ensemble with the large-scale environment. Part III : Semi-prognostic test of the Arakawa-Schubert cumulus parameterization. *J. Atmos. Sci.*, **39**, 88-103.
- \_\_\_\_\_, and A. Arakawa, 1980 : Interaction of a cumulus ensemble with the large-scale environment. Part II. *J. Atmos. Sci.*, **37**, 2677-2692.
- \_\_\_\_\_, W. C. Chao and A. Arakawa, 1982 : Interaction of a cumulus ensemble with the large-scale environment. Part IV : The discrete model. *J. Atmos. Sci.*, **39**, 104-113.
- Lungren, T. S. and F. C. Wang, 1973 : Eddy viscosity models for free turbulent flows. *Phys. Fluids.*, **16**, 174-178.
- Manabe, S., and F. Möller, 1861 : On the radiative equilibrium and heat balance of the atmosphere. *Mon. Wea. Rev.*, **89**, 503-532.
- \_\_\_\_\_, and R. T. Wetherald, 1967 : Thermal equilibrium of the atmosphere with a given distribution of relative humidity. *J. Atmos. Sci.*, **24**, 241-259.
- McClatchey, R. A., R. W. Fenn, J. E. A. Selby, F. E. Volz, and J. S. Goring, 1972 : Optical properties of the atmosphere, AFCRL 72-0497, 108 pp.
- Oort, A. H., 1983 : Global atmospheric circulation statistics, 1958-1973. NOAA Professional Paper 14. 180 pp.
- Orlanski, I., 1976 : A simple boundary condition for unbounded hyperbolic flows. *J. Comp. Phys.*, **21**, 251-269.
- Pearson, R. A., 1974 : Consistent boundary conditions for numerical models of systems that admit dispersive waves. *J. Atmos. Sci.*, **31**, 1418-1489.

- Randall, D., 1976 : The interaction of the planetary boundary layer with large-scale circulations. Ph. D. dissertation, The University of California, Los Angeles, 247 pp.
- \_\_\_\_\_, 1980 : Conditional instability of the first kind upside-down. *J. Atmos. Sci.*, **37**, 125-130.
- Rodgers, C. D., 1967 : The radiative heat budget of the troposphere and lower stratosphere. Planetary Circulation Project, Department of Meteorology, MIT, Rep. No. 2, 99 pp.
- Sasamori, T., 1968 : The radiative cooling calculation for application to general circulation experiments *J. Appl. Meteorol.*, **7**, 721-729.
- Schlesinger, M. E., 1976 : A Numerical simulation of the general circulation of atmospheric ozone. Ph. D. dissertation, University of California, Los Angeles, 376 pp.
- \_\_\_\_\_ and Y. Mintz, 1979 : Numerical simulation of ozone production, transport and distribution with a global atmospheric general circulation model. *J. Atmos. Sci.*, **36**, 1325-1361.
- Schubert, W. H., 1973 : The interaction of a cumulus ensemble with the large-scale environment. Ph. D. Dissertation, UCLA, 168 pp.
- Schutz, C. and W. L. Gates, 1972 : Global climatic data for surface, 800mb, 400mb.: July. Advanced Research Projects Agency, Rep. R-1029-ARPA, Rand Corporation, Santa Monica, 180 pp.
- Stull, R. B., 1976 : The energetics of entrainment across a density interface. *J. Atmos. Sci.*, **33**, 1260-1267.
- Suarez, M. J. and A. Arakawa, 1981 : First Conference on Climate Variation, AMS, 19-23 January 1981, San Diego, Calif.
- \_\_\_\_\_, \_\_\_\_\_ and D. A. Randall, 1983 : The parameterization of the planetary boundary layer in the UCLA general circulation model : formulation and results. *Mon. Wea. Rev.*, **111**, 2224-2243.
- Tokioka, T., 1978 : Some considerations on vertical differencing. *J. Meteor. Soc. Japan*, **56**, 98-111.
- \_\_\_\_\_, A. Kitoh, I. Yagai and K. Yamazaki, 1985 : A simulation of the tropospheric general circulation with the MRI atmospheric general circulation model. Part I : The January performance. *J. Meteor. Soc. Japan*. (to be published)
- \_\_\_\_\_ and I. Yagai, 1984 : On the January simulation of stratospheric circulations with the MRI general circulation model : Preliminary results. *Dynamics of the Middle Atmosphere*, Ed. J. R. Holton and T. Matsuno, Reidel, Dordrecht-Holland, 527-537.
- Winninghoff, F. J., 1968 : On the adjustment towards a geostrophic balance in a simple primitive equation model with application to the problems of initialization and objective analysis. Ph. D. Dissertation, Dept. of Meteorology, UCLA, 161 pp.
- Wurtele, M. G., J. Paegle and A. Sielecki, 1971 : The use of open boundary conditions with the storm-surge equations. *Mon. Wea. Rev.*, **99**, 537-544.
- Yamada, T., 1976 : On the similarity functions A, B and C of the planetary boundary layer. *J. Atmos. Sci.*, **33**, 781-793.
- Yamamoto, G., 1952 : On a radiation chart. *Sci. Rept. Tohoku Univ.*, S. 5, Geophysics, **4**, 9-23.
- Yanai, M., J.-H. Chu, T. E. Stark and T. Nitta, 1976 : Response of deep and shallow tropical maritime cumuli to large-scale processes. *J. Atmos. Sci.*, **33**, 976-991.

# 気 象 研 究 所

1946 (昭和21年) 設立

所 長 : 理 博 竹 内 清 秀

予報研究部	部 長 :	吉 田 泰 治
台風研究部	部 長 :	理 博 相 原 正 彦
物理気象研究部	部 長 :	理 博 岡 林 俊 雄
応用気象研究部	部 長 :	真 島 恒 裕
気象衛星研究部	部 長 :	工 博 内 藤 恵 吉
地震火山研究部	部 長 :	理 博 市 川 政 治
海洋研究部	部 長 :	理 博 飯 田 隼 人
高層物理研究部	部 長 :	理 博 嘉 納 宗 靖
地球化学研究部	部 長 :	秋 山 勉

## 気象研究所技術報告

編集委員長 : 真 島 恒 裕

編集委員 : 山 崎 孝 治 近 藤 洋 輝 伊 藤 朋 之  
吉 川 友 章 青 柳 二 郎 岡 田 正 實  
遠 藤 昌 宏 小 寺 邦 彦 伏 見 克 彦

事務局 : 西 田 圭 子 湯 原 有 哉

気象研究所技術報告は、気象学、海洋学、地震学、その他関連の地球科学の分野において、気象研究所職員が得た研究成果に関し、技術報告、資料報告及び総合報告を掲載する。

気象研究所技術報告は、1978年(昭和53年)以降、必要の都度刊行される。

昭和60年3月30日発行 I S S N 0386-4049

編集兼発行所 気 象 研 究 所

茨城県筑波郡谷田部町長峰1-1

印 刷 所 東 京 都 小 石 川 1 - 3 - 7

勝美印刷株式会社